DOCTOR OF PHILOSOPHY

Development of a method for automating effective patient diameter estimation for digital radiography

Worrall, Mark

Award date:
2019

Development of a method for automating effective patient diameter estimation for digital radiography

Mark Worrall

PhD Thesis

University of Dundee

October 2019

Contents

Figures

Abbreviations

AAPM: American Association of Physicists in Medicine

A&E: Accident and Emergency

AEC: Automatic exposure control

ALARA: As Low As Reasonably Achievable

AP: Anterior-Posterior

BEIR: Committee on the Biological Effects of Ionising Radiation

BIPM: Bureau International des Poids et Mesures

BMI: Body mass index

BSSD: Basic Safety Standards Directive

CLT: Central limit theorem

COMARE: Committee on Medical Aspects of Radiation in the Environment

CR: Computed Radiography

CT: Computed Tomography

CTDI: Computed Tomography Dose Index

DDI: Detector dose indicator

DDR: Direct digital radiography

DHSC: Department of Health and Social Care

DI: Deviation index

DICOM: Digital Imaging and Communications in Medicine

DLP: Dose Length Product

DMS: Dose management system

DNA: Deoxyribonucleic Acid

DRL: Diagnostic Reference Level

EC: European Commission

ECD: Equivalent Cylindrical Diameter

EI: Exposure index

ESD: Entrance surface dose

EU: European Union

FDD: Focus to detector distance

HE: High equivalency

HPA: Health Protection Agency

HVL: Half Value Layer

IAEA: International Atomic Energy Agency

ICRP: International Commission on Radiological Protection

ICRU: International Commission on Radiation Units and Measurements

IEC: International Electrotechnical Commission

IPEM: Institute of Physics and Engineering in Medicine

IPSM: Institute of Physical Sciences in Medicine

IRAS: Integrated Research Application System

IR(ME)R: Ionising Radiation (Medical Exposure) Regulations

JCGM: Joint Committee for Guides in Metrology

KAP: Kerma Area Product

LDRL: Local Diagnostic Reference Level

LNT: Linear no threshold

LUT: Look up table

MDT: Multi-disciplinary team

MGD: Mean Glandular Dose

MHRA: Medicines and Healthcare products Regulatory Agency

MPE: Medical Physics Expert

NCRP: National Council on Radiation Protection and Measurements

NDRL: National Diagnostic Reference Level

NHS: National Health Service

NICE: National Institute for Health and Care Excellence

NIST: National Institute of Standards and Technology

NRC: National Research Council

NRPB: National Radiological Protection Board

PACS: Picture Archive and Communication System

PDC: Patient dose calibrator

PHE: Public Health England

PIS: Patient information sheet

PMMA: Poly(methyl methacrylate)

POPUMET: Ionising Radiation (Protection of Persons Undergoing Medical Examination or Treatment)

QC: Quality control

PV: Pixel value

RBE: Relative biological effectiveness

RCR: Royal College of Radiologists

R/F: Radiographic / Fluoroscopic

RIS: Radiology information system

SOP: Standard operating procedure

SSDL: Secondary standards dosimetry laboratory

STP: Signal transfer property

TCIA: The Cancer Imaging Archive

TZM: Titanium Zirconium Molybdenum

UNSCEAR: United Nations Scientific Committee on the Effects of Atomic Radiation

USB: Universal serial bus

WHO: World Health Organisation

Acknowledgements

Particular thanks go to my primary supervisor, Professor David Sutton, for making it possible for me to undertake this work and for his support and assistance throughout.

Thanks also to my second supervisor, Dr Sarah Vinnicombe, for her input to the project and assistance with the clinical validation study.

Finally, thanks and love to Jo for her support throughout.

Declaration

I declare that I am the author of this thesis, that all references cited have been consulted and that the work of which this thesis is a record has been done by myself. I further declare that the work presented in this thesis has not previously been accepted for a higher degree.

Signed

Mark Worrall

Summary

National patient dose audit of paediatric radiographic examinations is complicated by a lack of data containing a direct measurement of the patient diameter in the examination orientation or height and weight. This has meant that National Diagnostic Reference Levels (NDRLs) for paediatric radiographic examinations have not been updated in the UK since 2000, despite significant changes in imaging technology over that period.

This work is the first step in the development of a computational model intended to automate an estimate of paediatric patient diameter. Whilst the application is intended for a paediatric population, its development within this thesis uses an adult cohort. The computational model uses the radiographic image, the examination exposure factors and a priori information relating to the x-ray system and the digital detector.

The computational model uses the Beer-Lambert law. A hypothesis was developed that this would work for clinical exposures despite its single energy photon basis. Values of initial air kerma are estimated from the examination exposure factors and measurements made on the x-ray system. Values of kerma at the image receptor are estimated from a measurement of pixel value made at the centre of the radiograph and the measured calibration between pixel value and kerma for the image receptor. Values of effective linear attenuation coefficient are estimated from Monte Carlo simulations. Monte Carlo simulations were created for two x-ray systems. The simulations were optimised and thoroughly validated to ensure that any result obtained is accurate. The validation process compared simulation results with measurements made on the x-ray units themselves, producing values for effective linear attenuation coefficient that were demonstrated to be accurate.

Estimates of attenuator thickness can be made using the estimated values for each variable.

The computational model was demonstrated to accurately estimate the thickness of single composition attenuators across a range of thicknesses and exposure factors on three different x-ray systems. The computational model was used in a clinical validation study of 20 adult patients undergoing AP abdominal x-ray examinations. For 19 of these examinations, it estimated the true patient thickness to within ±9%. This work presents a feasible computational model that could be used to automate the estimation of paediatric patient thickness during radiographic examinations allowing for automation of paediatric radiographic dose audit.

Chapter 1 - Introduction

Overview

This chapter summarises the effect of radiation on the body and the linear no threshold model of risk. The link between these and the need for optimisation is explained. The role of local and national dose audit in optimisation is discussed along with the difficulties in undertaking dose audit for paediatric patients. The proposed method for automating the estimate of patient thickness to facilitate paediatric patient dose audit is introduced and the structure of the thesis is described.

1.1 Deterministic and stochastic effects

The biological effects of ionising radiation are broadly classified as deterministic and stochastic effects [1]. Deterministic effects are a result of radiation induced cell death. Following high level damage, when the cell next attempts mitosis it dies. The damage is evident on a timescale consistent with the rate of mitosis expected for that type of cell. Therefore, acute deterministic responses to radiation are associated with tissues that normally have a rapid rate of cell turnover. These include bone marrow, the skin and the gastric mucosa. Late tissue responses are associated with tissues that have a low rate of cell renewal as normal. These include the liver, the kidney and muscle tissue. Late responses can also be observed in tissues that exhibit acute responses; the skin and cells along the gastrointestinal tract are examples of this. The late responses in these tissues are associated with different reactions, including tissue fibrosis and vascular damage [2-4].

The severity of both early and late onset deterministic effects is related to the acute exposure equivalent dose. For the skin, 2Gy is the threshold for an early transient erythema, with secondary ulceration occurring at 20Gy [5].

Stochastic effects are related to cell damage. The development of cancer in tissues is a multistage process that can be summarised by the stages of neoplastic initiation, promotion, conversion and progression [4]. Neoplastic initiation is the process that leads to cells having the capacity for unlimited proliferation, promotion sees events such as intercellular communication further boost a cell's capacity for unlimited proliferation. Conversion sees these pre-neoplastic cells converted to malignant cells via the accumulation of mutations in other genes due to a loss of genomic stability. Progression into an invasive cancer is dependent upon further mutations in the unstable genome [4].

As cancer induction following exposure to ionising radiation is a complex multistage process that is dependent upon certain events occurring at each step, it is not possible to

make any predictions relating to cancer induction for an individual following exposure. Additional factors, such as the relative biological effectiveness (RBE) of the radiation, the dose rate and an individual's unique susceptibility to ionising radiation would have to be taken into account [4]. At present, the role of genetic susceptibility in individual risk of radiation induced cancer is not well understood.

Although estimates cannot be made for an individual, risk models do exist for populations [1, 4].

1.2 Epidemiology and the linear no threshold model

Epidemiological studies have been undertaken to estimate the excess cancer risk for a population exposed to ionising radiation compared with an unexposed control group. Such studies include the study of disease and mortality rates of Hiroshima and Nagasaki atomic bomb survivors, the survival rates of patients with ankylosing spondylitis who had been treated with radiotherapy, the study of disease for tuberculosis patients who were given routine chest fluoroscopies, the study of disease for children who had been irradiated to eradicate ringworm of the scalp and the national registers of radiation workers [4, 6-9].

The latency period – the time between exposure to ionising radiation and the emergence of a cancer – is long, estimated at a minimum of 2 years for leukaemia with a peak of 10 years and 10 to 60 years for solid tumours [4]. Therefore the follow up of the exposed and control groups in these epidemiological studies must also necessarily be long. Typically the studies release updated data every few years following ongoing monitoring of the participants.

The data from these studies is analysed by the Committee on the Biological Effects of Ionising Radiation (BEIR) [10] and the United Nations Scientific Committee on the Effects of

Atomic Radiation (UNSCEAR) [11]. Both of these expert committees analyse the data to better understand the relationship between exposure to ionising radiation and risk to the exposed individual. The BEIR have used such data to publish figures relating to an individual's lifetime attributable risk of cancer incidence and lifetime attributable risk of cancer mortality [4]. This data is subdivided by cancer type, gender and age at the time of exposure. As is expected, the risk of both cancer incidence and mortality is higher for individuals that are younger at the time of exposure and is highest for children.

The International Commission on Radiological Protection (ICRP) [12] interpret the results of these epidemiological studies and issue guidance on radiation protection which is updated periodically as new evidence becomes available. The ICRP introduced [13] and continue to recommend [1] the linear no threshold (LNT) model for managing the risk of exposure to low doses of radiation at low dose rates. This hypothesis assumes that there is a positive linear relationship between dose and risk to the exposed individual and that there is only zero risk at zero dose (i.e. no threshold). Using this hypothesis, it is clear that in order to reduce an individual's risk from exposure to ionising radiation as much as possible, it is necessary to reduce their dose as much as possible. This is true of patients undergoing examinations using ionising radiation and individuals exposed as either workers or members of the public.

Whilst no major international body has endorsed it, there has always been an argument in favour of a hormesis model of biological effect following exposure to low dose radiation [14]. Support for the hormesis model persists and is increasing [15]. However, in their most recent commentary on the subject (published 2018) [16], the National Council on Radiation Protection and Measurements (NCRP) [17] confirmed their ongoing support for the LNT model.

1.3 The As Low As Reasonably Achievable principle and international recommendations

Given the consequences of the LNT model – that any single exposure has a non-zero risk of cancer induction – the ICRP advise an 'As Low As Reasonably Achievable' (ALARA) approach to medical imaging undertaken using ionising radiation [1]. This means that all exposures should use the lowest amount of radiation consistent with achieving an image that fulfils the diagnostic purpose. This requires the optimisation of x-ray examinations, which is a process that should be undertaken at a local level. The recommendations of the ICRP [1] were most recently adopted in the European Union's (EU) 2013 Basic Safety Standards Directive (BSSD) [18], which meant that all EU members states had to adopt the requirements of the BSSD into their national legislation. In the UK, the patient exposure aspects of the BSSD are addressed within the Ionising Radiation (Medical Exposure) Regulations 2017 (IR(ME)R2017) [19] which require that all patient exposures be optimised and that special attention be paid to the optimisation of exposures of children.

The optimisation of examinations is a process that should be undertaken by a multi-disciplinary team (MDT). The Committee on Medical Aspects of Radiation in the Environment (COMARE) [20] recommended in their 16th report [21] that this MDT (which it refers to as a team of 'radiation protection champions') consist of representatives from the staff group that will be responsible for reporting the images (usually, but not exclusively, radiologists), the staff group acting as operators (usually, but not exclusively, radiographers), a Medical Physics Expert (MPE) familiar with the equipment and the imaging technique and a representative of the manufacturer where necessary. Whilst this COMARE report was specifically focussed on computed tomography (CT), an MDT approach to examination optimisation is best across all imaging modalities.

Whilst examination optimisation is undertaken at a local level, it is not done so in isolation. A comparison of technique, image quality and radiation dose with other sites performing a similar examination for a similar diagnostic purpose on a broadly similar patient cohort can reveal differences that indicate sub-optimal practice that should be investigated and corrected.

1.4 Dose audit and Diagnostic Reference Levels

Local audit of patient doses from commonly undertaken medical examinations is an important exercise for an imaging facility to undertake in order to understand the level and range of doses they deliver for each examination [22]. This understanding is crucial in the optimisation process, as is information relating to how the doses at one site's facility compared to those of another site, regionally, nationally or internationally. Such a comparison can reveal whether a site's performance is in line with others or if they are an outlier, which would make the examination a focus for urgent optimisation.

The concept of a reference dose for an examination was proposed in a joint publication by the Royal College of Radiologists (RCR) [23] and the National Radiological Protection Board (NRPB) (which became the Health Protection Agency (HPA) and is now Public Health England (PHE)) [24], 'Patient dose reduction in Diagnostic Radiology' [25]. The reference dose was intended to act as a means of identifying abnormally high doses by comparing the average dose for an examination at a single facility with the third quartile value of the distribution of the average doses from many sites. In the 1990 report [25], the contributing sites were those who participated in a national patient dose survey conducted in the mid-1980s. As time passed, the concept became more refined. Later in 1990, the ICRP published recommendations [26] in which the same concept of reference doses was introduced. In 1992 the Institute of Physical Sciences in Medicine (IPSM) (now the Institute

of Physics and Engineering in Medicine (IPEM)) [27] published a report [28] containing further guidance on comparing local performance against reference doses. This included ensuring that the local evaluation of average patient dose was from a sample of standard sized patients to account for the expected variability in dose as a result of patient size. In 1996 the ICRP published further guidance [29] in which the terms local diagnostic reference level (LDRL), referring to the average dose for an examination at a single facility, and national diagnostic reference level (NDRL), referring to the third quartile value of the distribution of the average doses from many sites, were coined. The report recommended that NDRLs be selected by professional medical bodies. In the UK, the NRPB/HPA/PHE have been responsible for undertaking national dose surveys and publishing the results alongside recommended national reference levels. The department of health and social care (DHSC) [30] have always been responsible for formally setting NDRLs which is simply the adoption of the recommended national reference levels. The terms LDRL and NDRL remain those which are used today and appeared most recently in the 2007 recommendations of the ICRP [1]. These most recent recommendations of the ICRP recommend that DRLs only be established for the most common diagnostic examinations and that they not be applied in a precise manner. They remain an indicator of sites exhibiting abnormal practice and a guide to examinations most urgently requiring optimisation.

In 2004 IPEM published report 88; 'Guidance on the Establishment and Use of Diagnostic Reference Levels for Medical X-Ray Examinations' [31]. Their recommendations further elaborated on the idea of a standard sized patient. They recommended that dose audit be undertaken with only patients of weight between 50 and 90kg and that the average weight of the patient sample should be within 65 – 75kg. They recommend that all factors relevant to patient dose be recorded. This could be the Kerma Area Product (KAP) or the kV and mAs for the examination to allow the calculation of an Entrance Surface Dose (ESD)

for radiographic examinations. For fluoroscopy, KAP, ESD or screening time were recommended. Since IPEM report 88 was published, fluoroscopy systems now routinely include a measurement of patient skin dose which can also be used as a metric for patient dose audit. For mammography examinations, the factors necessary to calculate the Mean Glandular Dose (MGD) should be recorded, and for CT examinations the Computed Tomography Dose Index (CTDI) and Dose Length Product (DLP) should be recorded. IPEM report 88 recommends that by taking the average dose (whichever metric has been recorded for the examination, KAP will be used as the representative example for radiographic examinations hereout) from at least 10 patient examinations, a LDRL can be proposed. This average should be compared to a relevant NDRL if there is one for the examination. If it is below the current NDRL it is appropriate to adopt as a LDRL. If it is above the current NDRL, it can still be adopted as a LDRL but only with special written justification for the reason it is above the NDRL [19].

The first national patient dose audit in the UK was in the mid 1980s, though this predated the LDRL and NDRL concepts. The first after the introduction of these concepts was in 1996 for radiography examinations, undertaken by the NRPB [32]. Subsequent national patient dose audits for radiographic examinations were undertaken in 2000 [33], 2005 [34] and 2010 [35]. After each, the body undertaking the national dose audit (the NRPB / HPA / PHE) was able to propose recommended reference levels which the DHSC subsequently adopted as NDRLs. The most recent NDRLs, those adopted following the 2010 national dose audit, are available online [36].

The IR(ME)R 2017 [19] require all sites performing diagnostic imaging examinations to undertake regular audit of examination doses for regularly undertaken examinations and compare the results at a local, national and international level. As has been described throughout §1.4, the mechanisms for this in the UK have been in place for decades, as best

practice and because it is required by the IR(ME)R 2017 [19] and its predecessors IR(ME)R 2000 [37] and The Ionising Radiation (Protection of Persons Undergoing Medical Examination or Treatment) Regulations 1988 (POPUMET) [38].

1.5 Radiographic dose audit for paediatric patients

It has always been acknowledged that different values for DRLs are required for paediatric patients since they are generally smaller than adults. There is a large variation in patient size across the paediatric age range however, covering newborn to 15 years old. Therefore it is not possible to have a single DRL that is representative of all paediatric patients. The earliest suggestion made by the European Commission (EC) was that paediatric patients should be grouped by age to facilitate a meaningful comparison of average examination dose. The EC recommended that the age groups be 0 – 1 month, 1 – 12 months, 1 – 5 years, 5 – 10 years and 10 – 15 years. There is still substantial variation in size between paediatric patients of equivalent age however, which means this approach does not work - a paediatric patient dose audit that was undertaken throughout Europe for common radiographic examinations in the early 1990s failed to find any clear correlation between average examination dose and age [39]. It is clear that examination dose is dependent upon patient size, and that the method used for paediatric patient dose audit must account for it.

A method for undertaking patient dose audit for paediatric patients that accounts for patient size was proposed by the NRPB in 2000 in their report NRPB-R318 ‘Reference Doses and Patient Size in Paediatric Radiology’ [40]. Their proposal involved defining five standard sized paediatric patients in terms of their height, weight and equivalent cylindrical diameter (ECD), defined as;

$$ECD = 2\left[\frac{weight}{\pi \, x \, height}\right]^{0.5} \qquad \text{[equation 1.1]}$$

The standard sized patients correspond to ages 0, 1, 5, 10 and 15. For paediatric patient dose audit, the ECD of each individual patient to be included in the audit should be directly measured or calculated using the patient's measured height and weight. A factor can then be derived to normalise the patient's ECD to that of the nearest standard sized patient, irrespective of the age of the patient. This factor should then be applied to the measured KAP of the patient examination which results in a KAP value that is normalised to a standard sized patient. It is the average of these normalised values of KAP that should then be used for proposing an LDRL for that standard aged patient.

In the same report [40], the NRPB reanalysed the data of Kohn et al [39] applying the normalisation to a standard sized patient approach they recommended. They found an upward trend in average examination dose with standard patient age. This is suggestive that the methodology is appropriate for paediatric dose audit of radiographic examinations and the report concluded that it should be adopted in the UK.

This approach continues to receive international endorsement. It has been recommended by the International Atomic Energy Agency (IAEA) [41, 42] and the ICRP [43]. However, national patient dose audits performed in the UK in 2000 [33] and 2005 [34] contained only an 8% and 4% contribution of paediatric examinations to the total data submitted. In both cases, there was not enough data that included height and weight measurements to allow the NRPB's analysis methodology to be used and so there were no national reference doses proposed for any paediatric radiographic examination. In the 2010 national patient dose audit [35], a special effort was made to obtain paediatric data with the organisers directly liaising with 16 children's hospitals throughout the UK. Despite this, paediatric data accounted for only 3% of the total data submitted and that which came from the children's hospitals gave only height and weight measurements (where it gave anything at all) and

not the NRPB's preferred direct measurement of patient thickness. This led the authors of the report on the 2010 national patient dose audit to conclude that *"it appears likely that measurement of patient thickness is a less practical option in x-ray departments"* [35]. There was also insufficient data containing height and weight measurements to allow the proposal of updated NDRLs for any paediatric radiographic examination. Where three national patient dose audits have been undertaken across 10 years and none have received enough data with height and weight measurements to allow for a proper analysis, it seems reasonable to conclude that these measurements are not a practical option in x-ray departments either.

International guidance has subsequently moved towards encouraging patient weight (or weight bands) as the sole means of accounting for patient size variation in paediatric x-ray examinations. This is recommended by ICRP report 135 [44] and represents an attempt to facilitate paediatric dose audit by requiring only minimal patient data, and that which is easiest to measure.

Given the problems with the three most recent national patient dose audits [33-35], the current UK NDRLs for paediatric radiographic examinations [36] remain those adopted following the recommendations in the NRPB report in 2000 [40]. The data collected for this report was from imaging procedures undertaken using film-screen image receptors. In the early 2000s, the National Health Service (NHS) throughout the UK moved to Computed Radiography (CR) systems, and in the time since the use of direct digital radiography (DDR) systems has become widespread. Any LDRLs established for paediatric examinations at a site are being compared with NDRLs that were derived using outdated image receptor technology, making the results of the comparison hard to interpret. For paediatric radiographic examinations, this important indicator of examinations urgently requiring optimisation is lost.

This inability to publish updated NDRLs is a source of frustration for medical physicists in the UK, as discussed in publications presenting work on the optimisation of paediatric x-ray examinations [45].

Given the increased risk to paediatric patients due to their increased radiosensitivity and longer post-examination life expectancy, it is important that some means of overcoming the problems with radiographic paediatric dose audit be devised.

1.6 Automating the estimate of paediatric patient thickness - the proposal

With the author having raised the issue locally in optimisation MDTs, radiographer colleagues who act as operators undertaking paediatric radiographic examinations gave many reasons for not making direct measurements of patient thickness and not taking a measurement of patient height and weight. In general these reasons can be summarised as not wanting to undertake any action involving the patient that is not absolutely necessary for the successful completion of the examination. Extra patient measurements take time, which delays the paediatric patient's examination and has a knock on effect on the patients that follow. Paediatric patients attending for x-ray examinations are often upset; there are concerns that the use of callipers or some equivalent device for the direct measurement of patient thickness could cause further upset. Height and weight measurements also require some degree of patient cooperation that may not be forthcoming quickly, further delaying the examination. There is also the patient's accompanying parent, guardian or carer to consider. Local radiographers take the view that the undertaking of any measurement relating to the patient's physical size could be misconstrued by their parent, guardian or carer since they themselves may be upset as a result of the circumstances that led to the patient having to attend for an x-ray.

Measurements of either patient diameter in the examination projection or of patient weight are not going to be made at the time of a paediatric patient's x-ray examination. Some other means of estimating patient size is required to facilitate effective patient dose audit. This work presents the design, creation, testing, optimisation and validation of a computational model that will estimate the patient diameter in the examination projection without the need for any measurements of the patient. Instead, it will use the digital image produced following the examination, the exposure factors used to undertake the examination (specifically the kV_p, mAs, tube focus, measured KAP and the focus to detector distance (FDD)) and a priori knowledge of the characteristics of the x-ray unit and the image receptor used for the exposure, to make an estimate of the patient's thickness. The work concludes with a clinical validation study to assess the accuracy of the computational model in clinical use.

Whilst the intended application of this work is for a paediatric population, the development and validation of the computational model presented in this work uses an adult cohort. This is because of a greater access to the data necessary to create the computational model for an adult cohort and a far greater throughput of adult patients undergoing x-ray examinations on which to validate the computational model in a clinical setting. If successfully implemented for an adult cohort, the creation of the computational for a paediatric cohort should be possible with sufficient paediatric data. The applicability of the work to a paediatric cohort is further discussed in §7.3.

The computational model estimates patient thickness using the Beer-Lambert law. In its best known form, the Beer-Lambert law is;

$$I = I_0 e^{-\mu x} \qquad \text{[equation 1.2]}$$

Where;

- I is the intensity of an x-ray beam having passed through thickness x of an attenuator
- I_0 is the initial intensity of the x-ray beam
- μ is the linear attenuation coefficient of the attenuator material
- x is the thickness of the attenuator

For the purposes of this work;

$$k_d = k_0 e^{-\mu_{eff} x}; x = \frac{Ln\left[\frac{k_d}{k_0}\right]}{-\mu_{eff}} \qquad \text{[equation 1.3]}$$

Where;

- k_d is the kerma of the x-ray beam at the image receptor, having passed through thickness x of a patient
- k_0 is the unattenuated kerma of the x-ray beam at the detector
- μ_{eff} is the effective linear attenuation coefficient, which accounts for the broad beam and polyenergetic nature of the x-ray beam
- x is the thickness of the patient

The kerma of the x-ray beam at the image receptor, k_d, is estimated from measurements made on the x-ray image. The initial air kerma, k_0, is estimated from the examination exposure factors. The effective linear attenuation coefficient, μ_{eff}, can be estimated using measurement and Monte Carlo simulations. μ_{eff} differs from μ in that it accounts for the broad beam and polyenergetic nature of the incident x-ray beam [40]. The thickness of the attenuator can then be calculated.

The Beer-Lambert law is single phase and is only technically true for a narrow beam that is monoenergetic. We will present a method that uses the Beer-Lambert law for this work

and will demonstrate that it works successfully for a multi-phase problem that includes polyenergetic, broad x-ray beams.

To the best of the author's knowledge, there is no published work involving the estimation of the true patient thickness in the manner presented in this work. The 'Myxraydose' dose management system (DMS) [46] does contain a feature that can calculate a water equivalent thickness for a patient following a radiographic exposure. The x-ray transmission through the patient is estimated using data from the Digital Imaging and Communications in Medicine (DICOM) header based on the signal to the detector and the intensity of the x-ray beam that exited the tube. Relationships between water equivalent thickness and transmission, with due regard to examination kV_p, the kV waveform, the anode angle, the anode material, the composition and thickness of the filtration, the collimated beam size, the grid factor and the attenuation of the table, have been created using Geant4 [47] Monte Carlo simulations [48]. The water equivalent thickness could be used as a representative measure of patient size for the purposes of paediatric patient dose audit, though as it requires data directly from DICOM headers it can only be used with DDR systems. The water equivalent thickness is not a true measure of patient thickness, but it does offer a good means of comparison from patient to patient that could be used to facilitate patient dose audit. Widespread use of the water equivalent thickness metric of patient size as used by the 'MyXrayDose' DMS would require its universal adoption; this is unlikely at present as it is only offered by one single DMS. As the estimate of patient thickness made by the computational model presented in this work is an estimate of the true patient thickness, values obtained using the computational model can be compared with values obtained by direct measurement elsewhere. This approach potentially provides a much greater pool of data for national patient dose audit.

1.7 The structure of the thesis

The main body of the thesis starts with chapter 2, which introduces the Monte Carlo simulations that are used throughout this work to derive effective linear attenuation coefficients, μ_{eff}. The creation of a Monte Carlo model for running simulations in a broad beam geometry is described in detail. The process of optimisation for the model is explained. Finally, the comprehensive validation of the Monte Carlo model, which involved the comparison of simulated results against measurements made on the simulated x-ray unit for an equivalent exposure is described. The validation included exposures that varied the field size, the kV_p, attenuator composition and attenuator thickness to ensure the final Monte Carlo model was capable of producing accurate values of μ_{eff} for a range of clinically relevant exposure scenarios.

Chapter 3 describes the creation of the computational model in detail. Two methods for the calculation of the initial air kerma, k_0, are presented. The significance of the relationship between beam quality and attenuator thickness in a broad beam geometry is introduced and its application for the calculation of kerma at the image receptor, k_d, explained. The method for calculating effective linear attenuation coefficients, μ_{eff}, using kerma measurements is introduced and applied to a single composition attenuator. The computational model is then optimised for the specific case of estimating the thickness of a single composition attenuator.

Chapter 4 describes the validation of the computational model created in chapter 3 by using it to estimate the thickness of a single composition attenuator. The computational model is first used on the Fuji CR imaging system for which the computational model in chapter 3 was created and optimised. To demonstrate that the computational model works on DDR systems, and on systems of more than one manufacturer, the computational model is adjusted and validated for use on Fuji and Xograph-Canon DDR systems. The

validation process involved exposures of varying thicknesses of attenuator, varying kV_p and mAs values and varying field sizes to fully evaluate the accuracy of the computational model for a range of relevant exposure conditions.

Chapter 5 considers how the computational model must be adapted to account for the composition of patients. The natural variation in patient size and composition for chest, abdomen and pelvis examinations is examined using CT examinations previously undertaken at the local radiology department. The process through which these patients were used to create patient models for use in Monte Carlo simulations to evaluate the range of μ_{eff} values as a result of natural patient variation is explained. The chapter concludes by presenting a means of determining an appropriate μ_{eff} for an examination based on the estimate of k_d and k_0.

Chapter 6 presents the results of a clinical validation study involving 20 patients. The Anterior-Posterior (AP) thickness of the patient at the level of the iliac crest was estimated using the computational model and compared with the true value, which was measured with the patient in the examination position immediately prior to the x-ray exposure. The results of the clinical validation study showed that the computational model estimated the patient thickness to within ±9% of the measured value for 19 of the 20 patients.

Chapter 7 summarises the work and discusses the further work that would be necessary to create a computational model that could be used on a paediatric cohort.

There is no formal literature review in the thesis. Literature is discussed in context where relevant.

Chapter 2 - Monte Carlo simulations of radiographic x-ray exposures

Overview

This chapter presents the creation and validation of a Monte Carlo model of a radiographic x-ray unit in a broad beam exposure geometry. The model will be used to run simulations that will be used to derive values of effective linear attenuation coefficients as required throughout this work.

2.1 Introduction

The computational model that is discussed throughout this thesis selects values of effective linear attenuation coefficient, μ_{eff}, that are appropriate for the examination under consideration from look up tables (LUT). The LUTs contain values that are appropriate for all combinations of clinically relevant x-ray exposure factors, geometries and patients. The values in the LUTs cannot practicably be measured, nor can they be empirically derived. The intention is to use Monte Carlo simulations to estimate values of μ_{eff}. A Monte Carlo model of a radiographic x-ray unit was created and optimised for a broad beam exposure geometry. This chapter describes the final version of the Monte Carlo model of the Philips Optimus 50 radiographic x-ray unit that will be used throughout chapter 3 to create the computational model. If the values of μ_{eff} are to be taken as accurate, the Monte Carlo model must first be validated against measurements made on the radiographic unit. Both the process for, and the results of, the validation are presented in this chapter.

2.2 An introduction to Monte Carlo

Monte Carlo methods rely on random sampling to obtain numerical results and can, in principle, be used to solve any problem that has a probabilistic interpretation. An early application, and one which is good for demonstrating the concept, involved the estimation of π by dropping needles onto a floor on which there was a circle with a radius of 1 within a square of dimensions 2 x 2. After discounting any needle drops which fell outwith both the circle and square, π can be estimated by $\frac{4N_c}{N}$ where N_c is the total number of needle drops falling within the circle and N is the total number falling within the circle or square combined [49]. In this example, the random nature is introduced by the unpredictability of the needle's resting point after bouncing off the floor. Probability dictates that it will more

often than not be within the circle. As is common to all problems of a statistical nature, the Central Limit Theorem (CLT) dictates that the result tends towards the correct answer with more data; that is to say that the best estimate of π is achieved as the number of needle drops tends to infinity.

Other applications for Monte Carlo methods include traffic flow simulations, environmental sciences, astrophysics, molecular modelling and semiconductor modelling [49]. Of relevance to this work however is the Monte Carlo method as applied to radiation transport.

Monte Carlo techniques are ideally suited to the transport of photons through a medium as they can interact many times before being absorbed and directly computing the combined effects of several interactions is very difficult. Monte Carlo techniques can be used to examine a distribution of photon interactions [3]. For any given photon within a Monte Carlo simulation, a random distance to its next interaction is chosen from a probability distribution function that is related to total interaction cross-sections, in a direction chosen from another probability distribution function related to the differential cross section. The photon is then transported to that location, provided that location remains within the confines of the defined geometry. Where the photon loses all energy and is absorbed, its history is terminated. Where the photon loses some or no energy and is scattered, the process repeats itself until the photon falls outwith the defined geometry or it is absorbed. The same process is then applied to another photon with the same starting position and initial energy as the first; by simulating enough of these initial photons, an accurate picture of the final photon or deposited energy distribution is constructed [49].

The process is similar for charged particles, except that they undergo so many collisions before being absorbed that event-by-event simulation is impractical. Since most of these interactions have a negligible effect on particle energy and direction, the effects of these

small interactions are combined in fewer simulated large interactions. This is known as a condensed history simulation and the associated probability distribution functions are designed to take this approach into account [3].

The Monte Carlo radiation transport simulation has few key components; a random number generator, all relevant probability distribution functions for all radiation types, a means of tracking and accumulating the results (particle, photon and energy bookkeeping) and physics information – such as interaction cross sections - for all radiation types and the geometry of the simulation.

The statistical nature of Monte Carlo simulations means that there will be a statistical uncertainty associated with any result. This statistical error can be reduced by increasing the number of simulated events, where the trade-off is an increased computation time. Most radiation transport Monte Carlo programs include variance reduction techniques to shorten simulation times. These can be applied in various ways; one example is to increase the probability of particles scattering towards the direction of the user's interest. This makes a deliberate alteration to one of the many probability distribution functions used by the Monte Carlo code. Simulation time is saved by not simulating those particles moving away from the user's area of interest to an area where the user does not intend to examine the particle distribution or energy deposition [50].

Although physical measurement of the characteristics of an x-ray beam is the most obvious and desirable method for obtaining information relating to the beam, there are four main reasons why this is not always possible. The first is time; measuring the change in a single characteristic as a result of changes to the exposure factors or geometry could potentially involve thousands of measurements where the changes are incrementally small. The second is a concern over measurement accuracy where the equipment used for measurement would be placed in a beam or geometry that is significantly different from its

calibration, capability or intended use. The third is an inability to make simultaneous measurements at different locations due to detectors being of a fixed and limited size, only having a limited number of detectors or a concern that any one of the measurements could affect any of the others. The fourth is an inability to make some measurements at all due to a lack of access to a suitable detector or being unable to create the conditions required for the detector to work accurately.

These problems can be overcome if the x-ray system and exposure geometry could be accurately simulated using Monte Carlo techniques. Simulations could be run as a batch process, changing whichever variables the user desires whilst allowing the user to work on other things as the results accrue. A high level of measurement accuracy can be achieved in any location in the simulation provided the simulation has been well validated and the behaviours of the Monte Carlo code are well understood. Any number of measurements can be made in the same simulation simultaneously without any one measurement affecting the others and the type of measurement that can be made is only constrained by the capabilities of the Monte Carlo code.

2.3 The selection of a Monte Carlo code

2.3.1 The Monte Carlo codes available

The first complete coupled electron-photon transport code was developed by Berger in 1963 [51]. The method was described by the author; “the diffusion process is imitated by letting the particles carry out an (artificially constructed) random walk, each step of which takes into account the combined effect of many collisions”.

As of now, there are many Monte Carlo codes available that are suitable for the simulation of an x-ray system; these include MCNPX [52], Geant4 [47], Penelope [53], Fluka [54] and EGSnrc [55].

All of these Monte Carlo codes have been used for applications in radiation physics [56-60]. Many were trialled in the early stages of this work and all have their advantages and disadvantages. EGSnrc was designed with medical applications in mind however and this gave it an ease of use that was unmatched by the others for this particular application. All of the Monte Carlo work described within this thesis was undertaken using EGSnrc.

2.3.2 EGSnrc and BEAMnrc

EGSnrc, an acronym of Electron-Gamma-Shower National Research Council, is a general purpose package for the Monte Carlo simulation of the coupled transport of electrons and photons in arbitrary geometry in the low keV to hundreds of GeV range [55]. It was developed by staff at the National Research Council (NRC) of Canada. The BEAMnrc software component was formerly a separate package built upon the EGS code [61], however it is now included within the EGSnrc Monte Carlo program.

The specific focus of BEAMnrc is modelling radiotherapy sources; it was developed as part of the OMEGA project that aimed to develop a 3-D Radiotherapy treatment planning system [62]. Commonalities in the physics of x-ray production and improvements made over the years to the low energy physics in the EGSnrc program [63] mean that BEAMnrc can now also be used for the simulation of diagnostic x-ray systems.

To avoid confusion, the Monte Carlo code used throughout this work will from this point forward be referred to as BEAMnrc.

2.3.2.1 BEAMnrc geometry

The BEAMnrc program simplifies the Monte Carlo simulation of a diagnostic x-ray system by providing 'component modules' that contain customisable geometry pertaining to the general form of a component of a diagnostic x-ray system or radiotherapy linear accelerator. The customisation of these component modules extends to the definition of their dimensions and the material from which they are constructed, but the BEAMnrc program restricts their geometry in that the centre of each component module shares a common origin. The user is able to define how far they are apart from one another however. Should any of the component modules provided with the code not be suitable for the simulation of any component of an x-ray machine or linear accelerator, the BEAMnrc manual [64] includes instructions on how to create a new component module; that was not necessary for this work.

2.3.2.2 BEAMnrc Physics

BEAMnrc can only be used for the simulation of electron and photon transport. Like all Monte Carlo codes, electrons are simulated in BEAMnrc using the condensed history technique first introduced by Berger [51]. This technique involves grouping multiple track segments of the electron's passage through a material into a single event. This significantly speeds up the simulation of electrons since an electron undergoes many elastic interactions that do not change its energy state [65]. The BEAMnrc code contains the physics required to simulate electron energy loss via inelastic collisions with atomic electrons, bremmstrahlung radiation and positron annihilation.

Photon transport is simulated with due regard to the many different interactions that a photon can undergo in a material. The BEAMnrc code contains the physics required to

simulate photon energy loss via materialisation into an electron / positron pair in the electromagnetic field of the nuclei and surrounding atomic electrons, Compton scattering with atomic electrons, photo-electric absorption and Rayleigh scattering with the atoms or molecules of the scattering medium [65].

BEAMnrc does not contain the physics of electromagnetism [65]. As a result, in the simulation of a diagnostic x-ray unit electrons are not emitted from a cathode and accelerated towards the anode, instead they are simulated at their user-defined energy at the surface of the anode. Many of the simulated electrons recoil from the target into the vacuum. Whereas these electrons should be reaccelerated towards the anode, in the BEAMnrc code system once their kinetic energy falls below a set level they are terminated. This means there is no simulation of extra-focal radiation.

There is no agreed method for the measurement and quantification of extra-focal radiation [66]. Kuhn and Gajewski [67] reported that the estimate of extra-focal radiation can vary from 5 – 22% for the same x-ray tube depending on the measurement technique. Other studies, using varying measurement techniques, estimate it as contributing 5 – 25% of the total air kerma [3, 68-74].

Ali and Rogers modified a version of BEAMnrc to simulate off-focal radiation [75]. In comparing the effect on the x-ray beam for a simulation including off-focal radiation to one without, they concluded the incident kerma increased as a consequence of the off-focal radiation by 11%. As the off-focal radiation is of a softer quality, the Half Value Layer (HVL) reduced by 7% with the off-focal radiation included.

There is no mechanism in BEAMnrc to simulate voltage ripple. The simulated electrons all have the same single user-defined energy. This is not a limitation if the simulated system uses a high frequency generator [76] as is the case with the Philips Optimus 50 radiographic

x-ray unit on which the Monte Carlo model is based. For single phase generators, the typical voltage ripple is of the order of 0 – 15% [3].

There is no means of simulating tube wear and tear. Over time, the anode becomes roughened [77], creating superficial cracks and other non-uniformities. This is another limitation when attempting to accurately simulate a radiographic x-ray unit which has been in use for many years (the system was installed as new in 2010).

2.3.2.3 BEAMnrc output

'Scoring zones' are planes that extend to the full extent of the simulation geometry in which the program records the position, energy and direction of all electrons and photons that travel through the plane. They can be placed immediately after any component module, allowing them to be placed before, inside or at the exit surface of an attenuator. This restricts scoring zones to regions in the direction of the primary x-ray beam, which limits the application of the BEAMnrc program to investigations into the primary x-ray beam and transmission through, and localised scatter as a result of, objects placed within the primary x-ray beam. This is not a limitation for the simulations undertaken in this work.

For each scoring zone used in the simulation, the data relating to the position, energy and direction of all electrons and photons travelling through it is written to a phase space file. This file simply contains a list of all of the information recorded; there is no tabulation or accumulation of values applied. For the extraction of meaningful summary information from the simulation, a further complimentary computer program is provided with BEAMnrc; BEAMDP [78] can be used to analyse any phase space file and provide fluence or energy fluence vs. position, spectral distributions, energy fluence distributions, mean

energy distributions and angular distributions for any user-defined region within the scoring zone in the BEAMnrc simulation [79].

2.3.2.4 Computational considerations

All of the simulations run throughout this thesis used BEAMnrc from the 2018 EGSnrc release and were run for between $1x10^9$ and $1x10^{11}$ iterations. The number of iterations for each simulation varied with geometry and attenuator; in each case it was demonstrated as the level at which the average statistical accuracy is better than 10% (calculations of energy fluence return a statistical uncertainty per energy bin). The initial simulations were created and optimised on previous releases of EGSnrc and were run using a computational environment that had 4 Intel Xeon CPU 5140 processors each running at 2.33GHz with 7.8GB of RAM. The operating system was Ubuntu version 16.04 LTS. Simulation times were considerable, with simulations using a single processor taking up to 240 hours. The simulation time was reduced using parallel processing, where the total number of simulation iterations are divided evenly across any user specified number of processors up to the maximum available. Nevertheless, it was clear that the simulations required for the work presented in this thesis could not be completed in a reasonable timescale without further computational resources.

A second computational environment was specified for the sole purpose of running Monte Carlo simulations. Performance monitoring of the first computer whilst running simulations indicated that the simulation speed was more dependent upon the processor than any other hardware component. The second computational environment had 20 Intel Silver 4114 CPU processors each running at 2.20GHz with hyperthreading capability and 64GB of RAM. This computer also ran Ubuntu version 16.04 LTS as its operating system.

As a benchmarking exercise, both computers were used to run the same simulation of an x-ray beam measuring 43x43cm at a 100cm distance from the focus at 81kV$_p$ on a single processor only. The first computer ran at 13,147,488 histories per hour, the second at 29,521,804 histories per hour. This was despite the first having processors that ran at a higher clock speed and shows the benefit and efficiency of the hyperthreading capability. Given the increased number of processors on the second computer, it is at least 11 times faster at running Monte Carlo simulations.

2.3.3 Summary

BEAMnrc can be used to simulate the primary x-ray beam from a diagnostic x-ray unit. Scoring zones, which record data pertaining to the number, position, energy and direction of all photons crossing them can be used to examine the properties of the x-ray beam at any position along the path of the primary beam, allowing for a comparison with data from an equivalent position that has been measured, published or otherwise computed.

There are limitations in the physics used by BEAMnrc. Of most significance, the code does not contain the physics of electromagnetism, meaning extra-focal radiation cannot be simulated. This will affect the accuracy of the simulated x-ray beam and this must be taken into account during the validation of the simulation.

The total simulation time for each individual Monte Carlo simulation was considerable, even with the additional computational capacity that was acquired specifically for this work.

2.4 Creating a Monte Carlo simulation of a radiographic x-ray unit

A simulation of any specific radiographic x-ray unit in BEAMnrc can be created by specifying the materials used in the x-ray unit in their correct quantities, thicknesses and position relative to all other materials. In this work, information on the materials and geometry of the Philips Optimus 50 radiographic x-ray unit was gathered from a range of sources, including manufacturer's data, physical measurements on the x-ray unit and textbooks on the subject.

The Philips Optimus 50 radiographic x-ray unit that was simulated is in the main radiology department at Ninewells Hospital. The system was installed in March 2010 and was supplied by Philips with a technical manual [80] that included information and the specification relating to the x-ray tube model RO 1750 contained within the x-ray tube assembly model ROT 360.

2.4.1 Nomenclature

To ensure consistency of nomenclature, figure 2-1 defines the axes that will be referred to throughout the remainder of this chapter. The x-axis describes the anode-cathode axis, the y-axis is in the same plane as, and perpendicular to, the x-axis and the z-axis is in the direction of the x-ray beam.

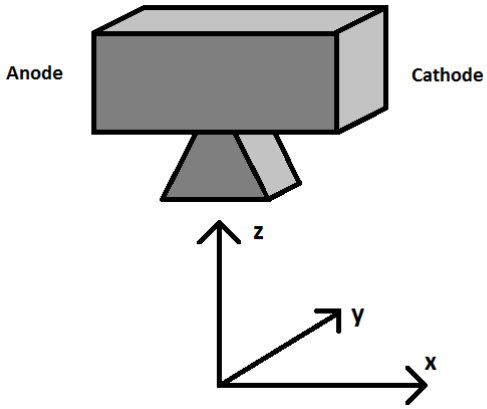

Figure 2-1: the nomenclature used for the Monte Carlo simulation

2.4.2 Technical information used to create the Monte Carlo model

The technical information supplied by Philips [80] with the unit confirms the following information relating to the x-ray tube assembly that is relevant to Monte Carlo simulation design;

- The total minimum filtration of the x-ray tube assembly is 2.5mm Aluminium equivalent at 75kV$_p$; this is made up by a 1.7mm Aluminium filter plate with 0.8mm Aluminium equivalent inherent filtration
- The anode material is given as a rhenium alloyed tungsten compound anode: RT / Titanium Zirconium Molybdenum (TZM). This means that the target material is a rhenium alloyed tungsten, embedded in an anode of TZM molybdenum, itself an alloy of 0.5% titanium, 0.08% zirconium, 0.02% carbon with the remainder molybdenum [81]
- Collimation near the focus is provided by lead aperture plates
- The x-ray tube is air cooled
- Oil is only present in the x-ray tube assembly at the cathode side; the oil is present to activate the temperature switch via expansion when the oil reaches 85°C

- The focal spot sizes are 0.6 and 1.2mm, fine and broad focus respectively
- The maximum nominal x-ray tube voltage is 150kV$_p$
- The anode angle is 13 degrees
- The anode disk diameter is 90mm
- The centre of the focal spot is 35mm below the centre of the anode disk
- The maximum usable field size at 1m is 43 x 43cm
- The focus to collimator coupling flange distance is 64 ± 2mm
- The filament diameter is 250μm
- The evacuated glass chamber housing the cathode and anode disk has a maximum diameter of 131mm
- The thickness of the glass wall of the evacuated glass chamber is 1.2mm

The x-ray tube assembly is entirely contained and cannot be opened, therefore physical measurements of the individual components cannot be made. As the tube focus position is marked on the outer casing of the x-ray tube assembly however, it is possible to confirm by measurement that;

- The focus to collimator distance is 25cm
- The focus to the centre of the Kerma Area Product (KAP) meter distance is 27.5cm

The information from the Philips technical manual and physical measurements of the unit are not enough to create a Monte Carlo model. The remaining unknown information was obtained from the literature as is described throughout §2.4.3.

2.4.3 The specification of the Monte Carlo model

The Monte Carlo model was optimised using an iterative process of changing individual parameters and then comparing the results of the simulation with output measurements

made on the x-ray unit. Each comparison involved some or all of the validation analysis that is presented in §2.5. Changes were retained where they resulted in a closer agreement to the results of the practical exposures or discarded where the change led to a poorer agreement. It is not the intention of this chapter to present any of the optimisation process, instead this section describes the final construction of the Monte Carlo model. This model is deemed the most accurate that could be achieved and it is the only model that is used throughout this thesis.

The final construction of the geometry for the model was as shown in figure 2-2.

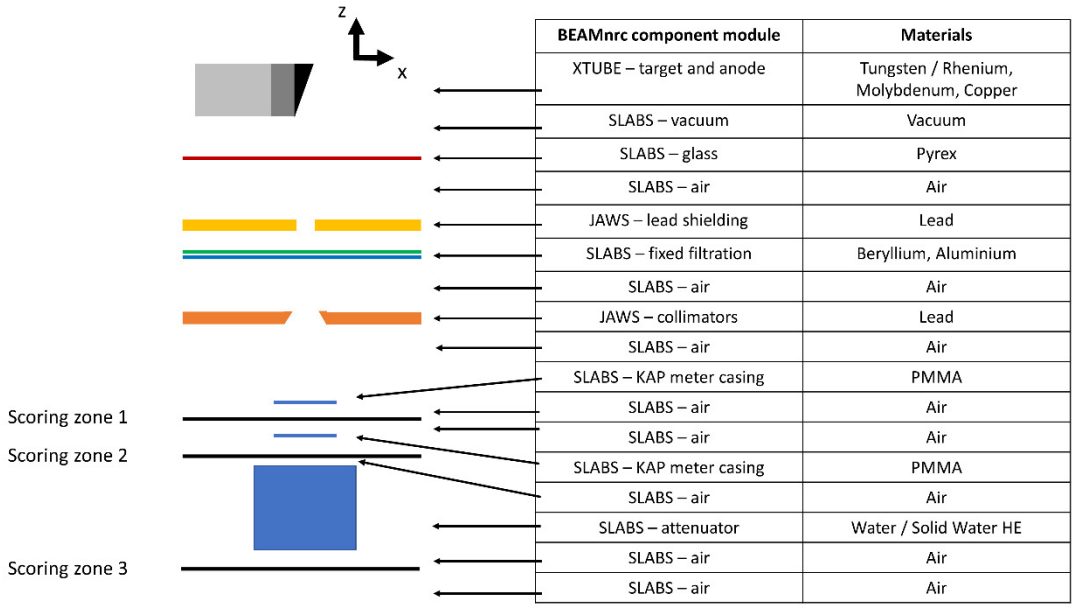

BEAMnrc component module	Materials
XTUBE – target and anode	Tungsten / Rhenium, Molybdenum, Copper
SLABS – vacuum	Vacuum
SLABS – glass	Pyrex
SLABS – air	Air
JAWS – lead shielding	Lead
SLABS – fixed filtration	Beryllium, Aluminium
SLABS – air	Air
JAWS – collimators	Lead
SLABS – air	Air
SLABS – KAP meter casing	PMMA
SLABS – air	Air
SLABS – air	Air
SLABS – KAP meter casing	PMMA
SLABS – air	Air
SLABS – attenuator	Water / Solid Water HE
SLABS – air	Air
SLABS – air	Air

Figure 2-2: the construction of the Monte Carlo model as it appears in the x-z plane. Not to scale

There are 17 component modules shown with their BEAMnrc ID and equivalence to real life component described. The 3 scoring zones (SZ) are shown. This figure is not to scale.

Each of the individual component modules is now discussed in more depth.

2.4.3.1 XTUBE – the x-ray tube target and anode

The component module name 'XTUBE' is a misnomer; this component module only allows inputs pertaining to the x-ray tube target and anode, not the entire x-ray tube. The target thickness in the z-direction was selected as 25mm as this is the minimum required by the program. It is mandatory that the centre of the focal spot is fixed at the centre of the target; this places the centre of the focal spot at z = 12.5mm. The size of the focal spot can be varied in the x-y plane. Nominal focal spot sizes were given in the Philips technical information as 1.2mm for broad focus and 0.6mm for fine focus.

In the Philips x-ray tube, the centre of the focal spot is 10mm from the edge of the anode disk; in the BEAMnrc simulation it is 12.5mm from the edge of the anode disk because of the minimum target size. This difference of 2.5mm is not significant however, since the x-rays are travelling through a vacuum at this point, except those x-rays being attenuated by the target itself.

The anode angle was set at 13°. The target material was added to the Monte Carlo code, as the rhenium alloyed tungsten compound was not one of the default compounds provided. The Philips technical information did not specify the ratio of the rhenium alloyed tungsten compound, however a literature review suggested a ratio of 10% rhenium and 90% tungsten to be plausible [3, 77]. There was no information on how thick the target layer is. X-rays are known to be generated following electron interaction to a depth of a few tens of micrometres [77]. In the model, increasing target thickness was only observed to change the intensity of the x-ray spectra produced due to self-absorption of the x-rays, but there was no discernible change to the shape of the spectrum. A thickness of 1mm was used in the model.

The target was simulated as being attached to an anode made of 10mm of Molybdenum affixed onto 50mm of copper, which was intended to represent the rotor that facilitates

anode rotation [3]. The simulation of TZM molybdenum instead of molybdenum was not observed to make any difference to the results, therefore it was not included to keep the model as simple as possible. The addition of a graphite heat sink, used to aid dissipation of heat from the anode by black body thermal radiation at the back of the anode, was not observed to make any difference to simulations and so was omitted. The area in front of the target (corresponding to the space between the cathode and the anode) was simulated as a vacuum.

The XTUBE component module extends from 0 to 25mm in the z-dimension, with the focal spot at the centre of the component module, at the surface of the centre of the target. The construction of the XTUBE component module is shown in figure 2-3.

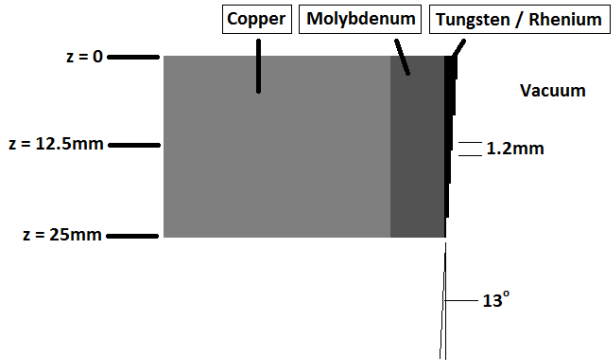

Figure 2-3: the construction of the XTUBE component module used in the final Monte Carlo model. Not to scale

2.4.3.2 SLABS – the vacuum

This component module simulates a vacuum and extends from 25mm (i.e. at the interface of where the XTUBE component module ends and this component module begins) to 42.5mm in the z-dimension. Where the maximum diameter of the evacuated glass chamber is known to be 131mm [80], the anode diameter is 90mm and assumed to be positioned centrally within the chamber, the focus to glass wall distance is 31mm.

2.4.3.3 SLABS – the glass wall of the vacuum chamber

This component module simulates the glass wall of the vacuum chamber, of known thickness 1.2mm. It extends from the vacuum to 43.7mm in the z-dimension. The glass used in an x-ray tube is a borosilicate such as, or similar to, Pyrex [82]. Pyrex is a compound that is available within BEAMnrc; this was used in the model.

2.4.3.4 SLABS – the air between the glass and the lead shielding

This component module simulates the air between the glass and the x-ray tube's lead shielding. As the x-ray equipment was known to be air cooled, there was no oil to simulate in the path of the primary x-ray beam.

The exact positioning of the component modules up to the collimators (which was known to be 250mm from the focus) is unknown. The position of each was not found to have any effect on the simulated results. Air was taken as extending to 79mm in the z-dimension.

2.4.3.5 JAWS – the lead shielding of the x-ray tube

The lead shielding of the x-ray tube was simulated using the JAWS component module; this component module was intended to simulate collimators but works just as well for the lead shielding underneath the x-ray tube. An opening in both the x and y-axes was created within the component module. The edges of the lead are not straight; they are sloped as to match the x-ray path as they diverge from the focus. Using similar triangles, the edges were created such that the opening in between the lead is consistent with the largest field size at 100cm for the Philips Optimus 50 radiographic x-ray unit, which was known to be 43 x 43cm. The thickness of the lead was 3mm in both the x and y axis. The creation of this

component module had the effect of ensuring that the only x-rays that left the x-ray tube were in the direction of the primary x-ray beam.

2.4.3.6 SLABS – the fixed filtration

This component module simulates the exit from the x-ray tube and the fixed filtration present at the tube exit. A thin window is required over the opening in the lead shielding to maintain the integrity of the x-ray tube. The construction material for this window in the Philips Optimus 50 radiographic x-ray unit is unknown; beryllium, plastic and glass are all materials that are commonly used for this purpose [82]. This model used a 1mm window of beryllium extending from the air opening in the lead shielding to 87mm in the z-dimension. There is then a 3.5mm gap filled with air before the aluminium filter. It is known from the technical specification that there is a 1.7mm fixed aluminium plate. However, optimal agreement between simulation and experimental measurements were achieved with a 1.4mm aluminium plate.

Whilst knowingly specifying a different thickness aluminium plate in the model from that specified in the technical manual may seem inaccurate, the measurement in the technical manual is subject to an unspecified uncertainty. In addition, the simulated aluminium is pure whereas the physical aluminium will contain impurities including iron, silicon and copper [83]. Further, the inherent filtration of the Philips Optimus 50 radiographic x-ray unit is known to be equivalent to 0.8mm of aluminium [80]. However, this cannot be precisely replicated because the construction of the thin window at the opening in the lead shielding is not contained within the technical information [80]. There are also other components likely to be missing, for example the tilted mirror used to direct the light beam in the z-axis. Given these arguments, a difference of 0.3mm in the simulated and manufacturer specified thickness is small.

2.4.3.7 SLABS – air between filter and collimator

This component module simulates the air between the aluminium filter and the collimator. It extends from the aluminium filter for 92mm in the z-dimension to the known location of the upper surface of the collimator at 250mm from the focal spot.

2.4.3.8 JAWS – the x-y collimators

This component module simulates the lead collimators in the x and y dimensions. As for the lead shielding, an opening in the x, then y axis was created within the component module. The edges of the lead are not straight, they are sloped to match the x-rays diverging from the focus. The opening was altered in size from simulation to simulation depending on the desired field size at 100cm from the focus; the opening at the collimator level was calculated using similar triangles. The x and y collimators were both made of lead and simulated to be 5mm thick. The inclusion of this component module ensured that only x-rays travelling through the air in between the collimator blades reached the attenuator and/or scoring zones further down in the z-dimension.

2.4.3.9 SLABS – the air between collimators and kerma area product meter

This component module simulates the air between the exit surface of the collimator and the top of the KAP meter.

2.4.3.10 SLABS – the upper kerma area product meter casing

Whereas the component module 'chamber' was intended to be used to simulate ionisation chambers, the KAP meter in the simulation was simulated using four 'SLABS' component modules. This was necessary to allow a scoring zone to be placed at the centre of the KAP meter (scoring zones must be placed after a component module, not in the centre of one) so that an estimate of kerma could be made within the KAP meter which could be used to normalise the kerma measured elsewhere in the simulation. The upper casing of the KAP meter was simulated as 2mm of Poly(methyl methacrylate) (PMMA).

2.4.3.11 SLABS – the air in the upper half of the kerma area product meter

The internal dimension of the KAP meter in the z-dimension was known to be 12mm; thus this component module simulated 6mm of air from the exit surface of the uppermost layer of PMMA to the centre of the KAP meter.

A scoring zone was placed at the end of this component module. The scoring zone records the position, energy and direction of all photons that travel through the plane. This allows for calculations of air kerma that can be used to normalise simulations for relevant comparisons.

2.4.3.12 SLABS – the air in the lower half of the kerma area product meter

This component module simulated the 6mm of air from the centre of the KAP meter to the bottom layer of PMMA.

2.4.3.13 SLABS – the lower kerma area product meter casing

The lower casing of the KAP meter was simulated as 2mm of PMMA.

2.4.3.14 SLABS – air to 750mm from focus

This component module simulates air from the exit of the KAP meter to a 750mm distance from the focus. This is to allow a scoring zone to be placed at 750mm from the tube focus, allowing for a direct comparison between the output spectrum of this simulation and that of the Institute of Physics and Engineering in Medicine's (IPEM) report 78 spectrum generator [84], which gives all results at 750mm from the focus.

2.4.3.15 SLABS – air from 750mm from the focus to the attenuator

This component module simulates air from 750mm from the focus to the entrance surface of whatever attenuator is being simulated. The thickness in the z-dimension of this component module changes with attenuator thickness so that the simulation output can be maintained at 100cm from the focus.

2.4.3.16 SLABS – the attenuator

This component module simulates the attenuator; validation of the simulation saw exposures made on the Philips Optimus 50 radiographic x-ray unit using water and solid water High Equivalency (HE) as the attenuator in varying thicknesses. The attenuator was always simulated such that the simulation output was maintained at 100cm from the focus, which matches the position of the dosemeter in the validation exposures.

Note that whilst water is already present in the BEAMnrc code, solid water HE had to be added. The elemental composition of solid water HE came with the material on purchase, which allowed the addition of the material to the code. Solid water HE is made of hydrogen, carbon, nitrogen, oxygen and chlorine [85]. The nominal percentage contribution of each element to the compound was provided by the manufacturer, meaning the atomic mass of each element of the compound could be calculated and manually added to the code.

2.4.3.17 SLABS – the air between attenuator and dosemeter

This component module simulates the 10mm of air between the exit surface of the attenuator and the Raysafe Xi radiographic / fluoroscopic (R/F) detector used during the validation exposures.

A scoring zone placed behind this component module returns results from the simulation at 100cm from the focus. These can be compared to the measurements of the dosemeter in the validation exposures.

2.4.3.18 SLABS – air to infinity

The Raysafe Xi R/F detector used in the validation exposures is lead backed, therefore it does not measure any backscattered radiation. Although the placement of a lead sheet at the end of the simulation was considered for the removal of backscatter from the scoring zone, optimal agreement between the results of the simulation and the validation exposures was achieved when the scoring zone was free in air, that is to say this component module added a superfluous additional 100cm of air to the end of the

simulation, effectively extending it to infinity, so there would be no backscattered radiation passing through the scoring zone.

2.5 Validation of the Monte Carlo simulations

Monte Carlo techniques are complex; across all available Monte Carlo programs there are many selections that can be varied. These range from slight differences in the choice of data for particle interactions (there are many databases available and these have slight variances in values) to more significant variations in the results that arise because of the way an individual Monte Carlo program performs an aspect of the simulation. In short, there is much that can go wrong, which can result in an erroneous simulated beam spectra. Whilst significant errors will be obvious from the shape of the spectra, subtle errors will be harder to detect. The results of a Monte Carlo simulation should not be accepted without having been subjected to some kind of validation to ensure that the modelling has been undertaken as intended.

There is no agreed methodology for validation of a Monte Carlo simulation. The validation process should take into account the intended purpose of the simulation. For the purposes of this work, the Monte Carlo simulations will be used to derive values of effective linear attenuation coefficient, μ_{eff}. Therefore the validation process focussed on how accurately these values can be estimated for attenuators for which the true value can be measured.

The American Association of Physicists in Medicine (AAPM) in their report 195 [86] have provided six reference sets of simulations using four Monte Carlo codes with a complete description of the conditions under which the simulations were run. The intention is that the user's Monte Carlo simulations can be validated against these results. The results of the reference sets themselves have not been validated against measured data, but the

closeness of the agreement between each of the Monte Carlo codes for each simulation is taken as confirmation of their accuracy. These were not used for validation of the Monte Carlo simulations used for this work as it would have involved changing the geometry of the simulation to match that of one of the reference cases and would only confirm general agreement with a simulation of a non-specific x-ray unit. Instead, the validation used for the Monte Carlo simulation developed for this work involves comparison with nominal values and measurements made directly on the Philips Optimus 50 radiographic unit that was simulated using a Raysafe Xi R/F detector. The aim is to achieve an agreement between the two that is within the measurement or experimental uncertainty in each case. Where this is achieved, further adjustment of the Monte Carlo simulation cannot be determined to have improved the simulation accuracy.

2.5.1 The validation process

Simulations were run with alterations made to the geometry or the composition and thickness of materials as required to achieve close agreement with the measurements to which the results of the simulation were compared. At the end of each simulation, BEAMnrc created three phase space files containing the energy, position and direction of every photon that passed through the scoring zone. These scoring zones were placed at the centre of the KAP meter (directly after component module 11), in air at a 75cm distance from the x-ray tube focus (directly after component module 14) and at the position of the Raysafe Xi R/F detector (directly after component module 17). The program BEAMDP was used to interrogate each phase space file and produce the required analysis.

Simulation validation involved both non-measurement based validation, where the output of the Monte Carlo simulation was compared to a nominal value or the results produced by the IPEM report 78 spectrum generator [84], and measurement based validation, where

the output of the Monte Carlo simulation was compared to equivalent measurements made using a Raysafe Xi R/F detector on the Philips Optimus 50 radiographic x-ray unit.

2.5.2 Dosemeter selection for validation work

The validation of the Monte Carlo simulation will rely upon accurate dosimetric measurement in a variety of geometries. There are two types of dosemeter capable of making these measurements; ionisation chambers and semiconductor detectors [3]. Neither is perfectly suited to kerma measurement in all geometries.

Both exhibit an energy dependence, though the International Electrotechnical Commission (IEC) standard IEC-61674 imposes a ±5% limit on the variation of energy response within the 50 – 150kV$_p$ range [87]. The International Atomic Energy Agency (IAEA) exemplified this by referring to the energy dependence of the response of three semiconductor detectors and three ionisation chambers [3]. The results were variable; at least one semiconductor detector and one ionisation chamber measured 5% above the true kerma at a beam quality equivalent to 6.5mm Al HVL. The IAEA publication [3] notes that energy dependence for both semiconductor detectors and ionisation chambers is dependent upon detector design and that the energy dependence characteristics should be investigated when relevant, especially for non-specified beam characteristics. Martin [88] undertook an evaluation of ionisation chambers and semiconductor detectors for diagnostic x-ray dosimetry measurements in 2007. This work included the assessment of a Raysafe Xi R/F semiconductor detector and a Keithley 15cc pancake ionisation chamber (Keithley Instruments Inc.). The Raysafe Xi R/F detector was found to have an energy dependence relative to the Keithley 15cc pancake ionisation chamber. Of all the ionisation chambers referenced by the IAEA [3], the Keithley appeared to have the most significant energy dependence.

Both semiconductor detectors and ionisation chambers exhibit a directional dependence that is dependent upon detector construction and physical size [3]. Parallel plate design ionisation chambers exhibit a directional dependence at large incident angles whereas most semiconductor detectors have a directional dependence because of their lead backing and the placement of filters above the semiconductor elements to attenuate incoming radiation. The IAEA suggest that the angular dependence of semiconductor detectors is comparable to that of parallel plate ionisation chambers [3], but Martin [88] found the Raysafe Xi R/F detector had a significant directional dependence (measuring lower than 90% of the incident kerma) outside of a 27° arc.

As semiconductor detectors are generally lead backed [3], they do not detect backscattered radiation unlike ionisation chambers. Despite the presence of a 1mm lead backing plate, Martin [88] found that the Raysafe Xi R/F detector measured a 6% contribution from backscattered radiation.

Detector size must also be considered. Whereas the sensitive area of general-purpose semiconductor detectors is very small, ionisation chambers used in diagnostic radiology are much larger. Whilst kerma measurements are normalised to the same volume, the uniformity of the radiation across the detector cannot be assumed and is less likely with increasing detector size. The directional response will also be different for detectors of different sizes [88].

For this work, a Radcal 60cc ionisation chamber (Radcal Corporation, CA, USA) and a Raysafe Xi R/F semiconductor detector (Unfors Raysafe AB, Sweden) were available for use. The Raysafe Xi R/F detector was an improved model on that used in the evaluation by Martin [88]. It had a 2mm thick lead backing plate and active energy compensation to reduce its energy dependence [89]. To determine which dosemeter was best suited to the measurements required throughout this work, an evaluation of each was performed.

The Raysafe Xi R/F detector has an ease of use that the Radcal ionisation chamber cannot match. The Radcal 60cc ionisation chamber also suffers from leakage in the stem, cable and electrometer which can reduce the accuracy of measurement [90].

2.5.2.1 Dosemeter calibration

The Raysafe Xi R/F detector had an up to date calibration certificate issued by the manufacturer throughout the duration of this work. The calibration certificate stated that the expanded uncertainty of kerma measurement was ±5% in the 50 – 150kV_p range with 2.5mm Al total filtration. The active energy compensation was also tested at 80kV_p by the manufacturer with an additional 26mm Al filtration. The Radcal 60cc ionisation chamber was internally calibrated against the Raysafe Xi R/F detector once a year. The method for this internal calibration and its associated uncertainty budget is described in Worrall and Sutton [91]. This internal calibration process ensured that the accuracy of kerma measurement was ±5.31% in the 50 – 120kV_p range with 2.7mm Al total filtration.

2.5.2.2 Measurement of backscattered radiation

Whilst ionisation chambers do exhibit a directional dependence at large incident angles, they are expected to measure backscattered radiation. Solid state detectors are lead backed so they measure less backscattered radiation. Martin [88] found that the Raysafe Xi R/F detector measured a 6% contribution from backscattered radiation. This detector used in Martin's work had a 1mm lead backing plate; the detector available for use with this work had a 2mm thick lead backing plate and active energy compensation. It was anticipated there would be no backscatter detected.

To investigate this, the Raysafe Xi R/F detector was placed on top of a calibration jig. The jig was developed for the internal calibration of dosemeters [91] and was designed to hold detectors free in air, 30.4cm above the floor at the centre of the x-ray field. The focus to detector distance (FDD) was 100cm with a field size of 43x43cm at the detector. Three exposures were made at each of 60, 81 and 102kV_p and 10mAs and each time an average of the three measurements was taken. Next, the R/F detector was placed on top of 20cm of solid water High Equivalency (HE); the FDD and field size at the detector were the same as for the free in air case. The exposures were repeated, and the results compared to evaluate how much of the backscatter from the solid water HE was detected.

The difference in measured kerma between the with and without backscatter cases was less than 1% across the kV_p range; it is concluded that the R/F detector does not measure backscattered radiation.

2.5.2.3 Dosemeter angular dependence

To assess the angular dependence of the Raysafe Xi R/F detector it was placed at the centre of the x-ray field at a 100cm FDD in a retort stand and rotated through increments of 5°. Exposures were made at 81kV_p and 5mAs at each angle following the methodology of Martin [88]. The equivalent measurements were also made for the Radcal 60cc ionisation chamber for comparison.

The results are shown in figure 2-4.

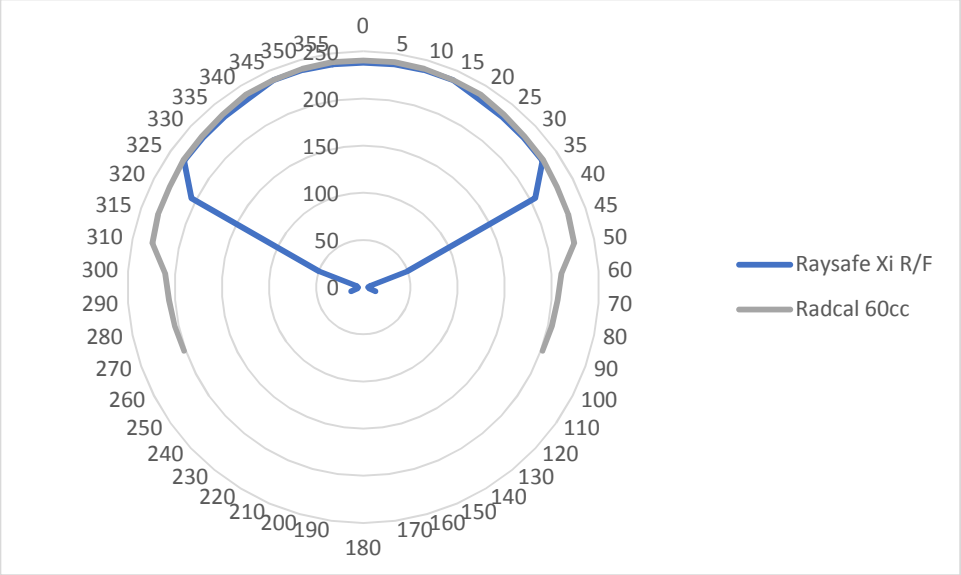

Figure 2-4: the angular dependence of the Raysafe Xi R/F detector and the Radcal 60cc ionisation chamber shown in a polar plot. The units of kerma are µGy, with a measurement uncertainty of ±6%

The Radcal 60cc ionisation chamber is observed to measure a consistent kerma from 0° to 50° to each side, after which there is a slight reduction in the measured kerma which is, to some extent at least, explained by the reduced solid angle of the detector relative to the x-ray source. The Raysafe Xi R/F detector measures a consistent kerma from 0° to 35° to each side, beyond which there is a sharp reduction to zero. This represents a significant difference in the angular dependence of the Raysafe Xi R/F detector compared with the Radcal 60cc ionisation chamber, and one which must be considered when selecting the dosemeter to be used for this work. The results are in agreement with those of Martin [88].

2.5.2.4 Dosemeter energy dependence

Energy dependence was first assessed in a scatter free environment. The Radcal 60cc ionisation chamber and the Raysafe Xi R/F detector were placed in turn on top of the calibration stand at the centre of the x-ray field, at a 100cm FDD with a 43x43cm field size at the detector. Three exposures were made at each of 60, 81 and 102kV$_p$ at 10mAs and an average of the three measured kerma taken. Additional filtration of 0.5 and 1.5mm of copper were then added at the x-ray tube output and the same measurements taken. The results are shown in figure 2-5, along with the kerma measurements predicted by the IPEM report 78 spectrum generator [84] using matching kV$_p$s of 60, 81 and 102, an anode angle of 13°, a voltage ripple of 0%, a target material of tungsten, a fixed filtration of 3mm Al and additional copper of 0.5 and 1.5mm. These combinations produced x-ray beams with first HVLs within the range of 2.32 – 11.13mm Al, covering the standard beam quality RQA ranges of RQA2 – RQA8 [90].

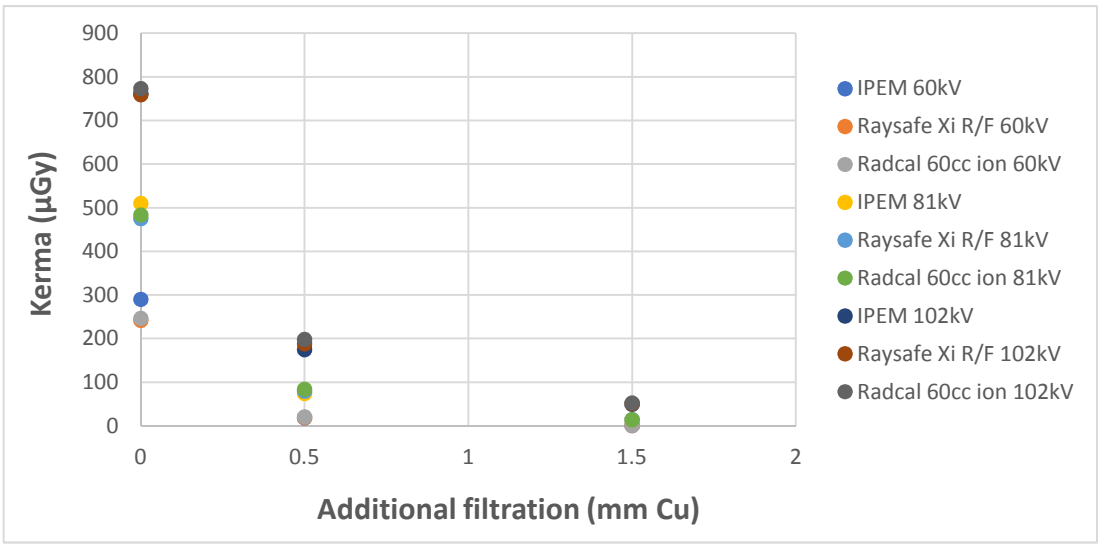

Figure 2-5: the kerma measured by the Raysafe Xi R/F detector, the Radcal 60cc ionisation chamber and as estimated by the IPEM report 78 spectrum generator for varying thicknesses of added copper filtration

For the free in air geometry, the kerma measured by the Radcal 60cc ionisation chamber and the Raysafe Xi R/F detector agree to within ±5% across the full range of kV_p and added copper filtration. The measured results are lower than those predicted by the IPEM report 78 spectrum generator as is expected given the theoretical basis of the IPEM report 78 spectrum generator. The measured results are a close match to those estimated by the IPEM report 78 spectrum generator, confirming that neither dosemeter has an energy dependence in a free in air geometry within a 60 – 120kV_p range.

2.5.2.5 Dosemeters in geometry inclusive of scatter

Many of the measurements that will be required throughout this work will be made with the dosemeter at or near the exit surface of a phantom. As such, the dosemeter will have to detect transmitted primary and scattered radiation. The transmitted primary will have an increased average energy due to beam hardening whereas the scattered radiation will have an increased low energy component and will be incident upon the detector from angles across a near-180° range.

To evaluate the response of each dosemeter in a geometry inclusive of scatter, a block of solid water HE measuring 20cm in all directions was used to provide attenuation and scatter. Each dosemeter was placed in turn in contact with the exit surface of the solid water HE at the centre of the block and in line with the centre of the x-ray beam. The dosemeters were fixed at 120cm FDD throughout. The x-ray field size was set at 45x45cm at 120cm FDD throughout to ensure full irradiation of the solid water HE with ever exposure. The solid water HE and the detectors were held free in air using minimalist apparatus (that did not itself introduce a source of scatter) throughout to ensure the Radcal 60cc ionisation chamber would not detect any backscattered x-rays from any

supporting surface. The geometry is shown in figure 2-6, and is similar to that used by Martin [88].

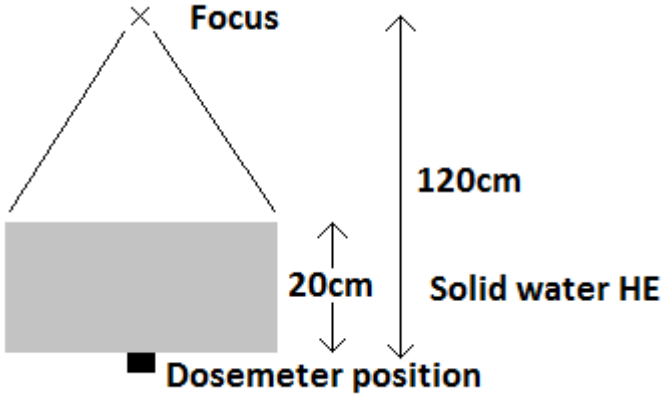

Figure 2-6: the geometry used to assess dosemeter response in a position inclusive of transmitted primary radiation and scatter

Whilst this is the best experimental geometry that could be devised with the equipment available, it has a significant limitation. The detectors are different sizes; the Raysafe Xi R/F detector uses diodes with a very small diameter; the sensitive region of the detector measures 2mm in width. The Radcal 60cc ionisation chamber has an active diameter of 8cm and a thickness of 1cm. Whilst both report a kerma normalised to a $1cm^3$ volume, the kerma will not be uniform over the Radcal 60cc ionisation chamber's sensitive area due to the anode heel effect and the fact that a 20x20x20cm block of solid water HE cannot be regarded as providing an infinite scatter plane for a detector that has an active diameter of 8cm. The higher average energy transmitted primary and the lower energies in the scatter component may fall out with the range of beam energies assessed in §2.5.2.4, so it is not certain that one or both of the dosemeters will not exhibit an energy dependence when used in this geometry. For these reasons, and the angular dependence assessed in §2.5.2.3, it is not expected that the two detectors will produce the same result.

To provide a further assessment of the expected kerma, Monte Carlo simulations were run using the BEAMnrc simulation presented throughout §2.4.3, amended to match the geometry shown in figure 2-6 and as described throughout this section. The Monte Carlo simulation was used to evaluate relative differences in kerma, meaning there was no calibration required using either dosemeter that would bias the result. Results were extracted from the Monte Carlo simulation over an area of $1mm^2$.

Three exposures were made for each combination of 60 and $81kV_p$ and 10, 20 and 32mAs. An average of the three measurements was taken as the result of each kV_p and mAs combination. After this, a separation between the exit surface of the solid water HE and the dosemeter was introduced to evaluate the change in relative response. The dosemeter's position was maintained relative to the x-ray tube; the solid water HE was moved towards the x-ray tube to produce the separation. Separations between the solid water HE and dosemeter of 10, 20, 23, 35, 40 and 50mm were introduced. At each separation, three exposures were made for each combination of 60 and $81kV_p$ and 10, 20 and 32mAs and the average of the results taken.

To estimate the magnitude of the transmitted primary radiation and the scattered radiation, the solid water HE was moved towards the output of the x-ray tube (introducing a 75cm separation between the exit surface of the solid water HE and the dosemeter). In this geometry it was expected that the transmitted primary beam will be measured, with very little scattered radiation detected. The measurements with the solid water HE at the x-ray tube output were only made with the Raysafe Xi R/F detector as the results of §2.5.2.4 indicated the measurements were likely to be in agreement with the Radcal 60cc ionisation chamber in this geometry and with this beam quality.

The measured kerma at varying separations between the exit surface of the solid water HE and the dosemeter is shown for both the Raysafe Xi R/F detector and the Radcal 60cc

ionisation chamber for 81kV$_p$ and 10mAs in figure 2-7. The results at all other kV$_p$ and mAs combinations showed the same trend. Figure 2-7 also shows the estimated kerma in a 1mm^2 region at the position of the dosemeter in the corresponding Monte Carlo simulations. As there was no dosemeter derived calibration used for the Monte Carlo simulation, the results were normalised to the kerma measured at 75cm separation using the Raysafe Xi R/F detector to assess the magnitude of the transmitted primary radiation.

Finally, figure 2-7 also shows the transmitted primary kerma measured by the Raysafe Xi R/F detector at 75cm from the exit surface of the solid water HE; note that this was a single value that has been extended across the x-axis of figure 2-7 for clarity, there was no variation in separation introduced.

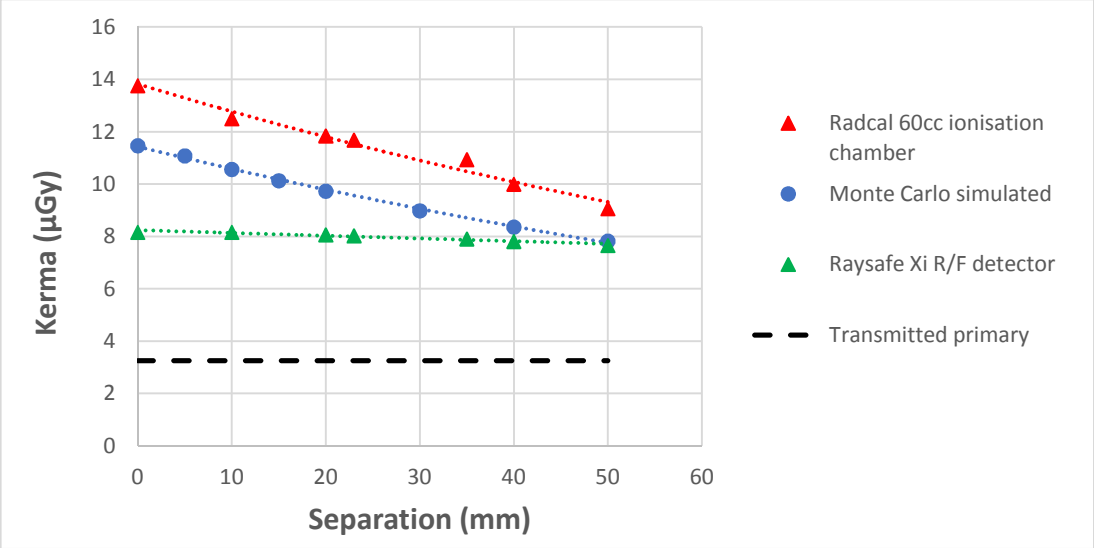

Figure 2-7: measured kerma with varying solid water HE to dosemeter separation at 81kV$_p$ and 10mAs for the Raysafe Xi R/F detector and the Radcal 60cc ionisation chamber. The results of the corresponding Monte Carlo simulations are also shown, along with an estimate of the proportion of transmitted primary radiation

The inclusion of the measured transmitted primary radiation shows that most of the kerma measured by the detectors is from scattered radiation. The kerma measured by the Raysafe Xi R/F detector and the Radcal 60cc ionisation chamber is different, both in terms

of the absolute value and the trend with increasing separation. The kerma estimated from Monte Carlo simulations does not agree with either detector, though the Monte Carlo data follows the same trend in measured kerma with separation as the Radcal 60cc ionisation chamber.

The difference in the trend with increasing separation between the Raysafe Xi R/F detector and the Radcal 60cc ionisation chamber and Monte Carlo simulation is most likely related to the Raysafe Xi R/F detector's directional dependence. The difference between the results of the Monte Carlo simulation and the Radcal 60cc ionisation chamber could be related to an energy dependence in the response of the Radcal 60cc ionisation chamber at these beam qualities. At a 23mm separation the Raysafe Xi R/F detector measures 70% of that measured by the Radcal 60cc ionisation chamber. This is in broad agreement with the results of Martin [88], who found the solid state detector to measure 74% of the Keithley ionisation chamber at a separation of 25mm.

The difference between the results of the Raysafe Xi R/F detector, the Radcal 60cc ionisation chamber and the Monte Carlo simulation could also be related to the size of the detector. The scattered radiation across the 8cm active diameter of the Radcal 60cc ionisation chamber cannot be considered uniform. It is far more uniform across the 2mm diameter of the Raysafe Xi R/F detector and the 1mm diameter of the region used to estimate kerma from the Monte Carlo simulation. For an indicative evaluation of the kerma across the diameter of the Radcal 60cc ionisation chamber, the measured kerma was assessed in 1cm increments across the central 20cm length of the Monte Carlo simulation geometry for all separations in the anode-cathode axis. The results are shown in figure 2-8.

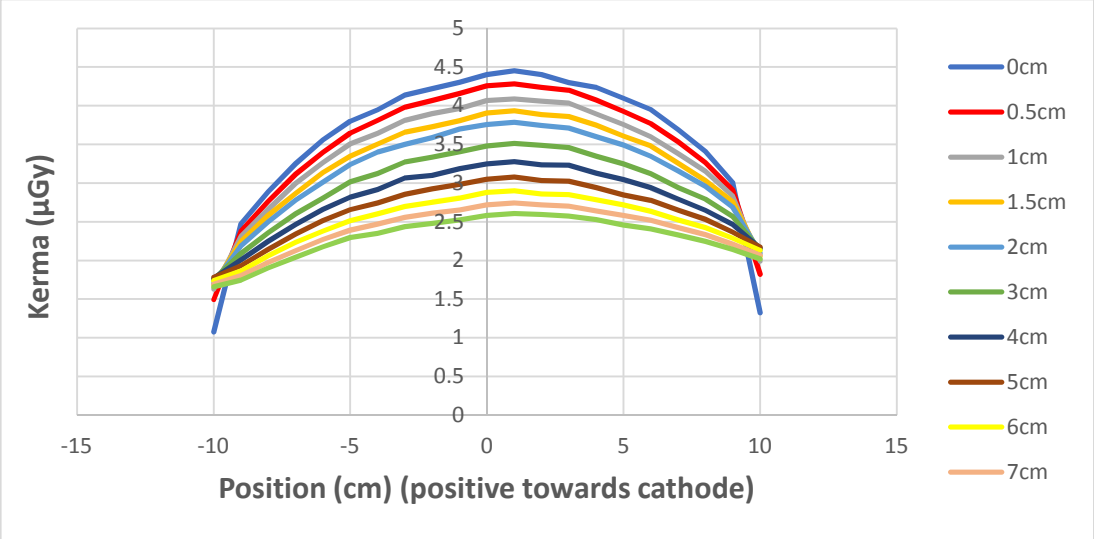

Figure 2-8: the variation in kerma across the central 20cm in the anode-cathode axis at 1cm increments with increasing separation between the exit surface of the solid water HE and the detector, as derived from Monte Carlo simulations

The results of the Monte Carlo simulation indicate an 11% difference between the maximum and minimum kerma across the central 8cm (i.e. corresponding to the sensitive area of the Radcal 60cc ionisation chamber). This is consistent across all the simulated separations between the exit surface of the solid water HE and the detector. This provides one further potential explanation as to the difference between the kerma measured by the Radcal 60cc ionisation chamber, the Raysafe Xi R/F detector and the Monte Carlo simulations.

The trend in measured kerma with separation measured by the Raysafe Xi R/F detector is different from that measured by the Radcal 60cc ionisation chamber and estimated from the Monte Carlo simulations. As figure 2-7 shows, there is only a slight downward trend in the measured kerma with increasing separation. This is likely to be because of the limited angular sensitivity of the R/F detector, which prevents its detecting much of the scattered radiation that is incident upon it, especially close to the solid water HE. As the separation

increases, scattered radiation is detected from a wider area which makes up for much of the scattered radiation that is lost from measurement because of the increased separation.

To assess the angulation in the scattered radiation incident upon the detectors, the angle of all particles was extracted from the Monte Carlo simulations for a central 1cm^2; the results are shown in figure 2-9.

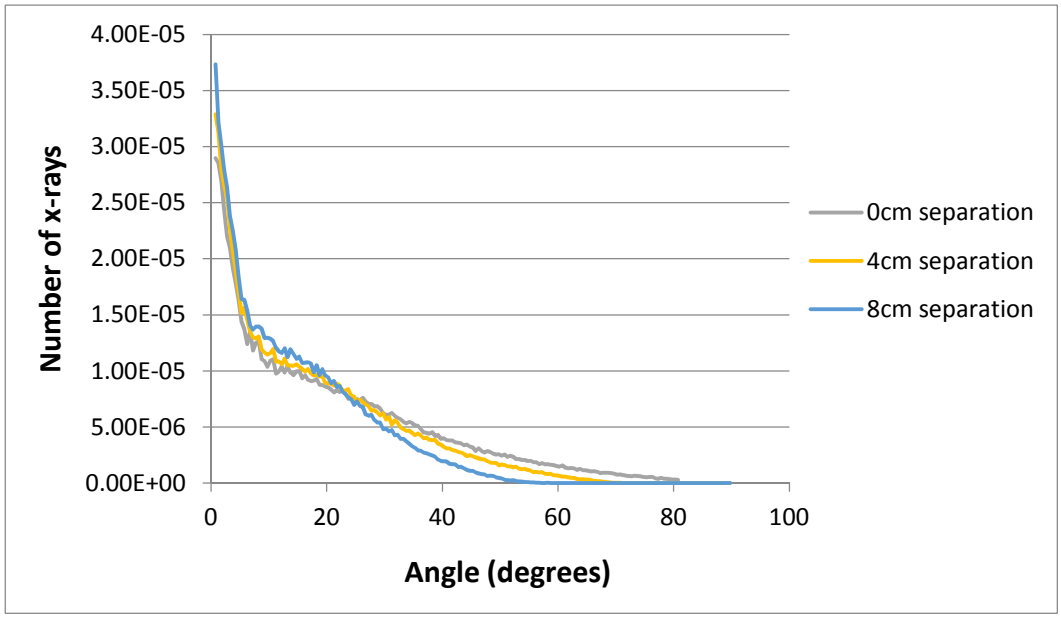

Figure 2-9: the total number of x-rays passing through the central 1cm^2 travelling at each angle relative to the primary beam (at 0°), with increasing separation. The number of x-rays at 0° is not shown

As shown in figure 2-9, most of the x-rays are incident upon the detector at an angle that is less than the 35° that was measured in §2.5.2.3 to be the limit of the Raysafe Xi R/F detector's sensitivity. At 0cm separation, 99.15% of the x-rays are travelling through the central 1cm^2 at an angle of less than 35°, at 4cm separation 99.47% of the x-rays are travelling at an angle of less than 35° and at 8cm separation 99.77% of the x-rays are travelling at an angle of less than 35°. As expected, the angular evaluations follow the general trend of fewer x-rays travelling through the central 1cm^2 at steeper angles with increased separation.

2.5.2.6 Summary

It is unlikely that either dosemeter gives an accurate measurement of kerma when used in broad beam geometries inclusive of a lot of scattered radiation. The Monte Carlo simulations suggest that the Raysafe Xi R/F detector underestimates the kerma whilst the Radcal 60cc ionisation chamber overestimates the kerma. This work will proceed by using the Raysafe Xi R/F detector for all measurements because of its superior ease of use and reliability. For validation of the Monte Carlo simulation, some quantitative aspects will be undertaken in a largely scatter free geometry. If the simulation results match those measurements undertaken in both geometries that are scatter free and inclusive of scatter, the use of the Raysafe Xi R/F detector for this purpose is valid.

Where the Raysafe Xi R/F detector will also be used for measuring the kerma at the exit surface of the solid water HE to represent that incident upon a computed radiography (CR) plate and a direct digital detector, it is worth noting that nothing is known about the energy or angular responses of either of these types of detector.

2.5.3 Non-measurement based validation

2.5.3.1 IPEM report 78

Direct measurements of x-ray spectra are possible with the use of very sophisticated detection equipment [92]; however, accurate results with this equipment are hard to obtain and there was no access to such equipment for this work.

The IPEM report 78 spectrum generator [84] was first issued by IPEM in 1997 and was subsequently updated in 2016. The program is capable of producing spectra from Tungsten, Molybdenum or Rhodium targets at tube voltages of 20 – 150kV$_p$, anode angles

of 6 - 22° and voltage ripples of 0 – 30% having passed through any user defined combination and thickness of the various attenuating materials available. The data comes from the 'Catalogue of Spectral Data for Diagnostic X-Rays' published in 1979 [93]. The resultant spectra is given in 0.5keV intervals for a pencil beam created using the conditions specified by the user and travelling directly through the attenuating materials with no contribution from scatter. In addition to the spectra, the program also returns the average energy, HVL and kerma for the x-ray beam at a 750mm distance from the tube focus.

The IPEM report 78 spectrum generator [84] has been used as a comparison for Monte Carlo simulations before [56, 86, 94, 95]. There is merit in comparing the shape of the x-ray beam spectra along the centre line of the x-ray beam generated for the Monte Carlo simulation with that given by the IPEM report 78 spectrum generator for the closest possible exposure factors. This will highlight any obvious errors with the Monte Carlo simulation. The two cannot be expected to be an exact match however, as the target and filtration materials are different and the spectra from the IPEM report 78 spectrum generator does not include any contribution from scattered radiation where the Monte Carlo simulations will.

A Monte Carlo simulation was run at 81kV$_p$ with no attenuator in the beam (this space was filled with air) and a beam size consistent with 1cm^2 at 100cm from the focus. The energy spectra was obtained using BEAMDP for the central 0.5cm^2 region from the scoring zone positioned 750mm from the x-ray tube focus. The comparative spectra in the IPEM report 78 spectrum generator was generated using a Tungsten target, 81kV$_p$, 0% voltage ripple and a 2.5mm aluminium attenuator and was converted from photon fluence (Φ) to energy fluence (Ψ). The two were normalised to the energy fluence at 46keV which was close to the average energy of each spectrum. The energy fluence spectra of the two can be seen in figure 2-10.

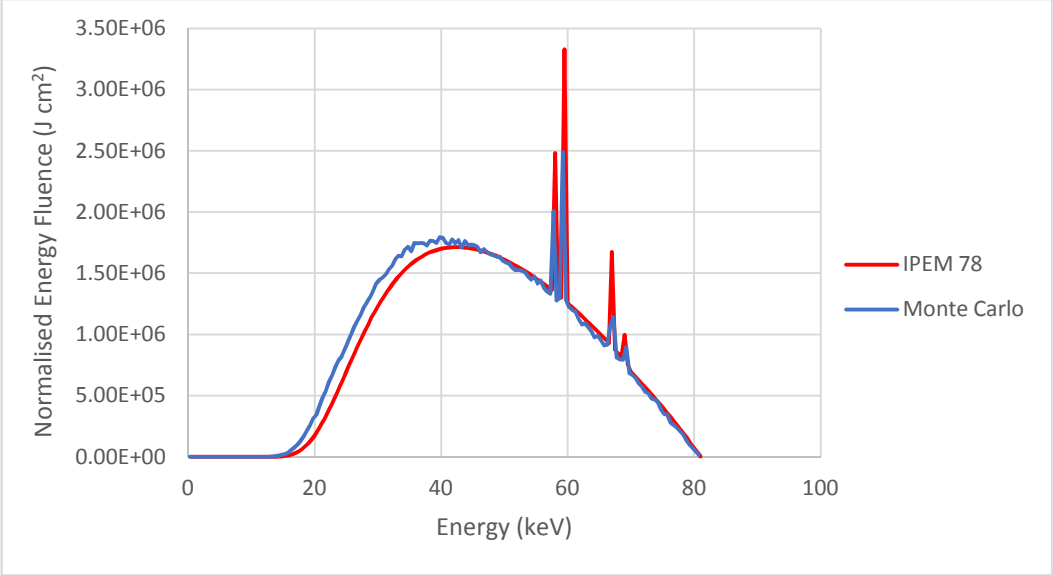

Figure 2-10: the energy fluence spectra generated for an 81kV$_p$ exposure using IPEM report 78 and the BEAMnrc Monte Carlo simulation

The shape of the bremsstrahlung curves are a close match, which is consistent with the findings of comparisons made between the spectra generated by the IPEM report 78 spectrum generator and Monte Carlo simulations elsewhere [56, 86, 95]. The Monte Carlo simulation spectra has less characteristic radiation than that of the IPEM report 78 spectrum generator; this agrees with the findings of comparisons made elsewhere [86].

Although the Monte Carlo spectra has been generated using an x-ray beam measuring 1x1cm at a 100cm distance from the focus, there will still be a contribution to the spectra from scattered radiation. In addition, the Monte Carlo spectrum was generated using a Tungsten-Rhenium target, and not pure Tungsten as in the IPEM report 78 spectrum generator and uses pyrex, beryllium, aluminium and PMMA as filtration materials whereas the IPEM report 78 spectrum generator uses only aluminium. The results confirm that there is no gross error in the energy fluence spectrum generated from the Monte Carlo simulation.

The results of the comparison between the two across the 40 – 120kV_p range were similar as for the 81kV_p case; they were consistently close.

2.5.3.2 Validation of simulation geometry

Estimates of measured kerma in the absence of, and at the exit surface of, an attenuator are dependent upon the field size. A simple test of the exposure geometry involves measuring the extent of the x-ray field at a 100cm focus to detector distance (FDD) for simulations intended to produce 10x10cm and 43x43cm fields at a 100cm FDD. The field size was varied by changing the position of the x and y-collimators (component module 8 in figure 2-2); confirming the expected field size at a 100cm FDD for each field verified that this adjustment produced the expected result.

For a simulation using 81kV_p, BEAMDP was used to produce a scatter plot for the x and y positions of all photons from the phase space file corresponding to the scoring zone at a 100cm FDD (scoring zone 3 in figure 2-2). The data files for the 10x10cm and 43x43cm field sizes contained data for over 5 and 81.9 million photons respectively. The x and y positions of the first 10,000 of each are shown in figure 2-11(a&b).

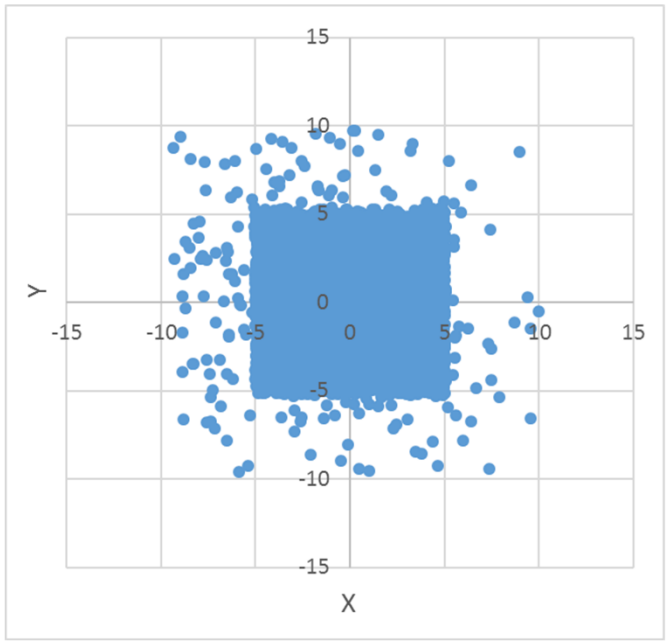

(a)

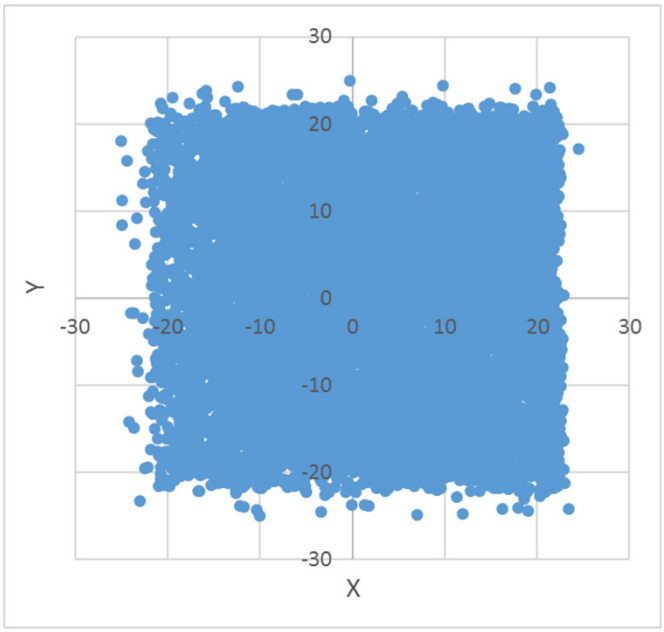

(b)

Figure 2-11: a scatter plot showing the position of 10,000 x-ray photons for a Monte Carlo simulation for (a) 10x10cm and (b) 43x43cm field sizes

As can be seen in figure 2-11, the simulated field sizes are as expected for both field sizes. Whilst there are some x-ray photons falling just outside the field, these are 3.8% of the total number of photons for the 10x10cm field and 2% of the total number of photons for the 43x43cm field. These results are consistent with x-rays that have undergone scattering

at some stage in the simulation, changing their direction resulting in their falling outwith the nominal field size.

2.5.4 Measurement based validation

Comparative information was obtained from the Monte Carlo simulations by using BEAMDP to create an energy fluence (Ψ) distribution from the phase space file created at the appropriate scoring zone within the simulation. The distribution was created using x-rays present in the centremost 1cm^2 of the scoring zone in all cases, with further regions of 1cm^2 added in other locations as required for the specific purpose of the validation exercise (those concerning the anode-heel effect in particular). Energy bins of 0.5keV were used from 0 to the keV that matched the examination kV_p for each simulation. For each energy bin, the energy fluence was converted to kerma using the mass energy transfer coefficient ($\frac{\mu_{tr}(E)}{\rho}$). The mass energy transfer coefficient was calculated from the mass energy absorption coefficient, ($\frac{\mu_{en}(E)}{\rho}$), via;

$$\mu_{tr} = \frac{\frac{\mu_{en}}{\rho}}{(1-g)} \times \rho \qquad \text{[equation 2.1]}$$

Where g is the fraction of initial electron energy converted to photon energy on slowing to rest in a material. Values of g were linearly interpolated for initial energy from those published in the International Commission on Radiation Units and Measurements (ICRU) report 37 [96]. Although g is very small (6.62×10^{-4} at 100keV in air), it was included to maintain a thorough approach.

Kerma was then calculated for each energy bin using;

$$K_E = \Psi_E(E)\ \frac{\mu_{tr}(E)}{\rho} \qquad \text{[equation 2.2]}$$

For each energy bin, the median value of keV was used to derive a value of mass energy transfer coefficient from the National Institute of Standards and Technology (NIST) database [97] to be applied to the whole energy bin.

The total kerma was calculated by summating the individual kermas from each energy bin;

$$K_{Tot} = \int K_E \, dE \qquad \text{[equation 2.3]}$$

Since the physics of electromagnetism are not included with the BEAMnrc Monte Carlo code, it is not possible to simulate an exposure mAs that would produce the approximate number of electrons, and therefore x-ray photons, that would be expected in the real exposure. For the validation, the simulations will be used to calculate relative differences, which only requires a means of normalising the simulation so that it can be meaningfully compared to the relative difference of the measurements made of the actual exposure. Each simulation was normalised by applying a correction factor, C_n, to the kerma in each energy bin;

$$K_{Tot} = \int (K_E \times C_n) \, dE \qquad \text{[equation 2.4]}$$

A value of C_n was derived for each simulation to ensure K_{Tot} = 100µGy for a 1cm x 1cm region at the centre of scoring zone 1.

$$C_n = \frac{100}{K_{Tot}} \qquad \text{[equation 2.5]}$$

Where the same value of C_n is then applied to any equivalent sized region in scoring zone 3, the difference in kerma is then as a result of the attenuator provided the accelerating potential and x-ray beam size are the same. This normalisation is shown in figure 2-12.

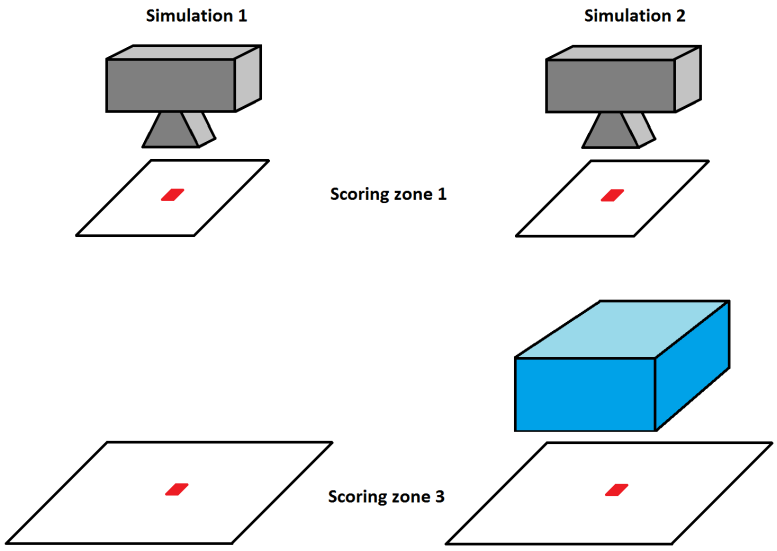

Figure 2-12: the process for normalising the results of Monte Carlo simulations. Central regions of 1cm^2 are shown in scoring zones 1 and 3. Scoring zone 2 is not shown, but is positioned in air 750mm from the x-ray tube focus

With reference to figure 2-12, a C_n value was calculated using equation 2.5 for each of the simulations 1 and 2. When each value of C_n was applied to scoring zone 1 in each simulation, it resulted in a total kerma of 100µGy for the central 1cm^2 (the region is shown in red in figure 2-12). When each value of C_n was applied to scoring zone 3 in each simulation, in simulation 1 it gave the total kerma in a 1cm^2 area 100cm from the tube focus in the absence of an attenuator. In simulation 2, it produced the total kerma in a 1cm^2 area 100cm from the tube focus at the exit of the attenuator. As the total kerma for a 1cm^2 area at the centre of scoring zone 1 was equal for both simulations 1 and 2, the total kerma for any equivalent area at scoring zone 3 was directly comparable between simulations 1 and 2 provided the only difference between the simulations was related to the attenuator (i.e. same kV_p, same field size etc.). This technique could be used to look at differences in kerma at the exit of different attenuators as well as differences in kerma at different positions across the x-ray beam (any position in scoring zone 3 provided the area remained 1cm^2).

The value of C_n derived for each simulation of equivalent kV_p and field size was consistently observed to be very close (Coefficient of Variation, $\% \frac{Std\ Dev}{Mean}$ < 0.1%), differing only as a result of the statistical uncertainty of the Monte Carlo simulation. This is as expected where there has been no change to any parameter that could affect the simulated x-ray beam at scoring zone 1.

2.5.4.1 Validation of kerma across the x-ray field

The kerma is known to vary across the x-ray field, primarily as a result of the anode-heel effect. The extent of this variation is dependent upon the construction of the x-ray tube. The anode angle and size will affect this, as will the composition, thickness and position of all filtration. Measurements were made of the kerma at 1cm increments along the centre of the x and y axes at 81kV_p and 10mAs, as shown in figure 2-13, using the Raysafe Xi R/F detector. The Raysafe Xi R/F detector is lead backed meaning backscatter did not contribute to the measured kerma. The FDD was 100cm and the field size was 40x40cm. The Raysafe Xi R/F detector has no significant angular dependence; this was confirmed by angling the x-ray tube in 1° increments from -15° to + 15° with the centre of the x-ray beam incident upon the centre of the Raysafe Xi R/F detector for each exposure. The differences in the measured kerma were consistent with the effect of the increased difference in distance between the tube focus and Raysafe Xi R/F detector as a result of the angulation. Therefore, all of the measurements undertaken to characterise the anode-heel effect have the same uncertainty of ±5%.

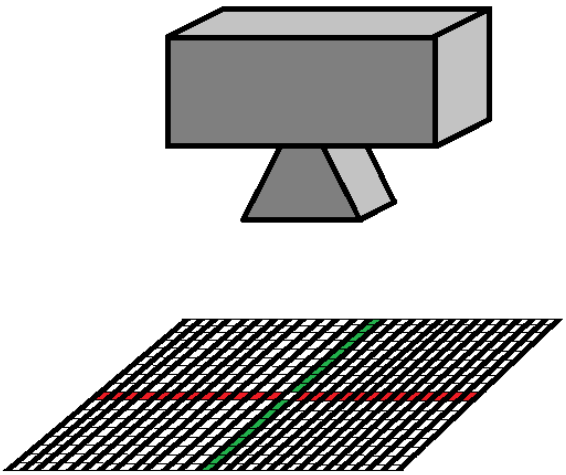

Figure 2-13: measurements of kerma made along the centre of the x and y axes in increments of 1cm at 81kV$_p$ and 10mAs

The comparison between the measured and simulated kerma across the x-ray field is shown in figure 2-14.

(a)

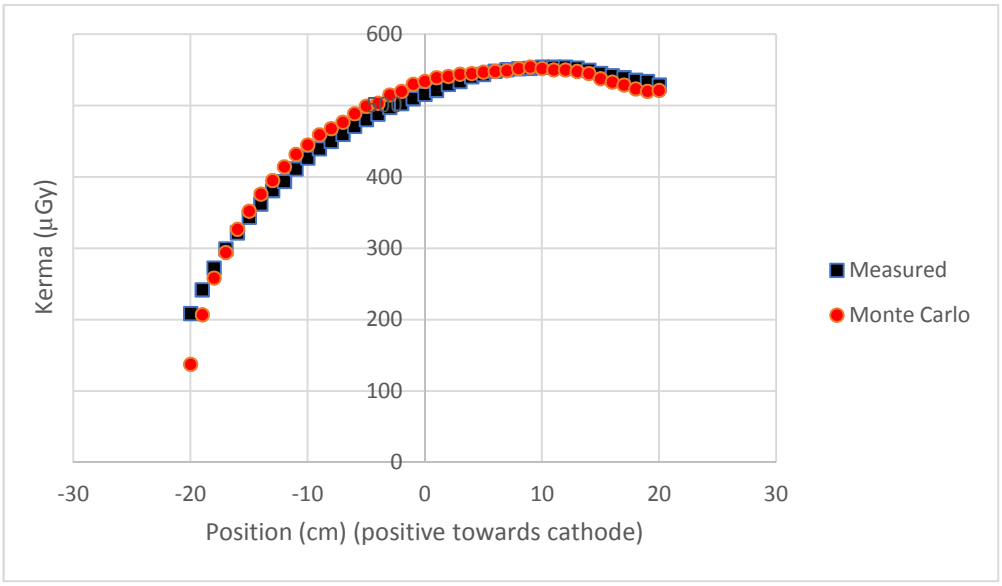

(b)

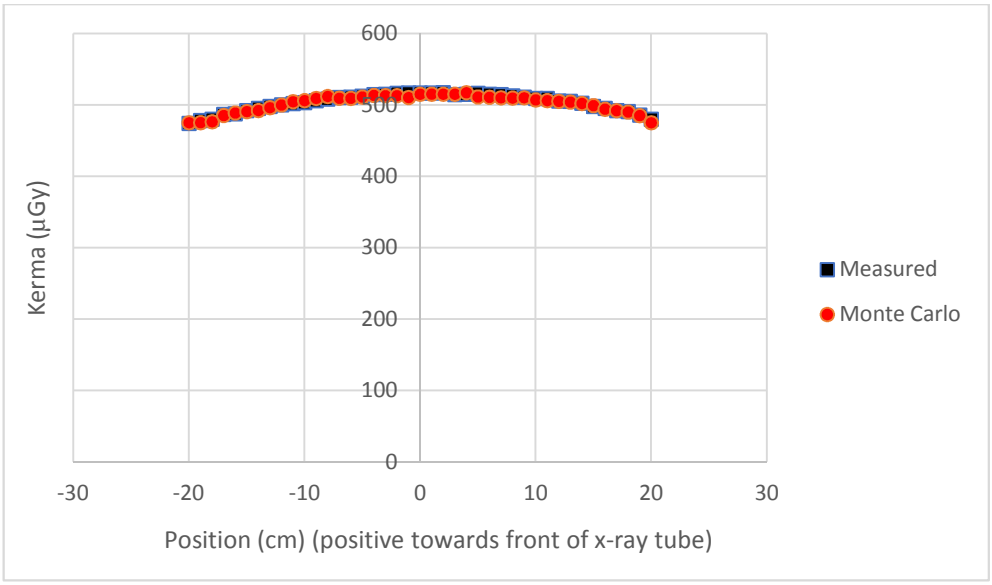

Figure 2-14: measured and Monte Carlo simulated kerma along the full length of the centre of the (a) x and (b) y axes for a 40x40cm field size. The uncertainty in the measured kerma is ±5%, the uncertainty in the Monte Carlo simulated kerma is approximately ±5.4%

In the x (anode-cathode) axis, the Monte Carlo data agrees with the measured data to within 5% across the full field except at the periphery of the field towards the anode (positions -19 and -20 in figure 2-14(a)) where the Monte Carlo simulated data underestimates the kerma by 15 – 30%. This is likely to be related to the thickness of the target and anode combination in the z-axis which is subject to a minimum value of 25mm by BEAMnrc. The results in figure 2-14(a) suggest it should be slightly thinner than this for a closer agreement at the periphery. Where the Monte Carlo simulation will use kerma values at, or near, the centre of the x-ray beam, the reduced contribution of scatter as a result of the underestimated kerma at the periphery of the x-ray beam is not a significant source of uncertainty as it reduces in intensity by at least 18^2 before reaching the centre of the field.

In the y axis, the Monte Carlo data agrees with the measured data to within 1.3% across the full field.

2.5.4.2 Validation of simulation half value layer measurements

The first and second HVLs are a good measure of the quality of the x-ray beam. Measurements of the 1st and 2nd HVL at the centre of a 10x10cm and 40x40cm x-ray field at a 100cm FDD were made on the Philips Optimus 50 radiographic x-ray unit in the 50 – 109kV$_p$ range using the Raysafe Xi R/F detector and incrementally increasing thicknesses of aluminium. The aluminium that was used was of 99% minimum purity, available in 10x10cm sheets up to a total thickness of 10mm with any thickness between 0.1mm and 10mm in 0.1mm increments available.

The first and second HVLs were derived for the Monte Carlo simulation at the equivalent kV$_p$ for a 1cm^2 region at the centre of the field using equation 2.6, which is slightly modified from Ali [94].

$$\frac{K_{air}(t)}{K_{air}(0)} = \frac{\sum_{i=1}^{n}\left(\frac{\mu_{tr}}{\rho}\right)_{E_i}^{air}\frac{d\Psi_{E_i}}{dE_i}exp\left(-\left(\mu_{E_i}^{abs}-\mu_{E_i}^{air}\right)t\right)\Delta E_i}{\sum_{i=1}^{n}\left(\frac{\mu_{tr}}{\rho}\right)_{E_i}^{air}\frac{d\Psi_{E_i}}{dE_i}\Delta E_i} = \frac{1}{2} \qquad \text{[equation 2.6]}$$

Where;

- $K_{air}(t)$ and $K_{air}(0)$ are the air kerma at the measurement plane with and without the attenuator, of thickness t, respectively
- E_i is the energy at the centre of bin i
- ΔE_i is the width of bin i
- n is the number of energy bins
- $\left(\frac{\mu_{tr}}{\rho}\right)_{E_i}^{air}$ is the mass energy transfer coefficient for air at energy E_i
- $\mu_{E_i}^{att}$ and $\mu_{E_i}^{air}$ are the linear attenuation coefficients at energy E_i for the attenuating material and for air respectively
- $\frac{d\Psi_{E_i}}{dE_i}$ is the differential energy fluence at energy E_i

The results for the 1st and 2nd HVL as measured and derived from the Monte Carlo simulation are shown in table 2.1, along with the percentage deviation between the two. The uncertainty in the measured HVLs is ±10%. The uncertainty was the result of an

uncertainty budget determined using methods outlined in work published by the author on uncertainty budgets [91] and takes consideration of the following factors; dosemeter calibration, uncertainty in the thickness of the aluminium filters, uncertainty relating to the interpolation of a value from a plot of kerma and attenuator thickness, exposure reproducibility and geometry reproducibility.

kV_p	10x10cm field						40x40cm field					
	1^{st} HVL			2^{nd} HVL			1^{st} HVL			2^{nd} HVL		
	Measured	Simulated	Deviation	Measured	Simulated	Deviation	Measured	Simulated	Deviation	Measured	Simulated	Deviation
50	2.21	2.13	-3.57%	5.48	5.23	-4.60%	2.15	2.08	-3.16	4.84	5.10	5.31%
60	2.69	2.57	-4.31%	6.88	6.59	-4.16%	2.51	2.48	-1.12%	5.93	6.42	8.25%
70	3.16	3.03	-4.15%	8.37	8.06	-3.68%	2.93	2.91	-0.82%	7.28	7.81	7.21%
81	3.58	3.44	-4.02%	9.95	9.50	-5.48%	3.39	3.31	-2.39%	8.46	9.28	9.66%
90	4.02	3.85	-4.35%	11.50	10.94	-5.12%	3.79	3.66	-3.46%	9.79	10.55	7.71%
102	4.46	4.25	-4.82%	13.10	12.47	-5.75%	4.22	4.03	-4.43%	11.03	12.08	9.47%
109	4.73	4.54	-4.06%	14.30	13.63	-4.69%	4.48	4.27	-4.80%	12.52	13.07	4.35%

Table 2.1: the measured and simulated 1^{st} and 2^{nd} HVLs for field sizes of 10x10cm and 40x40cm at a 100cm FDD across the diagnostic kV_p range

As table 2.1 shows, the HVLs derived from Monte Carlo simulations match those measured to within 10% in all cases. This close agreement between measured and simulated HVLs for an x-ray path along the centre of two significantly different field sizes demonstrates that the effects of scattered radiation are being accurately simulated.

2.5.4.3 Validation of effective linear attenuation coefficient

The application for Monte Carlo simulation throughout this work is the estimation of effective linear attenuation coefficients, μ_{eff}. A linear attenuation coefficient, μ, is a measure of the fraction of x-rays of a single given energy that are attenuated by a material, per unit thickness. X-ray beams used clinically are polyenergetic and have a broad beam geometry, therefore these values cannot be used. A μ_{eff} is required, a value that pertains to the fraction of a specific polyenergetic beam in a broad beam geometry that is attenuated by a material, per unit thickness. For a single material attenuator, μ_{eff} can be determined using measurements of the attenuator exit kerma and the kerma without any attenuator present using equation 2.7.

$$\mu_{eff} = -\frac{Ln(\frac{Attenuator\ exit\ kerma}{Attenuator\ free\ kerma})}{Attenuator\ thickness}$$ [40] [equation 2.7]

A Monte Carlo simulation can be used to determine values of μ_{eff}, but accurate estimates of μ_{eff} can only be achieved where the simulation accurately simulates attenuation and scatter.

The best validation of this is by comparing the μ_{eff} estimated by simulation at the exit surface of varying thicknesses of attenuator with the measured μ_{eff} for equivalent materials in an equivalent geometry.

Water is a compound that is available within the BEAMnrc Monte Carlo software. A series of simulations were created by adjusting the model to simulate a water phantom extending 10cm from the centre in both the x and y axes with depths of 10, 50, 75, 100, 125, 150, 175 and 200mm. The phantom was positioned such that the exit surface was always 98.5cm from the tube focus, with estimates of μ_{eff} made for a central $1cm^2$ region at a 100cm FDD. Simulations were run at 60, 70 and 81kV_p for beam sizes of 10x10 and 40x40cm for all depths of water. Values of μ_{eff} were calculated using equation 2.7 following estimates of kerma made using equations 2.2 and 2.3 in the absence of, and at the exit of, the water attenuator, as shown in figure 2-12.

The equivalent x-ray geometry saw a container extending 10cm in both directions along the x and y axes positioned with the exit surface of the basin at 98.5cm from the x-ray tube focus and 1.5cm above the Raysafe Xi R/F detector. The basin was filled with water to the same eight depths as were simulated. Measurements of kerma were made at 60, 70 and 81kV_p at 20mAs using broad focus and field sizes of 10x10 and 40x40cm for each depth of water. For each unique combination, three measurements of kerma were made and an average of the three taken as the result. The Raysafe Xi R/F detector was placed directly on the floor; being a solid state dosemeter it has lead backing and, as such, radiation backscattered from whatever material it sits upon does not influence the result. This means that the surface upon which the dosemeter sits does not need to be included in the Monte Carlo simulation, which instead extended the simulation beyond the detector position with 100cm of air, as per the design of the model. μ_{eff} was calculated from the measured kerma using equation 2.7.

The deviation between the measured μ_{eff} and the μ_{eff} estimated from the simulations is shown in figure 2-15. The uncertainty of the measured μ_{eff} is ±7.1% (two individual uncertainties of ±5% combined in quadrature). There is an additional unquantified

uncertainty related to the difference between the pure water simulated in the Monte Carlo simulations and the impure water used for the measurements of kerma.

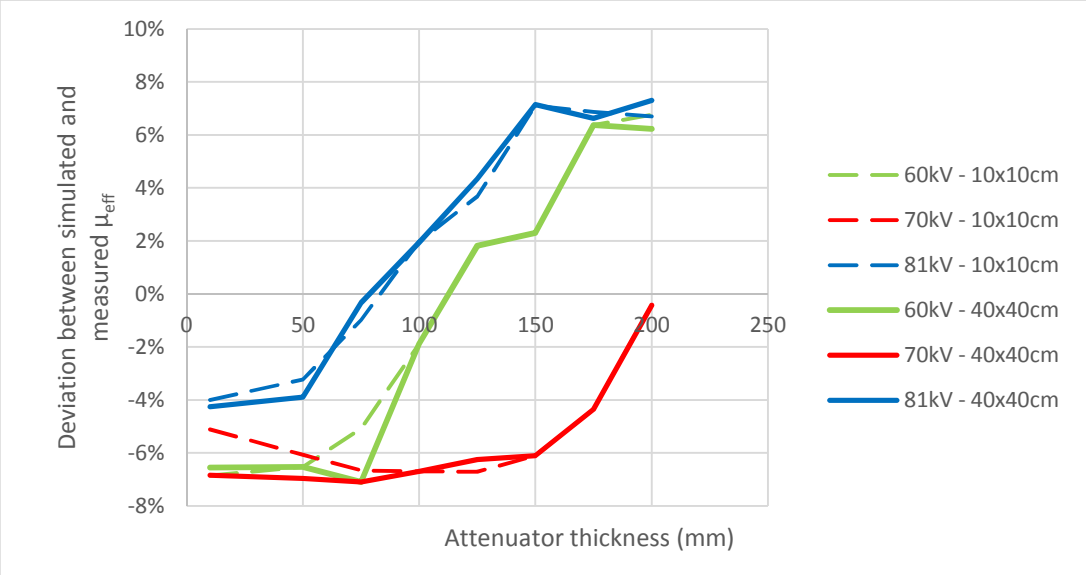

Figure 2-15: the deviation between effective linear attenuation coefficients, μ_{eff}, calculated using measured and simulated data for varying depths of water, kV_p and field size

As can be seen in figure 2-15, the values of μ_{eff} derived from Monte Carlo simulations agree with those calculated using measured values of kerma to within ±7.1% in all cases, with the highest deviation 7.1% and the average absolute deviation 4.9%. This demonstrates that the Monte Carlo simulation accurately accounts for the attenuation and scattering of x-rays by water.

Compounds can be added to the BEAMnrc code where their elemental composition and density are known. The intended use of the Monte Carlo simulations throughout this work mean that it will be necessary to add compounds relating to organs and tissues. In order to ensure that new compounds could be added accurately, a new compound – Solid Water HE (Gammex) – was purchased. The Solid Water HE was available in 20 x 20cm blocks of total thickness 200mm divided such that any thickness can be achieved between 5 and 200mm

in 5mm increments. Solid Water HE uses nanospheres to create homogeneous slabs that mimic true water within 0.5% at diagnostic energies [98].

The chemical composition of the Solid Water HE was provided with the material on purchase [85]. This was used to add it to the list of available materials in BEAMnrc and allows for a comparison between measured values and simulation to verify that it has been added correctly and further validate the simulation.

The validation process undertaken for the water attenuator was repeated with solid water HE. The deviation between the measured μ_{eff} and the μ_{eff} estimated from the simulations is shown in figure 2-16. As was the case for water, the uncertainty of the measured μ_{eff} is ±7.1%.

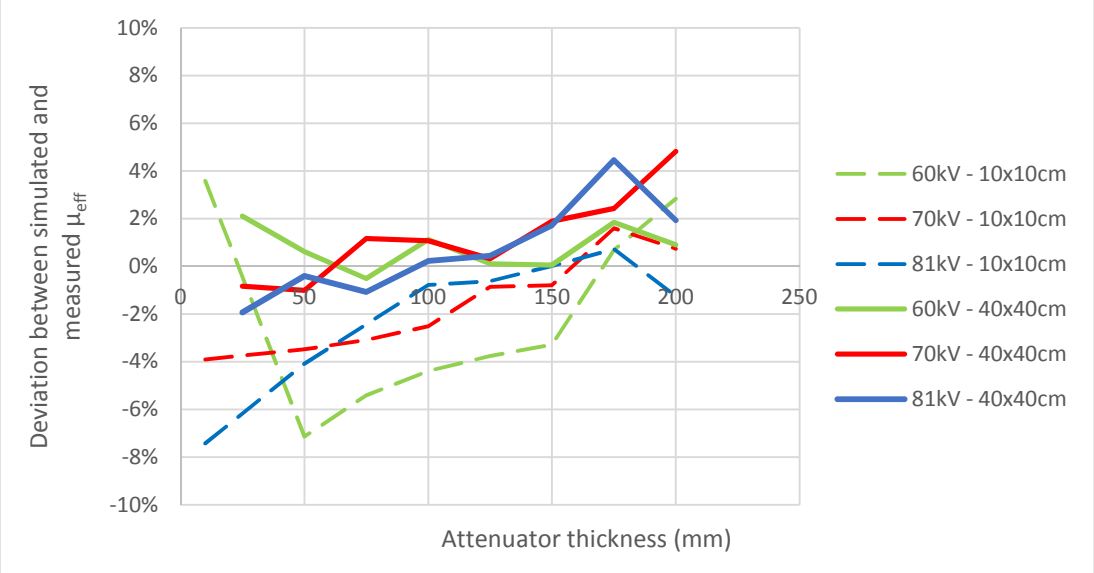

Figure 2-16: the deviation between effective linear attenuation coefficients, μ_{eff}, calculated using measured and simulated data for varying thicknesses of solid water HE, kV_p and field size

As can be seen in figure 2-16, the values of μ_{eff} derived from Monte Carlo simulations agree with those calculated using measured values of kerma to within ±7.1% in all cases, with the highest deviation 7.1% and the average absolute deviation 2.7%. This demonstrates that

the Monte Carlo simulation accurately accounts for the attenuation and scattering of x-rays by a compound that has been added to the code.

2.6 Summary

A Monte Carlo model of a Philips Optimus 50 radiographic x-ray unit has been created, optimised and presented in this chapter. The results of the final simulation construction have been validated against nominal values, the output of the IPEM report 78 spectrum generator and measurements made on the radiographic x-ray unit. It has been shown that the field size of the simulation at a 100cm FDD matches the intended, that the energy fluence spectrum broadly matches that produced by the IPEM report 78 spectrum generator, that the output varies across the full extent of the x and y axes in the same manner as measured, that the 1^{st} and 2^{nd} HVLs agree with the measured to within the experimental uncertainty and values of μ_{eff} derived using the result of the simulation agree with those calculated using kerma measurements to within experimental uncertainty. The validation process also confirmed that a material that is not in the EGSnrc code can be accurately added where the elemental composition and density is known. This Monte Carlo model can be amended as required and then used to accurately derive the values of μ_{eff} that are required throughout this work.

Chapter 3 – Creation of the computational model

Overview

This chapter presents the creation of the computational model for the specific case of deriving the thickness of a single composition attenuator. The methods for obtaining values for the initial air kerma at the detector, the final intensity at the detector and the effective linear attenuation coefficients are explained in detail. The uncertainty in the estimate of each variable is quantified.

3.1 Introduction

Chapter 1 introduced the concept of using the Beer-Lambert law as the basis of a computational model for estimating the thickness of an attenuator. The rearranged form of the Beer-Lambert law is;

$$x = -\left[\frac{Ln\left(\frac{k_d}{k_0}\right)}{\mu_{eff}}\right] \qquad \text{[equation 3.1]}$$

Where for the purposes of this work;

- x is the estimated thickness of the attenuator (mm)
- k_d is the kerma at the image receptor (μGy)
- k_0 is the initial air kerma (μGy)
- μ_{eff} is the effective linear attenuation coefficient (mm^{-1})

To test whether the idea works in principle, the first computational model created was for the simplest possible application.

This chapter describes the creation and optimisation of a computational model for the specific case of deriving the thickness of a single composition attenuator. The uncertainty in the estimate of each variable is quantified. A simple overview of the design of the computational model is shown in figure 3-1.

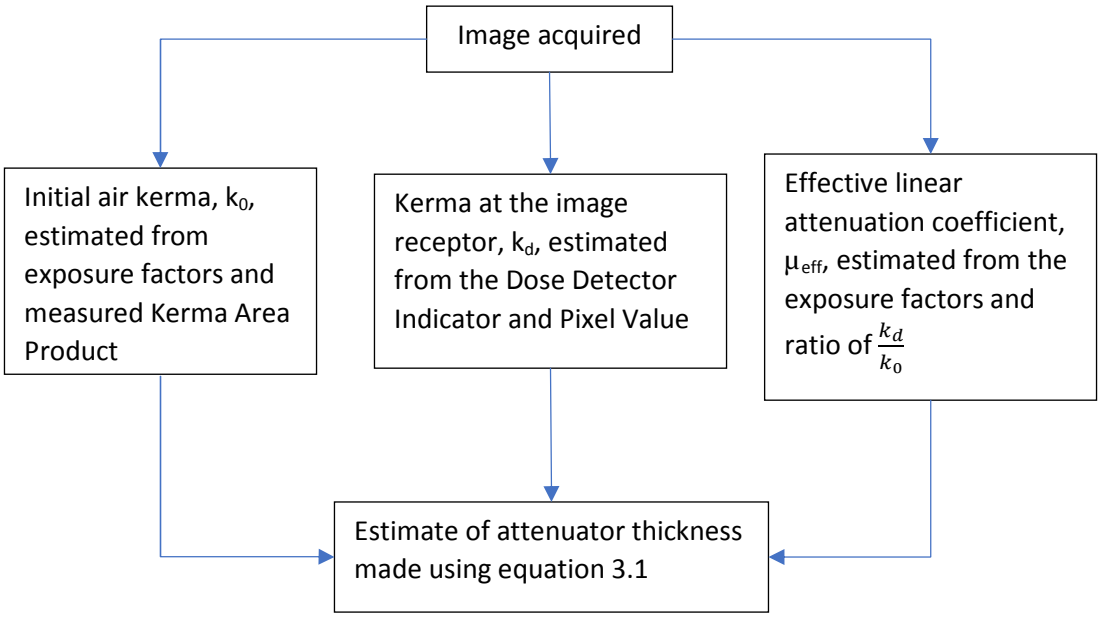

Figure 3-1: the design of the computational model for the specific case of deriving the thickness of a single composition attenuator

The estimate of each variable used in the computational model - the initial air kerma, k_0, the kerma at the image receptor, k_d, and the effective linear attenuation coefficient, μ_{eff}, is discussed in turn. The look up tables (LUT) used by the computational model to select an appropriate value for each of these variables are introduced, as are the methods used to derive the values within the LUTs. The uncertainty associated with the value selected by the computational model from the LUTs for any given examination is quantified in order to evaluate the limitations of the computational model. The steps taken to optimise the values within the LUTs and the process for the selection of values by the computational model are presented.

3.2 Materials

The materials and equipment used throughout the work presented in this chapter are described in the following sections.

3.2.1 Radiographic x-ray equipment

All of the exposures presented in this chapter were undertaken on a Philips Optimus 50 radiographic x-ray unit. The system was installed in March 2010 in the radiology department of Ninewells Hospital, Dundee and is typical of that used for a general-purpose x-ray room. Capable of exposures across a kV_p range of 50 – 125, it has a total filtration of 3.39mm of Aluminium at $81kV_p$ measured at a 100cm focus to detector distance (FDD). The x-ray system was up to date in terms of its preventative maintenance visits and medical physics led quality control (QC) programmes and was confirmed by the author to be performing to within the manufacturer's specification throughout. With previous work having demonstrated a dependence for measured radiation output on the number of exposures undertaken following a period of non-use for this system [91], the unit was warmed up with a minimum of 10 exposures prior to any use. This has previously been demonstrated as adequate to ensure consistency from exposure to exposure [91]. The x-ray unit had a kerma area product (KAP) meter attached at the tube output; KAP values for each exposure were routinely recorded to ensure consistency from exposure to exposure when required. The KAP meter was calibrated across the full kV_p range of the equipment, traceable to a national standard. The unit has 2 focal spot sizes; broad focus (1.2mm) and fine focus (0.6mm).

3.2.2 Single composition attenuator

The attenuator used throughout this chapter is solid water High Equivalency (HE) (Gammex). This was purchased especially for this work and was available in 20 x 20cm blocks, with a total thickness of 200mm divided such that any thickness can be achieved between 5 and 200mm in 5mm increments. According to the manufacturer, solid water HE uses nanospheres to create homogeneous slabs that mimic true water within 0.5% at diagnostic energies [98]. Included with the purchase of this material was a certificate detailing its complete elemental composition; this meant the material could be accurately included in the Monte Carlo model introduced in chapter 2. §2.5.4.3 included a comparison of simulated and measured μ_{eff} with a solid water HE attenuator. The closeness of the agreement between the two confirmed that the material had been correctly added to the Monte Carlo code and that the elemental composition provided with it was accurate.

3.2.3 Radiation dosemeter

All of the kerma measurements presented throughout this chapter were made using a Raysafe Xi radiographic / fluoroscopic (R/F) detector [99]. At all times throughout this work, the Raysafe Xi R/F detector had an up to date calibration, undertaken at a secondary standards dosimetry laboratory (SSDL) by representatives of the manufacturer. The calibration uncertainty for kerma measurements was 5%, quoted on the SSDL's calibration certification and traceable to a national standard.

3.2.4 Digital image receptors

At the start of this work it was anticipated that the computational model could be used on any digital imaging system; this includes both direct digital radiography (DDR) and computed radiography (CR) systems.

The wide dynamic range of digital imaging systems means that images do not appear over-exposed, even when they are acquired with more radiation than necessary to produce a diagnostic image. For this reason, in the UK the Medicines and Healthcare products Regulatory Agency (MHRA) recommended that all digital equipment be provided with a detector dose indicator (DDI) intended as a single numerical value that represents the exposure received by the detector [100]. If provided with a range of expected values for well undertaken clinical examinations for comparison, the operator can use these values to judge whether the exposure used for the examination was appropriate. All manufacturers of digital imaging equipment have developed their own DDI; the International Electrotechnical Commission (IEC) have since proposed a standard DDI [101] but this has not yet been widely adopted. The pixel values (PV) selected for the display of each image are based upon the signal transfer property (STP) calibration. As with DDI, this relationship varies with equipment manufacturer.

At present, NHS Tayside has too few DDR systems to achieve the access necessary to undertake this work. Instead the work presented in this chapter was undertaken using a Fuji CR system. Exposure information will be entered manually into the computational model where required. The Fuji CR system uses the s-value as its DDI.

Whereas DDR uses a limited number of detectors – assigned per room or interchangeable between a limited number of compatible x-ray units – CR systems are supplied with a great many cassettes to allow multiple examinations to be undertaken simultaneously across many rooms and to allow for the selection of an optimally sized cassette for the patient and

examination. Cassettes are subject to accidental and mechanical damage and a decrease in sensitivity over time with use [102]. Users should include a test monitoring the sensitivity of each cassette in their QC programme and ensure that all cassettes are checked regularly for artefacts [103]. It is generally necessary for users to operate a rolling CR cassette replacement programme to ensure artefact free images. This means that cassettes in clinical use will not all be of the same age, which could mean there are differences in their sensitivity to radiation.

It is known that image receptors do not exhibit a consistent response with beam quality; Asai et al [104] characterised the response of a Fuji CR cassette in 2008 and found it to have a peak sensitivity at just under 40keV with a steady decline as the keV was increased from this point.

In order to examine the sensitivity of the Fuji CR cassettes used locally with varying beam quality, two CR cassettes were selected at random and uniformly exposed to the level required to produce an s-value of 100 at all available kV_p settings on the Philips Optimus 50 radiographic x-ray unit (24 unique kV_ps, ranging from 40 to 125). There was no additional filtration added for these exposures so the beam quality was altered only by the change in kV_p. The exposure required to achieve an s-value of exactly 100 at each kV_p was obtained by adjusting both the mAs and FDD.

The field size was set to maximum for all exposures, thereby exposing the full cassette and well beyond. This ensured a consistency of scattered radiation regardless of the FDD used. There was a consistent delay between cassette exposure and readout – this was 10 seconds.

When an s-value of 100 had been achieved, the KAP for the exposure was recorded as displayed on the x-ray unit. The CR cassette was replaced by the Raysafe Xi R/F detector at the centre of the x-ray beam and the same exposure was undertaken three times with the

kerma from the Raysafe Xi R/F detector and the KAP recorded each time. Exposure reproducibility was confirmed where each value of measured KAP agreed with the average of the three to within 2%. Where this was the case, an average of the 3 kerma results measured by the Raysafe Xi R/F detector was taken as the exposure required to produce an s-value of 100 for that kV_p. The results for each cassette (the unique identifier of each are shown in the legend) are shown in figure 3-2.

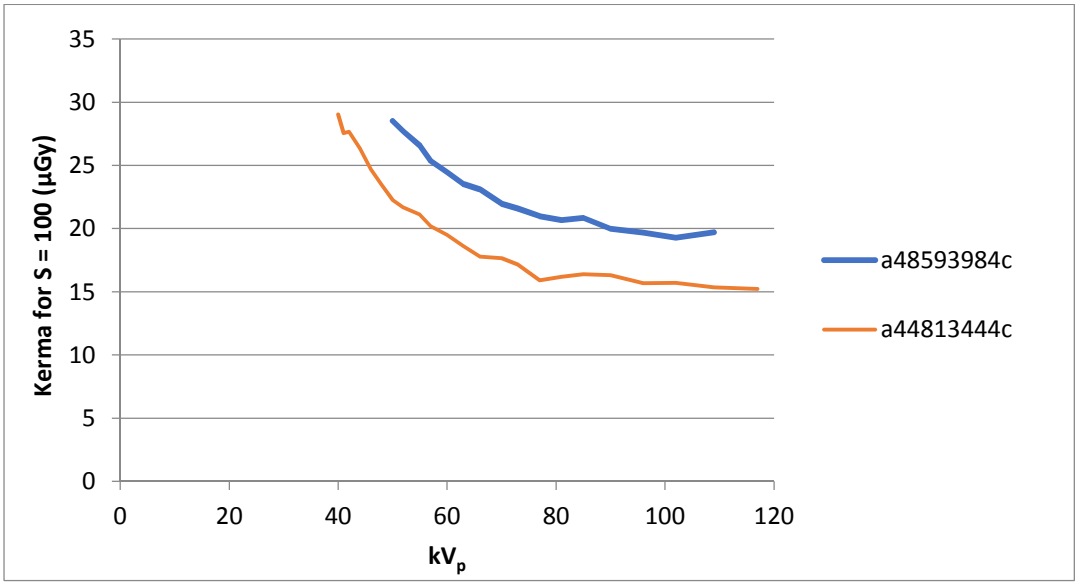

Figure 3-2: the measured sensitivity and energy dependence of two Fuji CR cassettes exposed using the same x-ray equipment to the kerma required to produce an s-value of 100 across a range of kV_p. The uncertainty in kerma measurement is < 5.4%

Whilst Fuji give a single calibration for the s-value of all CR cassettes, figure 3-2 clearly demonstrates that there can be significant differences between the sensitivity of two cassettes across the diagnostic energy range. Where the intention in this work is to estimate the kerma at the detector from a calibration of s-value or the STP, it is clear that the use of a single set of calibrations for all of the CR cassettes on site could be a source of significant uncertainty. Whilst it would be possible to perform calibrations on each individual CR cassette, this would be a significant undertaking and is not a practicable option. As CR cassettes are known to lose sensitivity with time and use, these calibrations

would need to be periodically revisited, making the use of the computational model for CR systems even less attractive.

To reduce the uncertainty of the results that rely upon the calibration of the image receptor throughout this work, a new Fuji 24 x 30cm CR cassette was purchased solely for this work. This cassette was the only cassette used from this point forward and was not used for any other purpose. The same Fuji XG5000 CR multi-loader was used for processing the cassette after every exposure. The use of a single CR cassette with x-ray exposure information manually added to the computational model mimics the use of a single detector DDR system.

3.3 The creation of look up tables for the computational model

3.3.1 Estimating initial air kerma

There are two ways of estimating the initial air kerma, k_0. The first uses the examination kV_p, mAs, FDD, focal spot selection and field size, the second uses the examination kV_p and measured KAP. For both methods it was hypothesised that it would be possible to accurately estimate k_0 for any exposure using measured values or relationships and correction factors. This hypothesis is explored for each method in the sections that follow.

3.3.1.1 Estimating initial air kerma using calculated radiation output

The measured output of an x-ray machine in terms of µGy mAs^{-1} will vary with kV_p, mAs, FDD, field size and focal spot selection. The effect on radiation output by changes in kV_p, mAs and FDD is well understood for theoretical exposures in ideal conditions [3], though exposures in a realistic setting will not follow these theoretical relationships exactly.

Therefore, some empirical confirmation is required. The effect of field size and focal spot selection are less intuitive.

To examine the effect of field size on radiation output, the Raysafe Xi R/F detector was placed on the floor at the centre of the field of view at a 100cm FDD. As the Raysafe Xi R/F detector is lead backed, there was no backscatter contribution to the measurements. Exposures were made at 60, 81 and 102kV_p and 10mAs with broad focus for field sizes that varied in 5cm increments in both axes parallel and perpendicular to the anode-cathode axis from 5-40cm in each. Three exposures were made at each field size and an average of the kerma measured by the Raysafe Xi R/F detector for the three taken. The average kerma for each field size was normalised to that measured for a field size of 20x20cm. The average results for the 81kV_p exposures across the full field are expressed as a ratio with the kerma measured for a 20x20cm field size in table 3.1.

		Field size parallel to anode-cathode axis (cm)							
		5	10	15	20	25	30	35	40
Field size perpendicular to anode-cathode axis (cm)	5	0.948	0.939	0.956	0.961	0.965	0.973	0.966	0.972
	10	0.952	0.959	0.967	0.968	0.980	0.978	0.982	0.977
	15	0.962	0.968	0.973	0.990	0.994	0.996	0.999	1.000
	20	0.974	0.978	0.996	1.000	1.003	1.012	0.961	1.014
	25	0.976	0.981	0.995	1.016	1.018	1.025	1.029	1.019
	30	0.988	0.992	1.003	1.016	1.026	1.034	1.042	1.039
	35	0.989	1.003	1.012	1.030	1.038	1.043	1.045	1.048
	40	0.996	1.003	1.018	1.038	1.047	1.054	1.051	1.053

Table 3.1: average measured kerma at varying field sizes expressed as a fraction of that measured at a field size of 20x20cm, for 81kV_p, 10mAs and at a 100cm FDD

As the results in table 3.1 show, radiation output has a significant dependence on field size. The difference between the measured kerma at 5 x 5cm and 40 x 40cm is greater than 10%.

Any LUT used to estimate k_0 must account for the field size. The results were very similar for 60 and 102kV$_p$. The average difference between the values in table 3.1 and those for 60kV$_p$ was 0.47%. The average difference for 102kV$_p$ was 0.16%. It is concluded that there is no kV$_p$ dependence on the field size correction.

To examine the effect of focal spot size on radiation output, the Raysafe Xi R/F detector was placed on the floor at the centre of the field of view at a 100cm FDD with a 20x20cm field size. Exposures were made at 60, 81 and 102kV$_p$ and 10mAs using broad focus, then fine focus. Three measurements were made at each kV$_p$ and an average of the results taken. The measured output for broad focus was higher in all cases; 4.3%, 3.1% and 2.3% for 60, 81 and 102kV$_p$ respectively. Any LUT used to estimate k_0 must account for the focal spot used for the examination.

Given these dependencies, the estimate of k_0 using calculated radiation output needs to account for examination kV$_p$, mAs, FDD, field size and focal spot selection. Values can be selected from a LUT with appropriate corrections made to match the examination exposure factors and geometry. The LUT of output values, $k_{0,LUT_{output}}$, was created as follows;

- All exposures were made at 100cm FDD, with a field size of 20x20cm using broad focus. The Raysafe Xi R/F detector was placed at the centre of the x-ray field
- Output values were measured for kV$_p$ values in steps of approximately 10, or the nearest allowed by the generator, from minimum (50kV$_p$) to maximum (125kV$_p$)
- The output was measured at 0.5mAs, being the lowest the x-ray unit was capable of delivering, and then every discrete mAs step up to 8mAs (0.63, 0.8, 1.0, 1.25, 1.6, 2.0, 2.5, 3.2, 4.0, 5.0, 6.3). A review of the QC records for this x-ray unit showed that the measured output becomes linear with mAs at 8mAs. Below 8mAs there is a non-linearity which is especially pronounced below 1mAs. This is a result of the very short exposure time, meaning the system barely reaches, or does not reach,

the selected mA before the end of the exposure which leads to a lower than expected output for the exposure

The following corrections to the values in the LUT can be applied;

- The output for values in-between the kV_p values in the LUT can be accurately interpolated using a power fit as it is known that output increases with kV_p^2 for a unit functioning as it should. This correction is referred to as k_{kV_p}
- Above 8mAs, a linear correction with mAs can be applied to the output value measured at 8mAs. This correction is referred to as k_{mAs}
- Output values for a FDD different from 100cm can be calculated using an inverse square correction. This correction is referred to as k_{FDD}
- Output values for any field size can be linearly interpolated using the fractions presented in table 3.1. This correction is referred to as k_{field}
- Output values can be adjusted for the selection of focal spot as necessary, using the known difference in output between broad and fine focus at the examination kV_p. This correction is referred to as k_{focal}

The estimate of k_0 for a given kV_p, mAs, FDD, field size and focal spot selection using the radiation output, $k_{o_{output}}$, is undertaken as follows;

$$k_{0_{output}} = k_{0,LUT_{output}} \times k_{kV_p} \times k_{mAs} \times k_{FDD} \times k_{field} \times k_{focal} \qquad \text{[equation 3.2]}$$

3.3.1.2 Uncertainties with the derivation of initial air kerma using output measurements

There are uncertainties associated with this method for estimating k_0. A total uncertainty can be assigned after the completion of an uncertainty budget, which identifies each source of uncertainty, measures or estimates a value for the uncertainty then calculated

the standard uncertainty of each individual source of uncertainty by considering its probability distribution and applying a divisor. The overall uncertainty is obtained by adding the individual contributions in quadrature. This is the approach recommended by the Joint Committee for Guides in Metrology (JCGM) of the Bureau International des Poids et Mesures (BIPM) [105] and as applied to radiation dosimetry by the International Atomic Energy Agency (IAEA) [90]. As part of the preparation for this project, the author carried out a comprehensive analysis of the uncertainty budget for the internal cross-calibration of dosemeters used for radiographic units [91]. The methodology adopted was used to create uncertainty budgets for the estimate of k_0.

Table 3.2 presents an uncertainty budget for the determination of k_0 using output measurements.

Source of uncertainty	Type of uncertainty	Value	Probability distribution	Divisor	Standard uncertainty	Rationale
Calibration of dosemeter used for output measurement	B	±5%	Normal	2	±2.5%	The SSDL certify that the accuracy of a kerma measurement made using the dosemeter is subject to this uncertainty
Reproducibility of x-ray tube output	A	±2%	Normal	$\frac{s}{\sqrt{n}}$	±0.63%	Measured output from the x-ray tube is not consistent from exposure to exposure. Slight variations in kV_p, mAs and the stochastic nature of x-ray production are accounted for with this uncertainty, which was derived from multiple reproducibility measurements made across the kV_p range and kerma ranging from 50 - 500μGy
Variation in output with time	B	±2%	Rectangular	$\sqrt{3}$	±1.15%	Output from the x-ray tube reduces throughout the lifetime of the tube with age and use. Constant electron bombardment of the focal track causes damage over time, which manifests itself with the tungsten cracking on a minute scale. Electrons can travel further into the tungsten by entering these cracks – the x-rays generated at this depth are unlikely to escape the tungsten and so the radiation output is reduced [82]. This estimate is quantified by using historical survey data and accounts for potential output reduction for 1 year
Field size estimation	B	±0.7%	Rectangular	$\sqrt{3}$	±0.40%	The value of k_0 obtained from the LUT is dependent upon the field size. The measurement of field size when populating the LUT and for the examination of interest is subject to an uncertainty, estimated to be ±5mm in both axes, which translates to the uncertainty stated here
Correction for FDD	A	±1%	Normal	$\frac{s}{\sqrt{n}}$	±0.45%	The value of k_0 obtained from the LUT is dependent upon the FDD. The measurement of FDD for an examination is subject to an uncertainty, as is the correction using the inverse square law
Correction for mAs	A	±1.5%	Rectangular	$\sqrt{3}$	±0.87%	Any correction made to the value of k_0 obtained from the LUT for examination mAs will have an associated uncertainty. This was estimated from measurements
Combined standard uncertainty			Assumed normal		±3.01%	
Expanded uncertainty			Assumed normal (k=2)		±6.02%	

Table 3.2: the uncertainty budget for the estimate of k_0 using output measurements

This uncertainty budget is only applicable when the output values in the LUT and correction factors are updated annually. The uncertainty over a greater period of time is difficult to quantify but is likely to be significantly larger. It would make sense to match the frequency of these measurements to the lower frequency of equipment Quality Control (QC) (recommended 1-2 yearly by IPEM report 91 [106]). This would involve measurements in addition to those made for the purposes of routine QC however, since variation in output with field size is not a recommended test in IPEM report 91 [106].

The measurement of µGy mAs^{-1} made during equipment QC and for the LUT is at the centre of the x-ray field. This is appropriate for the use of the computational model being developed for the single composition phantom; since the attenuator is uniform in size and composition, the measurement of PV can be made at the centre of the x-ray beam.

3.3.1.3 Estimating initial air kerma using measured kerma area product

In the case of an examination undertaken on a DDR system, the KAP meter measures the KAP during the examination and the digital x-ray system records the x-ray beam field size at the detector (calculated using the position of the collimators at the x-ray tube output and the known FDD). Therefore it is straightforward to calculate a value for kerma simply using;

$$kerma\ (\mu Gy) = \frac{KAP\ (\mu Gy\ m^2)}{Field\ size\ (m^2)} \qquad \text{[equation 3.3]}$$

This value for kerma represents the kerma at the detector where there is no attenuation of the x-ray beam, since the KAP is measured before the attenuator. Further, this assumes that the x-ray beam is of uniform intensity across its area, which is not the case because of the anode-heel effect and the small contribution from diverging x-rays having travelled different distances to reach the detector. A series of correction factors can be derived to

give the true value of k_0 at any location across the detector, however these are specific to a single anode angle, a single tube focus and vary with field size and FDD.

As an illustrative exercise, correction factors were derived for the Philips Optimus 50 radiographic x-ray unit. The Raysafe Xi R/F detector was placed at the centre of a 43x43cm x-ray beam (this was confirmed by measuring the light beam) at a 100cm FDD and exposed three times at 81kV$_p$ and 10mAs using the broad focus. The KAP was recorded for each exposure and an average of the measured kerma and KAP recorded. The Raysafe Xi R/F detector was then moved in increments of 1cm along the centre axis parallel and perpendicular to the anode-cathode axis, resulting in 43 measurements taken along each axis. Correction factors were derived by taking the ratio of the average kerma in each position to the kerma per unit area calculated using;

$$k_{field} = \frac{Measured\ kerma}{\left(\frac{KAP}{43x43}\right)} \qquad \text{[equation 3.4]}$$

The correction factors across both axes are shown in figure 3-3.

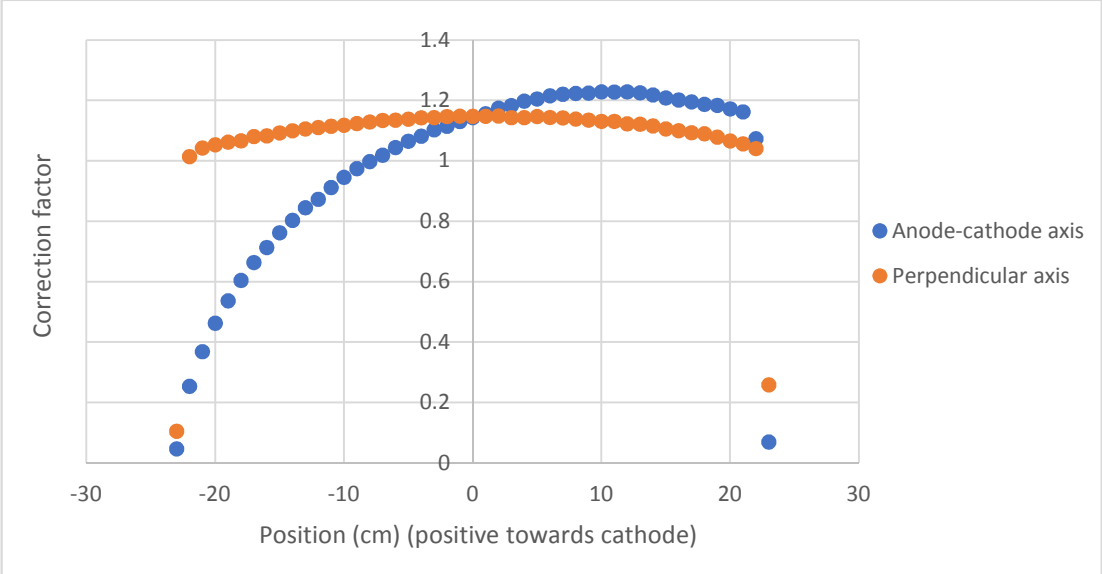

Figure 3-3: the ratio of measured kerma and kerma per unit area along the axes parallel and perpendicular to the anode-cathode axis. The anode-heel effect is clear in the anode-cathode axis

The results show that a correction factor, k_{field}, of 1.146 should be applied to the $\left(\frac{KAP}{43x43}\right)$ value for an accurate estimate of k_0 at the centre of the x-ray field. This correction factor does not vary with kV_p, but does with anode angle, tube focus, field size and FDD. Correction factors could be measured for all likely combinations of tube focus, field size and FDD but this would be impractical. Monte Carlo simulations could be used to derive the correction factors required for the computational model.

As the KAP meter is an ionisation chamber, any measurement it makes is subject to an uncertainty that will be kV_p dependent. The calibration of the KAP meter across the clinically relevant kV_p range is already a recommended test as part of a QC programme. This data was already available for the KAP meter on the Philips Optimus 50 radiographic x-ray unit at kV_p values ranging from 50 – 125kV_p in increments of 10kV_p (or as close as the unit will allow). They were derived by comparing the KAP measured by the unit to that measured by an independent large area ionisation chamber – the Radcal patient dose calibrator (PDC). The Radcal PDC had a calibration traceable to a national standard.

Given these dependencies, values of k_0 can be corrected using factors in a LUT. The LUT of correction factors was created as follows.

- The calibration of the KAP can be corrected for; this value is dependent upon the kV_p. This correction is referred to as k_{KAPcal}
- The correction factor for any field size can be linearly interpolated from those generated at all field sizes measured. This correction is referred to as k_{field}

The estimation of k_0 using the KAP, $k_{o_{KAP}}$, is undertaken as follows;

$$k_{0_{KAP}} = \left(\frac{KAP}{Field\ size}\right) \times k_{KAPcal} \times k_{field} \qquad \text{[equation 3.5]}$$

3.3.1.4 Uncertainties with the derivation of initial air kerma using measured kerma area product

Table 3.3 presents an uncertainty budget for the determination of k_0 using KAP measurements which uses the same methodology as outlined in §3.3.1.2.

Source of uncertainty	Type of uncertainty	Value	Probability distribution	Divisor	Standard uncertainty	Rationale
Calibration of dosemeter used for KAP calibration	B	±5.31%	Normal	2	±2.66%	The Radcal patient dose calibrator is calibrated internally against a Raysafe Xi R/F detector that has a calibration with an SSDL. The internal calibration protocol has an associated uncertainty budget [91]
Reproducibility of KAP meter measurement	A	±2%	Normal	$\frac{s}{\sqrt{n}}$	±0.63%	Measurements made using the KAP meter are not consistent from exposure to exposure, after correction for the variation of the x-ray tube output. This value is derived from measurement
Variation in KAP calibration with time	A	±2%	Normal	$\frac{s}{\sqrt{n}}$	±1.15%	The calibration of the KAP meter varies with time. This estimate is quantified by using historical survey data and accounts for the potential change in calibration over 1 year
Correction factor for x-ray field inhomogeneity	B	±2%	Rectangular	$\sqrt{3}$	±1.15%	The correction factors derived to account for x-ray field inhomogeneity are subject to an uncertainty. This was measured by taking repeat measurements of the ratio of measured kerma to $\left(\frac{KAP}{field\ size}\right)$ and comparing the results
Measurement of field size	B	±2.3%	Rectangular	$\sqrt{3}$	±1.33%	The light beam was measured as a surrogate for x-ray field size. The Philips Optimus 50 radiographic x-ray unit was known to be in good adjustment throughout, therefore the light beam agreed to the x-ray field size to within ±1cm at a 100cm FDD [106]
Combined standard uncertainty			Assumed normal		±3.34%	
Expanded uncertainty			Assumed normal (k=2)		±6.68%	

Table 3.3: the uncertainty budget for the estimate of k_0 using KAP measurements

This uncertainty budget is only applicable when the calibration factors are updated annually. It would make sense to match the frequency of these measurements to the lower frequency of equipment QC (recommended 1-2 yearly by IPEM report 91 [106]). This would not involve any measurements that are in addition to those already undertaken for the purposes of routine QC.

The correction factor to account for the inhomogeneity of the x-ray field is for the centre of the x-ray field. This is appropriate for the use of the computational model being developed for the single composition phantom; since the attenuator is uniform, the measurement of PV can be made at the centre of the x-ray beam.

3.3.2 Estimating kerma at the image receptor

The kerma at the image receptor, k_d, will be estimated using information from the radiographic image. There are two options for estimating k_d; the first is to use the DDI value from the examination of interest with a measured DDI calibration, the second is to use the measured average PV from a Region of Interest (ROI) drawn on the image with the measured STP calibration. For both methods, it was hypothesised that for a broad beam geometry there would be a single calibration for DDI and STP at each kV_p that could be used to estimate k_d for any exposure of an attenuator at an equivalent kV_p. This hypothesis is explored for each method in the sections that follow.

3.3.2.1 Calibrating the detector dose indicator

Depending on the manufacturer, the DDI is derived from the average exposure across the entire image receptor, or an area around the centre of the image receptor and can either increase or decrease with increasing kerma at the image receptor. The manufacturer

should provide their intended calibration, together with the beam quality under which this calibration is valid, with the equipment.

The exposure across the image receptor varies as a result of the inhomogeneity of the x-ray beam and the varying levels of attenuation and scatter across any material placed between the x-ray tube and the image receptor. Reducing the exposure across the image receptor to a single numerical value risks losing information about how the exposure varies across the image receptor and could lead to an underestimate or overestimate k_d for any given location.

Appropriate image processing, which is dependent upon the body part being examined, is generally automatically applied by a CR or DDR system prior to image presentation to ensure a clinically diagnostic image. Without this processing, images lack contrast and are undiagnostic. For some manufacturers, the application of processing affects the DDI. This would mean that a calibration for DDI and image receptor kerma would need to exist for all available processing. It is easier to derive the image receptor kerma from an unprocessed (or minimally processed where an unprocessed image cannot be obtained) image, which means all necessary DDI calibrations for the population of a LUT need only be undertaken once.

As the practical work in this chapter was undertaken using a Fuji CR system, consider the DDI calibration for Fuji (which Fuji call the s-value) in the absence of any clinical image processing. Fuji's stated calibration for the s-value is;

$$S = \frac{1740}{Kerma\ (\mu Gy)} \qquad \text{[equation 3.6]}$$

measured at 81kV_p with zero additional filtration [107]. Any change to the calibration condition – an alteration to the kV_p or the addition of any attenuating material, like a patient or test object - mean that the manufacturer's stated relationship no longer holds

because of the energy dependence of the detector demonstrated in §3.2.4. The form of the relationship;

$$s = a_{kV_p,HVL}\left(k_d(\mu Gy)\right)^{b_{kV_p,HVL}} \qquad \text{[equation 3.7]}$$

will still be correct. Therefore, for DDI calibrations undertaken using x-ray beams of varying beam quality, the constants $a_{kV_p,HVL}$ and $b_{kV_p,HVL}$ are observed to change.

The DDI calibration was measured for the Fuji CR cassette three times. All three calibrations were undertaken at 70kV$_p$ with a different attenuator - 1mm copper, 1.5mm copper and 21mm of aluminium - positioned at the x-ray tube output. The copper attenuators are as recommended by IPEM reports 91 [106] and 32 (part vii) [103] for consistency checking of DDI calibrations during equipment QC. The 21mm of aluminium was used in an attempt to get as close as possible to the standard beam quality RQA5, which is generally used as the reference radiation quality for attenuated beams for general radiography applications [90]. For each calibration, the Raysafe Xi R/F detector was placed at the centre of the x-ray beam at a 100cm FDD and the mAs incremented until at least 8 values across a kerma range of 1.5 – 18uGy were measured. The Fuji CR system does not attempt to form an image where the kerma at the image receptor is less than 1.5µGy and the signal is saturated above 18µGy, leading to a single value of DDI with no further variation with kerma. Once the kerma had been measured at each mAs, the CR cassette was positioned in place of the Raysafe Xi R/F detector and the exposure repeated. All images were captured using the 'sensitivity' processing option, which is as close to an unprocessed image as the Fuji CR system is able to provide. The measured DDI calibrations for the Fuji CR cassette are shown in figure 3-4.

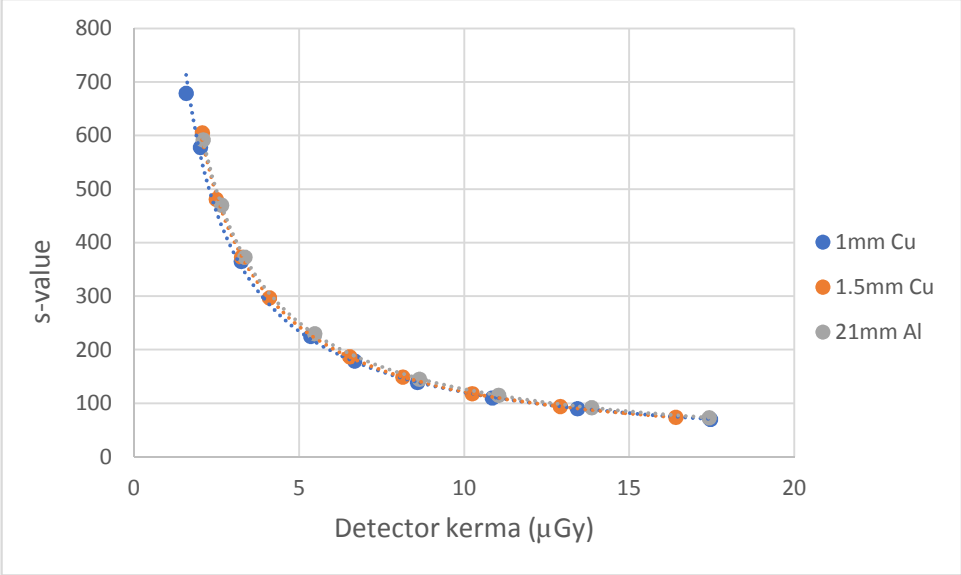

Figure 3-4: the measured s-value calibrations for the dedicated Fuji CR cassette at 70kV$_p$ for various attenuators placed at the x-ray tube output

A least squares fit was made to each of the data sets using Matlab; the coefficients along with the associated R^2 for each are shown in table 3.4.

	Measured DDI calibration		
Attenuator (cm)	$a_{kVp,HVL}$	$b_{kVp,HVL}$	R^2
1mm Copper	1102.3	-0.962	0.999
1.5mm Copper	1224.6	-1.004	0.999
21mm Aluminium	1227.0	-0.987	1.000

Table 3.4: the coefficients and correlation coefficient (r^2) following a least squares fit to each of the DDI calibration data sets

The calibrations for 1 and 1.5mm of copper are found to produce kerma values that are distinctly different for an equivalent s-value, further confirming the energy dependence of the Fuji CR cassette. The calibrations for 1.5mm of copper and 21mm of aluminium are very similar, suggesting a similar beam quality.

3.3.2.2 Calibrating the signal transfer property

The STP calibration determines how the image PV varies with kerma at the image receptor. As with DDI, this varies with manufacturer and the PV can either increase or decrease with increasing image receptor kerma. The manufacturer should provide their intended calibration, together with the beam quality under which this calibration is valid with the equipment.

The STP calibration is altered with clinical image processing, since this processing is intended to change the way an image is displayed. As with DDI, it is easier to derive the image receptor kerma from an unprocessed (or minimally processed where an unprocessed image cannot be obtained) image, which means all of the necessary STP calibrations to populate a LUT need only be undertaken once.

The STP for a Fuji CR system is of the form;

$$PV = a_{kV_p,HVL} Ln(k_d\ (\mu Gy)) + b_{kV_p,HVL} \qquad \text{[equation 3.8]}$$

where $a_{kV_p,HVL}$ and $b_{kV_p,HVL}$ are coefficients that are dependent upon beam quality of the x-ray beam incident upon the detector.

STP calibrations were measured for the Fuji CR cassette three times. All three calibrations were undertaken at 70kV$_p$ with a different attenuator - 1mm copper, 1.5mm copper and 21mm aluminium - positioned at the x-ray tube output. These were acquired in the same manner as for the DDI calibration described in §3.3.2.1 except that the s-value had to be fixed at 200 to ensure a variation in PV with kerma [107]. Once acquired, the images were extracted in native Digital Imaging and Communications in Medicine (DICOM) format directly from the CR reader console to prevent any processing being applied during the transfer to the Picture Archive and Communication System (PACS). Using the image analysis software package ImageJ [108], a 100mm^2 ROI was drawn at the centre of each

image to obtain the PV. The measured STP calibrations for the Fuji CR cassette are shown in figure 3-5.

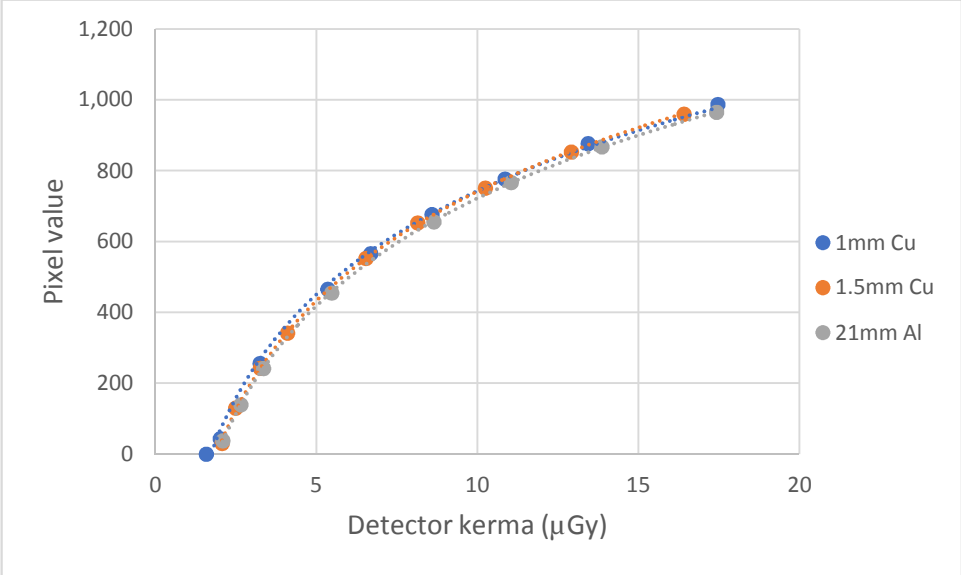

Figure 3-5: the measured STP calibrations for the dedicated Fuji CR cassette at 70kV$_p$ for various attenuators placed at the x-ray tube output

A least squares fit was made to each of the data sets using Matlab; the coefficients and associated R^2 for each are shown in table 3.5.

	Measured STP calibration		
Attenuator (cm)	$a_{kVp,HVL}$	$b_{kVp,HVL}$	R^2
1mm Copper	421.44	-227.73	0.998
1.5mm Copper	444.78	-283.17	0.999
21mm Aluminium	438.24	-287.02	1.000

Table 3.5: the coefficients and R^2 following a least squares fit to each of the STP calibration data sets

As was observed for the DDI, the STP calibrations for 1 and 1.5mm of copper are found to produce kerma values that are distinctly different for an equivalent PV and the calibrations for 1.5mm of copper and 21mm of aluminium are very similar.

3.3.2.3 Estimating image receptor kerma using the detector dose indicator or signal transfer property calibrations

As shown in figures 3-4 and 3-5, there are differences in the DDI and STP calibrations measured using different beam qualities. An estimate of detector kerma can be accurately made for an exposure undertaken with a known kV_p and beam quality where a calibration of DDI or STP is available for that combination of kV_p and beam quality. The estimate of patient thickness that forms the aim of this work will be undertaken in an environment where the kV_p of the exposure is known but the beam quality is not. Figures 3-4 and 3-5 suggest that it is not possible to use a single DDI or STP calibration to accurately estimate the kerma at the detector for any beam quality. The data can be used to show that for s-values in the range of 100 – 700, the values of kerma at the image receptor derived from the 3 DDI calibrations differ by up to 10.2%. For PV in the range of 100 – 1000, the values of kerma at the image receptor derived from the 3 STP calibrations differ by up to 11.1%. Such uncertainties are too high for an accurate estimate of attenuator thickness.

3.3.2.4 Investigating beam quality for clinical exposures

The calibrations shown in figures 3-4 and 3-5 were made with the attenuator positioned at the exit face of the x-ray tube. However, this is not clinically relevant since the patient is located as close to the detector as possible, which means that there is significantly more scattered radiation incident upon the image receptor than for a geometry involving an attenuator at the x-ray tube output. Whilst the intention of an x-ray grid is to remove as much of this scatter as possible, paediatric examinations are generally performed without a grid [3]. There is less need for a grid for paediatric patients as paediatric patients are

generally smaller than adults so less scatter is generated. The absence of a grid helps keep the radiation dose to the patient As Low As Reasonably Achievable (ALARA).

To investigate the difference in beam quality between an attenuator at the exit face of the x-ray tube (i.e. in air) and an attenuator at the digital detector, the half value layer (HVL) of the x-ray beams were measured free in air for the former and at the exit surface of an attenuator for the latter. In both cases the attenuator consisted of varying thicknesses of solid water HE, specifically 10, 20, 50, 100, 125, 150, 175 and 200mm.

For clarity, the free in air case will be referred to as the 'small field, reduced scatter geometry' and the exit surface of the attenuator case will be referred to as the 'broad field, inclusive scatter geometry'.

For the broad field, inclusive scatter geometry, the Raysafe Xi R/F detector was placed 100cm from the x-ray tube focus at the centre of the beam. Each thickness of solid water HE was positioned with the exit surface 1cm above the Raysafe Xi R/F detector. The x-ray field size measured 30x30cm at the Raysafe Xi R/F detector. Exposures were made at 60, 70 and 81kV$_p$ and 5 – 50mAs, varying with attenuator thickness to ensure a measured kerma in excess of 50µGy. Increasing thicknesses of aluminium were placed directly above the Raysafe Xi R/F detector until the measured kerma dropped to half of that measured with no aluminium present. A broad field, inclusive scatter HVL was then estimated for each of the thicknesses of solid water HE used from logarithmic plots of aluminium thickness vs. measured kerma.

The method was the same for the small field, reduced scatter geometry but the geometry was different; the Raysafe Xi R/F detector was placed 200cm from the x-ray tube focus at the centre of the beam. The exit surface of the attenuator was 69cm above the Raysafe Xi R/F detector. The x-ray field size measured 3x3cm at the Raysafe Xi R/F detector (this was the smallest that could be achieved with the Philips Optimus 50 radiographic x-ray unit).

Increasing thicknesses of aluminium were placed in a jig 20cm above the Raysafe Xi R/F detector. This small field, reduced scatter geometry is like the conventional technique used to verify x-ray tube filtration during equipment acceptance [109], except for the presence of the solid water HE attenuator.

The experimental set-ups for the broad field, inclusive scatter geometry and the small field, reduced scatter geometry are shown in figure 3-6.

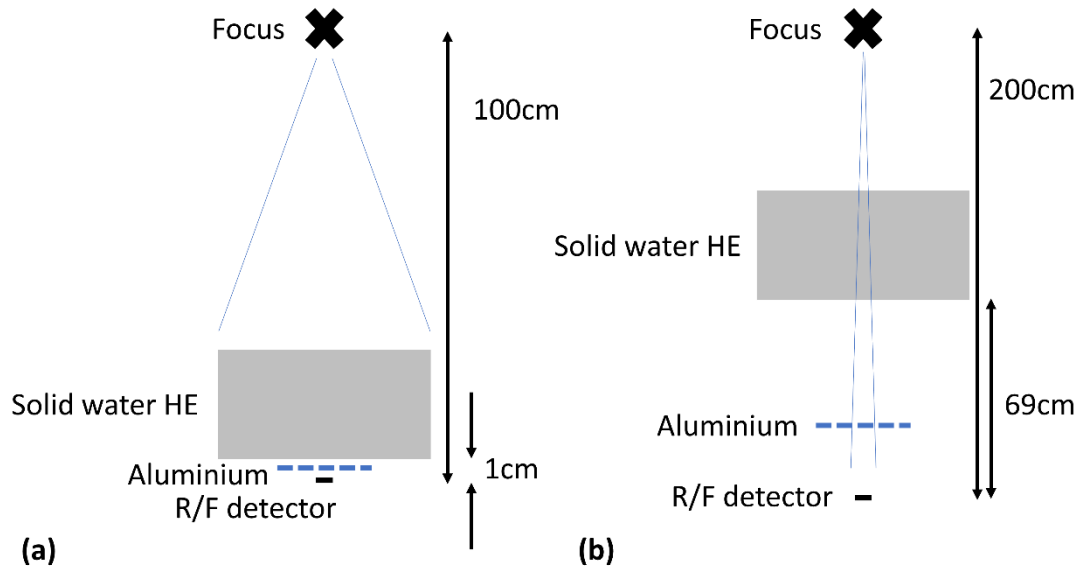

Figure 3-6: (a) the broad field, inclusive scatter geometry and (b) the small field, reduced scatter geometry used for measuring the HVL of the x-ray beam

The HVLs measured for the exit beam from increasing thicknesses of solid water HE attenuator in broad field, inclusive scatter and small field, reduced scatter geometries at 60, 70 and 81kV$_p$ are shown in figure 3-7.

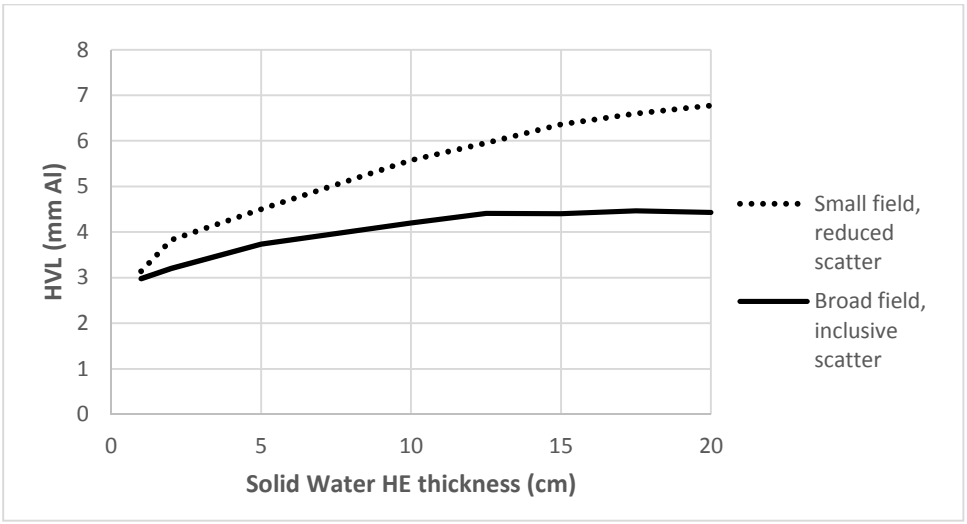

(a)

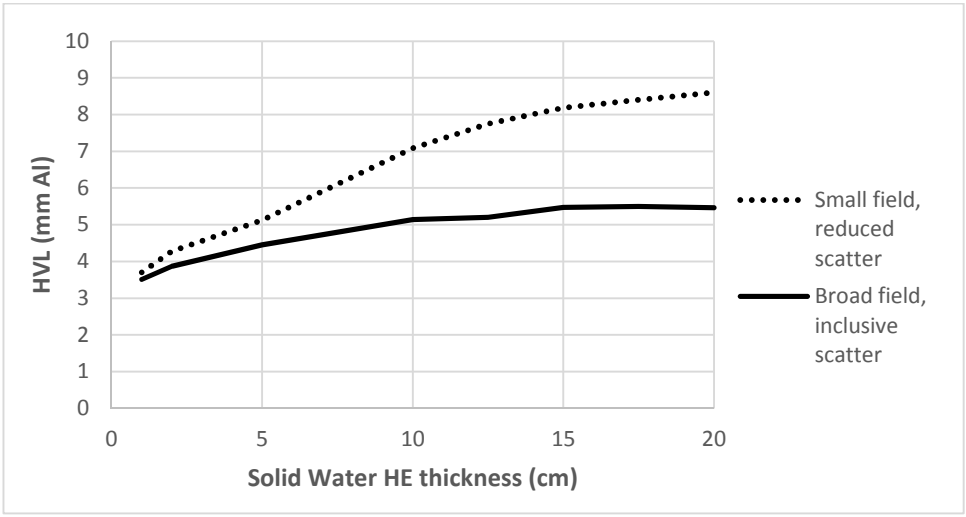

(b)

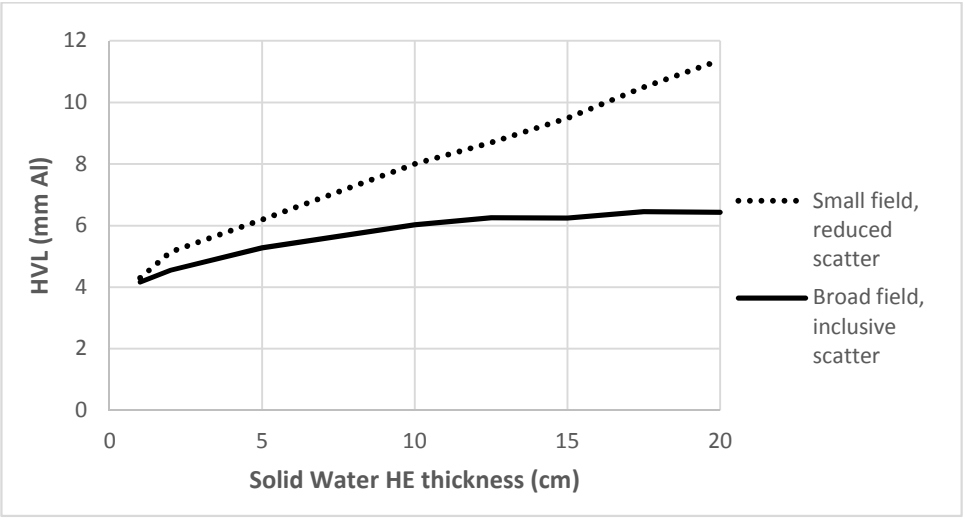

(c)

Figure 3-7: the measured HVLs for the broad field, inclusive scatter and small field, reduced scatter geometries for increasing thicknesses of attenuator at (a) 60kV$_p$, (b) 70kV$_p$ and (c) 81kV$_p$

As can be seen from figure 3-7, the HVL for the small field, reduced scatter geometry continues to increase with increasing attenuator thickness. This is following the expected trend for HVL in air as the beam quality changes with a shift towards a higher average x-ray energy with increasing attenuator thickness. This is not the case for the HVL of the broad field, inclusive scatter geometry however, which increases far less quickly after approximately 125mm of solid water HE attenuator at 60kV$_p$ and approximately 100mm of solid water HE attenuator at 70 and 81kV$_p$. This is because in addition to transmitted primary radiation, the image receptor is also measuring scattered x-rays whose average energy is significantly lower than the transmitted primary.

Given how close the HVLs are for the broad field, inclusive scatter geometry for a single kV$_p$ when the attenuator is greater than the equivalent of 100mm of solid water HE (or 125mm at 60kV$_p$), it is likely that a single calibration per kV$_p$ for DDI and STP could be used to accurately estimate the kerma at the detector. The clinical exposure of a paediatric patient - which would use a broad x-ray field, positions the patient as close to the detector as possible and does not use a grid - would meet the criteria for using a single calibration per kV$_p$ for abdomen and pelvis examinations as the patient diameter would be greater than the equivalent of 100mm of solid water HE for all but the smallest babies. Chest examinations may not produce a high enough HVL to use a single DDI or STP calibration because the air in the lungs does not contribute much to the attenuation of the x-ray beam.

3.3.2.5 Measuring detector dose indicator and signal transfer property calibrations for a broad beam geometry

In order to examine the effect of a broad beam geometry on DDI and STP calibration, DDI and STP calibrations were measured using varying thicknesses of solid water HE placed directly above the image receptor. The exposure geometry was as shown in figure 3-8.

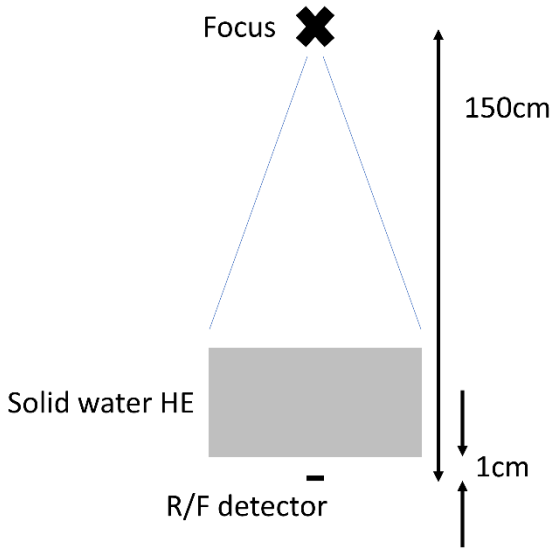

Figure 3-8: the exposure geometry used for the DDI and STP calibrations undertaken in a broad beam geometry

The Raysafe Xi R/F detector was placed 150cm from the x-ray tube focus on the x-ray table at the centre of the field. A thickness of 10mm of solid water HE was placed just above the detector with a 1cm separation from the exit surface to the detector. The field size at the detector was 40 x 40cm, ensuring full coverage of the Raysafe Xi R/F detector and the CR cassette. At 60, 70 and 81kV_p, exposures were made using incremental values of mAs to deliver air kermas in the range of 1.5 - 18µGy, encompassing the useful range of the CR cassette. The kerma for each combination of kV_p and mAs was measured three times using the Raysafe Xi R/F detector; the KAP measured by the KAP meter at the tube output was recorded each time to ensure repeatability between exposures.

Once the kerma measurements had been made, the process was repeated with the CR cassette in place of the Raysafe Xi R/F detector to record the s-value at each mAs. The 1cm separation between the exit surface of the attenuator and the image receptor was maintained. The flat look up table 'sensitivity' was used, providing as close to unprocessed images as can be achieved on the Fuji CR system. This provided all the information necessary for the DDI calibrations.

This process was repeated at 60, 70 and 81kV$_p$ for thicknesses of 20, 50, 100, 125, 150, 175 and 200mm of solid water HE.

For the STP calibrations, exposures of the CR cassette in the same conditions and for all the same thicknesses were repeated with the s-value fixed at 200 ensuring a variation in PV with kerma. These images were extracted directly in native DICOM format from the CR reader and a PV for a 100mm^2 ROI at the centre of these images was measured using ImageJ [108].

DDI calibrations at 60, 70 and 81kV$_p$ for all thicknesses of solid water HE attenuator are shown in figure 3-9. The equivalent STP calibrations are shown in figure 3-10.

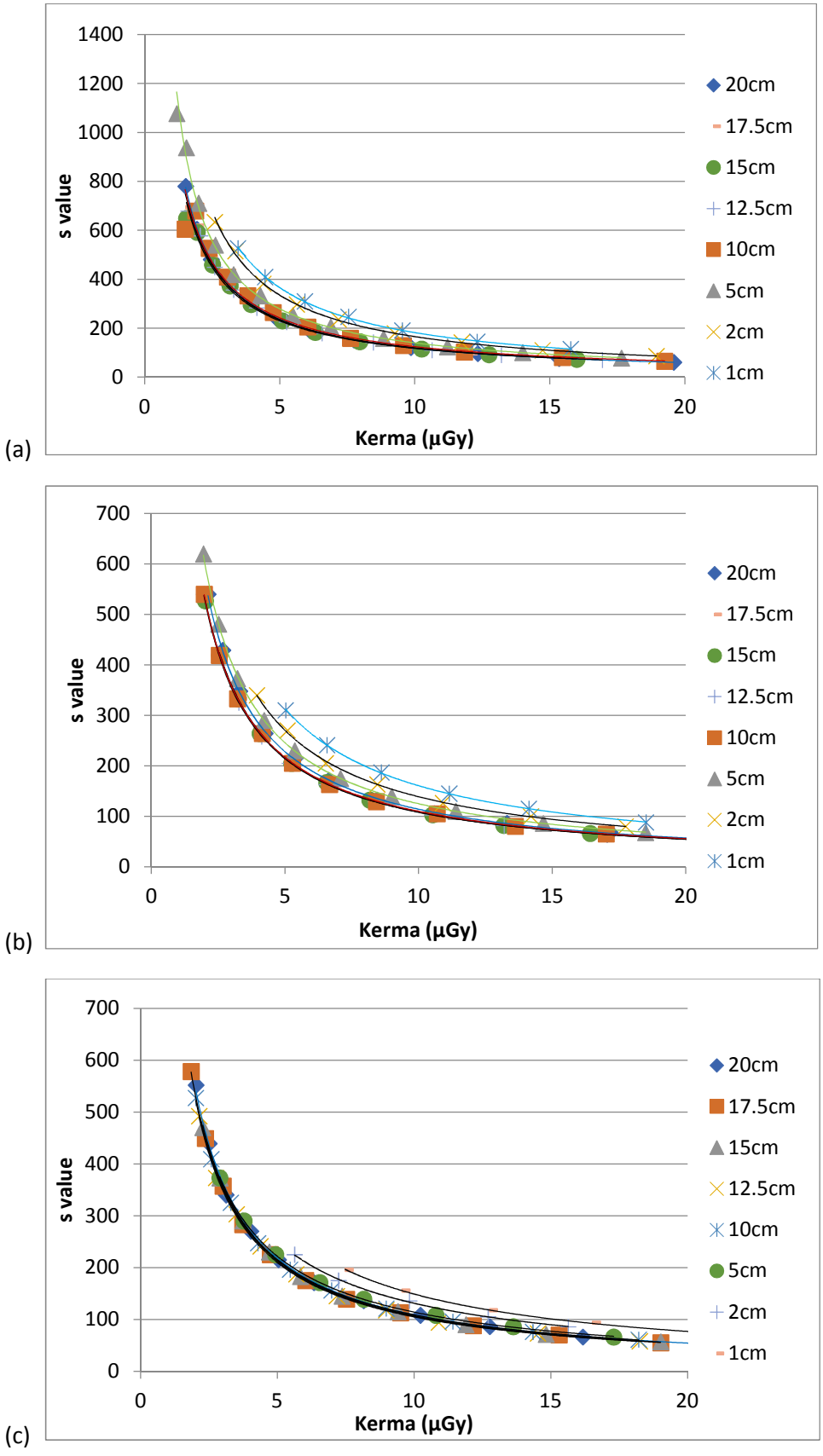

Figure 3-9: s-value calibrations at (a) 60, (b) 70 and (c) 81kV$_p$ for thicknesses of solid water HE attenuator varying from 10 – 200mm in a broad beam geometry

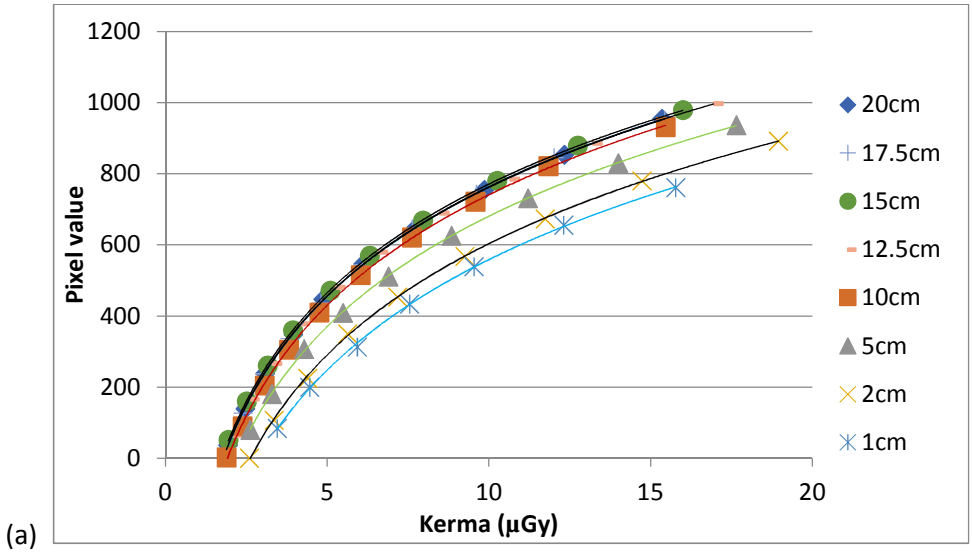

(a)

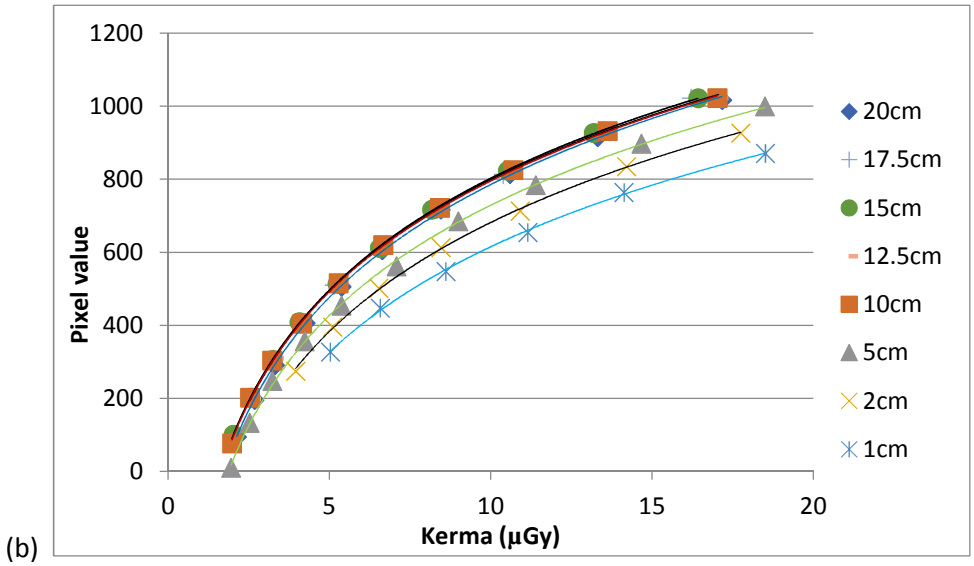

(b)

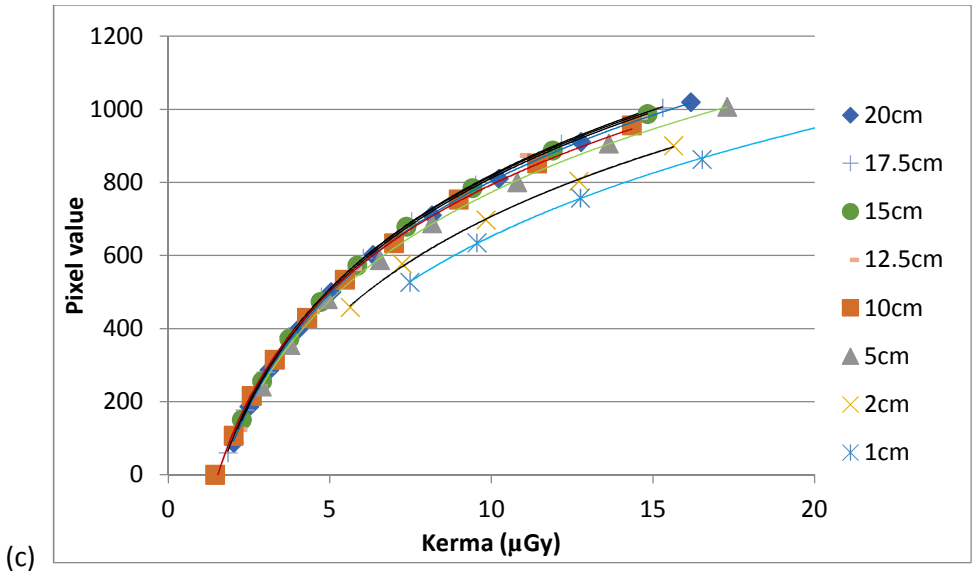

(c)

Figure 3-10: STP calibrations at (a) 60, (b) 70 and (c) 81kV$_p$ for thicknesses of solid water HE attenuator varying from 10 – 200mm in a broad beam geometry

Figures 3-9 and 3-10 show that the DDI and STP calibrations are distinctly different for each of the 10, 20 and 50mm of solid water HE attenuator at all kV_p values. The DDI and STP calibrations are indistinguishable from one another for all thicknesses of attenuator of 10cm and above. These results are as expected given the measurements of HVL for varying thicknesses of attenuator shown in figure 3-7 for a broad beam geometry. Where the HVL continues to increase up to 10cm, this results in distinctly different DDI and STP calibrations. Where the HVL stops demonstrating any significant upward trend above 100mm of solid water HE attenuator, this consistent beam quality results in very similar DDI and STP calibrations.

3.3.2.6 Assessing a high attenuation case

The DDI and STP calibrations presented in §3.3.2.5 were only measured for up to a 200mm thickness of solid Water HE attenuator; it was not possible to examine the effect of a single composition attenuator thickness in excess of this as there was only a total thickness of 200mm available locally. Yet it is important to assess whether the similarity of the calibrations continues to higher thicknesses as it is not inconceivable that a large adolescent presenting for an x-ray examination could have an abdominal or pelvic thickness in excess of the equivalent of 200mm of solid water HE.

To assess this, a single additional calibration of DDI and STP was made at $81kV_p$ for an attenuator consisting of 200mm of solid water HE with an additional 5mm of aluminium. The DDI and STP calibrations were acquired as described in §3.3.2.5. The DDI calibrations for 200mm of solid water HE and the 200mm with 5mm of aluminium cases at $81kV_p$ are shown in figure 3-11. The equivalent STP calibrations are shown in figure 3-12.

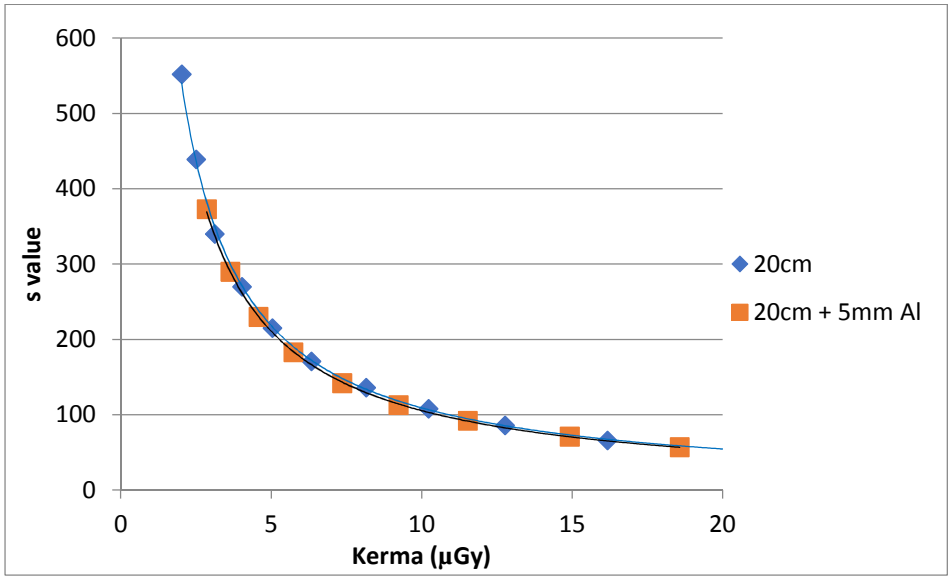

Figure 3-11: DDI calibrations at 81kV$_p$ for a 200mm thickness of solid water HE attenuator and 200mm of solid water HE with 5mm of aluminium in a broad beam geometry

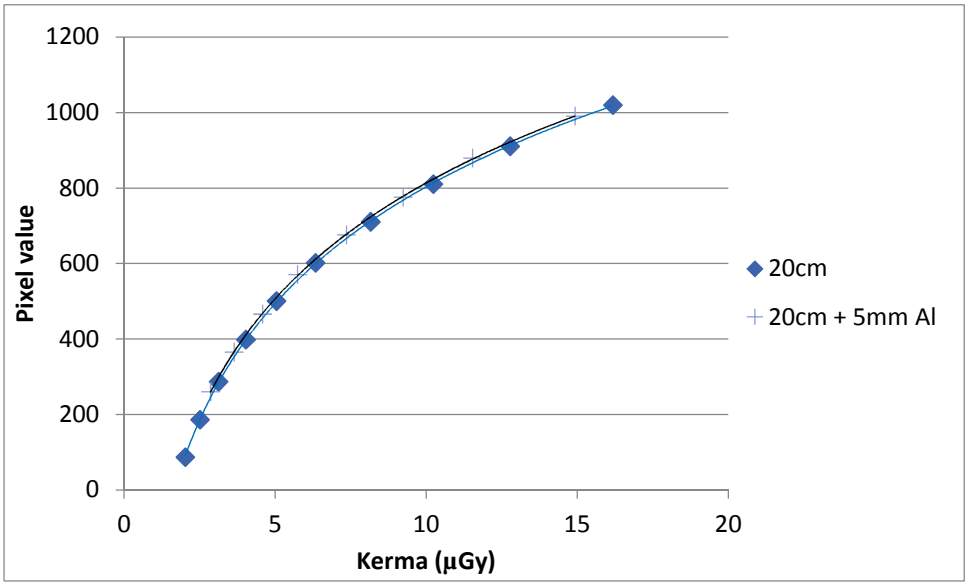

Figure 3-12: STP calibrations at 81kV$_p$ for a 200mm thickness of solid water HE attenuator and 200mm of solid water HE with 5mm of aluminium in a broad beam geometry

Figures 3-11 and 3-12 show that the DDI and STP calibrations remain indistinguishable from a clinically relevant attenuator of greater than 100mm solid water HE even when a significantly more attenuating object is considered, provided the exposure is undertaken in

a broad beam geometry. This is suggestive that a single DDI or STP calibration could cover any attenuator thickness that is in excess of the equivalent of 100mm of solid water HE for 60, 70 and 81kV_p.

3.3.2.7 Assessing the accuracy with the use of a single calibration

Figures 3-9 to 3-12 suggest that DDI and STP calibrations are essentially indistinguishable for attenuator thicknesses greater than 100mm of solid water HE if the exposure is undertaken in a broad beam geometry. This suggests that the kerma can be estimated from the examination DDI or a measurement of PV using a single calibration per kV_p provided it has been undertaken with an attenuator thickness of at least 100mm of solid water HE. The quantitative uncertainty associated with this was assessed as follows; a least squares fit was made using Matlab to all of the DDI and STP calibrations acquired at 100mm or higher at 60, 70 and 81kV_p using the general forms given in equation 3.7 for DDI calibrations and equation 3.8 for STP calibrations. The constants $a_{kVp,HVL}$ and $b_{kVp,HVL}$ for all the DDI and STP calibrations are shown with their associated correlation coefficient, R^2, in table 3.6.

		DDI calibration			PV calibration		
kV_p	Attenuator (cm)	$a_{kVp,HVL}$	$b_{kVp,HVL}$	R^2	$a_{kVp,HVL}$	$b_{kVp,HVL}$	R^2
60	10	1130.6	-0.958	0.989	448.8	-292.5	0.999
	12.5	1140.6	-0.983	0.999	442.1	-254.7	0.999
	15	1090.8	-0.967	0.997	441.3	-245.0	0.999
	17.5	1116.0	-0.969	0.998	442.4	-256.5	0.999
	20	1178.7	-0.999	0.999	443.8	-259.0	0.999
70	10	1052.7	-0.982	0.999	437.8	-212.7	0.999
	12.5	1050.3	-0.988	0.999	436.7	-206.7	0.999
	15	1061.1	-0.990	0.999	440.5	-211.4	0.999
	17.5	1076.2	-0.997	0.999	443.6	-219.2	0.999
	20	1142.8	-1.001	0.999	445.7	-240.6	0.999
81	10	1039.8	-0.980	0.999	422.7	-179.7	0.999
	12.5	1046.4	-0.998	0.999	450.1	-216.3	0.999
	15	1080.1	-1.003	0.999	446.7	-217.0	0.999
	17.5	1066.8	-1.002	0.999	445.5	-208.5	0.999
	20	1094.8	-1.002	0.999	445.6	-222.8	0.999
	20 + 5mm	1055.0	-1.000	0.999	442.3	-204.8	1.000

Table 3.6: The $a_{kVp,HVL}$ and $b_{kVp,HVL}$ values for DDI and STP calibrations of all thicknesses of solid water HE at 100mm or higher for 60, 70 and 81kV_p with the associated correlation coefficient, R^2, following a least squares fit

Next, for s-values and PV in the range of 100 – 800 and increasing in increments of 50, the constants in table 3.6 were used to calculate the detector kerma for each DDI and STP calibration at 60, 70 and 81kV_p. At each kV_p, the average detector kerma was calculated from the individual estimates made using each of the calibrations of DDI and STP at 10, 12.5, 15, 17.5 and 200mm of solid water HE. Finally, for each of the s-values and PVs, the deviation from the value for detector kerma calculated using the calibrations acquired with thicknesses of 100, 125, 150 and 175mm was compared with the value for detector kerma calculated from the calibration using 200mm of solid water HE.

This assessment of accuracy was used to determine whether calibrations undertaken with a 200mm thickness of solid water HE attenuator are an appropriate choice as a single calibration for the determination of detector kerma. The results are shown in figure 3-13 for s-value calibrations and figure 3-14 for STP calibrations. Note that there was no trend predicted for the accuracy with s-value or PV, the magnitude of the absolute deviation from the average value is the important factor.

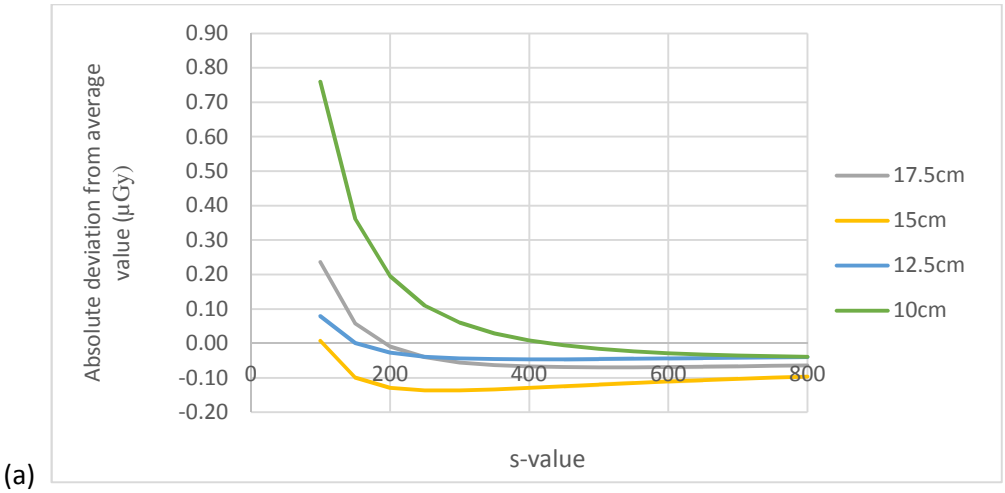

(a)

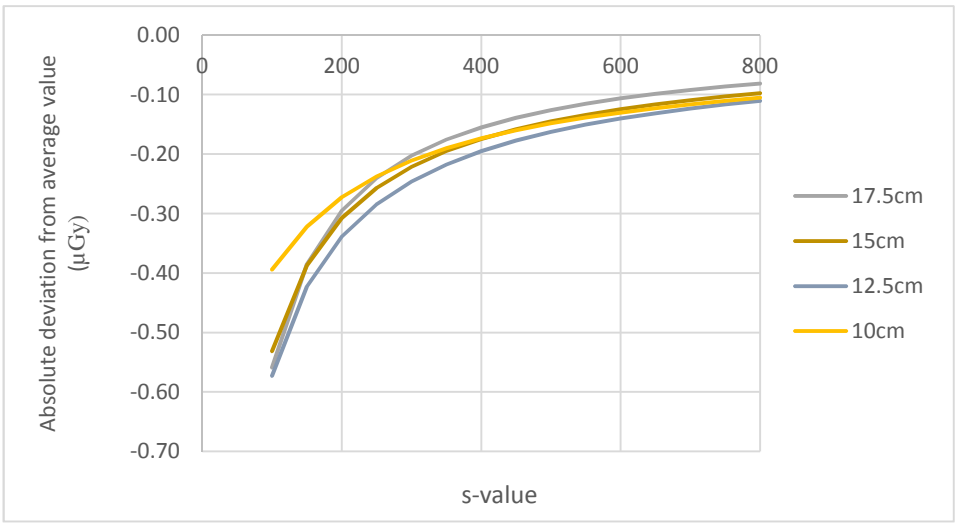

(b)

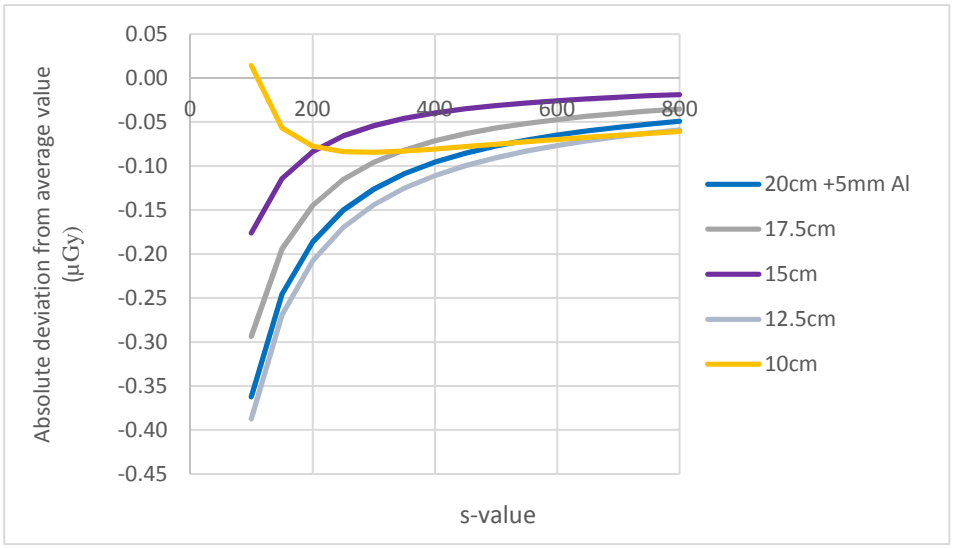

(c)

Figure 3-13: the absolute deviation between kerma calculated from the DDI calibration measured using the specified thickness of solid water HE and that using 200mm of solid water HE for s-values ranging from 100 - 800 at (a) 60, (b) 70 and (c) 81kV$_p$

(a)

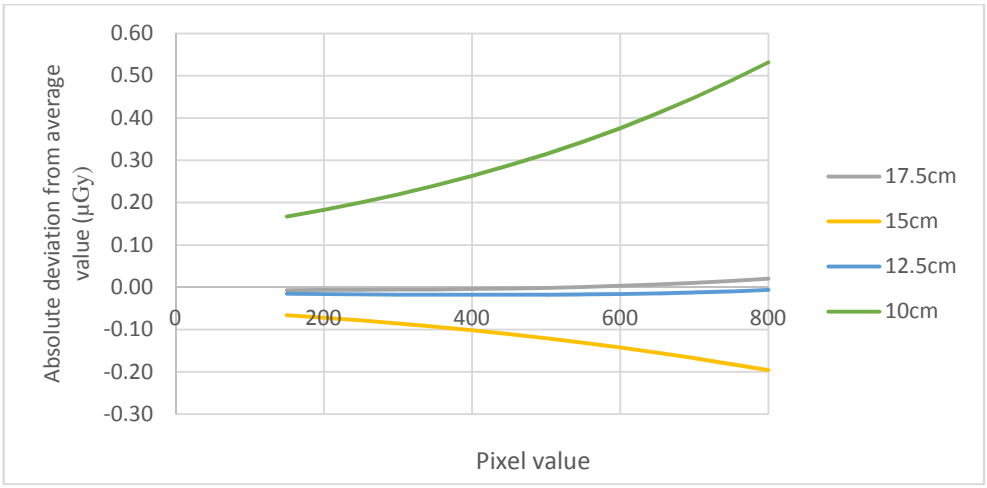

(b)

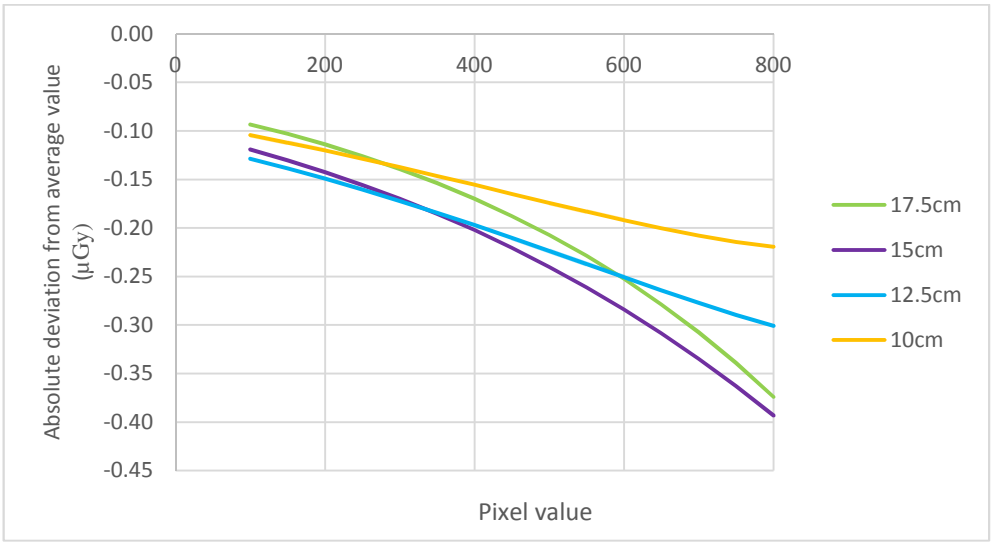

(c)

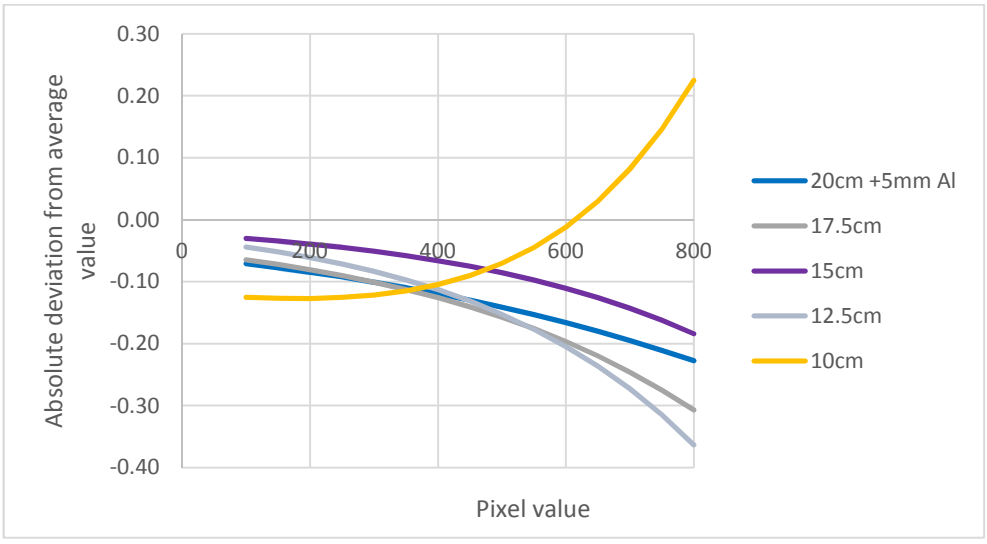

Figure 3-14: the absolute deviation between kerma calculated from the STP calibration measured using the specified thickness of solid water HE and that using 200mm of solid water HE for PVs ranging from 100 – 800 at (a) 60kV$_p$, (b) 70kV$_p$ and (c) 81kV$_p$

In all cases for both s-value and PV, the absolute deviations between kerma calculated from the calibration measured using the specified thickness of solid water HE and that measured using 200mm of solid water HE are small. The highest absolute deviation for any case was 0.76μGy but this was for a high detector kerma (in excess of 10μGy) for a comparison between calibrations undertaken at 100 and 200mm of solid water HE at 60kV_p. The trend for the deviation was consistent across all kV_p values and all attenuator calibrations for both s-value and PV – the deviation is greater for high detector kerma and becomes less towards a lower (and clinically relevant) detector kerma. Taking a clinically relevant range of detector kerma values as 2.5 - 6μGy, the highest absolute deviation for any case was 0.29μGy.

This is an extremely important result for this work; it demonstrates that provided the attenuator is of an adequate minimum HVL (equivalent to that provided by 100mm of solid water HE), a detector kerma can be accurately estimated from the DDI or measured PV using a single calibration of DDI or STP undertaken at an HVL in excess of the adequate minimum. For the convenience of selecting a single attenuator thickness with which to perform these calibrations throughout the rest of this work, 200mm of solid water HE was chosen. This has been demonstrated to give low deviations in the estimated detector kerma when compared with results calculated from calibrations using known thicknesses of solid water HE ranging between 100 – 175mm.

The LUT for DDI contains a calibration measured using 200mm of solid water HE in a broad beam geometry for kV_p values of 60, 70 and 81. The LUT for STP contains a calibration measured using 200mm of solid water HE in a broad beam geometry for kV_p values of 60, 70 and 81. Where the examination kV_p is between 60 – 81kV_p, values for kerma at the image receptor can be linearly interpolated from the values estimated by the closest two measured calibrations.

3.3.3 Estimating effective linear attenuation coefficient

The linear attenuation coefficient (μ) is a measure of the fraction of x-rays of a single given energy that are attenuated by a material, per unit thickness. Data on the mass attenuation coefficients (from which the linear attenuation coefficient can be calculated where the density of the material is known) is published by the National Institute of Standards and Technology (NIST) [97] for a large range of materials. X-ray beams used clinically are polyenergetic, therefore these values cannot be used. A μ_{eff} is required, a value that pertains to the fraction of x-rays of a specific range of energies (a specific polyenergetic beam) that are attenuated by a material, per unit thickness. For a single material attenuator, μ_{eff} can be determined using measurements of the attenuator exit kerma and the kerma without any attenuator present via;

$$\mu_{eff} = -\frac{Ln(\frac{Attenuator\ exit\ kerma}{Attenuator\ free\ kerma})}{Attenuator\ thickness}$$ [40] [equation 3.9]

or calculated in a similar manner using the results of Monte Carlo simulations.

As there are multiple energies, values of μ_{eff} are dependent upon a number of factors, including the beam quality, the x-ray field size and the attenuator thickness. It was hypothesised that it would be possible to accurately estimate μ_{eff} for any exposure using measured or simulated values and correction factors. This hypothesis is explored in the sections that follow.

3.3.3.1 Confirming the effect of kV_p

It was expected that an increase in the kV_p would lead to a decrease in μ_{eff}. To confirm this, exposures were made in the geometry shown in figure 3-15.

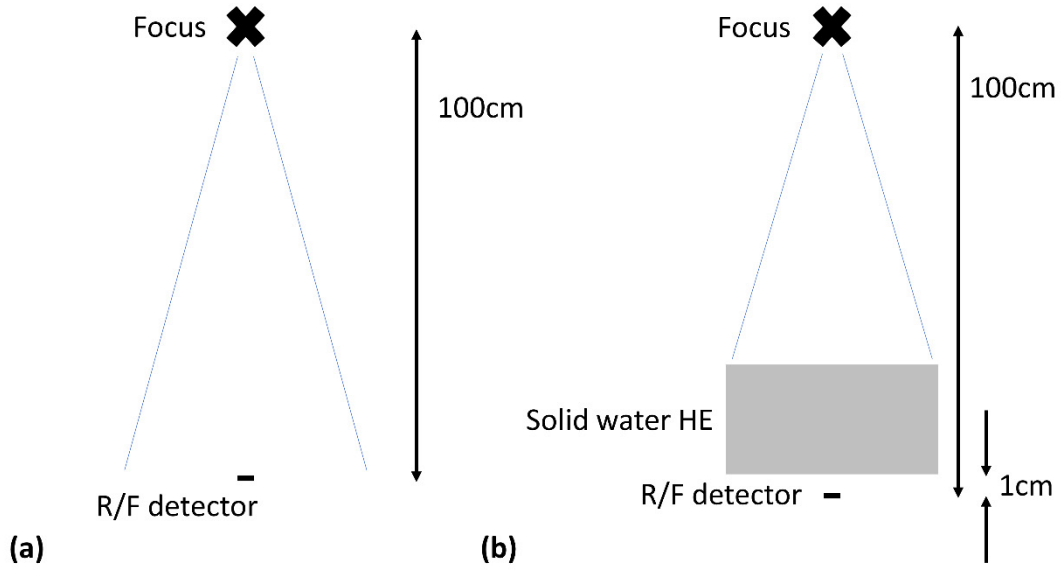

Figure 3-15: the exposure geometry used to measure the effective linear attenuation coefficient. (a) are exposures performed in the absence of an attenuator, (b) shows the position of the attenuator

The Raysafe Xi R/F detector was positioned at the centre of the x-ray field at a FDD of 100cm. The x-ray field was set to 40x40cm and three exposures made at each of 60, 70 and 81kV$_p$ at 10mAs. An average of the three measurements was taken for each kV$_p$ to represent the kerma in the absence of an attenuator. 10mm of solid water HE was placed on top of four spacers, one at each corner of the solid water HE such that the exit surface of the attenuator was 1cm from the Raysafe Xi R/F detector. Three measurements were made at each of 60, 70 and 81kV$_p$ and 10mAs. An average of the three measurements was taken for each kV$_p$ to be the attenuator exit kerma for a 10mm solid water HE attenuator at a field size of 40x40cm. As the two measurements of kerma (attenuator-free and the attenuator exit kerma) were made in the same location, no correction for distance is required.

The resultant μ_{eff} for each kV$_p$ is shown in table 3.7.

kV_p	Effective linear attenuation coefficient (mm^{-1})
60	0.028192
70	0.025289
81	0.023220

Table 3.7: measured effective linear attenuation coefficients for 10mm of solid water HE at a field size of 40x40cm at the detector

The measured μ_{eff} values shown in table 3.7 show significant differences with kV_p. This is to be expected, the lower average energy of a $60kV_p$ x-ray beam increases the probability of attenuation by any given material, with the higher average energy of the $81kV_p$ x-ray beam having the lowest probability of attenuation. The use of a single value of μ_{eff} for any beam quality for a fixed field size and attenuator thickness will have significant uncertainty associated with it. As an illustrative example, for a kerma at the image receptor of 5μGy and an initial air kerma of 1mGy, an estimate of attenuator thickness would be 163mm using the value of μ_{eff} for $60kV_p$, 181mm using the value for $70kV_p$ and 196mm using the value for $81kV_p$. This is a 10.7% and 20.3% increase on the value derived using $60kV_p$ for the 70 and $81kV_p$ values of μ_{eff} respectively and is an uncertainty that would be too large for the intended clinical application. It is clear that the value of μ_{eff} used in the computational model will need to be specific to the beam quality of the x-ray beam used in the examination. As it is impractical to measure all of these values, these can be interpolated from measured values using a logarithmic fit for μ_{eff} with kV_p or simulated using Monte Carlo techniques for any kV_p that could be used for a clinical examination.

3.3.3.2 Assessing the effect of field size

It can be predicted that the x-ray field size will effect μ_{eff}, but the relationship between the two is not intuitive. Larger field sizes result in more scattered radiation; this changes the quality of the x-ray beam as it progresses through the attenuating material. To assess the effect of field size on the measured μ_{eff}, the measurements of exit kerma as undertaken in §3.3.3.1 were repeated for field sizes measuring 10x10cm, 20x20cm, 30x30cm and 40x40cm at the detector at 60, 70 and 81kV_p with 10 – 200mm of solid water HE attenuator in increments of 10mm. The μ_{eff} was calculated using equation 3.9, as explained in §3.3.3. The results are shown in figure 3-16.

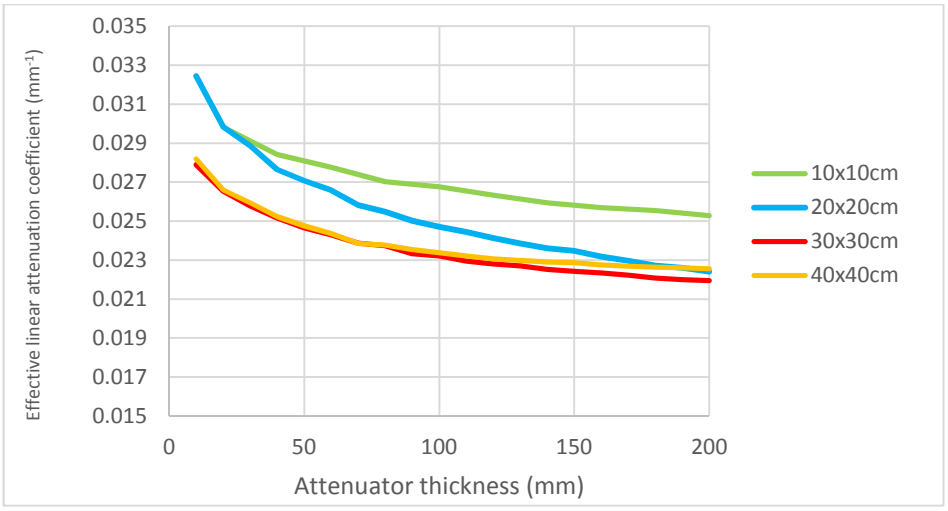

(a)

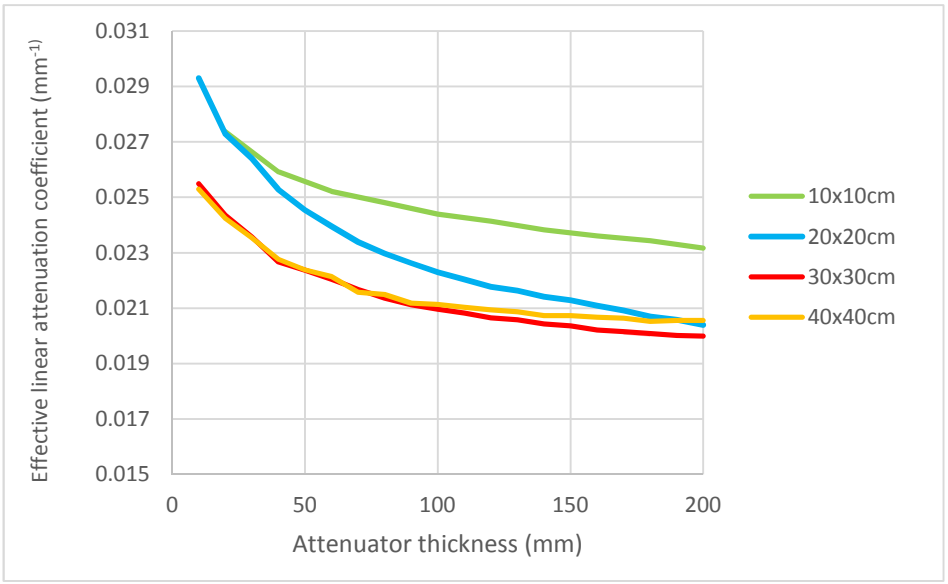

(b)

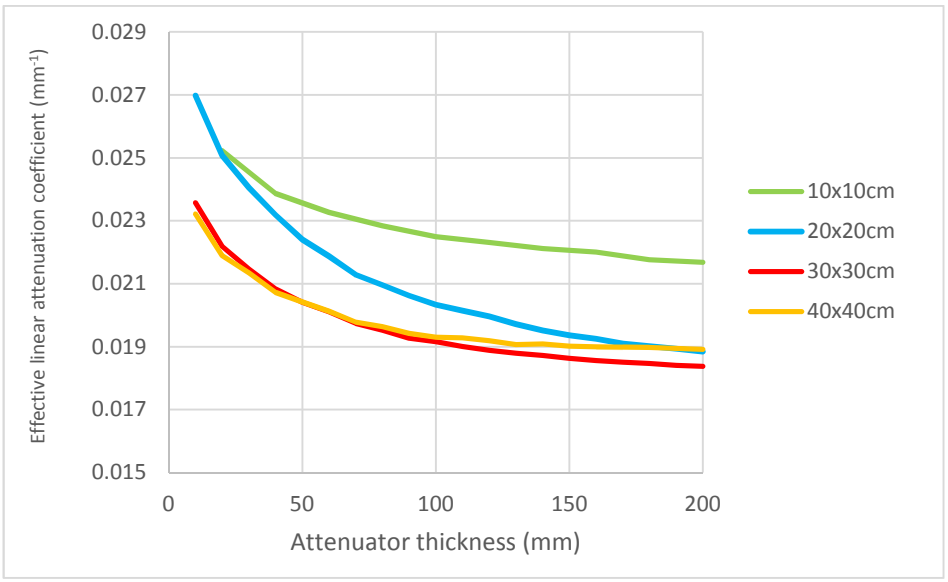

(c)

Figure 3-16: the effect of field size on measured effective linear attenuation coefficient at (a) 60, (b) 70 and (c) 81kV$_p$

The measured μ_{eff} shown in figure 3-16 show differences with field size, as expected. The increased scatter from larger field sizes increases the amount of radiation overall, reducing the overall attenuation by any given material. The lower amount of scatter from the 10 x 10cm field results in less radiation overall, increasing the overall attenuation by any given material. The trends observed in figure 3-16 – that in general μ_{eff} reduces with increasing field size – are the same as those reported in NRPB-R318 [40].

The use of a single value of μ_{eff} for field sizes of 10x10cm, 20x20cm, 30x30cm and 40x40cm for a fixed beam quality and attenuator thickness will have significant uncertainty associated with it. As an illustrative example, for a kerma at the image receptor of 5μGy and an initial air kerma of 1mGy, the estimate of attenuator thickness would range between 209.5 – 241.5mm for 60kV$_p$, 228.7 – 265mm for 70kV$_p$ and 244.3 – 288.3mm for 81kV$_p$. These are percentage differences of 15.2, 15.9 and 18% respectively. This would contribute too large an uncertainty to the computational model than would be acceptable for the intended clinical indication.

It is clear that the value of μ_{eff} used in the computational model will need to be specific to the field size used in the examination. As it is impractical to measure all of these values, these will need to be interpolated from measured values or simulated using Monte Carlo techniques for any field size that could be used for a clinical examination.

3.3.3.3 Assessing the effect of the attenuator thickness

μ_{eff} will vary with attenuator thickness. The poly-energetic nature of the x-ray beam means that each successive HVL will be greater than the preceding, therefore it is expected that the μ_{eff} will decrease with increasing attenuator thickness.

To assess the effect of attenuator thickness on μ_{eff}, the Raysafe Xi R/F detector was positioned at the centre of the x-ray field at a FDD of 100cm with a field size of 40x40cm. Measurements of attenuator exit kerma and the kerma with no attenuator present were made for thicknesses of solid water HE from 10 to 200mm in increments of 10mm at 60, 70 and 81kV$_p$. The variation in μ_{eff}, calculated using equation 3.9, with increasing thickness of solid water HE attenuator for 60, 70 and 81kVp is shown in figure 3-17.

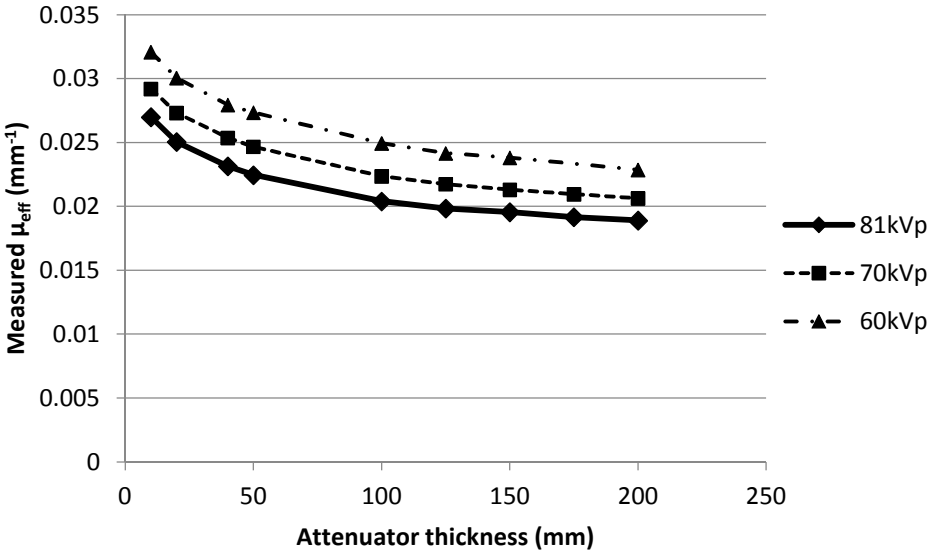

Figure 3-17: the variation in measured effective linear attenuation coefficient with increasing thicknesses of solid water HE attenuator for a 40x40cm field size at 60, 70 and 81kV$_p$

μ_{eff} is observed to decrease with increasing attenuator thickness. As the attenuator thickness will not be known in practice – indeed, the aim is to estimate this variable – it cannot be known which value of μ_{eff} should be used for any given examination. An estimate can be made using another rearranged form of equation 3.1. Using;

$$\frac{k_d}{k_0} = exp^{(-\mu_{eff}x)} \qquad \text{[equation 3.10]}$$

a relationship between $\frac{k_d}{k_0}$ and attenuator thickness x can be derived from the same experimental data used to produce the values of μ_{eff} presented in figure 3-17. An example

of this exponential fit for the data acquired at 81kV$_p$ for a field size of 40x40cm is shown in figure 3-18

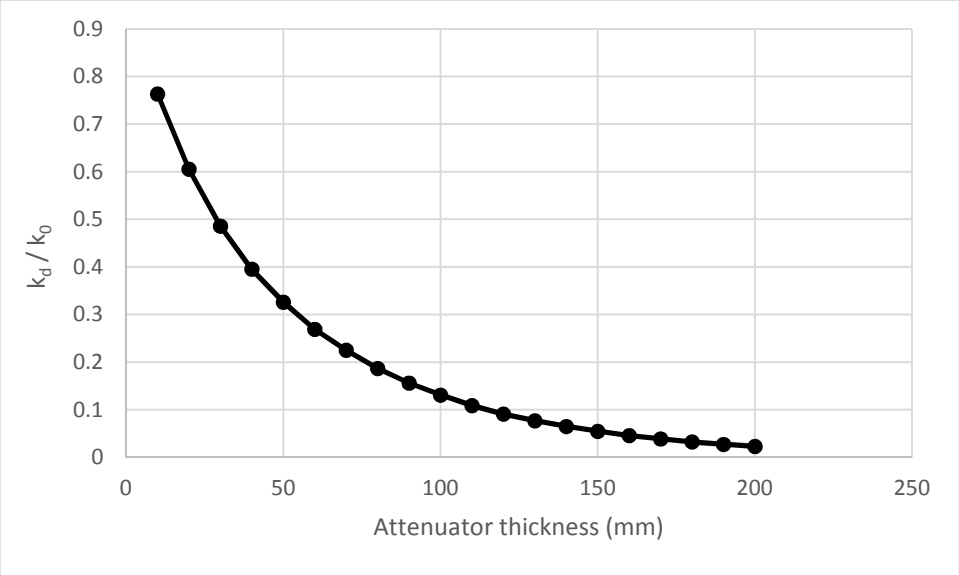

Figure 3-18: the exponential relationship between $\frac{k_d}{k_0}$ and attenuator thickness for exposures at 81kV$_p$ and a 40x40cm field size

For any given examination values of k_d and k_0 are calculated using the methods described in §3.3.2 and §3.3.1. By taking the ratio of $\frac{k_d}{k_0}$ and using the relationship of the form shown in figure 3-18 for the relevant kV$_p$ and field size, or following linear interpolation between the two closest values, an estimate of attenuator thickness can be made. This estimate can then be used to obtain an estimate of μ_{eff} from relationships of the form shown in figure 3-17 for the relevant kV$_p$ and field size. This technique of obtaining a broad estimate of attenuator thickness using $\frac{k_d}{k_0}$ is likely to be very effective for a single composition attenuator as the data can be directly measured. Its effectiveness for a multi-composition attenuator is discussed in chapter 5.

Given these dependencies, values of μ_{eff} can be corrected using factors in a LUT. The LUT of correction factors was created as follows.

- The correction factor for the approximate thickness of the attenuator can be derived from using the calculated value of $\frac{k_d}{k_0}$ with the measured exponential relationship between $\frac{k_d}{k_0}$ and attenuator thickness at the relevant kV_p to estimate an attenuator thickness. This correction is referred to as $k_{\mu_{eff_{thickness}}}$

The estimation of μ_{eff} using the values in the LUT, $\mu_{eff_{LUT}}$, is undertaken as follows;

$$\mu_{eff} = \mu_{eff_{LUT}} \times k_{\mu_{eff_{thickness}}} \qquad \text{[equation 3.11]}$$

3.4 Summary

This chapter has described the creation and optimisation of a computational model for the specific case of deriving the thickness of a single composition attenuator. The rearranged form of the Beer-Lambert law given in equation 3.1 can be used to estimate the attenuator thickness. Values for kerma at the image receptor, k_d, initial air kerma, k_0, and effective linear attenuation coefficient, μ_{eff}, can be estimated using LUT and correction factors that have been directly measured, interpolated from measured results or estimated using Monte Carlo simulations.

The quality of the x-ray beam as it exits the attenuator for a broad field, inclusive scatter geometry is observed not to vary much for an attenuator in excess of that equivalent to 100mm of solid water HE (as shown in figure 3-7) for a single kV_p. This is the key result that means k_d can be estimated using the radiographic image itself, as described throughout §3.3.2.5 – §3.3.2.7, with a low uncertainty as quantified in §3.3.2.7.

k_0 can be estimated using either the examination output – in which values from a LUT can be corrected for examination kV_p, mAs, tube focus selection, field size and FDD - as described throughout §3.3.1.1 or using the examination KAP – in which the ratio of

$\left(\frac{KAP}{Field\ size}\right)$ can be corrected for examination kV_p and field size as described throughout §3.3.1.3. The uncertainty budgets created for each method, as given in §3.3.1.2 and §3.3.1.4, demonstrate a similar level of uncertainty for each and show that this is the variable that is most difficult for the computational model to accurately estimate.

μ_{eff} can be estimated using values from a LUT that come from measurements of kerma made with and in the absence of varying thicknesses of solid water HE attenuator. The precise value of μ_{eff} can be better estimated using the ratio between estimated values for k_d and k_0, as described in §3.3.3.3 and should be corrected for field size as described in §3.3.3.2.

With low uncertainties associated with each of the variables to be used by the computational model, it is expected that the estimate of attenuator thickness will be accurate. Having now been created, the computational model described in this chapter is tested in chapter 4 for a single composition attenuator.

Chapter 4 – Validation of the computational model for a single composition phantom

Overview

This chapter presents the testing of the computational model created in chapter 3 for deriving the thickness of a single composition attenuator. In each case, the initial air kerma, k_0, kerma at the image receptor, k_d, and effective linear attenuation coefficient, μ_{eff}, were directly measured so the accuracy of the computational model's estimate of each variable could be assessed. The computational model was validated using three different combinations of x-ray unit and image receptor.

4.1 Introduction

The computational model created in chapter 3 can be used to derive the thickness of a single composition attenuator from an examination undertaken in the conditions for which the look up tables (LUT) that have been created are expected to be accurate. For the Fuji computed radiography (CR) system used with a Philips Optimus 50 radiographic x-ray unit, this includes a kV_p in the range of 60 – 81 and an attenuator composed of at least 100mm of solid water high equivalency (HE) placed directly onto the dedicated Fuji CR cassette.

This chapter describes the process used to test the accuracy of the computational model, and the measured results. X-ray examinations were undertaken using carefully selected combinations of attenuator thickness, kV_p, mAs and field size on the Philips Optimus 50 radiographic x-ray unit with Fuji CR. For each examination, the initial air kerma, k_0, the kerma at the image receptor, k_d, and the effective linear attenuation coefficient, μ_{eff}, were experimentally measured using the Raysafe Xi Radiographic / Fluoroscopic (R/F) detector. The computational model was used to estimate each variable and then to calculate an estimate of the attenuator thickness using the methods described throughout chapter 3. The estimate of each variable for each examination was compared against the measured value to determine the accuracy of the computational model's estimate of each. The estimated thickness was compared to the known attenuator thickness to determine the overall accuracy of the computational model.

To determine the accuracy with which the computational model works on other systems, the necessary LUTs as described throughout chapter 3 were created for an Xograph-Canon direct digital radiography (DDR) system and a Fuji DDR system, both of which were then subjected to the same test process as used for the Philips Optimus 50 radiographic x-ray unit with Fuji CR. This chapter describes the creation of the LUTs for these systems,

outlines the process used to test and validate the computational model and presents the results.

4.2 Fuji computed radiography system with Philips Optimus 50 radiographic x-ray unit

4.2.1 Test examinations

Nine unique thicknesses of solid water HE attenuator were selected between 100 and 200mm to match the availability of solid water HE thicknesses available. For each of these nine thicknesses, a kV_p of either 60, 70 or 81 was selected, along with a field size between 20x20cm and 40x40cm. The mAs for the exposure was chosen from a range of 0.63 to 2.5 to ensure a clinically relevant range of k_0 and k_d values. Where the notional speed of CR has a film speed equivalent of 400, local experience has shown that the average detector kerma would not be significantly in excess of 5μGy for a reasonably well undertaken examination. Furthermore, the CR reader cannot form a reliable image where the signal is too low. In this event, the pixel value (PV) measures zero throughout the image. The threshold for this is a detector kerma of approximately 1.5μGy.

All exposures were undertaken at 100cm focus to detector distance (FDD), with the attenuator placed directly on top of the dedicated CR cassette. The selections for each of the test exposures were as shown in table 4.1.

Examination number	Thickness of solid water HE (mm)	kV_p	mAs	Field size (cm)	
				Anode-cathode axis	Perpendicular axis
1	115	70	1.25	25	30
2	140	70	1.6	20	30
3	170	70	2	25	25
4	100	81	1	25	25
5	120	81	0.8	30	15
6	140	81	0.63	35	40
7	165	81	1.25	28	30
8	180	81	2	12	23
9	190	81	2.5	28	41

Table 4.1: the thicknesses of solid water HE, kV_p and field size used for each of the nine validation exposures on the Fuji CR system

Two exposures were acquired for each examination. Both exposures used the sensitivity processing option, providing as close to unprocessed images as the Fuji CR system is capable of and matching the calibration condition for all of the image receptor calibrations measured for the LUT created in §3.3.2.5. Since it is not possible on the Fuji CR system to have both the examination detector dose indicator (DDI) and PV vary with kerma in a single image, the first exposure fixed the mid-point PV to provide an accurate s-value for the examination and the second exposure fixed the s-value (at 200) to allow for an accurate measurement of the PV [1]. This has the consequence that the two will not have been acquired with exactly the same k_0 or k_d but the reproducibility of exposures on the Philips Optimus 50 radiographic x-ray unit was measured to be better than 2%, so the values will be very close. The measured kerma area product (KAP) for each exposure was recorded to ensure there was no appreciable difference from exposure to exposure. Images were

extracted directly from the CR reader in native Digital Imaging and Communications in Medicine (DICOM) format onto a universal serial bus (USB) drive.

To allow for an assessment of the accuracy of the values selected by the computational model from the LUTs, two further exposures were made for each examination in table 4.1. For the first of these, the Raysafe Xi R/F detector was positioned in place of the CR cassette so that a direct measure of k_d could be made. For the second, the Raysafe Xi R/F detector remained in place but the attenuator was removed so that a measurement of k_0 could be made. For both of these additional exposures, the examination KAP was recorded and found to be within 1.7% of those recorded for the examinations that produced the images. The true value of μ_{eff} was calculated using the measured values of k_d and k_0 and the known thickness of the attenuator using equation 3.9 (§3.3.3).

4.2.2 Estimate of initial air kerma

For each examination two estimates of k_0 were made. The first, $k_{o_{output}}$, used the examination kV_p, mAs, field size, tube focus selection and FDD to select a value from the LUT created in §3.3.1.1. The second, $k_{o_{KAP}}$, used the examination kV_p, KAP and field size to calculate k_0 with a correction made for beam non-uniformity as described in §3.3.1.3. Both estimates are shown alongside the value measured using the Raysafe Xi R/F detector in table 4.2.

Examination number	Initial air kerma, k_0, (µGy)				
	Measured value	$k_{o_{output}}$		$k_{o_{KAP}}$	
		Estimate	Deviation from measured	Estimate	Deviation from measured
1	42.72	42.96	0.57%	42.60	-0.28%
2	54.21	55.12	1.69%	55.46	2.31%
3	68.79	69.43	0.94%	72.30	5.11%
4	46.57	45.99	-1.24%	47.76	2.56%
5	35.71	35.90	0.54%	37.95	6.29%
6	29.49	28.67	-2.77%	30.65	3.95%
7	58.93	58.91	-0.03%	61.51	4.39%
8	93.22	93.09	-0.13%	92.02	-1.29%
9	122.80	123.73	0.75%	125.83	2.47%

Table 4.2: estimated values of initial air kerma, k_0, made using the examination mAs and KAP compared with the value measured using the Raysafe Xi R/F detector

Estimates of k_0 using both methods ($k_{o_{output}}$ and $k_{o_{KAP}}$) produce results that are close to the values of k_0 measured with the Raysafe Xi R/F detector. The difference between the estimates and the measured values are all within the total uncertainty budget for each method derived in §3.3.1.2 and §3.3.1.4.

The estimates made using $k_{o_{output}}$ are generally closer to the measured value than the estimates made using $k_{o_{KAP}}$. The average of the absolute individual deviations between measured and estimated values for $k_{o_{output}}$ is 0.96%. For $k_{o_{KAP}}$ the average of the absolute individual deviations between measured and estimated values is 3.18%. A t-test indicates that these differences are significant at the $p < 0.05$ level ($p = 0.018$).

4.2.3 Estimate of kerma at the image receptor

For each examination two estimates of kerma at the image receptor, k_d, were made. The first, $k_{d_{DDI}}$, used the examination kV_p to select the appropriate calibration between image receptor kerma and DDI acquired using 200mm of solid water HE attenuator as described in §3.3.2.5. The examination s-value was used with this calibration to estimate k_d. The second, $k_{d_{PV}}$, used the examination kV_p to select the appropriate calibration between image receptor kerma and PV acquired using 200mm of solid water HE attenuator as described in §3.3.2.5. The average PV from a $1cm^2$ ROI placed at the centre of the image was used with this calibration to estimate k_d. Both estimates of k_d are shown alongside the true value as measured using the Raysafe Xi R/F detector for each examination in table 4.3.

	Kerma at the image receptor, k_d (µGy)				
Examination number	Measured value	$k_{d_{DDI}}$		$k_{d_{PV}}$	
		Estimate	Deviation from measured	Estimate	Deviation from measured
1	3.23	3.36	4.09%	3.36	4.08%
2	2.58	2.72	5.51%	2.72	5.26%
3	1.93	1.98	2.32%	2.02	4.82%
4	5.63	5.72	1.61%	5.67	0.88%
5	2.88	2.93	1.85%	2.99	3.80%
6	1.73	1.77	1.91%	1.75	0.77%
7	2.38	2.44	2.53%	2.46	3.43%
8	2.87	2.80	-2.56%	2.97	3.43%
9	3.25	3.36	3.50%	3.37	3.87%

Table 4.3: estimated values of kerma at the image receptor, k_d, made using the DDI and measured PV compared with the value measured using the Raysafe Xi R/F detector

Estimates of k_d made using both methods ($k_{d_{DDI}}$ and $k_{d_{PV}}$) produce results that are close to the values measured with the Raysafe Xi R/F detector. The estimates made using $k_{d_{DDI}}$

are slightly closer to the measured value than the estimates made using $k_{d_{PV}}$. The average of the absolute individual deviations for $k_{d_{DDI}}$ is 2.88%. For $k_{d_{PV}}$ the average of the absolute individual deviation is 3.37%. A t-test indicates that these differences are not significant at the $p < 0.05$ level ($p = 0.232$).

4.2.4 Estimate of effective linear attenuation coefficient

For each examination one estimate of μ_{eff} was made. As described in §3.3.3.3, this estimate uses the ratio of $\frac{k_d}{k_0}$ for each examination and the measured relationship between μ_{eff} and attenuator thickness at the field size and kV_p used in the examination to make an initial estimate of the attenuator thickness. This initial estimate of thickness was then used with the measured relationship between μ_{eff} and attenuator thickness at the examination kV_p and field size to estimate a value for μ_{eff} for the examination. Where necessary, values of μ_{eff} were linearly interpolated for field size and interpolated using a logarithmic relationship for kV_p. For comparison, the known value of μ_{eff} refers to the value calculated using the measured k_d and k_0 and the known attenuator thickness using equation 3.9 (§3.3.3). The results are shown in table 4.4.

	Effective linear attenuation coefficient, μ_{eff} (mm^{-1})		
Examination number	Measured value	Estimated value	Deviation from measured
1	0.02247	0.02192	-2.42%
2	0.02174	0.02138	-1.67%
3	0.02102	0.02086	-0.74%
4	0.02114	0.02047	-3.13%
5	0.02099	0.01996	-4.9%
6	0.02025	0.01961	-3.17%
7	0.01946	0.01924	-1.15%
8	0.01934	0.01900	-1.75%
9	0.01912	0.01887	-1.28%

Table 4.4: estimated values of effective linear attenuation coefficient, μ_{eff}, compared with the true value calculated using the measured k_d, k_0 and the known attenuator thickness

The estimates of μ_{eff} made using the methods described in §3.3.3.3 are within 5% of the measured value, calculated using the measured values of k_d and k_0 for each examination and the known attenuator thickness. The highest deviation between the estimated and measured values is -4.9% and the average of the absolute individual deviations is 2.25%.

4.2.5 Estimate of attenuator thickness

For each examination, four estimates of attenuator thickness were made using every available combination of k_0 (using output and KAP) and k_d (using s-value and PV). Only one value of μ_{eff} was calculated – this was used in all four estimates. Estimates of attenuator thickness were made using equation 3.1 (§3.1). The results are compared to the known attenuator thickness in table 4.5.

Image number	Attenuator thickness								
	True (mm)	Using s-value ($k_{d_{DDI}}$) and output ($k_{o_{output}}$) (estimate A)		Using s-value ($k_{d_{DDI}}$) and KAP ($k_{o_{KAP}}$) (estimate B)		Using PV ($k_{d_{PV}}$) and output ($k_{o_{output}}$) (estimate C)		Using PV ($k_{d_{PV}}$) and KAP ($k_{o_{KAP}}$) (estimate D)	
		Estimate (mm)	Deviation from true (%)	Estimate (mm)	Deviation from true (%)	Estimate (mm)	Deviation from true (%)	Estimate (mm)	Deviation from true (%)
1	115	116.3	1.11%	115.9	0.78%	116.3	1.11%	115.9	0.78%
2	140	140.6	0.46%	140.9	0.67%	140.8	0.54%	141.0	0.74%
3	170	170.6	0.37%	172.6	1.51%	169.5	-0.32%	171.4	0.83%
4	100	101.8	1.85%	103.7	3.69%	102.2	2.20%	104.0	4.04%
5	120	125.3	4.62%	128.3	6.94%	124.6	3.82%	127.4	6.15%
6	140	142.2	1.56%	145.6	3.99%	142.8	1.97%	146.2	4.40%
7	165	165.6	0.37%	167.9	1.73%	165.2	0.10%	167.4	1.46%
8	180	184.5	2.50%	183.9	2.16%	181.4	0.75%	180.7	0.41%
9	190	191.0	0.55%	191.9	1.02%	190.9	0.45%	191.7	0.92%

Table 4.5: the estimates of attenuator thickness made by the computational model for all combinations of estimated values of initial air kerma, k_0, and kerma at the image receptor, k_d, compared with the known attenuator thickness

All estimates of attenuator thickness were within 7% of the true value of attenuator thickness. The average of the absolute deviation between estimated and true attenuator thickness is 1.49% for estimate A, 2.5% for estimate B, 1.25% for estimate C and 2.19% for estimate D.

Whilst all results are excellent, there is a slightly greater accuracy achieved using PV over s-value (1.25% compared with 1.49%, 2.19% compared with 2.5%) for the estimate of k_d (though not statistically significant at the $p < 0.05$ level ($p = 0.190$)) and output over KAP (1.49% compared with 2.5%, 1.25% compared with 2.19%) for the estimate of k_0 (statistically significant at the $p < 0.05$ level ($p = 0.0189$)). On average, the greatest accuracy is expected from using PV to estimate k_d and output to estimate k_0, though it is no more likely to provide the most accurate estimate for an individual examination than the use of s-value and output.

4.2.6 Summary

The computational model described throughout chapter 3 has been used to estimate the thickness of varying thicknesses of solid water HE using a Philips Optimus 50 radiographic x-ray unit and a Fuji CR system. The estimates of k_0, k_d and μ_{eff} made by the computational model were all compared to measured values and found to be consistently accurate across all of the validation examinations. The final estimate of attenuator thickness was accurate, with all estimates within 7% of the true value of attenuator thickness and an average deviation from the true value of attenuator thickness of 1.25 – 2.5% depending on the source used to derive the value of each variable. Based on this testing, the computational model shows great promise in the accuracy of its use.

4.3 Xograph Canon direct digital radiography system

To verify that the computational model works on more than just one manufacturer's system, it was applied to an Xograph-Canon DDR unit. The Xograph-Canon DDR system that was used is a fixed radiographic unit installed in 2016 in the radiology department of Aberdeen Royal Infirmary. The x-ray unit is typical of that used for a general-purpose x-ray room. It is capable of exposures across a kV_p range of 50 – 120 and has a total filtration of 3.58mm of Aluminium at 80kV_p, measured at a 100cm FDD. The unit was not under the remit of NHS Tayside's medical physics department, however it was confirmed with the local (NHS Grampian) medical physics department that the x-ray system was up to date in terms of its preventative maintenance visits and quality control (QC) programmes and was expected to be performing to within the manufacturer's specification on the day that the exposures described throughout §4.3 were undertaken.

As it is anticipated that all x-ray systems have some dependence for measured radiation output on the number of exposures undertaken following a period of non-use, the unit was warmed up with 10 exposures prior to use.

The x-ray unit had a KAP meter attached at the tube output; KAP values for each exposure were routinely recorded to ensure consistency from exposure to exposure when required. The calibration for the KAP meter, undertaken across the full kV_p range of the equipment and traceable to a national standard, was obtained from NHS Grampian. The unit has 2 focal spot sizes; broad focus (1.2mm) and fine focus (0.6mm).

The unit used an amorphous silicon wireless indirect digital detector, manufactured by Canon Inc. Canon's unique DDI is called the REX, which has a linear relationship with kerma at the image receptor. This is necessary to comply with the requirements of International Electrotechnical Commission (IEC) 62494-1 [101] which state that the exposure index

should be linear with kerma at the image receptor for DDR systems. A linear relationship allows for the specification of a deviation index (DI) defined as;

$$DI = 10Log_{10}\left(\frac{EI}{EI_T}\right) \qquad \text{[equation 4.1]}$$

where EI_T is the target exposure index (REX). The post-examination display of a DI allows the operator to see how far from the target REX the REX of the examination they have just undertaken is, which provides information relating to how well optimised the examination was.

In preparation for applying the computational model, it was first necessary to create the LUTs the computational model would use. As described in chapter 3, these include LUTs for estimating k_0, k_d and μ_{eff}. The process for creating the LUTs was the same as was described throughout chapter 3 for the Fuji CR system, therefore only the results and significant findings are discussed in the sections that follow.

4.3.1 Creating the look up tables for initial air kerma

LUTs were created for estimating k_0 using both the tube output and measured KAP.

4.3.1.1 Tube output

Mirroring the work undertaken in §3.3.1.1, the output at the centre of the x-ray field in terms of μGy mAs^{-1} at a 100cm FDD at 60, 80 and 100kV_p was measured for field sizes that varied in 5cm increments in both axes parallel and perpendicular to the anode-cathode axis from 5-40cm in each for broad focus. For a 20x20cm field size, the output was measured at 0.5mAs, being the lowest the x-ray unit was capable of delivering, and then every discrete

mAs step up to 8mAs (0.63, 0.8, 1.0, 1.25, 1.6, 2.0, 2.5, 3.2, 4.0, 5.0, 6.3). The same Raysafe Xi R/F detector that was used throughout chapter 3 was used for these measurements.

This provided all of the data necessary to create a LUT for tube output for the Xograph-Canon DDR x-ray system, like that described in §3.3.1.1.

4.3.1.2 Examination kerma area product

Mirroring the work undertaken in §3.3.2.1, correction factors for the KAP meter across the kV_p range were acquired from NHS Grampian's medical physics department. Correction factors for the non-uniform kerma per unit area were measured at the centre of the field for all field size combinations in 5cm steps between 5 and 45cm in both axis parallel and perpendicular to the anode-cathode using equation 3.4 (§3.3.1.3). The Raysafe Xi R/F detector was used for these measurements.

This provided all of the data necessary to create a LUT for correction factors for the KAP to determine k_0 for the Xograph-Canon DDR x-ray system, like that described in §3.3.1.3.

4.3.2 Creating the look up tables for kerma at the image receptor

The work undertaken in §3.3.2.5, suggests that only a single calibration of DDI or signal transfer property (STP) undertaken in a broad beam geometry with an attenuator thickness in excess of 100mm of solid water HE per kV_p is necessary to produce the calibrations from which the kerma at the image receptor can be estimated. This is a result of the quality of the x-ray beam as it exits the attenuator and will be independent of the x-ray equipment provided the inherent filtration of clinical x-ray units are similar. The total filtration of the Xograph-Canon unit is 3.58mm of aluminium measured at 80kV_p at a 100cm FDD, the total

filtration of the Philips Optimus 50 radiographic x-ray unit used throughout chapter 3 is 3.39mm of aluminium measured under almost identical conditions ($81kV_p$, not 80). Nevertheless, since this is only the second system on which the computational model will be tested, calibrations were undertaken using 25, 50, 75, 100, 125, 150, 175 and 200mm of solid water HE to verify that a single calibration undertaken at 200mm of solid water HE gives results for kerma at the image receptor that are accurate for all attenuator thicknesses of 100mm and above. The results for REX calibrations with varying thicknesses of attenuator at 60, 70 and $80kV_p$ are shown in figure 4-1.

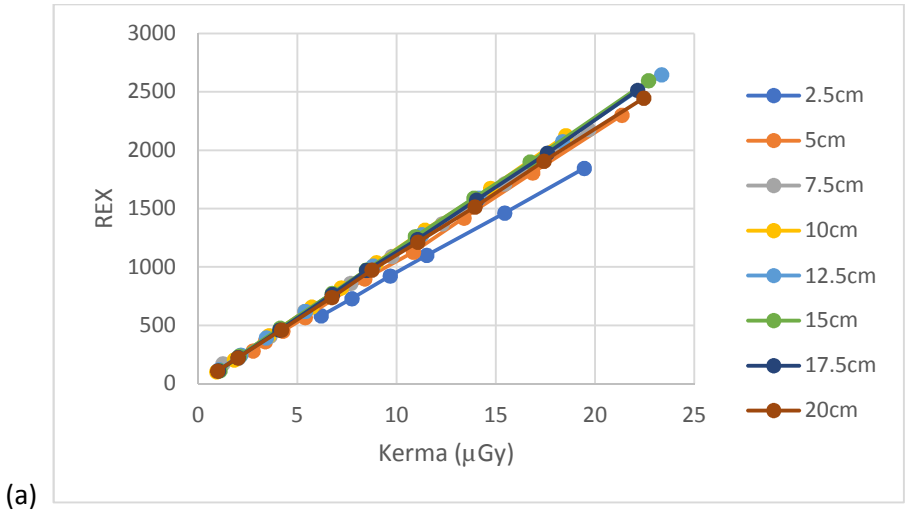

(a)

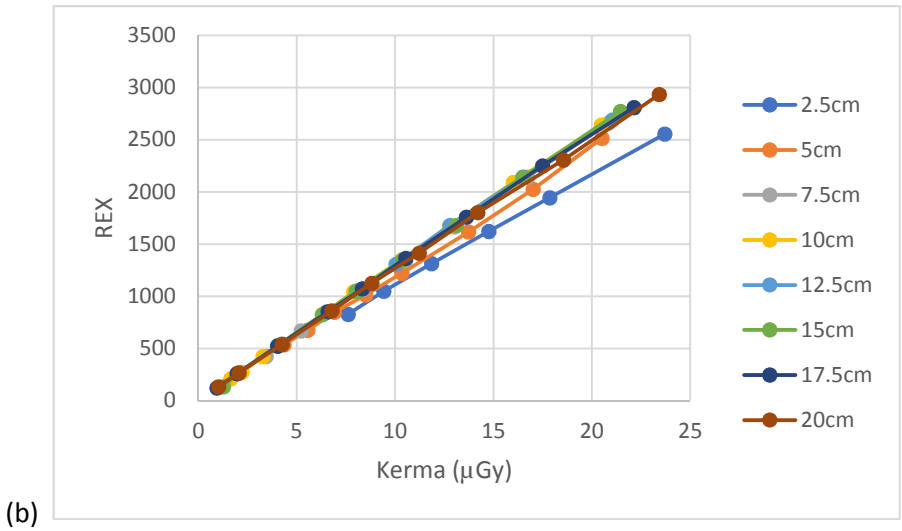

(b)

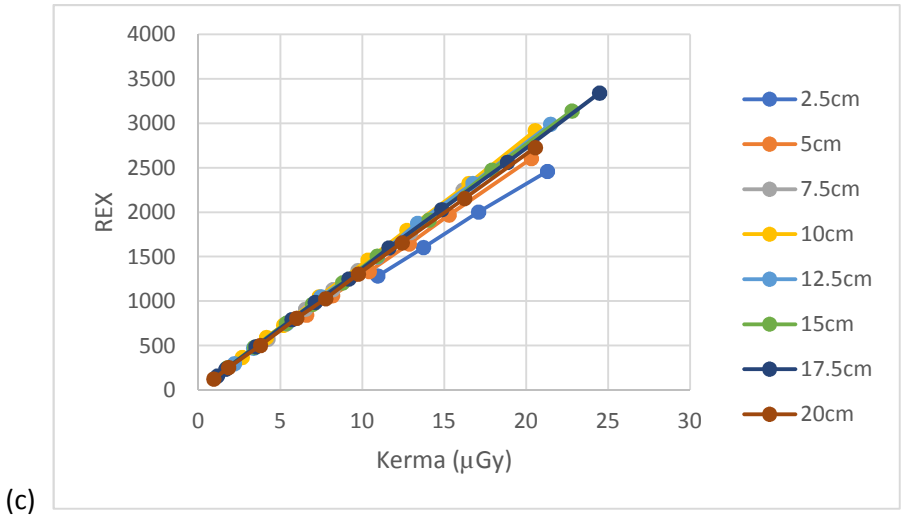

(c)

Figure 4-1: REX calibrations for the Xograph-Canon DDR system for varying thicknesses of solid water HE attenuator at (a) 60, (b) 70 and (c) 80kV$_p$. The uncertainty in kerma measurement is ±5%

Figure 4-1 suggests that the REX calibrations are indistinguishable for attenuator thicknesses greater than 75mm of Solid Water HE if the exposure is undertaken in a broad beam geometry. This suggests that the kerma can be estimated from the REX from a single calibration per kV_p provided it has been undertaken with an attenuator thickness of at least 75mm of Solid Water HE. In order to assess the quantitative uncertainty associated with this, a least squares fit was made to all of the REX calibrations acquired at 75mm or higher at 60, 70 and 80kV_p using MATLAB [110] and the general form of;

$$REX = a_{kV_p,HVL}\mu Gy + b_{kV_p,HVL} \qquad \text{[equation 4.2]}$$

Using the values of the constants a and b in equation 4.2 for each calibration, k_d was calculated for an incrementally increasing REX value from 200 to 2200 in steps of 100 for each calibration at 60, 70 and 80kV_p. For each kV_p, the detector kerma from the individual estimates made using each of the calibrations of REX at 75, 100, 125, 150 and 175mm of solid water HE was compared with the value for k_d calculated from the calibration using 200mm of solid water HE. This assessment of uncertainty will determine whether calibrations undertaken with a 200mm thickness of solid water HE attenuator are an appropriate choice as a single calibration for the determination of detector kerma. The results are shown in figure 4-2.

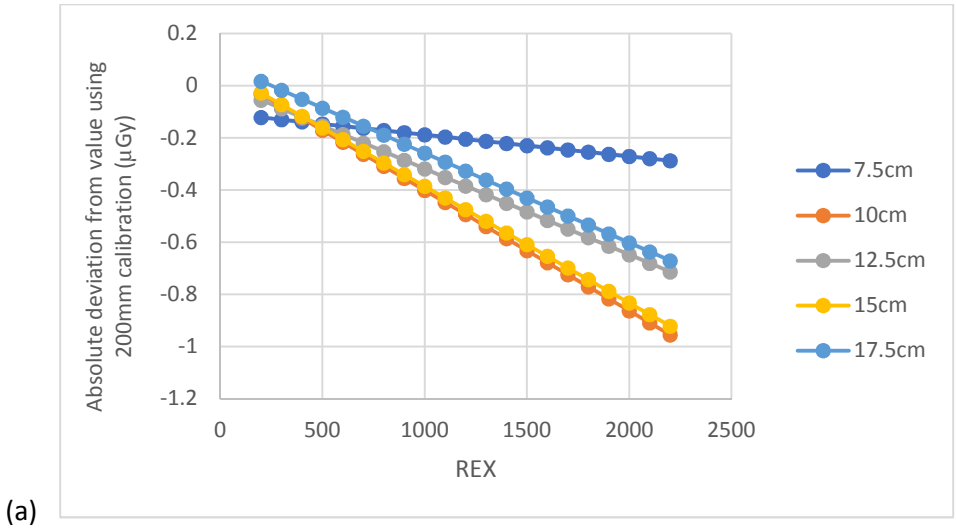

(a)

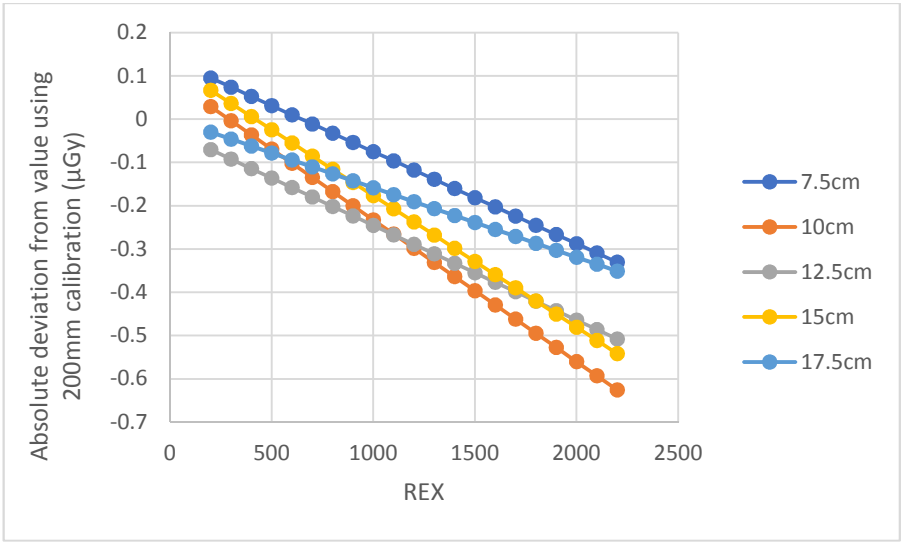

(b)

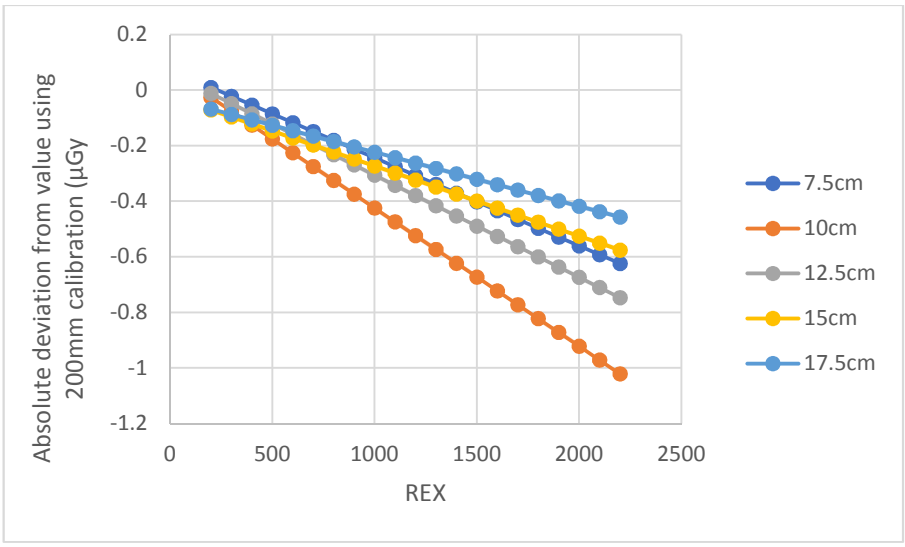

(c)

Figure 4-2: the absolute deviation between kerma calculated from the REX calibration measured using the specified thickness of solid water HE and that using 200mm of solid water HE for REX values ranging from 200 - 2200 at (a) 60, (b) 70 and (c) 80kV$_p$

In all cases, the absolute deviations between the kerma calculated from the calibration measured using the specified thickness of solid water HE and that measured using 200mm of solid water HE are small. The highest absolute deviation for any case was 1.02μGy and this was for a high detector kerma (in excess of 15μGy) for a comparison between calibrations undertaken at 100 and 200mm of solid water HE at 80kV$_p$. The trend for the deviation is consistent across all kV$_p$ values and attenuator calibrations; as was the case with the Fuji CR system, the deviation is greater for high detector kerma and becomes less towards a lower (and clinically relevant) detector kerma. Taking a clinically relevant range of detector kerma values as 2.5 - 6μGy, the highest absolute deviation for any case is 0.37μGy (a deviation of 5.6%). This is a very similar result as was achieved with the Fuji CR system (for which the highest absolute deviation for any case within a detector kerma value of 2.5 - 6μGy is 0.29μGy, as described in §3.3.2.7) and the conclusion remains the same; a detector kerma can be accurately estimated for any examination in which the attenuator has a thickness in excess of the equivalent of 100mm of solid water HE from the DDI using a single calibration of DDI undertaken using 200mm of solid water HE.

4.3.3 Estimating effective linear attenuation coefficient

Values of μ_{eff} were measured for thicknesses of solid water HE of 25, 50, 75, 100, 125, 150, 175 and 200mm at 60, 70 and 80kV$_p$ for a field size of 40x40cm at a 100cm FDD. The Raysafe Xi R/F detector was used for all measurements and was positioned at the centre of the x-ray field once and never moved throughout. Measurements of attenuator exit kerma and the kerma with no attenuator present were made for each of the thicknesses of solid water HE and the μ_{eff} calculated using equation 3.9 (§3.3.3). The variation in μ_{eff} with

increasing thickness of solid water HE attenuator for 60, 70 and 80kV$_p$ is shown in figure 4-3.

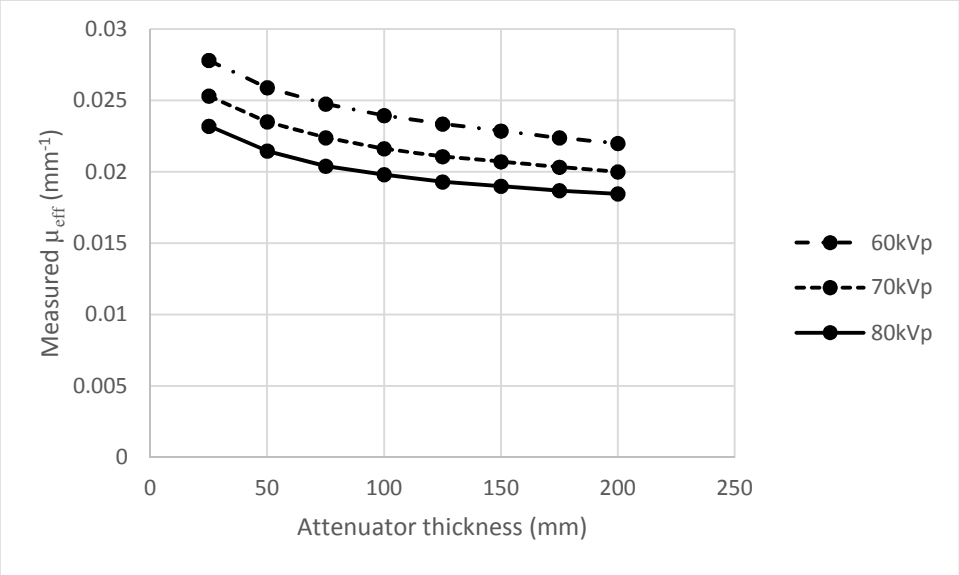

Figure 4-3: the variation in measured effective linear attenuation coefficient, μ_{eff}, with increasing thicknesses of solid water HE attenuator for a 40x40cm field size at 60, 70 and 80kV$_p$

The μ_{eff} shown in figure 4-3 demonstrate the same trends as were seen for the Fuji CR system, as described in §3.3.3.3. There are differences between the absolute values with beam quality, as expected, and the values decrease with increasing attenuator thickness.

The μ_{eff} values for the Xograph-Canon system are consistently 2 – 5% lower than those measured for the Fuji CR system. This can be explained by the difference in the total filtration of each system. The filtration of the Xograph-Canon system is 3.58mm of aluminium, compared with 3.39mm of aluminium for the Philips Optimus 50 radiographic x-ray unit used with the Fuji CR system. This is expected to result in a lower μ_{eff} for the Xograph-Canon system compared with the Philips Optimus 50 radiographic x-ray unit for an equivalent kV$_p$, as is found to be the case.

The LUT presented in §3.3.3 contains corrections for field size for the Philips Optimus 50 radiographic x-ray unit. These same corrections were used for the Xograph-Canon DDR unit.

4.3.4 Test examinations

To assess how well the computational model works with the Xograph-Canon system, test examinations were undertaken as they were for the Fuji CR system as described in §4.2.1. Eighteen test examinations were undertaken in total, six at each of 60, 70 and 80kV_p. For each group of six test examinations per kV_p, there were only four unique thicknesses of solid water HE attenuator. Test images were acquired three times for one thickness using the same exposure factors and geometry to additionally test the repeatability of the results generated using the computational model. Thicknesses of solid water HE attenuator were selected between 100 and 200mm to match the availability of solid water HE thicknesses available. Field sizes were selected between 20x20cm and 40x40cm. The mAs for the exposure was chosen from a range of 1.2 to 6.3 to ensure a clinically relevant range of k_0 and k_d values. This was based on the premise that the detector kerma would not be significantly in excess of 5µGy for a reasonably well undertaken examination, as previously explained in §4.2.1. All exposures were undertaken at 100cm FDD, with the attenuator placed directly on top of the Canon image receptor.

One image was acquired for each examination. Each used the local equipment testing protocol, configured by the manufacturer at the request of the local medical physics department not to apply any image processing to the system, resulting in a linear relationship between REX and kerma at the image receptor (as confirmed by the calibrations shown in figure 4-1, §4.3.2).

Images were extracted directly from the x-ray unit in native DICOM format using a USB drive.

To allow for an assessment of the accuracy of the values selected by the computational model from the LUTs, two further exposures were made for each examination. For the first of these, the Raysafe Xi R/F detector was positioned in place of the Canon detector so that a direct measure of k_d could be made. For the second, the Raysafe Xi R/F detector remained in place but the attenuator was removed so that a measurement of k_0 could be made. For both of these additional exposures, the examination KAP was recorded and found to be within 4.4% of those recorded for the examinations that produced the images. The μ_{eff} was calculated using the measured k_d and k_0 and the known thickness of the attenuator using equation 3.9 (§3.3.3).

4.3.4.1 Estimate of initial air kerma

For each examination two estimates of k_0 were made. The first, $k_{o_{output}}$, used the examination kV_p, mAs, field size, tube focus selection and FDD to select a value from the LUT created in §4.3.1.1. The second, $k_{o_{KAP}}$, used the examination kV_p, KAP and field size to calculate k_0 with a correction made for beam non-uniformity as described in §4.3.1.2. The percentage difference between the estimated values and those measured using the Raysafe Xi R/F detector are shown in figure 4-4.

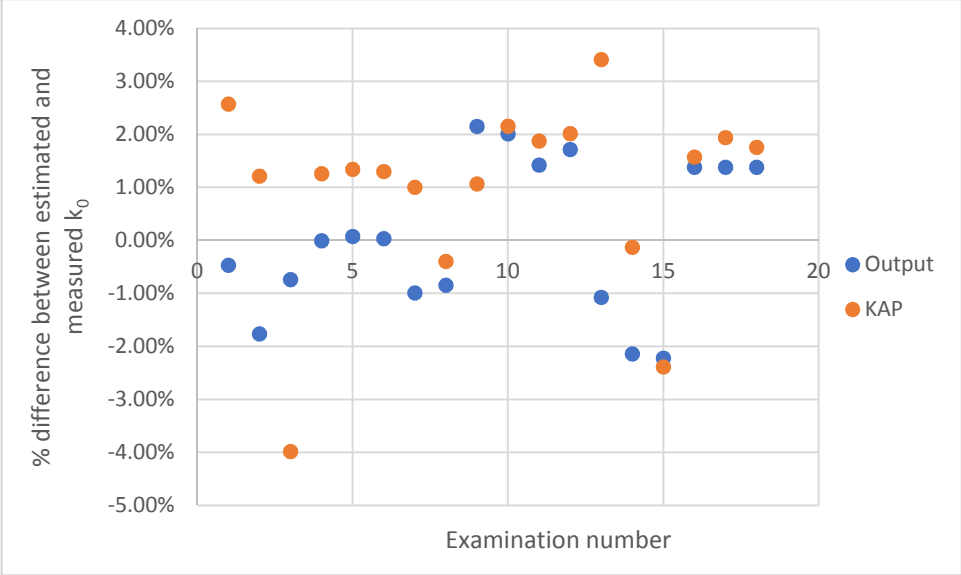

Figure 4-4: percentage difference between the values of initial air kerma, k_0, estimated using the examination mAs and KAP and the value measured using the Raysafe Xi R/F detector

Estimates of k_0 using both methods ($k_{o_{output}}$ and $k_{o_{KAP}}$) produce results that are close to the values of k_0 measured with the Raysafe Xi R/F detector. The difference between the estimates and the measured values are all well within the uncertainty budgets for each method shown in §3.3.1.2 and §3.3.1.4.

The average of the absolute individual deviations between measured and estimated values for $k_{o_{output}}$ is 1.21%. For $k_{o_{KAP}}$ the average of the absolute individual deviations between measured and estimated values is 1.74%. A t-test indicates that these differences are not significant at the $p < 0.05$ level ($p = 0.073$).

4.3.4.2 Estimate of kerma at the image receptor

For each examination one estimate of k_d was made. This used the examination REX value to predict $k_{d_{DDI}}$. The process used the examination kV_p to select the appropriate calibration between image receptor kerma and REX acquired using 200mm of solid water

HE attenuator as described in §4.3.2. The examination REX was used with this calibration to estimate k_d.

The percentage difference between the estimated value of k_d and the value measured using the Raysafe Xi R/F detector is shown in figure 4-5.

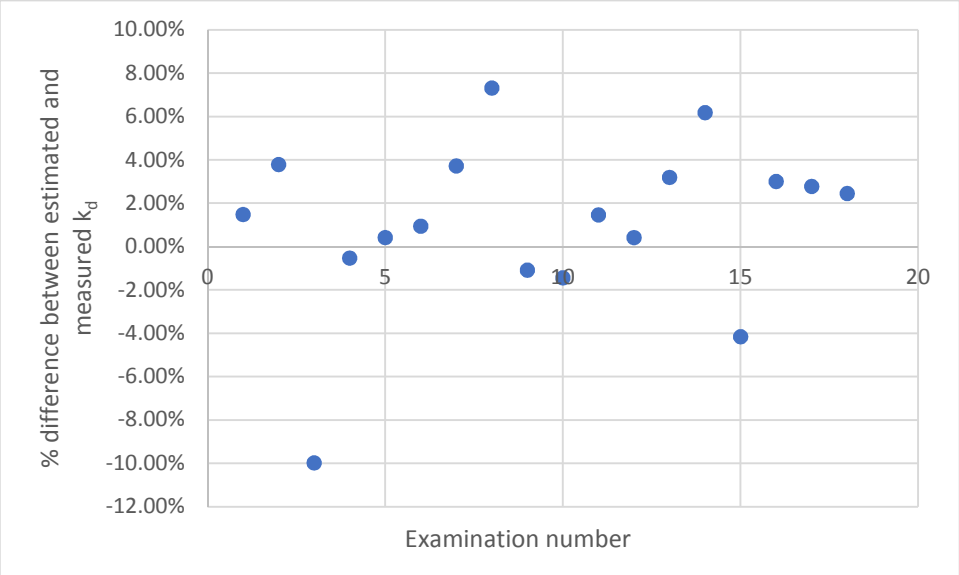

Figure 4-5: percentage difference between the values of kerma at the image receptor, k_d, estimated using the REX and the value measured using the Raysafe Xi R/F detector

Estimates of k_d made using the REX produce results that are close to the values measured with the Raysafe Xi R/F detector. The average of the absolute individual deviations for $k_{d_{DDI}}$ is 3.02%. The repeatability of the estimates of k_d for the 3 examinations that were repeated at 60, 70 and 80kV$_p$ was excellent. The highest deviation in k_d between any 2 equivalent examinations was 0.07µGy.

4.3.4.3 Estimate of effective linear attenuation coefficient

For each examination one estimate of μ_{eff} was made. As described in §3.3.3.3, this estimate uses the ratio of $\frac{k_d}{k_0}$ for each examination and a series of relationships between μ_{eff}

and attenuator thickness that had been measured for the Xograph-Canon unit at various field sizes and kV_p. The closest relationship for the field size and kV_p used in the examination was used to make a broad estimate of the attenuator thickness. This broad estimate of thickness was then used with the measured relationship between μ_{eff} and attenuator thickness at the examination kV_p and field size to estimate a value for μ_{eff} for the examination. Where necessary, values of μ_{eff} were linearly interpolated for field size. For comparison, the known value of μ_{eff} refers to the value calculated using the measured k_d and k_0 and the known attenuator thickness using equation 3.9 (§3.3.3). The results are shown in figure 4-6.

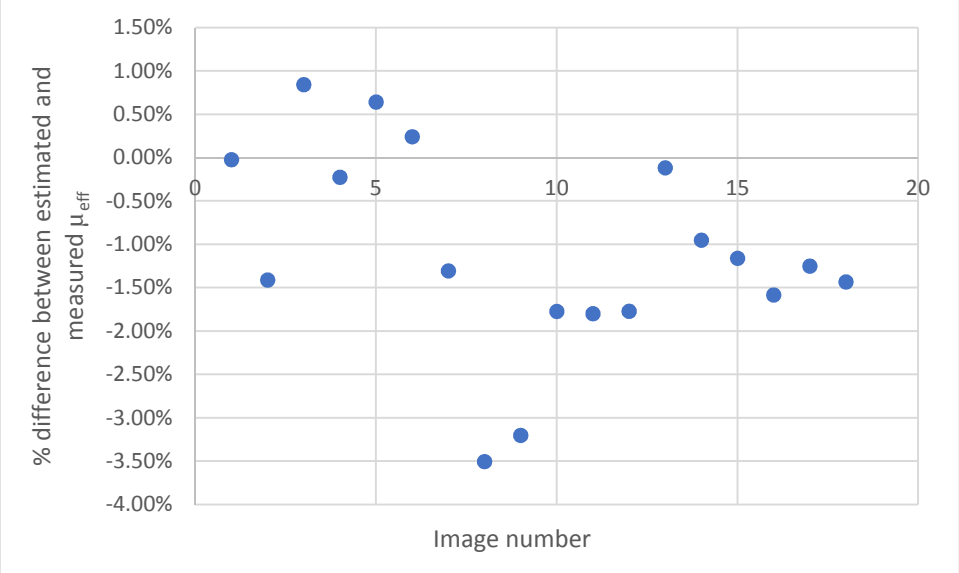

Figure 4-6: percentage difference between the estimated values of effective linear attenuation coefficient, μ_{eff}, and the value calculated using the measured k_d, k_0 and the known attenuator thickness

The estimates of μ_{eff} made using the methods described in §3.3.3.3 are consistently close to the true value, calculated using the measured values of k_d and k_0 for each examination and the known attenuator thickness. The highest deviation between measured and true values is -3.51% and the average of the absolute individual deviations is 1.3%.

4.3.4.4 Estimate of attenuator thickness

For each examination, two estimates of attenuator thickness were made using each estimate of k_0 (using output and KAP) and the estimate of k_d using the REX. Only one value of μ_{eff} was calculated – this was used in both estimates. The results are compared to the known attenuator thickness in table 4.6.

Image number	Attenuator thickness (mm)				
	True (mm)	Using REX ($k_{d_{DDI}}$) and output ($k_{o_{output}}$) (estimate A)		Using REX ($k_{d_{DDI}}$) and KAP ($k_{o_{KAP}}$) (estimate B)	
		Estimate (mm)	Deviation from true (%)	Estimate (mm)	Deviation from true (%)
1	115	114.2	-0.69%	115.5	0.42%
2	145	144.7	-0.23%	146.0	0.67%
3	160	163.0	1.88%	161.5	0.95%
4	190	190.7	0.35%	191.2	0.65%
5	190	188.6	-0.72%	189.2	-0.42%
6	190	189.1	-0.45%	189.7	-0.16%
7	130	129.5	-0.39%	130.4	0.34%
8	160	161.9	1.20%	162.1	1.34%
9	170	177.2	4.25%	176.7	3.94%
10	190	195.2	2.72%	195.2	2.76%
11	190	193.5	1.82%	193.7	1.94%
12	190	194.1	2.15%	194.2	2.22%
13	115	113.0	-1.76%	115.2	0.21%
14	130	127.0	-2.29%	128.1	-1.48%
15	160	162.9	1.84%	162.9	1.79%
16	190	192.2	1.16%	192.3	1.21%
17	190	191.7	0.88%	192.0	1.03%
18	190	192.2	1.16%	192.4	1.26%

Table 4.6: the estimates of attenuator thickness made by the computational model for both values of estimated initial air kerma, k_0, compared with the known attenuator thickness

All estimates of attenuator thickness were within 4.3% of the true value of attenuator thickness. The average of the absolute deviation between estimated and true attenuator thickness is 1.44% for estimate A and 1.27% for estimate B.

Whilst there is an apparent greater accuracy in the final estimate of attenuator thickness using KAP rather than output to determine the kerma at the image receptor, k_d, a t-test indicates that this difference is not significant at the $p < 0.05$ level ($p = 0.089$).

As was concluded in §4.2.5 when testing the computational model with the Fuji CR system, the testing presented with the Xograph-Canon DDR system demonstrates that the computational model shows great promise in the accuracy of its use on this system as well.

4.3.5 Summary

The computational model has been applied to an Xograph-Canon DDR system. LUTs specific to the Xograph-Canon system were created as required. The estimates of k_0, k_d and μ_{eff} made by the computational model were all compared to measured values and found to be consistently accurate across all of the validation examinations. The final estimate of attenuator thickness was accurate, with all estimates within 4.3% of the true value of attenuator thickness and an average deviation from the true value of attenuator thickness of 1.27 – 1.44% depending on the source used to derive the value of k_0. These results are similar to those achieved with the Philips Optimus 50 radiographic x-ray unit and Fuji CR system. The accuracy of the computational model is similar across two systems of different manufacture.

4.4 Fuji direct digital radiography system

Although a Fuji system has already been tested, as presented in §4.2, local access was also available to a Fuji DDR system, which was deemed to be sufficiently different from the CR system as to merit additional testing of the computational model. The Fuji DDR system uses a different DDI to the Fuji CR system, with a different relationship to kerma. Furthermore, the clinical validation study described in chapter 6 was undertaken on the Fuji DDR system, so ensuring the accuracy of the computational model on the system beforehand was required before the clinical validation study could proceed.

The Fuji DDR system was a radiographic mobile (the 'Fuji FDR Go digital mobile x-ray unit') with a wireless digital detector manufactured by Fujifilm Corporation. It was purchased in March 2016 by NHS Tayside and is used throughout Ninewells hospital. It is capable of exposures across a kV_p range of 40 – 130 and has a total filtration of 3.41mm of aluminium at $80kV_p$, measured at a 100cm FDD. The unit was up to date in terms of its preventative maintenance visits and QC programmes and was known to be performing to within the manufacturer's specification on the days that the exposures described within this chapter were undertaken. As it is anticipated that all x-ray systems have some dependence for measured radiation output on the number of exposures undertaken following a period of non-use, the unit was warmed up with 10 exposures prior to use.

The x-ray unit had a KAP meter attached at the tube output; KAP values for each exposure were routinely recorded to ensure consistency from exposure to exposure when required. The calibration for the KAP meter, undertaken across the full kV_p range of the equipment and traceable to a national standard, was available from recent QC testing. The unit has 2 focal spot sizes; broad focus (1.3mm) and fine focus (0.7mm).

The unit used an amorphous silicon wireless digital detector. On DDR units, Fuji's unique DDI is called the exposure index (EI), which has a linear relationship with kerma at the

image receptor. The EI complies with the requirements of IEC 62494-1 [101], allowing use of the DI defined by equation 4.1.

In preparation for applying the computational model, it was first necessary to create the LUTs the computational model would use. As described in chapter 3, these include LUTs for estimating k_0, k_d and μ_{eff}. The process for creating the LUTs was the same as was described throughout chapter 3 and §4.3, therefore only the results and significant findings are discussed in the sections that follow.

4.4.1 Creating the look up tables for initial air kerma

LUTs were created for estimating k_0 using both the tube output and measured KAP.

4.4.1.1 Tube output

The output at the centre of the x-ray field in terms of μGy mAs^{-1} at a 100cm FDD at 60, 70 and 80kV_p was measured for field sizes that varied in 5cm increments in both axes parallel and perpendicular to the anode-cathode axis from 5-40cm in each for broad focus. For a 20x20cm field size, the output was measured at 0.5mAs, being the lowest the x-ray unit was capable of delivering, and then every discrete mAs step up to 8mAs (0.32, 0.36, 0.4, 0.45, 0.5, 0.56, 0.63, 0.71, 0.8, 0.9, 1.0, 1.1, 1.2, 1.4, 1.6, 1.8, 2.0, 2.2, 2.5, 2.8, 3.2, 3.6, 4.0, 4.5, 5.0, 5.6, 6.3, 7.1). The same Raysafe Xi R/F detector that was used throughout chapter 3 was used for these measurements.

4.4.1.2 Examination kerma area product

Correction factors for the KAP meter calibration across the kV_p range were already known from the QC programme. Correction factors for the non-uniform kerma per unit area were measured for the centre of the field for all field size combinations in 5cm steps between 5 and 45cm in both axis parallel and perpendicular to the anode-cathode using equation 3.4 (§3.3.1.3). The Raysafe Xi R/F detector was used for these measurements.

4.4.2 Creating the look up tables for image receptor kerma

It was established on both the Philips Optimus 50 radiographic x-ray unit with the Fuji CR system and the Xograph-Canon DDR system that only a single calibration of DDI and STP undertaken in a broad beam geometry with an attenuator thickness in excess of 100mm of solid water HE per kV_p is necessary to produce the calibrations from which the kerma at the image receptor can be estimated. Calibrations of EI and STP are only presented for the Fuji DDR unit using 200mm of solid water HE attenuator. These are shown in figure 4-7(a – b) for EI and STP respectively.

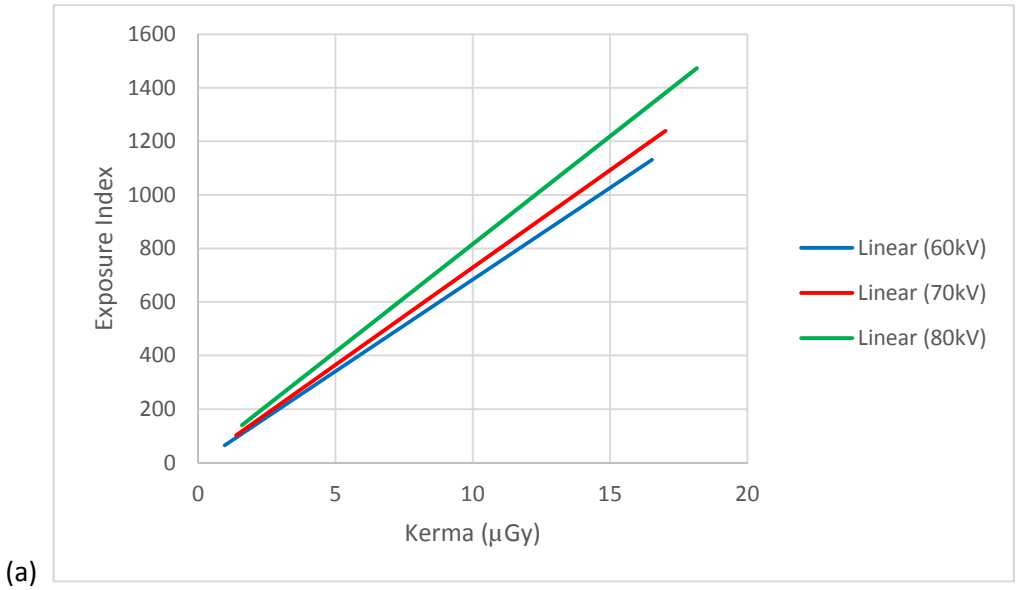

(a)

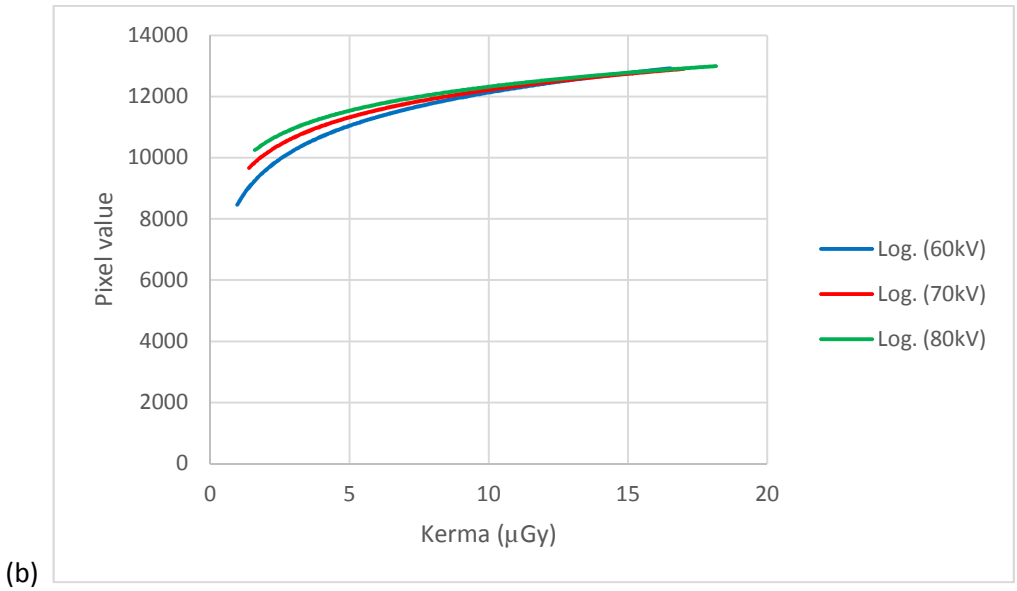

(b)

Figure 4-7: (a) EI and (b) STP calibrations for the Fuji DDR system for a 200mm thickness of solid water HE attenuator at 60, 70 and 80kV$_p$

A least squares fit was made to all calibrations using Matlab; the calibrations have the general forms;

$$EI = a_{kV_p,HVL}\mu Gy + b_{kV_p,HVL} \quad \text{[equation 4.3]}$$

$$PV = a_{kV_p,HVL} Ln(k_d\ (\mu Gy)) + b_{kV_p,HVL} \quad \text{[equation 4.4].}$$

4.4.3 Estimating effective linear attenuation coefficient

Values of μ_{eff} were measured for thicknesses of solid water HE ranging from 10 to 200mm in increments of 10mm at 60, 70 and 80kV$_p$ for field sizes of 20x20, 30x30 and 40x40cm at a 100cm FDD. The Raysafe Xi R/F detector was used for all measurements and was positioned at the centre of the x-ray field once and never moved throughout. Measurements of attenuator exit kerma and the kerma with no attenuator present were made for each of the thicknesses of solid water HE and the μ_{eff} calculated using equation 3.9 (§3.3.3). The variation in μ_{eff} with increasing thickness of solid water HE attenuator for 60, 70 and 80kV$_p$ is shown in figure 4-8(a-c) for field sizes of 20x20, 30x30 and 40x40cm respectively.

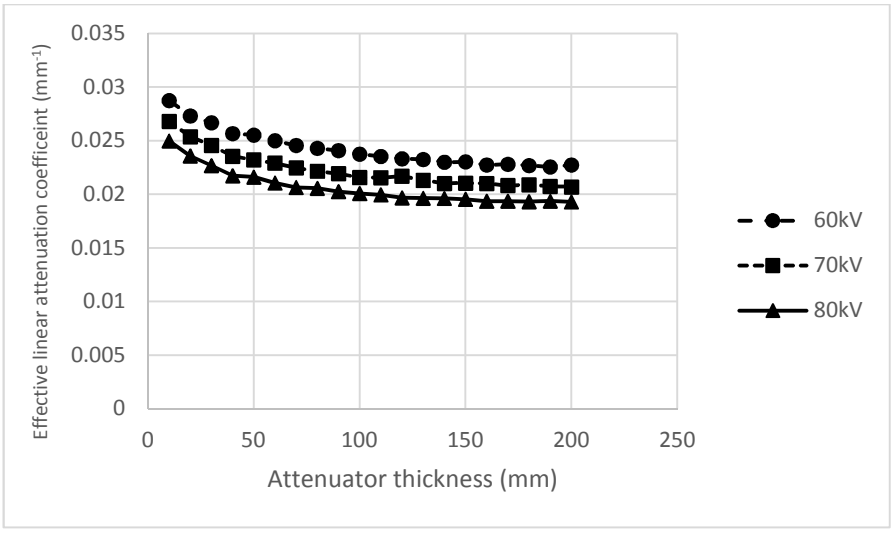

(a)

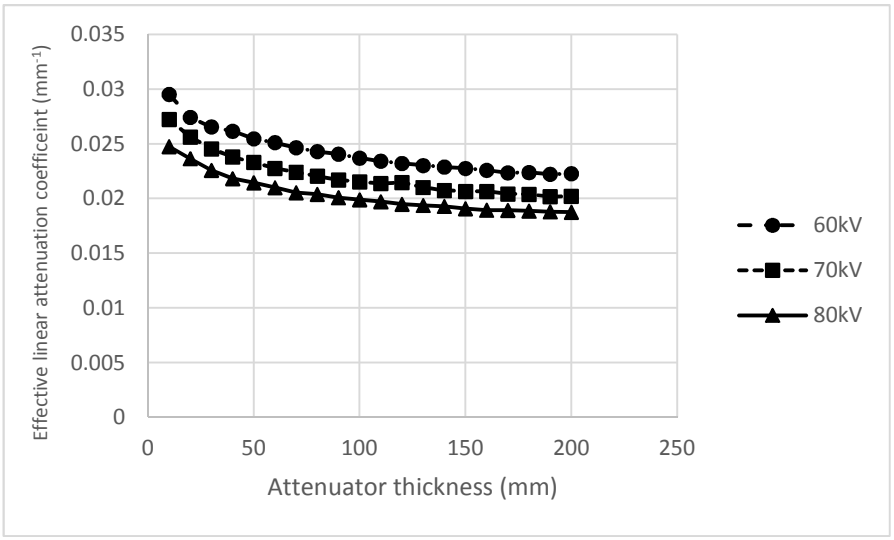

(b)

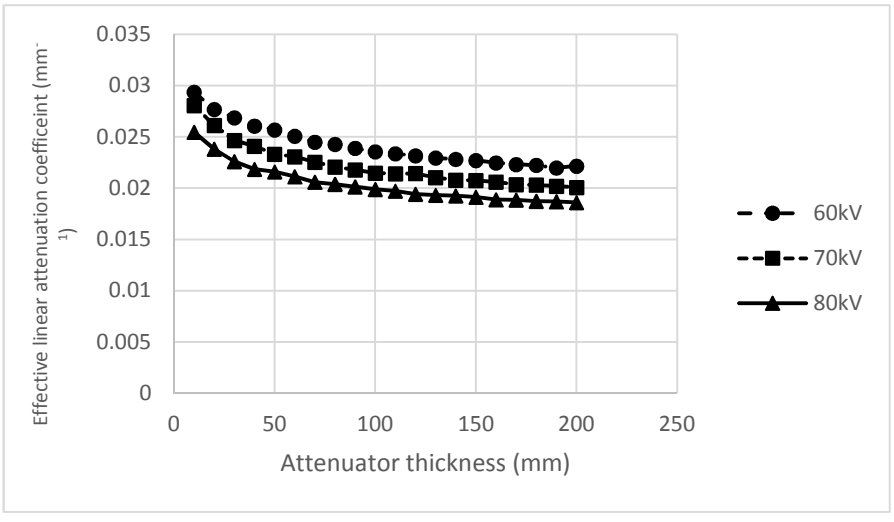

(c)

Figure 4-8: the variation in measured effective linear attenuation coefficient, μ_{eff}, with increasing thicknesses of solid water HE attenuator at 60, 70 and 80kV$_p$ for field sizes of (a) 20x20cm, (b) 30x30cm and (c) 40x40cm

The values of μ_{eff} shown in figure 4-8 demonstrate the same trends as were seen for the Fuji CR system, as described in §3.3.3.3 and the Xograph-Canon DDR system, as described in §4.3.3. There are differences between the absolute values with beam quality, as expected, and the values decrease with increasing attenuator thickness.

The values themselves are similar to those measured for the Fuji CR and the Xograph-Canon DDR systems. Those measured for the Fuji DDR system are on average 3.2% lower than for the Fuji CR system and 0.05% greater than the Xograph-Canon system. The inherent filtration of the Fuji DDR system is 3.41mm of aluminium, compared with 3.58mm of aluminium for the Xograph-Canon system and 3.39mm of aluminium for the Philips Optimus 50 radiographic x-ray unit used with the Fuji CR system. The beam quality is harder for the Xograph-Canon system and as is expected this results in the lowest μ_{eff} for an equivalent kV_p compared with the Philips Optimus 50 radiographic x-ray and Fuji DDR units.

4.4.4 Test examinations

To assess how well the computational model works with the Fuji DDR system, test examinations were undertaken as they were described for the Fuji CR system in §4.2.1 and the Xograph-Canon DDR system in §4.3.4. Twelve test examinations were undertaken in total, four at each of 60, 70 and 80kV_p. Thicknesses of solid water HE attenuator were selected between 100 and 200mm to match the availability of solid water HE thicknesses available. Field sizes were selected between 10x10cm and 40x40cm. The mAs for the exposure was chosen from a range of 1.1 to 4.0 to ensure a clinically relevant range of k_0 and k_d values. All exposures were undertaken at 100cm FDD, with the attenuator placed directly on top of the Fuji image receptor.

One image was acquired for each examination using the 'sensitivity' processing algorithm which applies as little processing to the image as is possible. These images would demonstrate a variance in EI, but not PV. It was possible on the Fuji DDR unit to copy the raw data from one image and apply different processing to it. Using this function, it was possible to create a copy of each image and apply the 'sensitivity' processing algorithm but with a fixed EI of 200 so that the PV would vary. As the images used for DDI and PV analysis would be identical, this removed one of the sources of error that existed for the Fuji CR system where it was necessary to acquire two images for each test. There will have been slight differences between them as a result of deviations in x-ray tube output from exposure to exposure and because of the stochastic nature of x-ray absorption.

All of the images were extracted directly from the x-ray unit in native DICOM format using a USB drive.

To allow for an assessment of the accuracy of the values selected by the computational model from the LUTs, two further exposures were made for each examination. For the first of these, the Raysafe Xi R/F detector was positioned in place of the Fuji image receptor so that a direct measure of k_d could be made. For the second, the Raysafe Xi R/F detector remained in place but the attenuator was removed so that a measurement of k_0 could be made. For both of these additional exposures, the examination KAP was recorded and found to be within 0.5% of those recorded for the examinations that produced the images. The μ_{eff} was calculated using the measured k_d and k_0 and the known thickness of the attenuator using equation 3.9 (§3.3.3).

4.4.4.1 Estimate of initial air kerma

For each examination two estimates of k_0 were made. The first, $k_{o_{output}}$, used the examination kV_p, mAs, field size, tube focus selection and FDD to select a value from the LUT created in §4.4.1.1. The second, $k_{o_{KAP}}$, used the examination kV_p, KAP and field size to calculate k_0 with a correction made for beam non-uniformity as described in §4.4.1.2. The percentage difference between the estimated values and those measured using the Raysafe Xi R/F detector are shown in figure 4-9.

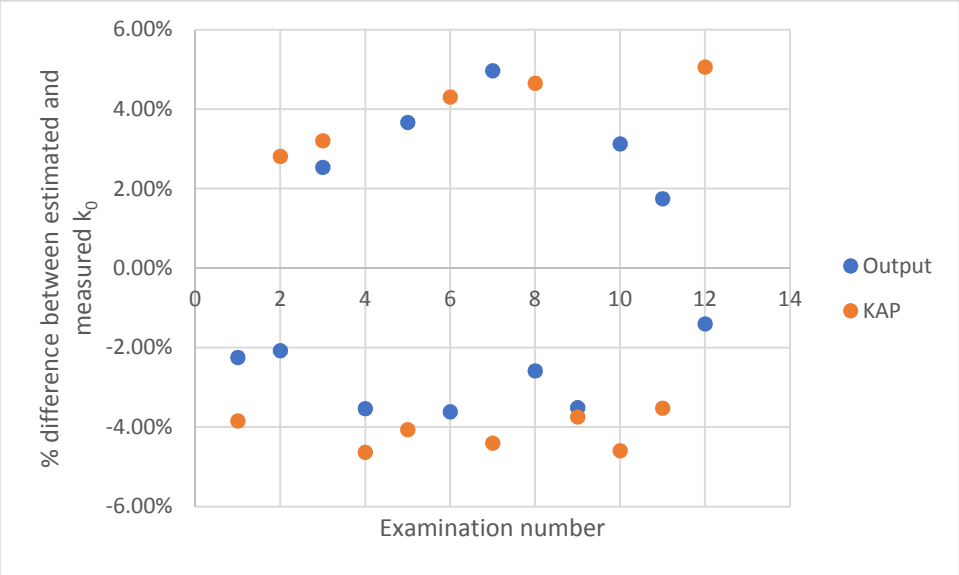

Figure 4-9: percentage difference between the values of initial air kerma, k_0, estimated using the examination mAs and KAP and the value measured using the Raysafe Xi R/F detector

Estimates of k_0 using both methods ($k_{o_{output}}$ and $k_{o_{KAP}}$) produce results that are close to the values of k_0 measured with the Raysafe Xi R/F detector. The difference between the estimates and the measured values are all within the uncertainty budgets for each method shown in §3.3.1.2 and §3.3.1.4.

The average of the absolute individual deviations between measured and estimated values for $k_{o_{output}}$ is 2.9%. For $k_{o_{KAP}}$ the average of the absolute individual deviations between

measured and estimated values is 4.1%. A t-test indicates that these differences are significant at the $p < 0.05$ level ($p = 0.0035$).

4.4.4.2 Estimate of kerma at the image receptor

For each examination two estimates of k_d were made. The first used the examination EI value to estimate $k_{d_{DDI}}$, the second used a measurement of PV from a 1cm^2 ROI at the centre of the image to estimate $k_{d_{PV}}$. The examination kV_p was used to select the appropriate calibration between k_d and EI and k_d and PV from those acquired using 200mm of solid water HE attenuator as described in §4.4.2.

The percentage difference between the estimated value of k_d and the value measured using the Raysafe Xi R/F detector is shown in figure 4-10.

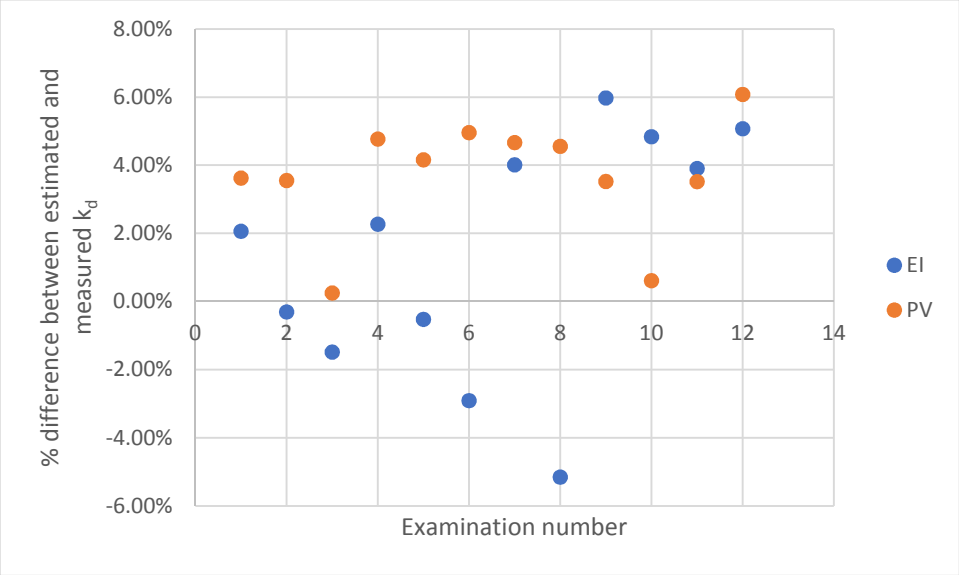

Figure 4-10: percentage difference between the values of kerma at the image receptor, k_d, estimated using the EI and measured PV and the value measured using the Raysafe Xi R/F detector

Estimates of k_d made using the EI and measured PV produce results that are close to the values measured with the Raysafe Xi R/F detector. The average of the absolute individual deviations is 3.2% for $k_{d_{DDI}}$ and 3.7% for $k_{d_{PV}}$. A t-test shows the difference between the two is not significant at the $p < 0.05$ level ($p = 0.50$).

4.4.4.3 Estimate of effective linear attenuation coefficient

For each examination one estimate of μ_{eff} was made. For comparison, the known value of μ_{eff} refers to the value calculated using the measured k_d and k_0 and the known attenuator thickness using equation 3.9 (§3.3.3). The results are shown in figure 4-11.

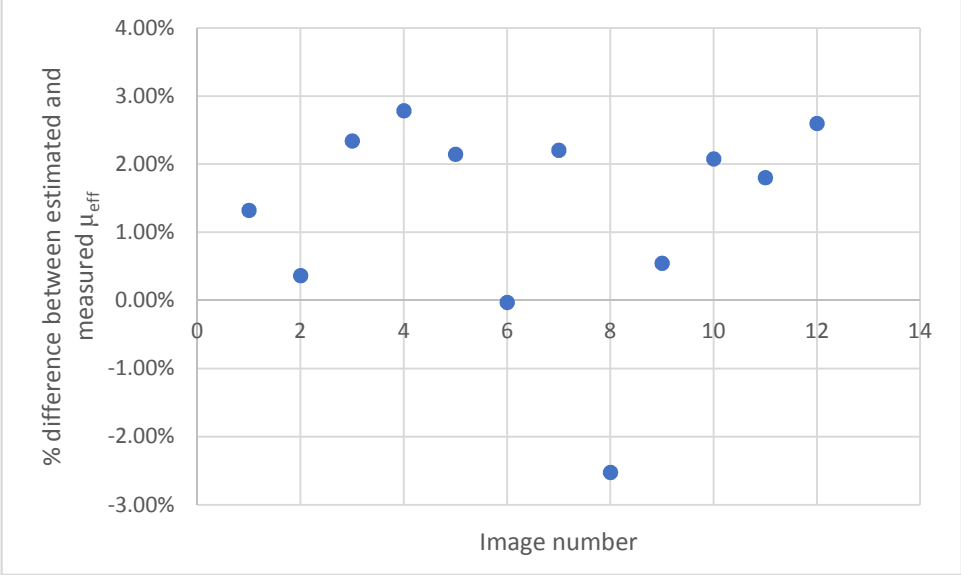

Figure 4-11: percentage difference between the estimated values of effective linear attenuation coefficient, μ_{eff}, and the value calculated using the measured k_d, k_0 and the known attenuator thickness

The estimates of μ_{eff} made using the methods described in §3.3.3.3 are consistently close to the true value, calculated using the measured values of k_d and k_0 for each examination and the known attenuator thickness. The highest deviation between measured and true values is 2.8% and the average of the absolute individual deviations is 1.7%.

4.4.4.4 Estimate of attenuator thickness

For each examination, four estimates of attenuator thickness were made using every available combination of k_0 (using output and KAP) and k_d (using EI and PV). Only one value of μ_{eff} was calculated – this was used in all four estimates. These are called estimates A - D in table 4.7. Estimates of attenuator thickness were made using equation 3.1 (§3.1). The results are compared to the known attenuator thickness in table 4.7.

Image number	Attenuator thickness (mm)								
	True (mm)	Using EI ($k_{d_{DDI}}$) and output ($k_{o_{output}}$) (estimate A)		Using EI ($k_{d_{DDI}}$) and KAP ($k_{o_{KAP}}$) (estimate B)		Using PV ($k_{d_{PV}}$) and output ($k_{o_{output}}$) (estimate C)		Using PV ($k_{d_{PV}}$) and KAP ($k_{o_{KAP}}$) (estimate D)	
		Estimate (mm)	Deviation from true (%)	Estimate (mm)	Deviation from true (%)	Estimate (mm)	Deviation from true (%)	Estimate (mm)	Deviation from true (%)
1	125	121.5	-2.79%	124.1	-0.71%	120.9	-3.31%	123.5	-1.23%
2	170	168.6	-0.83%	170.8	0.44%	166.9	-1.83%	169.1	-0.55%
3	140	136.3	-2.62%	138.8	-0.84%	135.6	-3.17%	138.1	-1.38%
4	110	104.5	-4.96%	108.0	-1.83%	103.5	-5.89%	107.0	-2.76%
5	135	130.6	-3.23%	134.3	-0.51%	128.4	-4.85%	132.1	-2.13%
6	190	189.7	-0.16%	193.6	1.90%	185.8	-2.20%	189.7	-0.13%
7	140	132.7	-5.23%	137.2	-2.03%	132.4	-5.44%	136.9	-2.24%
8	150	155.1	3.42%	158.5	5.64%	150.6	0.40%	153.9	2.62%
9	180	174.0	-3.33%	177.9	-1.18%	175.3	-2.64%	179.1	-0.48%
10	160	152.6	-4.64%	156.6	-2.11%	154.7	-3.28%	158.8	-0.76%
11	155	149.3	-3.67%	152.1	-1.90%	149.5	-3.55%	152.3	-1.77%
12	140	133.2	-4.89%	136.5	-2.54%	132.7	-5.25%	136.0	-2.89%

Table 4.7: the estimates of attenuator thickness made by the computational model for all combinations of predicted values of initial air kerma, k_0, and kerma at the image receptor, k_d, compared with the known attenuator thickness

All estimates of attenuator thickness were within 5.9% of the true value of attenuator thickness. The average of the absolute deviation between estimated and true attenuator thickness is 3.3% for estimate A, 1.8% for estimate B, 3.5% for estimate C and 1.6% for estimate D.

Whilst all results are excellent, there is a slightly greater accuracy achieved using KAP over output (deviations of 1.8% compared with 3.3% and 1.6% compared with 3.5%) for the estimate of k_0. Whilst the more accurate estimates of attenuator thickness are associated with estimates of k_0 made using the examination KAP, these estimates of k_0 were less accurate than those made using the x-ray tube output, as shown in §4.4.4.1. The consistent overestimate of k_0 using the examination KAP is simply balancing the inaccuracies with the other variables to give, on average, a more accurate estimate of attenuator thickness. A t-test indicates that the difference between estimates of attenuator thickness made using output and examination KAP are significant at the $p < 0.05$ level ($p = 4.55 \times 10^{-9}$ for both EI and PV). A t-test indicates that the difference between estimates of attenuator thickness made using EI and PV are not significant at the $p < 0.05$ level ($p = 0.099$ for both output and KAP).

4.4.5 Summary

The computational model has been applied to a Fuji DDR system. LUTs specific to the Fuji DDR system were created as required. The estimates of k_0, k_d and μ_{eff} made by the computational model were all compared to measured values and found to be consistently accurate across all of the validation examinations. The final estimate of attenuator thickness was accurate, with all estimates within 5.9% of the true value of attenuator thickness and an average deviation from the true value of attenuator thickness of 1.6 – 3.3% depending on the source used to derive the values of k_0 and k_d. These results are

similar to those achieved with the Philips Optimus 50 radiographic x-ray unit and Fuji CR and the Xograph-Canon DDR systems.

4.5 Conclusion

In this chapter the computational model developed and described in detail throughout chapter 3 was tested on 3 different x-ray imaging systems; a Fuji CR system with a Philips Optimus 50 radiographic x-ray unit, an Xograph-Canon DDR unit and a Fuji DDR unit. Test images were undertaken for each, with the accuracy of the estimate of each of the three variables k_0, k_d and μ_{eff} assessed along with the overall accuracy of the estimate of attenuator thickness.

For all three systems the results are excellent. Across all of the test exposures made on all three units the largest deviation in the estimate of k_0 is 6.3%, the largest deviation in the estimate of k_d is 7.3%, the largest deviation in the estimate of μ_{eff} is 3.5% and the largest deviation in the estimate of attenuator thickness is 7%.

It has been demonstrated that the computational model works accurately for a single composition attenuator and on CR and DDR units of two different manufacturers. This suggests that as long as the data required for the computational model's LUTs can be measured, and provided the system has a stable calibration for DDI and STP as it should [101], the computational model could be applied to any x-ray system. This is important, given the aim to develop a computational model that could be used to assist with dose audit of paediatric radiographic examinations.

The model must now be modified to account for attenuators composed of multiple materials if it is to be clinically useful. Chapter 5 considers the case of multi-composition phantoms.

Chapter 5 – considerations relating to patients

Overview

This chapter considers the implications for the computational model from using it on patients, who are significantly different from the single composition attenuators investigated so far. Use on patients has no effect on the estimate of initial air kerma, k_0, but its potential effect on the estimate of the kerma at the image receptor, k_d, is investigated. The effect on the estimate of the effective linear attenuation coefficient, μ_{eff}, is expected to be significant; this is thoroughly investigated for examinations of the abdomen, chest and pelvis. The necessary additions to the existing look up tables are presented.

5.1 Introduction

It was demonstrated in chapter 4 that the computational model can be used to accurately estimate the thickness of an attenuator with a single composition. If it is to be used to estimate the thickness of a patient, the model must also be able to account for attenuators composed of multiple and varied tissues. This chapter identifies the distinct tissue types of most relevance to x-ray examinations of the chest, abdomen and pelvis and assesses the effect of each on the estimate of effective linear attenuation coefficient, μ_{eff}, and tissue thickness. To assess the expected range in values of μ_{eff} from patient to patient, the natural variation in individual tissue thickness and total patient thickness from patient to patient is investigated in a retrospective study of chest, abdomen and pelvis computed tomography (CT) examinations. The data from the patients in these CT examinations are then added to the Monte Carlo model presented in chapter 2. Monte Carlo simulations were then run with models created using the data from the patients in the CT examinations to assess the expected variation in values of μ_{eff} from x-ray examinations of patients with a range of sizes and body habitus. The effect on the estimate of kerma at the image receptor, k_d, as a result of the variation in individual tissue and total patient thickness is also investigated using Monte Carlo techniques.

5.2 Choice of examination

When it first proposed a measurement of patient thickness as part of a method for paediatric dose audit, the National Radiological Protection Board's (NRPB) report R318 [40] considered four paediatric x-ray examinations. These were skull, chest, abdomen and pelvis examinations. Radiographic examinations of the skull are no longer routinely undertaken; the availability, sensitivity and specificity of CT examinations mean patients

that would have been referred for skull radiographs are referred for CT examinations instead. This is reflected in National Institute for Health and Care Excellence (NICE) guidelines [111], which recommend CT examinations for all assessment of head pathology or injury. Examinations of the chest, abdomen and pelvis are still relevant for the paediatric population. Each of these will be considered in this chapter.

Whilst the aim of this work is to develop, optimise and validate a tool for estimating the thickness of a patient to assist with paediatric patient dose audit, the feasibility of using the computational model to estimate the thickness of a patient will have to be assessed with a cohort of adult patients. NHS Tayside does not have any dedicated paediatric imaging facilities and has a low throughput of paediatric patients. Therefore, the data necessary to optimise and validate the computational model for paediatric patients is not available locally. However, the only difference between the application of the computational model for adult and paediatric patients are the absolute values of μ_{eff}. If it can be demonstrated that the methods used to derive values of μ_{eff} for adult patients are accurate, those same methods applied to a paediatric cohort will be equally accurate.

Monte Carlo simulations will be used to determine values of μ_{eff}. This requires the addition of one or more representative patients to the Monte Carlo model for each examination.

5.3 Existing computational phantoms for Monte Carlo simulations

There are many existing computational phantoms [112-123] available for use in Monte Carlo models. These computational phantoms represent adults and children of different ages, typically newborn, 1, 5, 10 and 15 years old. Voxelised computational phantoms [112-117] are based on segmented patient data. Mathematical computational phantoms

[118-122] are based on definitions of simple geometric shapes. One further computational model [123] is a hybrid of the two.

Voxelised phantoms are more realistic but are limited to the anatomy of the reference set, with no convenient means of varying patient anatomy or size. Mathematical phantoms can be manipulated to model anatomical variations but are less realistic. Both define organs to allow for estimates of organ and effective dose and the tissue properties for the individual organs can be changed as required.

This chapter considers the effect of varying patient size and composition on the μ_{eff}. The use of a single existing computational phantom only provides a value of μ_{eff} for a single patient diameter. The computational phantom could be changed to reflect a patient of a different diameter, however it is not obvious how to make this change. A larger patient could be created by adding layers of fat to the periphery of the existing phantom or by scaling the size of each individual organ upwards accordingly. Both would change the value of μ_{eff}, but it cannot be known if either would be relevant for a real patient.

For the reasons given above, the existing computational phantoms will not be used for this work. Instead, simple block phantoms will be used to simulate patients based on measurements of real patients taken from CT examinations undertaken at NHS Tayside. This will ensure that a representative range of patient size and composition is considered when assessing values of μ_{eff}, though it does sacrifice anatomical accuracy.

5.4 Considerations relating to the estimate of effective linear attenuation coefficient

5.4.1 Tissue types

For examinations of the chest, abdomen and pelvis, the compounds and tissue types that will be encountered by the x-ray beam are air, bone, blood, skeletal muscle, soft tissue (including bowel, intestine, kidneys, liver etc), water, lung tissue, breast tissue and adipose tissue [124]. The International Commission on Radiation Units and Measurements' (ICRU) report 44 [125] gives a chemical composition for all of these materials, except bone, meaning they can be added to the Monte Carlo code and used in simulations. Bone is more complex as there are two types, cortical and cancellous. Cortical bone is found in the shaft of long bones and in the periphery of joints and vertebrae around the cancellous bone within [124]. The bony structures that need to be simulated in the chest, abdomen and pelvis cannot be regarded as being made of only cortical bone as there is a significant quantity of cancellous bone present as well (the relative proportions vary with the shape of the bone [124]). ICRU report 44 [125] presents a material intended to mimic a composite of cortical and cancellous bone called spongiosa. Spongiosa comprises 33% cortical bone and 67% marrow by mass, where the marrow is assumed to be 50% red marrow and 50% yellow marrow by mass [125]. It has a density of 1180kg m^{-3}, significantly less than that of cortical bone (1920kg m^{-3}) and greater than that of bone marrow (1030kg m^{-3} for red marrow and 980kg m^{-3} for yellow marrow). The elemental composition for spongiosa is provided in ICRU report 44 [125] allowing it to be added to the Monte Carlo code.

Any change to the composition, total thickness or the relative thickness of the different compounds in an attenuator will change the value of μ_{eff}. As an illustrative exercise, the linear attenuation coefficient (μ) for the most relevant tissues for x-rays of the chest, abdomen and pelvis were obtained from the National Institute of Standards and

Technology (NIST) database [97] using the compositions recommended in ICRU report 44 [125]. The data for spongiosa came directly from ICRU report 44 [125]. These are shown in figure 5-1.

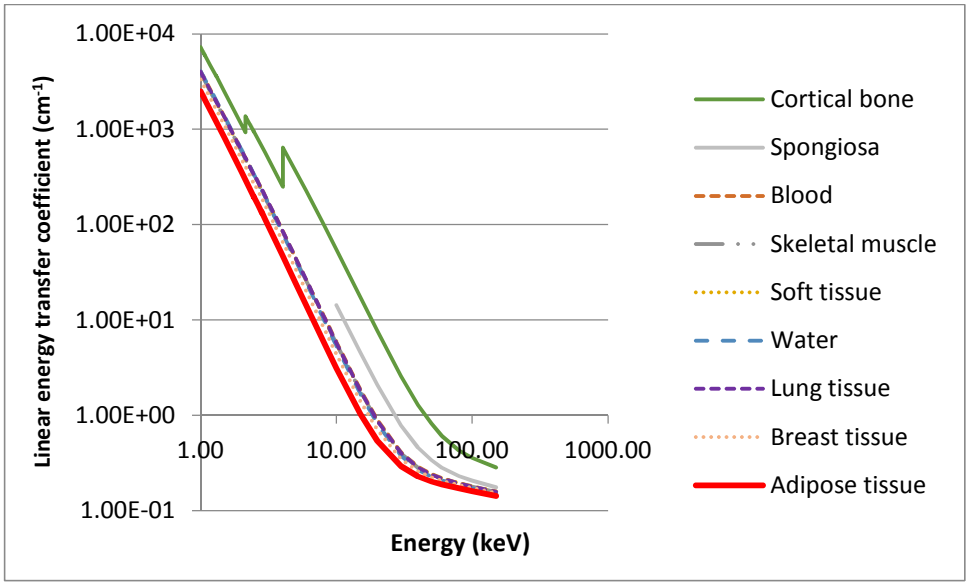

Figure 5-1: the linear attenuation coefficients with photon energy for tissues found in the chest, abdomen and pelvis

Figure 5-1 shows a range of μ values for tissues found in the chest, abdomen and pelvis. The estimate of patient thickness will be very sensitive to the relative proportion of each tissue type. To evaluate the effect each compound or tissue type has on the estimate of attenuator thickness, indicative estimates of attenuator thickness were made for each compound or tissue type. Each estimate used a $\frac{k_d}{k_0}$ of 0.1 and the μ value for an x-ray energy of 80keV. The results are shown in table 5.1

Compound or tissue type	Attenuator thickness (mm)
Cortical bone	53.8
Spongiosa	100.1
Blood	118.9
Skeletal muscle	120.3
Soft tissue	119.2
Water	125.3
Lung tissue	120.1
Breast tissue	124.9
Adipose tissue	134.7

Table 5.1: thickness required to attenuate an 80keV x-ray beam by 90% for each compound or tissue type

As is expected and as shown in table 5.1, the μ values for blood, skeletal muscle, soft tissue and lung tissue are sufficiently close that there is only a very small difference in the estimated attenuator thickness required to achieve $\frac{k_d}{k_0}$ = 0.1 (average thickness 119.6mm, maximum deviation for any single compound or tissue type 0.7mm). These values are close enough that for a Monte Carlo simulation undertaken to estimate values of μ_{eff} there is no need to differentiate between these tissues; soft tissue can be used to represent all of them. This is not true of water, breast tissue, adipose tissue, cortical bone or spongiosa, where the difference in μ leads to considerable differences in the estimated attenuator thickness required to achieve $\frac{k_d}{k_0}$ = 0.1. These tissues need to be explicitly included in a Monte Carlo simulation to estimate values of μ_{eff}, where present. This is clearly true of air as well.

In all of the Monte Carlo simulations that are presented throughout chapter 5, spongiosa was used as the material for all bone. All blood, skeletal muscle, soft tissue and lung tissue was simulated using the ICRU report 44 [125] composition of soft tissue which is already

included in the Monte Carlo code. The ICRU report 44 [125] composition of adipose tissue was used to add it to the Monte Carlo code. The proportion of adipose tissue was considered separately for each clinical site. The air in the lungs, and where encountered elsewhere in the body, was simulated as air.

5.4.2 Patient variation

For any single clinical site and x-ray projection, the composition of tissues the x-ray beam will pass through are known but the actual amount of each tissue will vary from patient to patient. There are many reasons why one patient might be larger or smaller than another, including differences in the amount of skeletal muscle, adipose tissue, air (as a result of bloating, for example), organ size or skeletal size. The estimate of μ_{eff} is dependent upon patient composition and will vary with the relative proportion of these tissues. The range of μ_{eff} values must be assessed to consider the implications for the computational model, but this must be for relative proportions of tissues that are clinically relevant. The only way of determining the clinically relevant range of thicknesses for each tissue encountered from patient to patient is to measure it. This was investigated using a series of CT images of the chest, abdomen and pelvis obtained from examinations undertaken at Ninewells Hospital in 2018. For chest, abdomen and pelvis examinations, 50 sequential patients who had undergone the examination in 2018 and who met the inclusion criteria were identified using the local Radiology Information System (RIS). The inclusion criteria were patients aged 18 or older and a mix of 25 male and 25 female patients. A filter was applied to the search on the RIS to return only patients that met the inclusion criteria.

For each examination, the slice that is most representative of the centreline for positioning the anterior-posterior (AP) radiographic projection was located in the z-axis and measurements of the thickness of each tissue along a path in the y-axis at the centre of the

x-axis (with axes as defined in figure 5-2) were made using the distance measurement tool on the Carestream Picture Archive and Communication System (PACS).

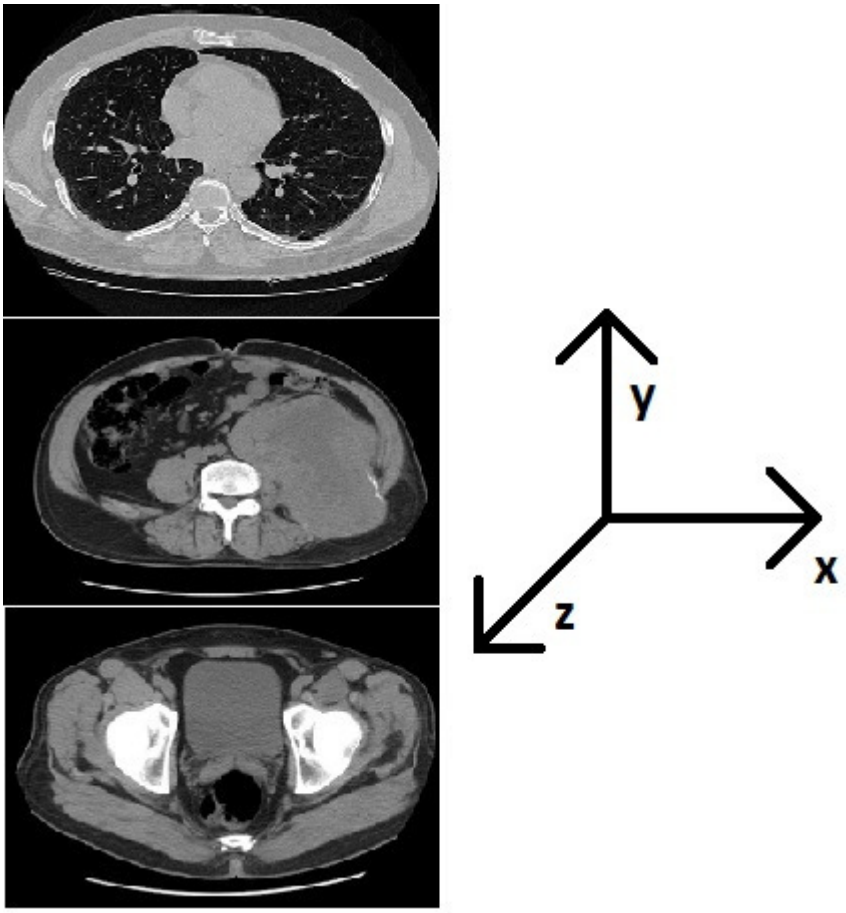

Figure 5-2: the definition of the x, y and z-axes with reference to the CT images used to measure the thickness of individual tissues. The images are only indicative, and are from publicly available studies hosted on The Cancer Imaging Archive (TCIA) [126]

The identification of the patients and the subsequent measurements of tissue thickness were made under an NHS Tayside Caldicott approval granted in accordance with NHS Tayside clinical governance procedures in October 2014. The approval runs for the duration of this project and is contingent upon no patient identifiable information being used or stored.

5.5 Estimating effective linear attenuation coefficient for each examination

Values of μ_{eff} can be estimated from Monte Carlo simulations where the simulated patients are constructed based on the measurements of actual patient tissue thicknesses. In §3.3.3.3 it was shown that the relationship between attenuator thickness and $\frac{k_d}{k_0}$ could be used to optimise an estimate of μ_{eff} for exposures of a single composition attenuator. To determine whether or not this was also true for a multi-composition attenuator, the value of $\frac{k_d}{k_0}$ was also calculated from the Monte Carlo simulations and the relationship between measured total patient thickness and $\frac{k_d}{k_0}$ considered. This was done for a) abdomen, b) chest and c) pelvis examinations.

5.5.1 Abdomen examinations

5.5.1.1 Study of patient size

Local NHS Tayside protocol is to align the centre of the x-ray beam for planar AP abdomen x-rays at the level of patient's iliac crest. Therefore, the iliac crest was located on CT scans of the abdomen for the 25 male and 25 female patients as described in §5.4.2. Measurements of the total AP thickness along the centreline (shown in red in figure 5-3) and of groups of similar tissues along the same path (shown in blue in figure 5-3, offset from the centre for clarity) were made using the electronic callipers on the PACS.

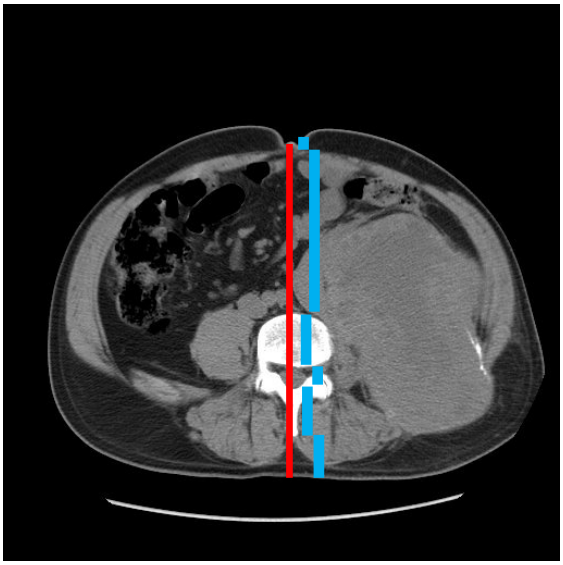

Figure 5-3: the location of the measurements of total (red line) and individual (blue lines, offset for clarity) tissue thickness through the centreline of a slice at the iliac crest. The representative image is from a study [127] hosted on TCIA [126]

The tissues were grouped together into the 6 distinct types shown by the blue lines in figure 5-3. The tissues were generally grouped as (from anterior to posterior); soft and adipose tissue (skin and fat), soft and adipose tissue (abdominal tissues and abdominal fat), bone (vertebra), soft tissue (spinal cord), bone (vertebra) and soft and adipose tissue (skin and fat).

The measurements outlined above were made for all 50 CT abdomen patients identified in §5.4.2. The results are shown in table 5.2.

Thickness (mm)	Skin / fat	Abdominal tissues	Vertebra	Spinal cord	Vertebra	Skin / fat	Total
Average ± Std Dev	24.3 ± 9.8	112.4 ± 33.4	35.6 ± 5.0	16.2 ± 8.3	30.6 ± 16.3	39.2 ± 16.3	258.4 ± 41.5
Median	25.3	113.3	35.5	15.6	31.4	36.7	260.4
Maximum	54.7	191.5	47.8	35.6	47.9	91.0	366.3
Minimum	8.5	41.2	26.8	9.5	13.4	16.7	176.8

Table 5.2: the results of the tissue and total patient thickness measurements undertaken for a study of 50 patient CT examinations of the abdomen

A t-test indicates that there are statistically significant differences (at the $p < 0.05$ level) between the male and female cohort. The p values for all tissues (from anterior to posterior) are as follows; the skin/fat ($p = 0.159$), soft tissue ($p = 0.017$), the vertebra ($p = 0.002$), the spinal cord ($p = 0.606$), the vertebra ($p = 0.072$), the skin/fat ($p = 0.005$) and the total thickness ($p = 0.261$).

This demonstrates that the differences between the male and female groups are such that the analysis should consider the entire sample and male and female cohorts separately.

5.5.1.2 Monte Carlo simulation of abdomen examinations

To assess the potential range of μ_{eff} values for the path of x-rays through the centreline of a patient at the iliac crest, each of the 50 patients in the study was modelled in a separate Monte Carlo simulation. The general form of the patient for each simulation is as shown in figure 5-4.

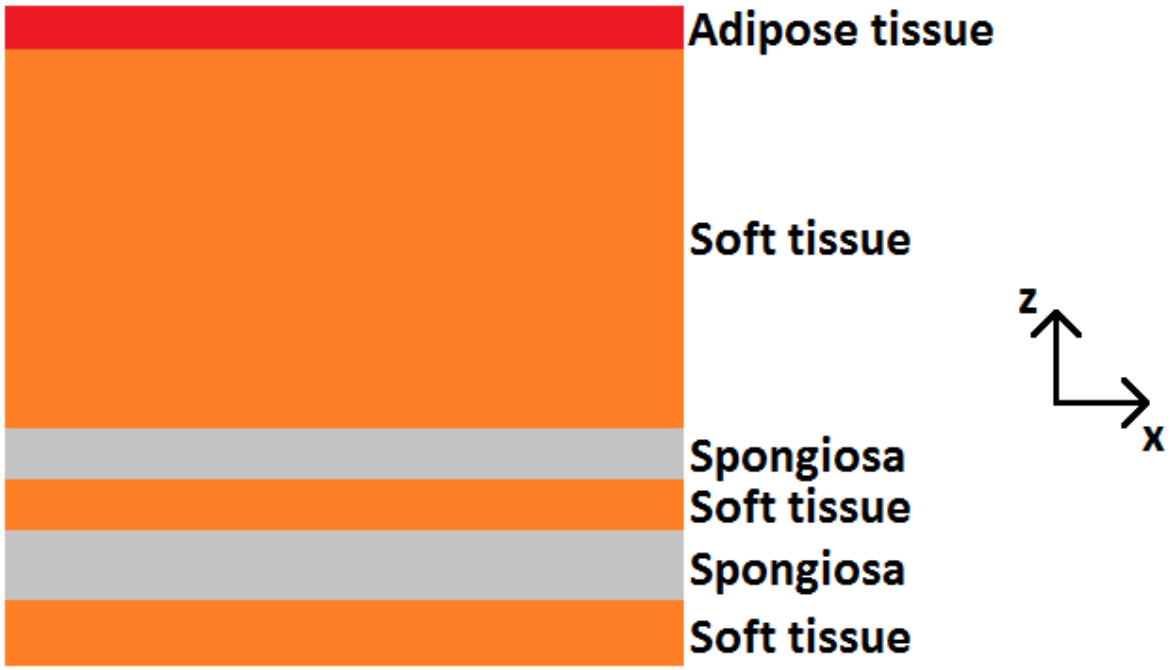

Figure 5-4: the general form of the patient's abdomen used in the Monte Carlo simulations, shown in the x-z axis

Each patient was modelled as a simple six layered block phantom which extended to 30cm in the x-axis. The first layer was simulated as adipose tissue. All humans have adipose tissue under the skin (subcutaneous), around the internal organs (visceral), in bone marrow, in muscle and in breast tissue [124]. Percentage body fat could be used as a surrogate for the amount of adipose tissue present. However, there is no single value or range for percentage body fat that is appropriate for everyone. Percentage body fat is known to be higher for females than males, increase with age, vary with ethnicity and significantly increase with body mass index (BMI) [124, 128]. A study in 2000 that evaluated the relationship between percentage body fat and BMI found that for a healthy BMI (the National Health Service (NHS) position is that a healthy BMI for adults is in the range of 18.5-24.9 [129]) percentage body fat varies from 26-30% for women and 14-18% for men in the 20-39 age range. Across all ages, ethnicities and BMIs, percentage body fat ranged from 8 – 43%. For all of the Monte Carlo simulated abdomen examinations, it was

decided to fix the percentage fat in the examination projection at 20%, the rationale being that this was a mid-range value from those in the literature [124, 128, 129]. To simulate this, adipose tissue was set at 20% of the total thickness of all adipose and soft tissues identified for each patient in the study (i.e. the thicknesses shown in columns 2, 3, 5 and 7 of table 5.2). The effect on the estimate of μ_{eff} of varying the percentage body fat was examined for abdomen examinations and follows in §5.5.1.4.

The totality of the spongiosa and soft tissue that followed was simulated as extending to the full 30cm width. Whilst it is acknowledged that the vertebrae do not extend so far from the centre-line, there is no means using BEAMnrc to simulate multiple materials in the x-y axis in a single slab of a simulation. The only alternative option would have been to have the spongiosa extending to 5cm in the x axis, with the remaining 25cm filled with air. This was thought to be less representative, since spongiosa is closer in its attenuation properties to soft tissue than air is. For completeness sake, different geometries are investigated in §5.5.1.5.

Simulations were run at 81kV_p and terminated when the statistical uncertainty was <10%. The simulated field size was 40x40cm at a 100cm FDD.

5.5.1.3 Simulation results for abdomen examinations

5.5.1.3.1 Values of effective linear attenuation coefficient

The values of μ_{eff} calculated from a region of 1cm x 1cm at the centre of scoring zone 3 (positioned 0.5cm from the exit of each simulated patient) for the simulations are summarised in table 5.3 and figure 5-5.

μ_{eff} (mm^{-1})	Male patients	Female patients	All patients
Average ± % Std Dev	0.0181 ± 2.8%	0.0178 ± 2.8%	0.0180 ± 2.9%
Minimum	0.0171	0.0168	0.0168
1st quartile	0.0179	0.0175	0.0176
Median	0.0181	0.0178	0.0180
Interquartile range	0.0006	0.0005	0.0008
3rd quartile	0.0185	0.0180	0.0184
Maximum	0.0190	0.0190	0.0190

Table 5.3: the values of effective linear attenuation coefficient, μ_{eff}, calculated from the simulations of abdomen examinations, grouped by male patients, female patients and all patients

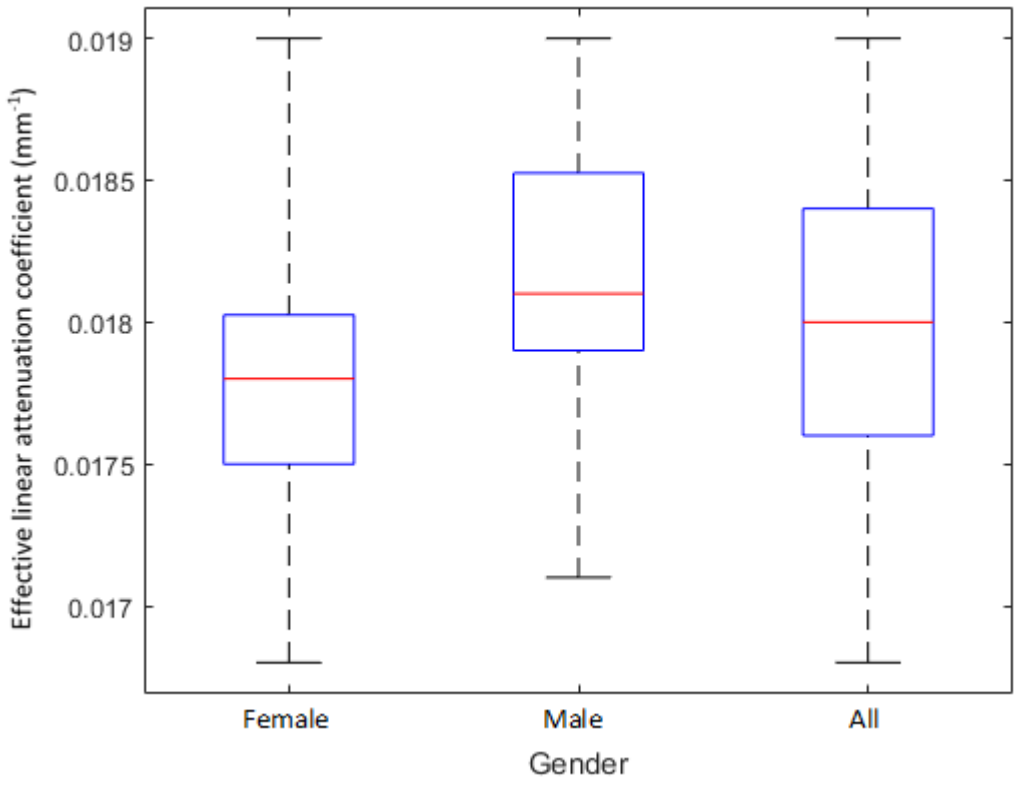

Figure 5-5: minimum, first quartile, median, third quartile and maximum values of effective linear attenuation coefficient, μ_{eff}, for abdomen examinations of female, male and all patients

As shown in table 5.3 and figure 5-5, there is little variation in μ_{eff} across the 50 simulations and no clear outliers. Values of μ_{eff} for the male and female patient cohorts were compared with a t-test. There was a statistically significant difference between the two at the $p < 0.05$ level ($p = 0.015$). Although the absolute difference between the values of μ_{eff} for the male and female patient cohorts is small, this suggests that separate gender specific values should be applied.

To determine whether the relationship between total patient thickness and $\frac{k_d}{k_0}$ can be used to optimise values of μ_{eff} for an examination, the relationship between measured total patient thickness and $\frac{k_d}{k_0}$ is shown in figure 5-6.

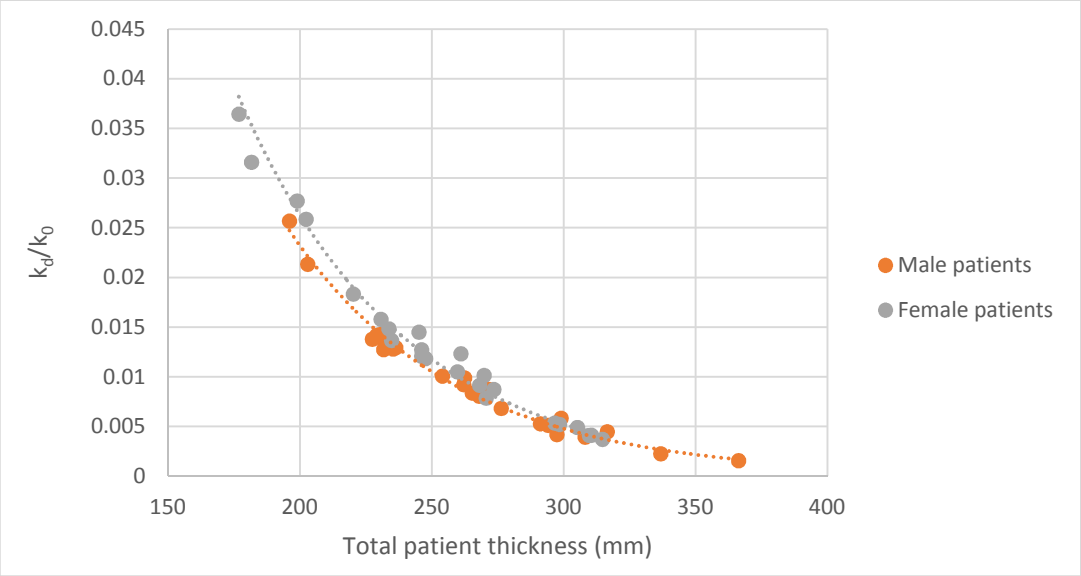

Figure 5-6: the relationship between measured total patient thickness and the calculated $\frac{k_d}{k_0}$ for each abdomen examination, grouped by male and female patients

Figure 5-6 shows a general exponential trend between the measured total patient thickness and the calculated $\frac{k_d}{k_0}$ for each abdomen examination for both male and female patients. This is expected given the exponential fit between attenuator thickness and calculated $\frac{k_d}{k_0}$ demonstrated for single composition attenuators in §3.3.3.3. The correlation

coefficient (r^2) for an exponential fit made using Matlab is 0.980 for male patients and 0.983 for female patients. This suggests that it will be possible to choose the value of μ_{eff} for an abdomen examination based on the ratio of $\frac{k_d}{k_0}$ as was the case with the single composition attenuator, provided there is a clear relationship between the total patient thickness and μ_{eff}.

The relationship between measured total patient thickness and the μ_{eff} calculated for each patient from Monte Carlo simulation is shown in figure 5-7.

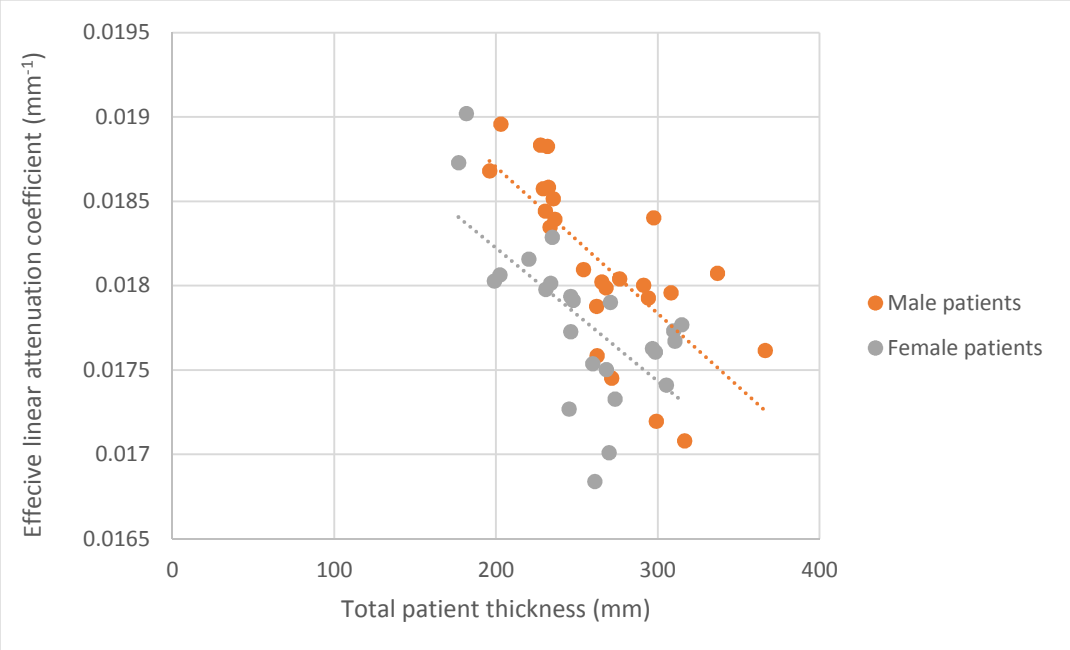

Figure 5-7: the relationship between measured total patient thickness and effective linear attenuation coefficient, μ_{eff}, for each abdomen examination, grouped by male and female patients

Figure 5-7 shows a general downward trend in μ_{eff} with increasing total patient thickness. A linear fit to this data can be used to optimise the value of μ_{eff} used for an examination based on the total patient thickness estimated from the ratio of $\frac{k_d}{k_0}$. Linear fits using Matlab had a correlation coefficient (r^2) of 0.521 for male patients and 0.429 for female patients.

5.5.1.3.2 Estimates of patient thickness

Estimates of total patient thickness were made for all 50 patients using equation 3.1 (§3.1), the optimised value of μ_{eff} derived using the gender-specific relationships shown in figures 5-6 and 5-7 and the ratio of $\frac{k_d}{k_0}$ calculated from the Monte Carlo simulation for each patient as shown in figure 5-6. This will help to determine the extent of the uncertainty when using the computational model on AP abdomen examinations. The percentage deviation from the estimated thickness and the thickness measured using the PACS for each patient is shown in figure 5-8. The patients have been ordered on the deviation between the estimated and known thicknesses.

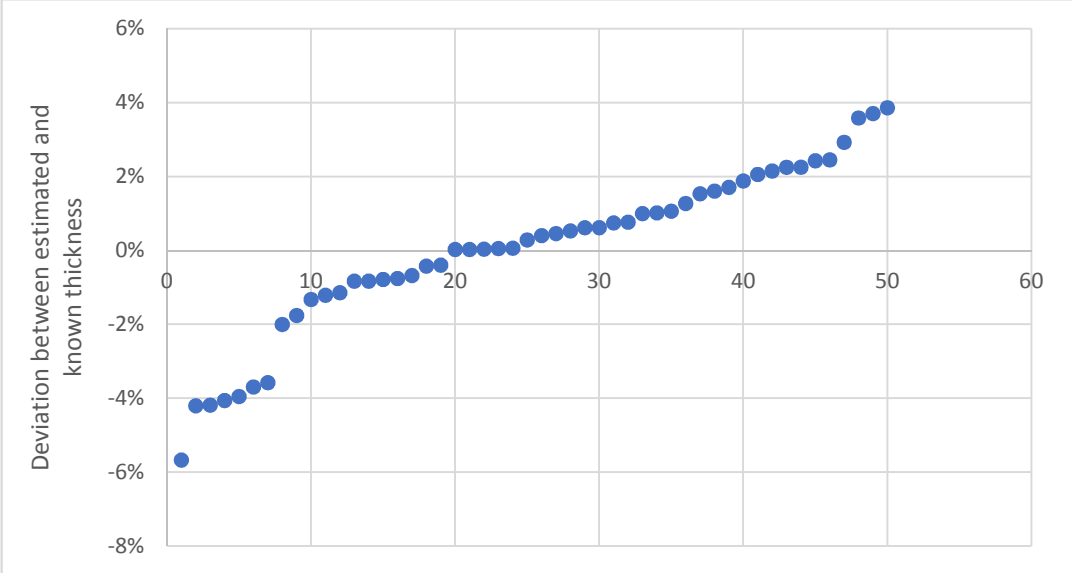

Figure 5-8: the percentage deviation between values of patient thickness estimated using optimised values of effective linear attenuation coefficient, μ_{eff}, and the measured total patient thickness for 50 abdomen CT examinations

The estimates are all acceptable. Of the 50 patients considered, the estimate of patient thickness is within 5% of the true value for 49 of them, and within 6% for all of them. In terms of absolute deviation between the estimated and true patient thickness, in 43 cases it is within 10mm and in all cases it is within 15mm.

There is a potential limitation in this method of determining the accuracy of the estimates of patient thickness that must be acknowledged. The estimates were made on the same group of 50 patients that were used to create the relationships between μ_{eff} and $\frac{k_d}{k_0}$ and total patient thickness. Crucially however, the estimate for each individual patient used the value of μ_{eff} as derived from those relationships and not that which was directly simulated for that patient. The creation of an additional 50 Monte Carlo simulations based on an entirely new group of 50 patient's abdomen CT examinations would have been a more robust validation of the technique for estimating patient thickness as the test data would have been independent of the data used to create the model. However, the implicit assumption made here – and that which is made during all patient dose audits used to derive reference levels – is that any two similarly sized large samples from the same general population can be regarded as similar.

To test this assumption, the variation in the effective diameter of 807 patients that had undergone abdominal CT examinations locally was assessed. Effective diameter is a concept proposed by the American Association of Physicists in Medicine (AAPM) in their report 204 [130]. It is defined as the diameter of the circle whose area is equal to the patient cross section, and so it is a good measure of patient size variation. The average of 50 randomly selected values of effective diameter from the 807 available was calculated. The random selection used the 'RANDBETWEEN' function of Microsoft Excel (Microsoft Corporation, Redmond, WA). The average of a further 49 selections of 50 randomly selected values of effective diameter from the 807 available was then calculated. This produced 50 average values of effective diameter, each calculated using a randomly selected sample of 50 values of effective diameter. The average of the 50 averages was 30.24cm, with a standard deviation of only 0.599, a minimum of 28.93cm and a maximum of 31.24cm. This is evidence of a very low variation in the average of similarly sized large

samples from the same general population which supports the view they can be regarded as similar.

Therefore, it is assumed for the purpose of this validation that the accuracy of the estimate of patient thickness will be similar for any other similarly sized group of patients having undergone an abdomen CT examination and no further Monte Carlo simulations have been created. The validity of this assumption will be further tested in the clinical validation study presented in chapter 6.

5.5.1.4 The effect of varying percentages of adipose tissue

Percentage body fat varies significantly from patient to patient. As described in §5.5.1.2, all of the simulations undertaken so far have assumed a 20% body fat ratio, implemented in Monte Carlo simulations by creating a patient with a thickness of adipose tissue that is equal to 20% of the total thickness of all adipose and soft tissues. To assess the effect of varying percentages of body fat, every Monte Carlo simulation for the abdomen examinations was re-run using a thickness of adipose tissue that varied from 5 – 90% of the total thickness of adipose and soft tissues in 5% increments and a value for μ_{eff} calculated from each simulation. No other changes were made to the Monte Carlo simulations, which were run as before until the statistical uncertainty was <10%. The average value of μ_{eff} from all 50 simulations at each percentage body fat normalised to the value of μ_{eff} for 20% body fat is shown in figure 5-9.

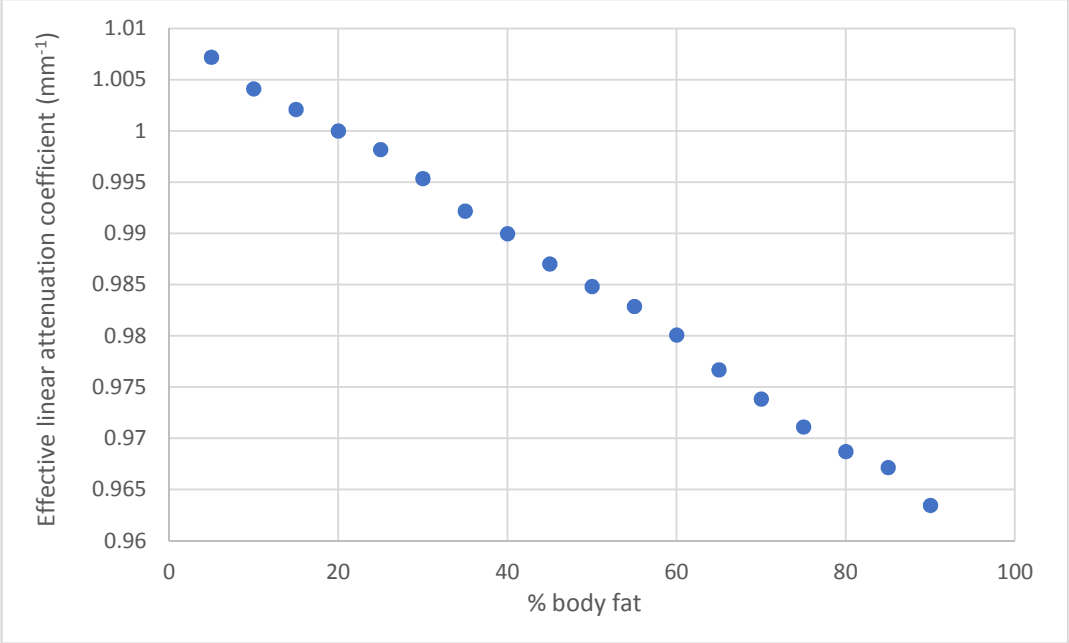

Figure 5-9: the average calculated effective linear attenuation coefficient, μ_{eff}, from Monte Carlo simulations of all abdomen patients undertaken using body fat percentages varying in 5% increments, each normalised to μ_{eff} for 20% body fat

As figure 5-9 shows, there is little variation in μ_{eff} as a result of even significant changes to the body fat percentage used in the simulations. For a k_d of 4μGy and using the average ratio of $\frac{k_d}{k_0}$ from all 50 abdomen patient simulations in §5.5.1, the estimated patient thickness calculated using equation 3.1 with the μ_{eff} from a 50% body fat simulation is 248.1mm. Using the μ_{eff} from a 5% body fat simulation gives 242.7mm and using the μ_{eff} from a 90% body fat simulation gives 253.8mm. With a maximum difference of 11.1mm (i.e. 4.6%) from the two most extreme values of body fat, this is clearly not a significant source of uncertainty. Anatomical variation and differences in bone thicknesses from patient to patient have a greater effect on the estimate of μ_{eff}. Simulations undertaken for this work will continue to use a 20% value of body fat.

5.5.1.5 Assessing the impact of varying patient geometry in BEAMnrc simulations

As acknowledged in §5.5.1.2, the model used to represent a patient in the Monte Carlo simulations cannot be considered representative as the spongiosa extends across the entire patient width. This is because of limitations in the creation of attenuating objects in BEAMnrc. To assess the impact of different patient geometries on the simulated values of μ_{eff}, two further geometries were created for 6 of the 50 abdomen CT patients. Patients 1-6 were chosen, which ensured 3 male and 3 female patients were included in the sample. The different geometries are shown in figure 5-10(a&b).

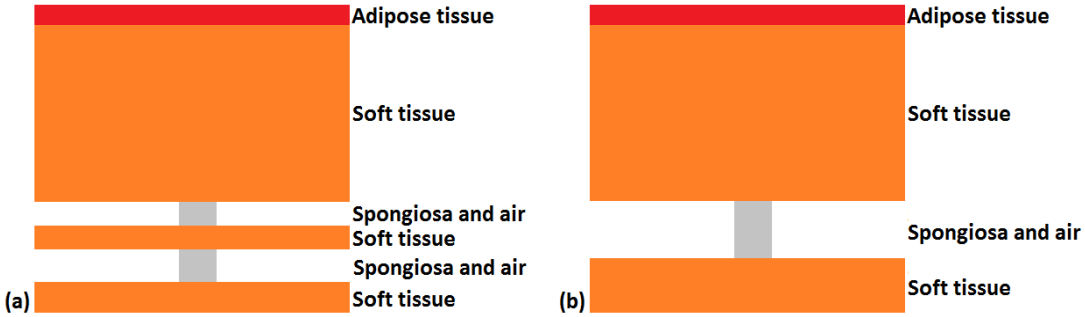

Figure 5-10: the revised abdomen geometries used in the BEAMnrc simulations. (a) places air either side of a central column of spongiosa, (b) combines the two layers of spongiosa and air into a single layer and combines the two most-posterior layers of soft tissue into a single layer of soft tissue

Figure 5-10(a) shows a patient geometry that is the same as used throughout §5.5.1.2 but with air on either side of a central column of the spongiosa representing the vertebrae. A 5cm width (extending 2.5cm either side of the centreline) was chosen as the median value of measured vertebrae width in the abdomen patient cohort. Figure 5-10(b) shows a patient geometry that combines the two layers of spongiosa with air on either side to limit the effect of having a layer of air so close to the exit surface of the attenuator. Note that the total patient thickness, as well as the corresponding contributions of adipose tissue, soft tissue and spongiosa, for patients 1-6 in the geometries shown in figures 5-10(a&b) were kept constant. Monte Carlo simulations were run at 81kV$_p$. Other than the changes

to patient geometry, there were no changes to those simulations run as described in §5.5.1.2.

The results for the simulated values of μ_{eff} are shown in table 5.4.

Patient number	Effective linear attenuation coefficient, μ_{eff} (mm^{-1})		
	Full width spongiosa (§5.5.1.2)	5cm spongiosa width (figure 5-10(a))	5cm spongiosa width (figure 5-10(b))
1	0.0180	0.0205	0.0191
2	0.0179	0.0184	0.0183
3	0.0184	0.0191	0.0191
4	0.0176	0.0185	0.0184
5	0.0175	0.0180	0.0171
6	0.0174	0.0185	0.0184

Table 5.4: the effective linear attenuation coefficients, μ_{eff}, calculated from the results of Monte Carlo simulations of patients 1-6 using three different patient geometries

As expected, the estimates of μ_{eff} from the simulations using the revised geometries for the abdomen are in general consistently higher than that of the original geometry. This is consistent with a greater attenuation. The absolute values of μ_{eff} are similar to those for the original simulations, meaning there is little difference in the estimated attenuator thickness as a result of using the revised estimates of μ_{eff}. Using a $\frac{k_d}{k_0}$ of 0.1, the maximum difference in estimated patient thickness for patient 1 was 15mm, but for patients 2-6 it was less than 7mm for both revised geometries shown in figure 5-10. It is concluded that whilst none of the geometries used to represent that abdomen in the Monte Carlo simulations are representative, the differences do not have a significant effect on the estimates of μ_{eff} and, by extension, patient thickness. The revised geometries will not be considered further, since this confirms the hypothesis in section §5.5.1.3.2.

5.5.1.6 Thickness estimation away from the centreline

As noted in §5.4.1, bone is one of the materials most likely to add to the uncertainty in the estimate of patient diameter as small variations in bone thickness and density from patient to patient have a more significant effect on the accuracy of the estimated value of μ_{eff} used by the computational model than any other tissue.

As the only bone in the abdomen is the vertebrae, there is the potential to estimate the patient thickness of an off-centre path through the patient that avoids all bone. As there will only be adipose and soft tissue to consider along the path of primary x-ray transmission (it is acknowledged that there will remain a contribution of scattered x-rays from the vertebrae), the variation in μ_{eff} across the 50 patients may reduce.

Corresponding values of k_0 can be calculated for an off-centre position using the anode-cathode output variations measured and simulated in §2.5.4.1. If the off-centre measurement is made to the cathode side the uncertainty in the estimate of k_0 for the precise position of the measurement is significantly reduced as the kerma shows little variation.

To assess the potential for reduced variation in estimated μ_{eff} values across the patient sample, off-axis estimates of μ_{eff} were made for patients 1-6 for the revised geometries shown in figure 5-10(a&b). Measurements were made 10cm from the centreline in the direction of the cathode. Patient thickness was measured to be on average 30mm lower at 10cm from the centreline than along the centreline.

The estimated μ_{eff} for each patient from each analysis is shown in table 5.5.

	Effective linear attenuation coefficient, μ_{eff} (mm^{-1})		
		10cm off-axis	
Patient	Original	Geometry as figure 5-10(a)	Geometry as figure 5-10(b)
1	0.0180	0.0128	0.0127
2	0.0179	0.0117	0.0115
3	0.0184	0.0135	0.0131
4	0.0176	0.0135	0.0134
5	0.0175	0.0125	0.0125
6	0.0174	0.0144	0.0142

Table 5.5: the effective linear attenuation coefficients, μ_{eff}, calculated from the results of Monte Carlo simulations of patients 1-6 measured 10cm from the centreline towards the cathode

The estimates of μ_{eff} from the measurements made 10cm towards the cathode from the centreline are consistently lower than that of the original simulation with measurements made along the central axis. This is consistent with a lower attenuation. It was anticipated that there might be a lower range of μ_{eff} values measured off-centre, however this is not the case. The range of μ_{eff} values for patients 1-6 along the centreline was 0.001, whereas at 10cm from the centreline it was 0.0027 for both geometries shown in figure 5-10(a&b). Whilst μ_{eff} values were only calculated for 6 patients, these results seem to indicate that there is little to be gained in trying to avoid bone along the path of estimated thickness. Furthermore, a measurement of patient thickness in an off-centre location, as will be necessary in the clinical validation study presented in chapter 6, is more difficult to make. Discussion with radiographer colleagues highlighted the practical issues this would present. The off-centre thickness estimation will not be considered further.

5.5.2 Chest examinations

5.5.2.1 Study of patient size

Local NHS Tayside protocol is to align the centre of the x-ray beam for planar AP chest x-rays at the base of the patient's sternum. The base of the sternum was located on CT scans of the chest for 25 male and 25 female patients as described in §5.4.2. Measurements of the total AP thickness along the centreline (shown in red in figure 5-11) and of groups of similar tissues along the same path (shown in blue in figure 5-11, offset from the centre for clarity) were made using the distance measurement tool on the PACS.

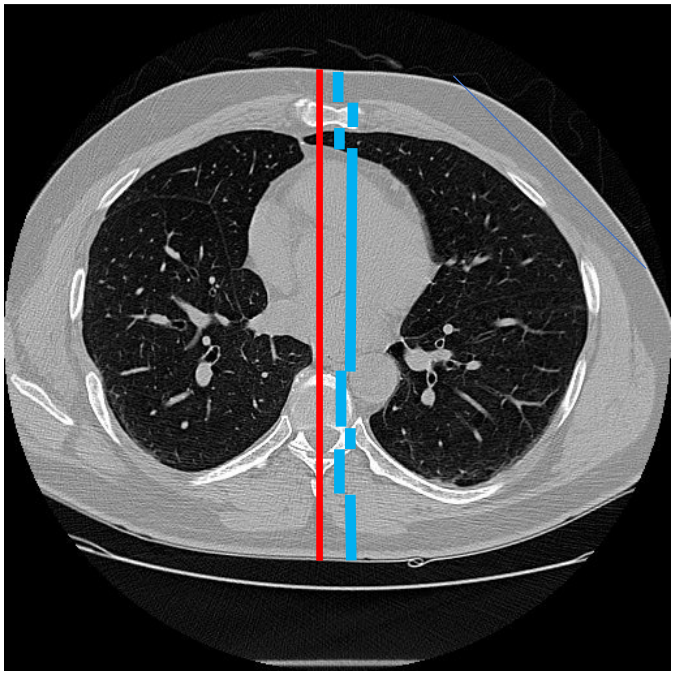

Figure 5-11: the location of the measurements of total (red line) and individual (blue lines, offset for clarity) tissue thickness through the centreline of an image at the base of the sternum. The representative image is from a study [131] hosted on TCIA [126]

The tissues were grouped together into the 8 distinct types shown by the blue lines in figure 5-11. The tissues were generally grouped as (from anterior to posterior); soft (skin) and adipose tissue (fat), bone (sternum), air (within the lungs), soft tissue (heart) mixed

with adipose tissue (abdominal fat), bone (vertebra), soft tissue (spinal cord), bone (vertebra) and soft (skin) and adipose tissue (fat).

These measurements were made for all 50 CT chest patients identified in §5.4.2. The results are shown in table 5.6.

Thickness (mm)	Skin / fat	Sternum	Lung / air	Heart / soft tissue	Vertebra	Spinal cord	Vertebra	Skin / fat	Total
Average ± Std Dev	16.1 ± 7.7	11.2 ± 2.2	17.0 ± 7.6	123.2 ± 19.9	33.7 ± 10.8	13.9 ± 5.9	21.2 ± 4.6	25.8 ± 10.1	248.4 ± 30.1
Median	16.2	11.5	14.7	126.7	30.3	13.2	21.6	25.5	249.0
Maximum	34.2	15.3	33.1	163.9	75.9	50.7	29.4	47.9	322.1
Minimum	4.3	5.8	5.5	70.3	21.8	7.6	7.9	7.2	171.0

Table 5.6: the results of the tissue and total patient thickness measurements undertaken for a study of 50 patient CT examinations of the chest

A t-test indicates that there are statistically significant differences (at the $p < 0.05$ level) between the male and female cohort. The p values for all tissues (from anterior to posterior) are as follows; the skin/fat ($p = 0.018$), the sternum ($p = 0.002$), the lung/air ($p = 0.004$), the heart/soft tissue ($p = 0.003$), the vertebra ($p = 0.068$), the spinal cord ($p = 0.336$), the vertebra ($p = 0.016$) and the skin/fat ($p = 0.224$).

As with the abdomen, there are enough differences between the two that analysis should consider the entire sample and male and female cohorts separately.

5.5.2.2 Monte Carlo simulation of chest examinations

To assess the potential range of μ_{eff} values for the path of x-rays through the centreline of a patient at the base of the sternum, each of the 50 patients in the study was modelled in a

separate Monte Carlo simulation. The general form of the patient for each simulation is as shown in figure 5-12.

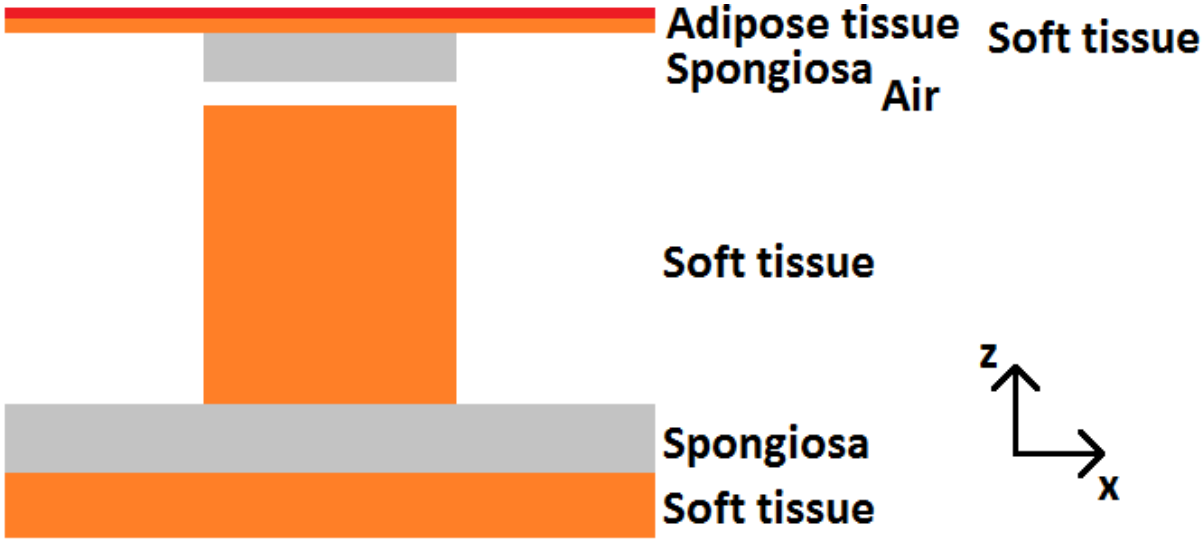

Figure 5-12: the general form of the patient's chest used in the Monte Carlo simulations, shown in the x-z axis

Each patient was created as a simple seven layered block phantom which extended to 30cm in the x-axis. The first layer was simulated as adipose tissue, which was fixed at 20% of the total thickness of all adipose and soft tissues identified for each patient in the study (i.e. the thicknesses shown in columns 2, 5, 7 and 9 of table 5.6).

The spongiosa used to simulate the sternum and the soft tissue used to simulate the heart both extended to only 5cm in each direction from the origin of the x-axis; this left an air-filled space on either side to simulate the lungs. The spongiosa used to simulate the vertebra and ribs and the soft tissue behind it both extended to the full 30cm in the x-axis.

Simulations were run at 81kV$_p$ and terminated when statistical uncertainty was <10%. The simulated field size was 40x40cm at a 100cm FDD.

5.5.2.3 Simulation results for chest examinations

5.5.2.3.1 Values of effective linear attenuation coefficient

The values of μ_{eff} calculated from a region of 1cm x 1cm at the centre of scoring zone 3 (positioned 0.5cm from the exit of the simulated patient) for the simulations are summarised in table 5.7 and figure 5-13.

μ_{eff} (mm^{-1})	Male patients	Female patients	All patients
Average ± % Std Dev	0.0200 ± 8.0%	0.0207 ± 9.4%	0.0204 ± 8.8%
Minimum	0.0134	0.0188	0.0134
1st quartile	0.0196	0.0199	0.0199
Median	0.0207	0.0205	0.0205
3rd quartile	0.0209	0.0209	0.0209
Maximum	0.0213	0.0294	0.0294

Table 5.7: the values of effective linear attenuation coefficient, μ_{eff}, calculated from the simulations of chest examinations, grouped by male patients, female patients and all patients together

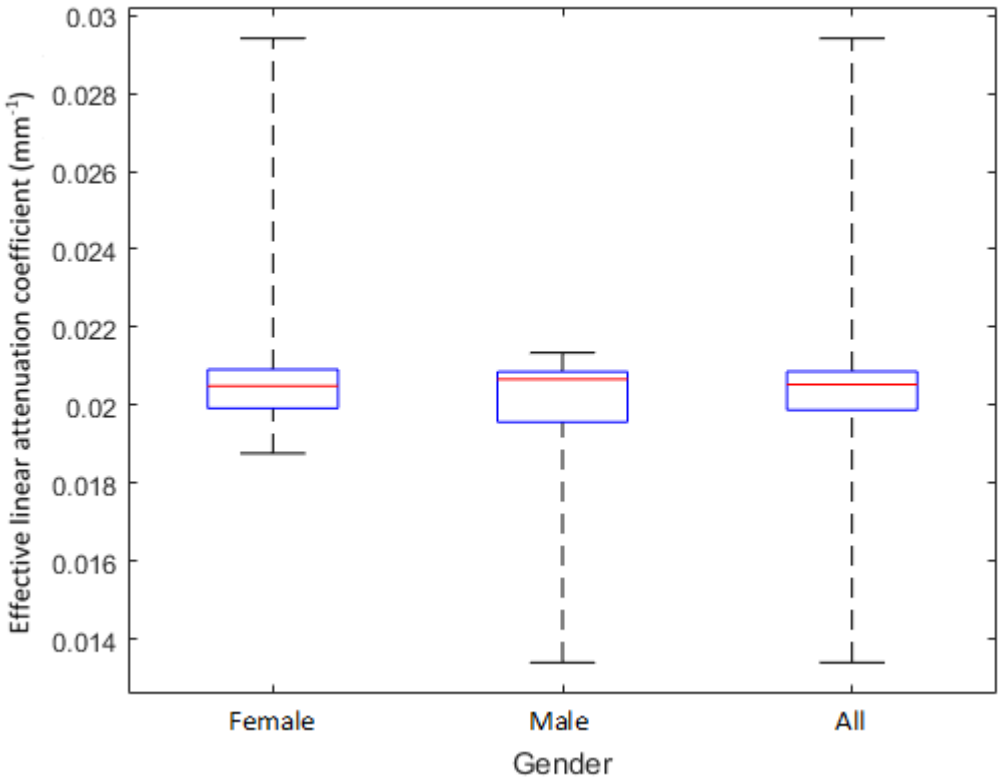

Figure 5-13: minimum, first quartile, median, third quartile and maximum values of effective linear attenuation coefficient, μ_{eff}, for chest examinations of female, male and all patients

As shown in table 5.7 and figure 5-13, there is, in general, little variation in μ_{eff} across the 50 simulations. There are two clear outliers – a male patient with a μ_{eff} of 0.0134mm^{-1} and a female patient with a μ_{eff} of 0.0294mm^{-1}. In both cases, the explanation lies in the ratio of the total thicknesses of bone and soft tissue. The male patient is in the 3rd quartile of total measured thickness, but the total thickness of his bones is less than for all other patients. As there is a greater contribution of less attenuating tissues, the μ_{eff} is reduced. The female patient is the smallest of all patients in terms of total measured thickness. However, the total thickness of her bones is average compared with all other patients. As there is a greater contribution of more attenuating tissue, the μ_{eff} is increased. Both of

these outliers are examples of the effect extreme anatomical variation can have on the estimate of μ_{eff}.

Values of μ_{eff} for the male and female patient cohorts were compared with a t-test. There was no significant difference between the two at the $p < 0.05$ level ($p = 0.33$). Despite the statistically significant differences in some of the individual tissue thicknesses identified in §5.5.2.1, there is no need to apply separate values for male and female patients.

To determine whether the relationship between total patient thickness and $\frac{k_d}{k_0}$ can be used to optimise values of μ_{eff} for an examination, the relationship between measured total patient thickness and $\frac{k_d}{k_0}$ is shown in figure 5-14.

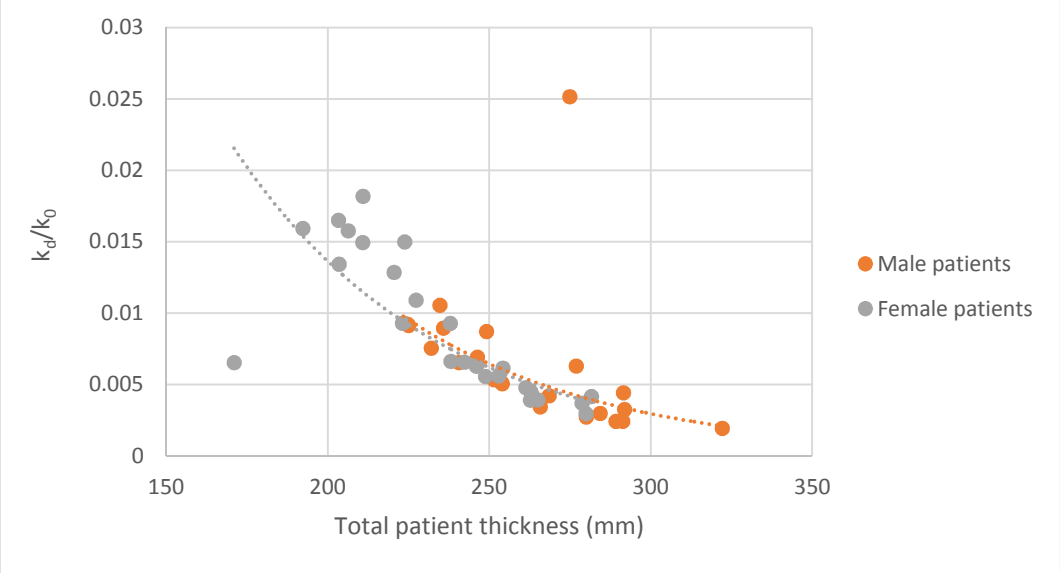

Figure 5-14: the relationship between measured total patient thickness and the calculated $\frac{k_d}{k_0}$ for each chest examination, grouped by male and female patients

Analysis of the data shown in figure 5-14 reveals a general exponential trend between the measured total patient thickness and the calculated $\frac{k_d}{k_0}$ for each chest examination for both male and female patients. The correlation coefficient (r^2) value for an exponential fit made using Matlab is 0.482 for male patients and 0.677 for female patients.

The relationship between measured total patient thickness and the μ_{eff} calculated for each patient from Monte Carlo simulation is shown in figure 5-15.

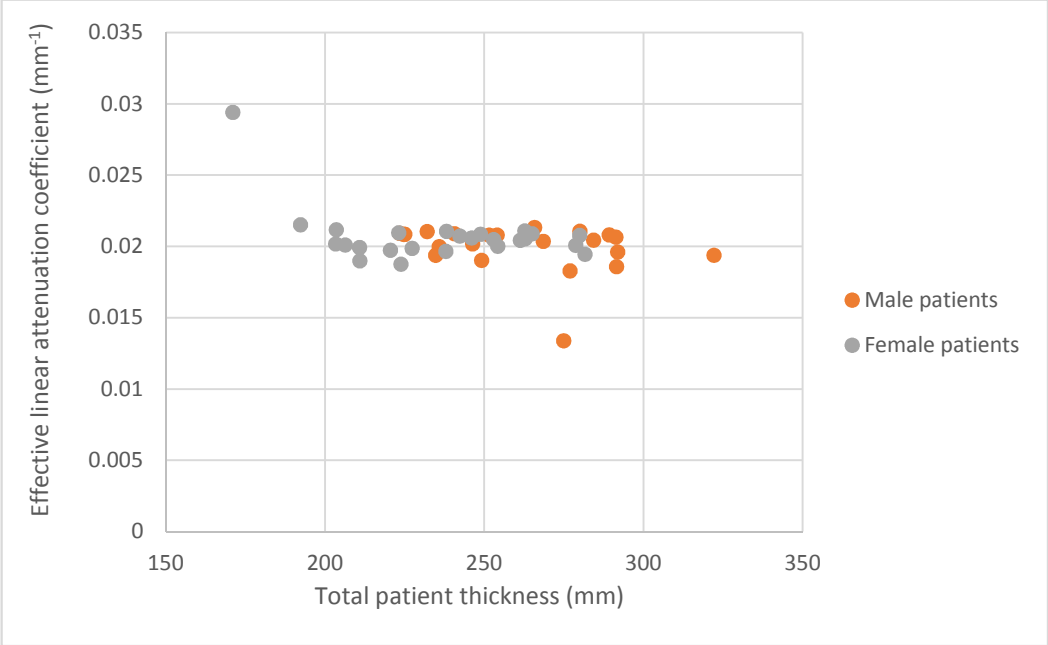

Figure 5-15: the relationship between measured total patient thickness and effective linear attenuation coefficient, μ_{eff}, for each chest examination, grouped by male and female patients

Figure 5-15 shows that other than the two outliers already identified from table 5.7, there is little variation in μ_{eff} with varying total patient thickness. This means that a single value of μ_{eff} can be used for all patients undergoing chest examinations and that there is nothing to be gained in trying to optimise the value of μ_{eff} based on the ratio of $\frac{k_d}{k_0}$.

5.5.2.3.2 Estimates of patient thickness

Estimates of total patient thickness were made for all 50 patients using equation 3.1 (§3.1), the median value of μ_{eff} for all patients as shown in table 5.7 and the ratio of $\frac{k_d}{k_0}$ calculated from the Monte Carlo simulation for each patient as shown in figure 5-12. This will help to

determine the extent of the uncertainty as a result of using a single value of μ_{eff} for all cases. The percentage deviation from the estimated thickness and the thickness measured on the PACS workstation for each patient is shown in figure 5-16.

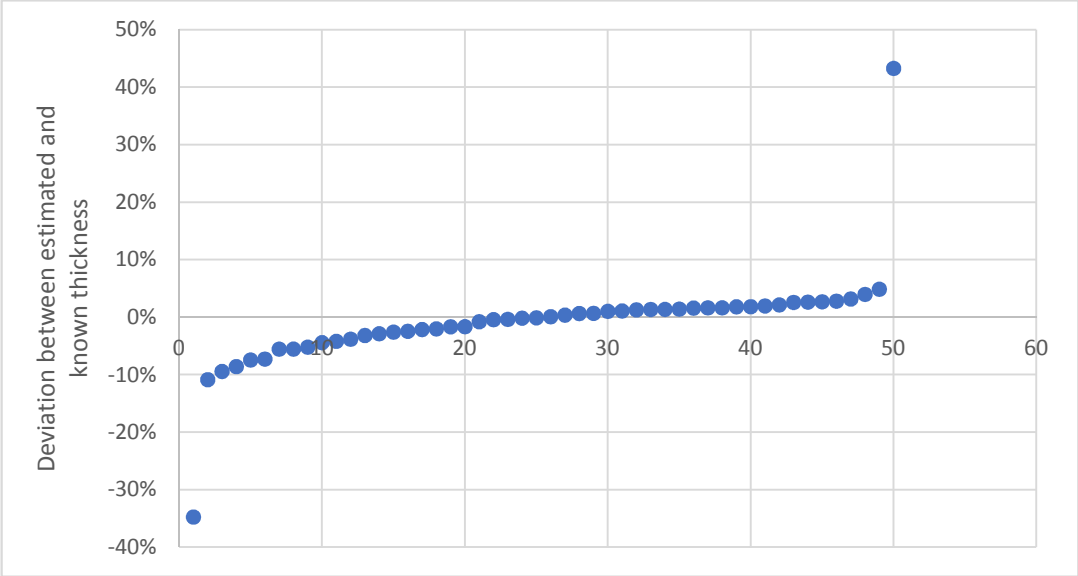

Figure 5-16: The percentage deviation between values of patient thickness estimated using the median value of effective linear attenuation coefficient, μ_{eff}, and the measured total patient thickness for 50 chest CT examinations

Two of the estimates are significantly incorrect; these correspond to the two patients already identified from table 5.7 and are a result of patient anatomy that is significantly different from the others in this patient cohort. Of the 50 patients considered, the estimate of patient thickness is within 5% of the true value for 40 of them. 47 of them are within 10% of the true value. In terms of absolute deviation between the estimated and true patient thickness, in 38 cases it is within 10mm and in 46 cases it is within 20mm.

This method for validating the accuracy of the patient thickness estimate has the same limitation as discussed in §5.5.1.3.2; namely that the estimates were made on the same group of patients used to create the relationships used by the model. As in §5.5.1.3.2, the

implicit assumption is that any two similarly sized groups from the same general population can be regarded as similar.

5.5.3 Pelvis examinations

5.5.3.1 Study of patient size

Local NHS Tayside protocol is to align the centre of the x-ray beam for planar AP pelvis x-rays at the top of the patient's femoral heads. The top of the femoral heads was located on CT scans of the pelvis for 25 male and 25 female patients as described in §5.4.2. Measurements of the total AP thickness along the centreline (shown in red in figure 5-17) and of groups of similar tissues along the same path (shown in blue in figure 5-16, offset from the centre for clarity) were made using the distance measurement tool on the PACS.

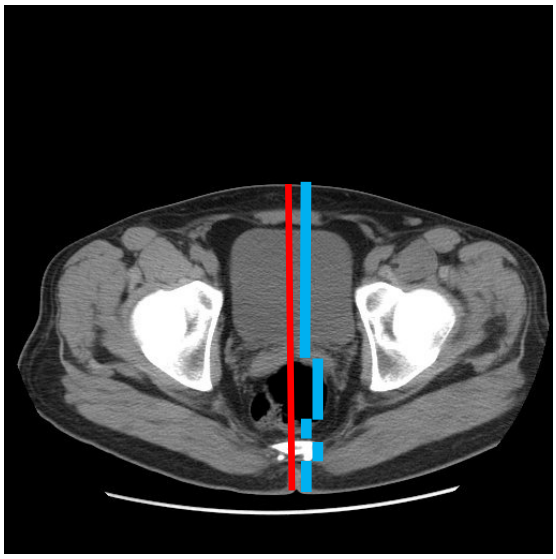

Figure 5-17: the location of the measurements of total (red line) and individual (blue lines, offset for clarity) tissue thickness through the centreline of a slice at the iliac crest. The representative image is from a study [127] hosted on TCIA [126]

The tissues were grouped together into the 5 distinct types shown by the blue lines in figure 5-17. The tissues were generally grouped as (from anterior to posterior); soft and

adipose tissue (skin and fat, bladder, fatty tissue), air (air within the colon), soft and adipose tissue (the intestines, fatty tissue), bone (vertebra) and soft and adipose tissue (skin and fat).

These measurements were made for all 50 CT pelvis patients identified in §5.4.2. The results are shown in table 5.8.

Thickness (mm)	Skin / fat / bladder	Air	Intestinal tissues	Vertebra	Skin / fat	Total
Average ± Std Dev	155.7 ± 43.2	24.4 ± 13.2	28.4 ± 22.5	11.2 ± 3.7	24.7 ± 11.4	230.6 ± 37.6
Median	159.5	20.9	24.2	10.6	23.7	227.2
Maximum	257.7	61.7	121.3	21.0	57.2	316.7
Minimum	26.9	5.5	4.2	5.3	8.4	136.0

Table 5.8: the results of the tissue and total patient thickness measurements undertaken for a study of 50 patient CT examinations of the pelvis

A t-test indicates that there are no statistically significant differences (at the $p < 0.05$ level) between the male and female cohort. The p values for all tissues (from anterior to posterior) are as follows; soft tissue ($p = 0.676$), air ($p = 0.447$), soft tissue ($p = 0.509$), the vertebra ($p = 0.095$), soft tissue ($p = 0.423$) and the total thickness ($p = 0.440$).

There is no need to consider male and female cohorts separately to the analysis for the entire sample, however for completeness and to provide a comparison with the abdomen and chest examinations, the sections that follow analyse male and female cohorts separately.

5.5.3.2 Monte Carlo simulation of pelvis examinations

To assess the potential range of μ_{eff} values for the path of x-rays through the centreline of a patient at the top of the femoral heads, each of the 50 patients in the study was modelled in a separate Monte Carlo simulation. The general form of the patient for each simulation is as shown in figure 5-18.

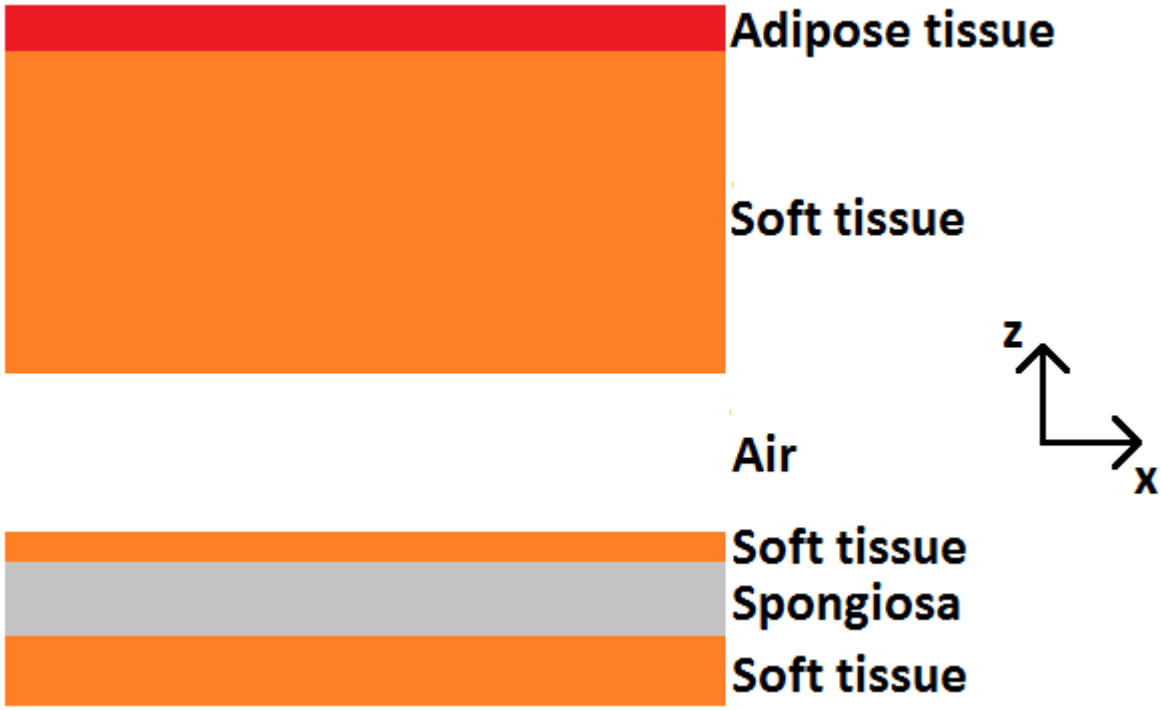

Figure 5-18: the general form of the patient's pelvis used in the Monte Carlo simulations, shown in the x-z axis

Each patient was created as a simple six layered block phantom which extended to 30cm in the x-axis. The first layer was simulated as adipose tissue, which was fixed at 20% of the total thickness of all adipose and soft tissues identified for each patient in the study (i.e. the thicknesses shown in columns 2, 4 and 6 of table 5.8). All of the spongiosa, air and soft tissue that followed was simulated as extending to the full 30cm width. Whilst it is acknowledged that the air and spongiosa do not extend so far from the centre-line, there is

no means using BEAMnrc to simulate multiple materials in the x-y axis in a single slab of a simulation.

Simulations were run at 81kV$_p$ and terminated when the statistical uncertainty was <10%. The simulated field size was 40x40cm at a 100cm FDD.

5.5.3.3 Simulation results for pelvis examinations

5.5.3.3.1 Values of effective linear attenuation coefficient

The values of μ_{eff} calculated from a region of 1cm x 1cm at the centre of scoring zone 3 (positioned 0.5cm from the exit of the simulated patient) for the simulations are summarised in table 5.9 and figure 5-19.

μ_{eff} (mm^{-1})	Male patients	Female patients	All patients
Average ± % Std Dev	0.0149 ± 14.1%	0.0146 ± 6.6%	0.0147 ± 10.9%
Minimum	0.0112	0.0122	0.0112
1st quartile	0.0142	0.0141	0.0142
Median	0.0145	0.0148	0.0148
3rd quartile	0.0152	0.0154	0.0154
Maximum	0.0232	0.0162	0.0232

Table 5.9: the values of μ_{eff} calculated from the simulations of pelvis examinations, grouped by male patients, female patients and all patients

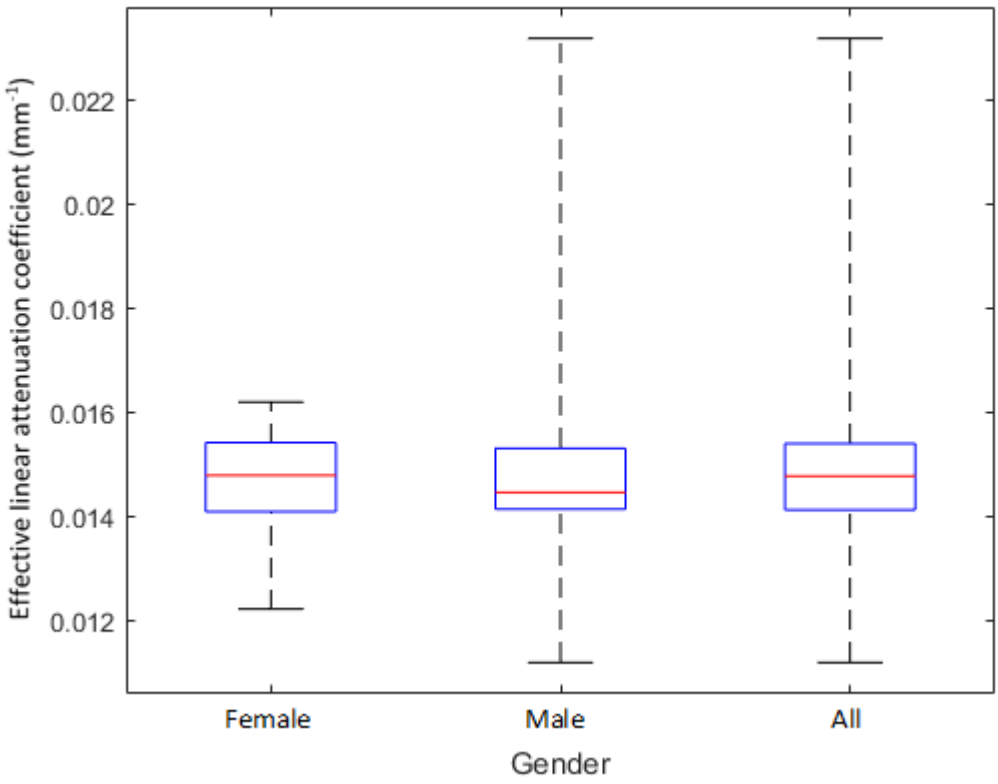

Figure 5-19: minimum, first quartile, median, third quartile and maximum values of effective linear attenuation coefficient, μ_{eff}, for pelvis examinations of female, male and all patients

As shown in table 5.9 and figure 5-19, there is some variation in μ_{eff} across the 50 simulations. There is one clear outlier – a male patient with a μ_{eff} of 0.0232mm^{-1}. The explanation for this lies in the ratio of the total thicknesses of bone and soft tissue. The patient is in the 3rd quartile for total patient thickness but has a higher ratio of bone to soft tissue than any other patient in the sample. As there is a greater contribution of more attenuating materials, the μ_{eff} is increased. This outlier is another example of the effect extreme anatomical variation can have on the estimate of μ_{eff}.

Values of μ_{eff} for the male and female patient cohorts were compared with a t-test. There was no significant difference between the two at the $p < 0.05$ level ($p = 0.639$).

To determine whether the relationship between total patient thickness and $\frac{k_d}{k_0}$ can be used to optimise values of μ_{eff} for an examination, the relationship between measured total patient thickness and $\frac{k_d}{k_0}$ is shown in figure 5-20.

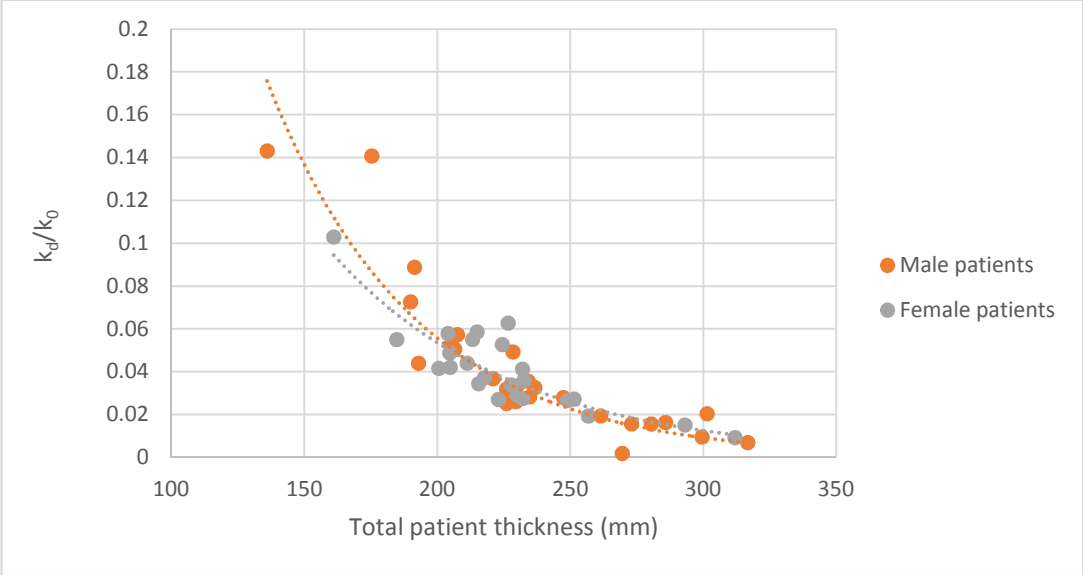

Figure 5-20: the relationship between measured total patient thickness and the calculated $\frac{k_d}{k_0}$ for each pelvis examination, grouped by male and female patients

Analysis of the data presented in figure 5-20 reveals a general exponential trend between the measured total patient thickness and the calculated $\frac{k_d}{k_0}$ for each pelvis examination for both male and female patients. The correlation coefficient (r^2) value for an exponential fit made using Matlab is 0.703 for male patients and 0.818 for female patients.

The relationship between measured total patient thickness and the μ_{eff} calculated for each patient from Monte Carlo simulation is shown in figure 5-21.

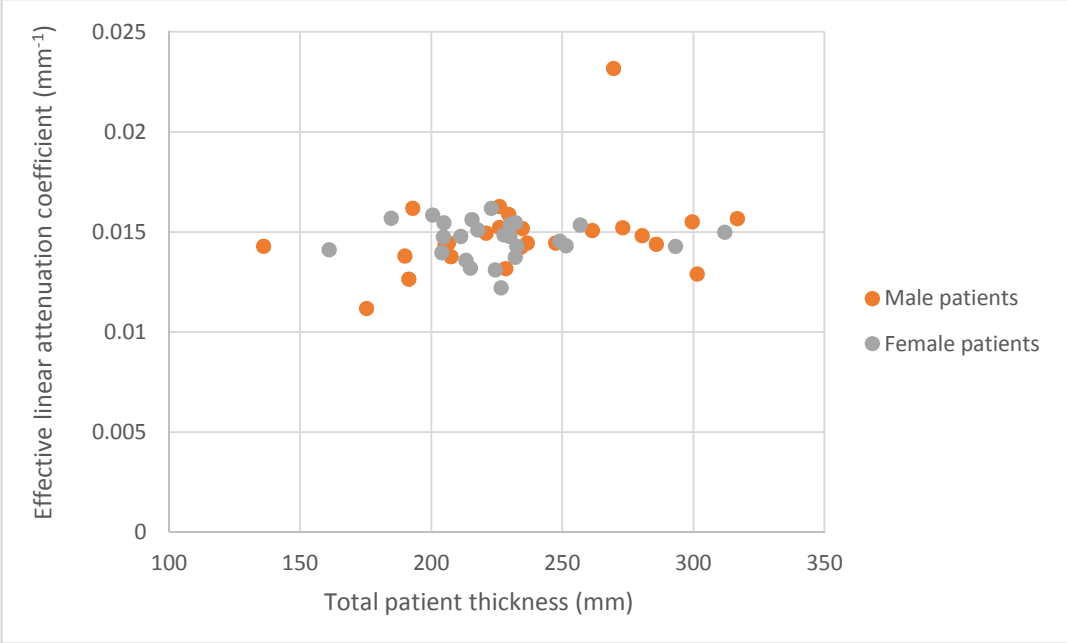

Figure 5-21: the relationship between measured total patient thickness and effective linear attenuation coefficient, μ_{eff}, for each pelvis examination, grouped by male and female patients

Figure 5-21 shows that other than the outlier already identified from table 5.9, there is little variation in μ_{eff} with varying total patient thickness. This means that a single value of μ_{eff} can be used for all patients undergoing pelvis examinations, and that there is nothing to be gained in trying to optimise the value of μ_{eff} based on the ratio of $\frac{k_d}{k_0}$.

5.5.3.3.2 Estimate of patient thickness

Estimates of total patient thickness were made for all 50 patients using equation 3.1 (§3.1), the median value of μ_{eff} as shown in table 5.9 and the ratio of $\frac{k_d}{k_0}$ calculated from the Monte Carlo simulation for each patient as shown in figure 5-18. This will help to determine the extent of the uncertainty as a result of using a single value of μ_{eff} for all cases. The percentage deviation from the estimated thickness and the thickness measured on the PACS for each patient is shown in figure 5-22.

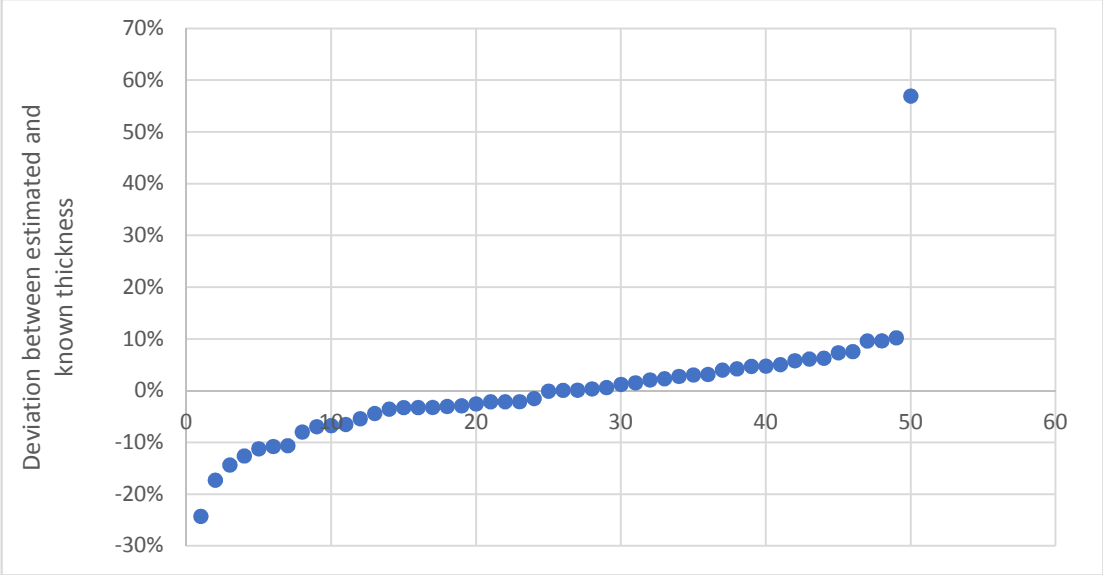

Figure 5-22: The percentage deviation between values of patient thickness estimated using the median value of effective linear attenuation coefficient, μ_{eff}, and the measured total patient thickness for 50 pelvis CT examinations

One of the estimates is significantly incorrect; this corresponds to the patient already identified from table 5.9 and is a result of patient anatomy that is significantly different from the others in this patient cohort. Of the 50 patients considered, the estimate of patient thickness is within 5% of the true value for 28 of them. 41 of them are within 10% of the true value. In terms of absolute deviation between the estimated and true patient thickness, in 26 cases it is within 10mm and in 40 cases it is within 20mm.

This method for validating the accuracy of the patient thickness estimate has the same limitation as discussed in §5.5.1.3.2; namely that the estimates were made on the same group of patients used to create the relationships used by the model. As in §5.5.1.3.2, the implicit assumption is that any two similarly sized groups from the same general population can be regarded as similar.

5.5.4 Summary

Values of μ_{eff} have been calculated for chest, abdomen and pelvis examinations using Monte Carlo simulations that have patients modelled on patient data from 50 chest, abdomen and pelvis CT examinations undertaken at NHS Tayside. These values are for examinations undertaken at 81kV$_p$ only, though the simulations can be repeated for any nominal kV$_p$. There is no means of verifying the accuracy of these values but they are individually within the wide range of values reported from the literature in NRPB-R318 [40] (though these were for a paediatric cohort). There is no data against which the absolute values can be accurately compared.

The analysis of data for 50 patients for each examination has provided a clinically relevant range of μ_{eff} values for each examination. The range of μ_{eff} values demonstrates that the use of a single value of μ_{eff} will not be appropriate for all patients, especially those with anatomy that is significantly different from the norm.

For chest and pelvis examinations, a single value of μ_{eff} has to be used by the computational model as there is no relationship observed between μ_{eff} and patient thickness. For abdomen examinations, the value of μ_{eff} can be optimised using the relationships between patient thickness, μ_{eff} and $\frac{k_d}{k_0}$. The estimates of patient thickness were more accurate for abdomen examinations than those for chest and pelvis examinations. Abdomen examinations were the only one that demonstrated a statistically significant difference in μ_{eff} between male and female patients.

The effect of varying values of percentage body fat on μ_{eff} was examined for abdomen examinations and found not to be significant. It is acceptable to use a fixed value of 20% adipose tissue for all simulations. Figure 5-9 shows that the difference between μ_{eff} between 5 and 20% and 20 and 90% is 0.7% and 3.7% respectively.

5.6 Considerations relating to the estimate of kerma at the image receptor

It was shown in §3.3.2.4, §4.3.2 and §4.4.2 that a single calibration of detector dose indicator (DDI) or signal transfer property (STP) can be used to accurately estimate k_d where the attenuation is equivalent to or in excess of 100mm of solid water high equivalency (HE). For multi-composition attenuators, this relationship might be dependent on the order in which the different compounds are positioned. A strongly attenuating compound, such as bone, could have a different effect on the quality of the x-ray beam exiting the attenuator depending on its position within the attenuator. This in turn could mean that the assumption that a single calibration of DDI or STP is all that is required is not valid. To determine the extent to which this could be an issue, the 1st and 2nd half value layers (HVL) and the average energy of the exit beam were calculated from Monte Carlo simulations of the same combination of tissues placed in a different order for an x-ray undertaken at 81kV_p. The average x-ray beam energy was calculated using the same method as for the average value of a histogram, as shown in equation 5.1.

$$Average\ energy = \frac{\left(\sum_{i=1}^{n} keV_{median_n} \times fluence_n\right)}{n} \qquad \text{[equation 5.1]}$$

Where;

- n is the total number of energy bins
- keV_{median_n} is the median keV of each energy bin
- $fluence_n$ is the total energy fluence of each energy bin

The HVL was calculated using equation 2.6 (§2.5.4.2).

The tissues selected were in keeping with those identified in the CT patient studies undertaken throughout §5.5, with the addition of cortical bone which, as the highest density component of skeletal bone, was included for a worst case scenario and the total

attenuator thickness was maintained at 250mm. The individual tissues and their thickness are shown in table 5.10.

Attenuator number	Attenuator material	Attenuator thickness (mm)
1	Adipose tissue	40
2	Soft tissue	70
3	Adipose tissue	100
4	Cortical bone	5
5	Spongiosa	10
6	Air	25

Table 5.10: the attenuators used in the Monte Carlo simulations to assess the average energy and half value layer (HVL) of the x-ray beam that exits the attenuator

The attenuator orders were as follows (using the attenuator numbers given in table 5.10);

- Case 1; 1, 2, 3, 4, 5, 6
- Case 2; 1, 4, 6, 2, 5, 3
- Case 3; 1, 6, 5, 3, 4, 2
- Case 4; 2, 6, 3, 4, 5, 1
- Case 5; 3, 4, 6, 2, 5, 1

These cases were chosen to represent some of the combinations of attenuator orders that are clinically relevant. The results for 1^{st} and 2^{nd} HVL and average energy are shown in table 5.11.

Case	1st HVL (mm Al)	2nd HVL (mm Al)	Av. Energy (keV)
1	9.0	21.2	52.8
2	7.9	19.1	51.6
3	8.6	20.4	52.3
4	8.6	20.5	52.5
5	8.8	20.8	52.5

Table 5.11: the 1st and 2nd half value layer (HVL) and average energy of the beam exiting an attenuator composed of the same materials in varying orders

For comparison, a Monte Carlo simulation of the high attenuation case considered in §3.3.2.6 (200mm of solid water HE with 5mm of aluminium) gave a 1st HVL of 10.2mm Al, a 2nd HVL of 23.8mm Al and an average energy of 54.2keV for an exposure undertaken at 81kV$_p$. None of the cases presented in table 5.11 have a beam quality or average energy that exceeds that of 200mm of solid water HE with 5mm of aluminium. A Monte Carlo simulation of the 100mm of solid water HE case gave a 1st HVL of 7.1mm Al, a 2nd HVL of 17.4mm Al and an average energy of 50.6keV. All the cases presented in table 5.11 have a beam quality and average energy that is greater than that of the 100mm solid water attenuator required for a single calibration of DDI or STP to be applicable (as shown in §3.3.2.5 and §4.3.2). The cases presented in table 5.11 would fall comfortably within the range of beam quality and average energy that allows for the use of a single calibration of DDI or STP to determine kerma at the image receptor. There is no need to adjust the method for deriving values of k_d when applying the computational model to patients.

5.7 Conclusions

In this chapter, the implications on the computational model for its use on patients have been considered. The first and most significant of these is the need to consider the effect of a patient, composed of many materials, on the value of μ_{eff} used by the computational

model for an examination. The effect was examined by measuring the total AP thickness of the patient and the individual thicknesses of broadly defined tissue types along the centreline for 50 chest, abdomen and pelvis CT examinations undertaken in NHS Tayside and creating a Monte Carlo simulation for each patient. A value for $\frac{k_d}{k_0}$ and μ_{eff} was calculated for each Monte Carlo simulation. Relationships between total patient thickness, $\frac{k_d}{k_0}$ and μ_{eff} were derived to determine if there is a means of optimising the value of μ_{eff} based on the ratio of $\frac{k_d}{k_0}$ for each patient examination. For chest and pelvis examinations, it has been shown that there is no means of optimising values of μ_{eff} on an examination by examination basis. It is possible to do so for abdomen examinations however. This resulted in the computational model giving the most accurate predictions of patient thickness for abdomen examinations when estimates were compared against the measured thickness of all 150 patients used to create the Monte Carlo simulations (50 each for chest, abdomen and pelvis examinations). The results for chest and pelvis examinations were generally accurate, but were subject to the occasional significantly incorrect estimate as a result of patients having distributions of tissues thicknesses that varied significantly from the other patients in the cohort. In these cases, the value of μ_{eff} used by the computational model was not appropriate.

The effect on the quality of the x-ray beam exiting the patient from the individual materials of an attenuator being placed in a different order was investigated to determine if there could be an effect on the calibrations used to derive a value of k_d. There was no significant effect found; the assumptions made regarding the estimate of k_d in chapter 3, that a single calibration of DDI or STP can be used provided it was derived with an attenuator in excess of the equivalent thickness of 100mm of solid water HE, are also true for examinations of patients.

As the computational model produced the most accurate estimates of patient thickness for abdomen examinations, it was decided that the computational model should be tested in clinical use in a clinical validation study involving patients undergoing AP abdomen x-ray examinations at NHS Tayside. Chapter 6 presents the preparation for, undertaking of and the results from this clinical validation study.

Chapter 6 – a clinical validation study of the computational model

Overview

This chapter presents the clinical validation study that was undertaken to test the accuracy of the computational model on patients undergoing anterior-posterior abdomen x-ray examinations at Ninewells Hospital. This includes the preparation for the clinical validation study including planning, study design, study sponsorship, ethical approval and all the modifications to the computational model that were necessary. The conduct of the clinical validation study is described, and the results of the clinical validation study presented.

6.1 Introduction

To test the accuracy of the computational model in the clinical environment, 20 patients were enrolled in a clinical validation study. The clinical validation study focussed on patients undergoing anterior-posterior (AP) abdomen examinations as the computational model demonstrated the greatest accuracy for this examination in chapter 5. The study was designed in detail, as was required prior to an application for study sponsorship to NHS Tayside and the University of Dundee. Once sponsorship for the clinical validation study was secured, an application for ethical approval was made using the Integrated Research Application System (IRAS) for consideration by a research ethics committee.

The clinical validation study received approval from an ethics committee and a final sign off from the NHS Tayside and University of Dundee research and development departments. During the clinical validation study patients that were already attending Ninewells Hospital for an AP abdomen x-ray examination were asked to participate. Where they were willing, each participant gave their written informed consent. A simple measurement of each patient's AP thickness at the level of the iliac crest was made with the patient in the correct position for the examination. Each patient's x-ray image was then used along with the examination exposure factors, look up tables (LUTs) and a priori information relating to the x-ray system and digital detector to estimate the patient thickness using the computational model. The estimated thickness was compared to the actual measurement of patient thickness. A full description of the clinical validation study and the results obtained are presented and discussed in this chapter. §6.2 outlines the planning and design of the clinical validation study, including the modifications that were made to the computational model. §6.3 describes the undertaking of the clinical validation study, along with the results.

6.2 Clinical validation study planning

In preparation for the clinical validation study, the following aspects had to be considered;

- Sponsorship of the clinical validation study
- The patient cohort that would be invited to participate
- The x-ray equipment on which the clinical validation study would be undertaken
- Any variation in examination technique from patient to patient that the computational model has to account for
- The study design
- The application for ethical approval
- The study methodology
- Any necessary modifications to the computational model

Each of these considerations is discussed in turn.

6.2.1 Clinical validation study sponsorship

The Medicines for Human Use (Clinical Trials) Regulations 2004 [132] require that all clinical trials have a sponsor. The sponsor has overall responsibility for management of the research [133]. Clinical trial investigators require the backing of a sponsor prior to submitting an ethics application. Sponsorship will be granted if the investigators can demonstrate that the clinical trial is justified, that it will be undertaken in a safe manner, that it will respect all relevant clinical governance procedures, that the study team has sufficient expertise to undertake the study and that the selection of the chief and principal investigators is appropriate. The chief investigator is responsible for the overall conduct of the study and the principal investigator is responsible for the conduct of the study at an individual site. Dr Sarah Vinnicombe, Honorary Consultant Radiologist at NHS Tayside and

Senior Lecturer at the University of Dundee, as well as secondary supervisor for this PhD project, was the chief investigator for the study. The author of this thesis was the principal investigator.

Comprehensive documentation describing the justification, planning, design and conduct of the clinical validation study was submitted to NHS Tayside and the University of Dundee. Following this, NHS Tayside and the University of Dundee agreed to act as co-sponsors for the clinical validation study described in this chapter.

6.2.2 Patient cohort

Whilst the ultimate aim of this work is to develop a tool for estimating the thickness of a patient to assist with paediatric patient dose audit, the computational model has so far been developed for an adult cohort. Therefore, the clinical validation study also used an adult cohort.

The considerations in applying the computational model to paediatric patients are discussed in §7.3.1. If it can be demonstrated that the computational model works for adult patients, the same model applied to a paediatric cohort will be equally applicable provided these considerations are investigated and accounted for as required.

6.2.3 X-ray equipment

Ambulatory patients having an AP abdomen x-ray examination at Ninewells Hospital would normally have the examination on a fixed radiographic unit using a grid and automatic exposure control (AEC). At the time of the clinical validation study however, Ninewells Hospital only had one digital x-ray unit that was suitable for use with the computational

model; the Fuji FDR Go digital mobile x-ray unit that was used in §4.4. Therefore it was necessary to divert patients to the mobile unit for their examination. As this was a mobile radiographic unit, the use of a grid and AECs was not possible. This has implications for image quality and patient dose, but the mobile unit was equipped with Fuji's virtual grid software [134], which had been commissioned locally and was in routine use. This software removes scatter in post-processing based on the exposure factors used for the examination and the signal received by the image receptor. This provides an improved image despite the absence of a physical grid at a lower patient dose than could be achieved with a physical grid. The use of the virtual grid software means that the patient receives a lower dose than they would have if their examination had taken place in a conventional radiographic room. It had previously been confirmed that local radiologists were content with the image quality of the AP abdomen examination images produced using the virtual grid software on this unit, so there would be no impact on any patient's care as a result of their participation in the study. The LUTs for the assessment of k_0 and the calibrations of detector dose indicator (DDI) and signal transfer property (STP) were already available following the work undertaken in §4.4. Values of μ_{eff} were calculated from Monte Carlo simulations, as will be described in §6.2.5.2.

6.2.4 Clinical practice and computational model refinements

Examinations undertaken in a radiographic room follow a standard operating procedure (SOP) that outlines how the examination should be performed. This includes details such as focus to detector distance (FDD), AEC chamber selections and density settings and baseline kV_p. The equipment itself is either programmed with all of this information to allow it to set up automatically or displays all of the information to allow the operator to manually set it up. This is not the case with a mobile unit. Whilst there is an SOP for each

examination, there is more variability in examination setup from patient to patient because there is no automatic positioning and no real time display of the FDD.

In preparation for the clinical validation study the radiographers at Ninewells Hospital were asked to use the Fuji FDR Go digital mobile x-ray unit for some routine AP abdomen examinations and record the variation in setup between examinations. This was done as it may have been necessary to consider the variations in the computational model. The first variation the radiographers reported was the FDD. Unlike a fixed radiographic unit that has automatic positioning or detent positions to ensure the FDD matches the grid focus distance, the FDD for an examination using a mobile unit is entirely dependent upon the operator. The FDD for each AP abdomen examination varied with the x-ray field coverage required at the detector (dependent upon patient diameter) and the height of the radiographer. The computational model presented so far has only considered examination FDDs of 100cm. It was therefore necessary to consider the effect of different FDDs on the computational model. The second variation the radiographers reported was the examination kV_p. This was expected, as whilst there is a baseline kV_p in the SOP, the kV_p is adjusted by the radiographer to suit the habitus of the patient. This is already accounted for by the computational model. The third variation the radiographers reported was the use of a mattress. The digital detector was placed on the x-ray table of a radiographic room. Whereas some patients lay directly on top of it, others could not tolerate this. For these patients, a standard x-ray couch mattress was placed between the detector and the patient to provide additional support and comfort. It is necessary to consider the effect of the mattress in the computational model.

6.2.5 Modifications to the computational model

6.2.5.1 Monte Carlo simulation of the Fuji FDR Go digital mobile x-ray unit

Values of μ_{eff} had already been calculated for the AP abdomen examinations described in chapter 5 using Monte Carlo simulations. However, these simulations were based on the Philips Optimus 50 radiographic x-ray unit, as described throughout chapter 2. As the clinical validation study was to be undertaken using a Fuji FDR Go digital mobile x-ray unit, it was necessary to create a Monte Carlo model of the mobile x-ray unit.

Using the Monte Carlo model of the Philips Optimus 50 radiographic x-ray unit as a starting point, the following modifications were made based on the technical manual for the Fuji FDR Go digital mobile x-ray unit [135] and measurements made on the unit itself;

- The anode angle is 16°
- The focal spot sizes are 0.7 / 1.3mm for fine and broad focus respectively
- The maximum nominal x-ray tube voltage is 130kV_p
- The total minimum filtration of the x-ray tube assembly is 3.4mm Aluminium equivalent at 80kV_p, measured at a 100cm FDD
- The focus to collimator distance is 27.5cm
- The focus to the centre of the kerma area product (KAP) meter distance is 30cm

The resulting Monte Carlo model was optimised in the same manner as described throughout chapter 2 and validated using the methods outlined in §2.5; the results were within the uncertainty of measurement in all cases.

6.2.5.2 Calculating values of effective linear attenuation coefficient

Using this validated Monte Carlo model of the Fuji FDR Go digital mobile x-ray unit, simulations for each of the 50 patients having undergone abdomen computed tomography (CT) examinations as described in §5.5.1 were used with the Monte Carlo model of the Fuji FDR Go digital mobile x-ray unit, creating 50 unique simulations. These all simulated an x-ray beam with a field size of 35x40cm at a 100cm FDD. As with all Monte Carlo simulations throughout this work, each simulation was run until the statistical uncertainty was < 10%. The process for calculating $\frac{k_d}{k_0}$ and effective linear attenuation coefficient, μ_{eff}, values from Monte Carlo simulations as presented in §5.5.1.3.1 was repeated for 70, 75, 80, 85 and 90kV$_p$. It was confirmed that this was the kV$_p$ range that would be used by the radiographers for AP abdomen x-ray examinations of adult patients using the Fuji FDR Go digital mobile x-ray unit. For each kV$_p$, the relationship between a) total measured patient thickness and $\frac{k_d}{k_0}$, and b) total measured patient thickness and μ_{eff} were derived. Following the calculation of $\frac{k_d}{k_0}$ these relationships can be used to estimate the total measured patient thickness and then a more accurate value of μ_{eff} for each individual patient participating in the clinical validation study.

These simulations are appropriate for the case where patients participating in the clinical validation study are able to lie directly on top of the digital detector. They may not give μ_{eff} values that are appropriate for use in the case where the patient lies on a mattress placed on top of the digital detector. To determine whether the addition of the mattress has a significant effect on the derived values of μ_{eff}, a 5cm thick mattress needs to be added to the Monte Carlo model. The mattress used clinically is part of a Philips Optimus 50 radiographic x-ray unit; the technical manual for the x-ray unit [80] states that it is made of polyurethane foam ($C_{27}H_{36}N_2O_{10}$) [136] with a nominal density of 30-40kg m^{-3}. Measurements were made on the mattress to confirm this; the measured density was 37kg

m^{-3} (±0.17%). Polyurethane foam was added to the Monte Carlo code using the ($C_{27}H_{36}N_2O_{10}$) chemical composition and a density of 37kg m^{-3}. New Monte Carlo simulations were run for all 50 test patients that included a 5cm thickness of polyurethane foam underneath the patient at 70, 75, 80, 85 and 90kV_p. Each simulation was terminated when the statistical uncertainty was < 10%. The general form of the patient used in these simulations is shown in figure 6-1.

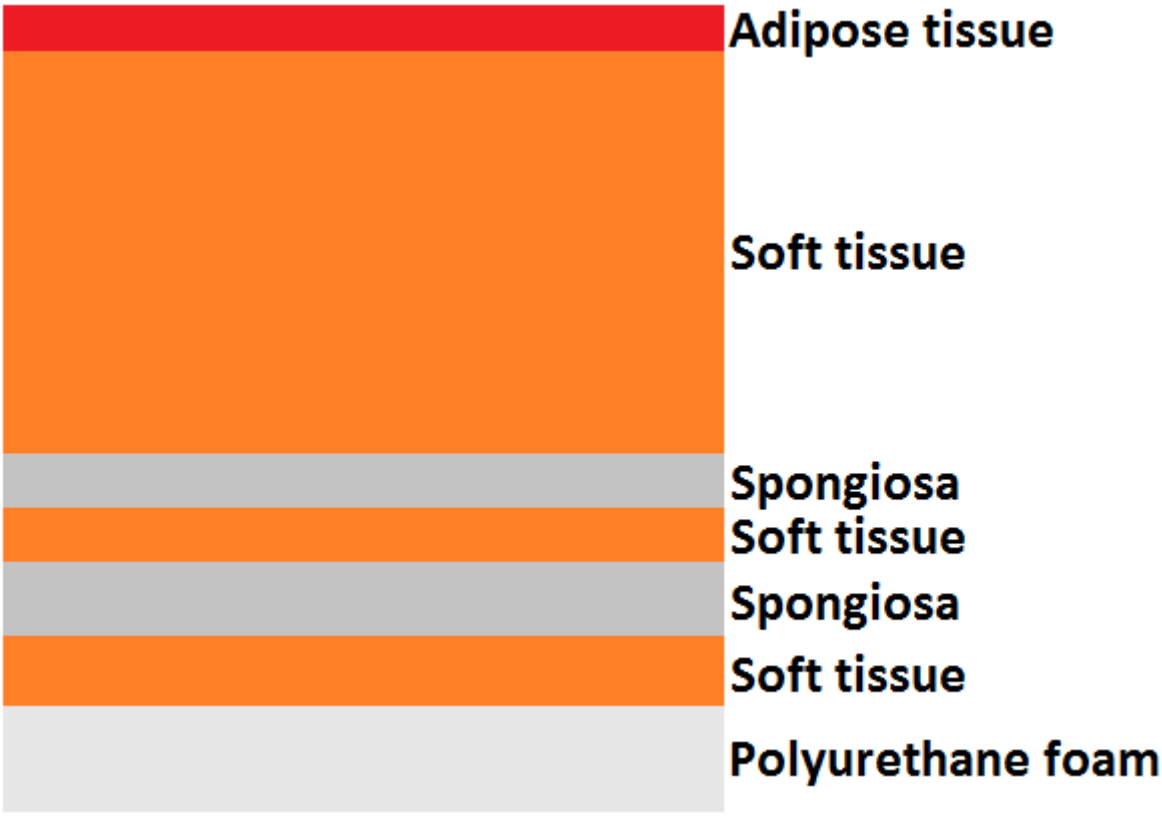

Figure 6-1: the general form of the patient's abdomen lying on top of polyurethane foam used in the revised Monte Carlo simulations, shown in the x-z axis

The average values of μ_{eff} derived from the 50 simulations undertaken at each kV_p value both with and without the mattress are shown in figure 6-2.

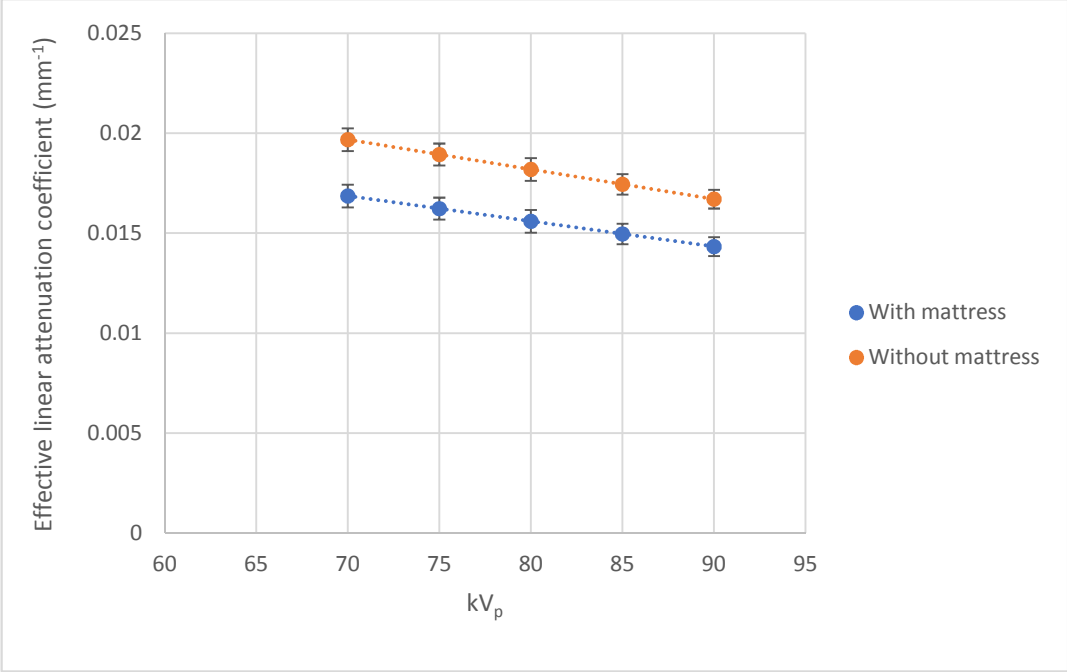

Figure 6-2: the average value of effective linear attenuation coefficient, μ_{eff}, from 50 Monte Carlo simulations at 70, 75, 80, 85 and 90kV$_p$ with and without the mattress between the detector and patient. The error bars represent one standard deviation

There is a systematic difference between values of μ_{eff} derived from simulations with and without the mattress. The difference is consistently equal to 14% of the value of μ_{eff} without the mattress across the simulated kV$_p$ range. If the μ_{eff} values derived from simulations without the mattress were used for examinations undertaken with the mattress in place, the patient thickness would be underestimated. To calculate the magnitude of this underestimate, estimates of attenuator thickness were made using the average value of μ_{eff} derived with and without the mattress at each kV$_p$. For these indicative calculations, the ratio of $\frac{k_d}{k_0}$ was fixed at 0.1. Table 6.1 shows the estimates of attenuator thickness for the 'with mattress' and 'without mattress' cases along with the difference in estimated attenuator thickness between the two.

Estimated attenuator thickness (mm)	kV_p				
	70	75	80	85	90
With mattress	136.5	141.4	148.1	136.5	160.4
Without mattress	117.0	121.1	127.0	117.0	137.6
Difference	19.5	20.3	21.1	19.5	22.8

Table 6.1: the attenuator thickness estimated using the average effective linear attenuation coefficient, μ_{eff}, values from 50 Monte Carlo simulations with and without the mattress between the detector and patient at various kV_p values

Table 6.1 shows that the difference in estimated attenuator thickness between the with and without mattress simulations is in excess of 19mm for a $\frac{k_d}{k_0}$ of 0.1, demonstrating the importance of replicating the true exposure geometry in the Monte Carlo simulations for accurate estimates of patient thickness.

6.2.5.2.1 Variation of effective linear attenuation coefficient, μ_{eff}, with focus to detector distance

The μ_{eff} values derived in §6.2.5.2 are only applicable for examinations undertaken with a field size of 35x40cm at an FDD of 100cm. An additional set of 50 Monte Carlo simulations was created for each of 5 FDDs; 80, 90, 110, 120 and 130cm. The field size was maintained at 35x40cm at the image receptor in each. This range of FDDs was selected as below an FDD of 80cm the x-ray unit cannot produce a large enough field size for an adult AP abdomen examination and the mobile x-ray unit is not capable of an FDD greater than 130cm where the patient is on the couch of an x-ray room. Each one of these simulations was run at 70, 75, 80, 85 and 90kV_p.

By way of example, the results for the average μ_{eff} from all 50 Monte Carlo simulations at 75kV_p for each FDD are shown in figure 6-3.

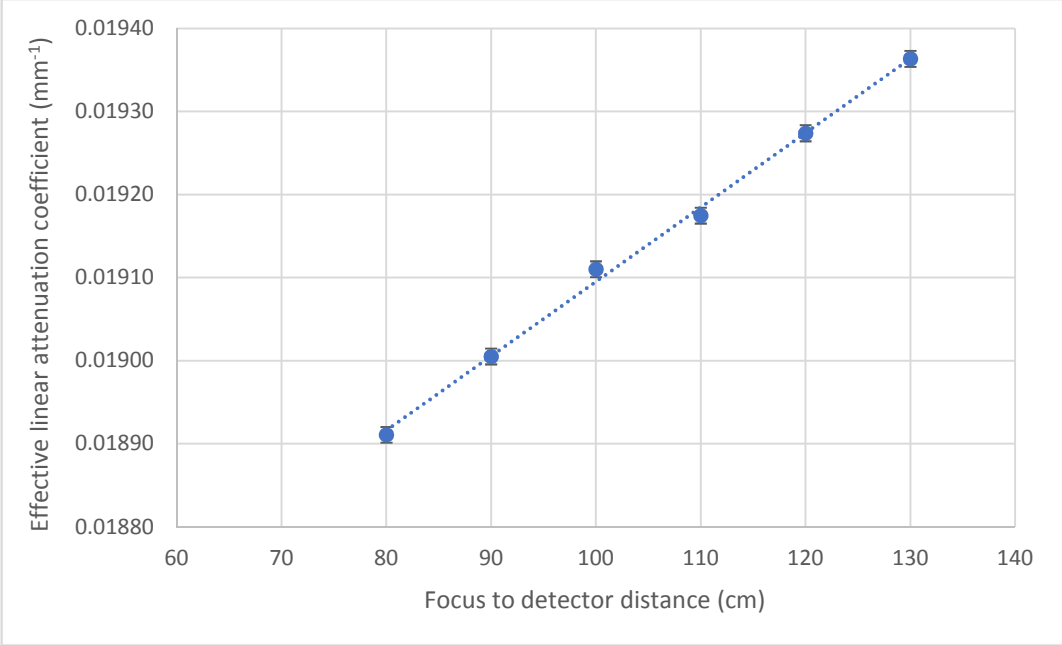

Figure 6-3: the average effective linear attenuation coefficient, μ_{eff}, from 50 examinations undertaken at each focus to detector distance (FDD) at 75kV$_p$. The error bars represent one standard deviation

The μ_{eff} increases linearly with FDD, however the average μ_{eff} only varies by 2.6% between 80 and 130cm FDD. The FDD has little effect on the value of the average μ_{eff}, suggesting that a value of μ_{eff} derived at a single FDD could be used for any examination without significantly impacting on the uncertainty budget. Similar results were obtained at 70, 80, 85 and 90kV$_p$. To calculate the magnitude of the effect that the use of a value of μ_{eff} derived from a single FDD for any examination would have on the attenuator thickness estimated by the computational model, estimates of attenuator thickness were made using the average value of μ_{eff} at each FDD for simulations undertaken at 75kV$_p$. For these indicative calculations, the ratio of $\frac{k_d}{k_0}$ was fixed at 0.1. Table 6.2 shows the estimates of attenuator thickness using μ_{eff} values derived at FDDs between 80 and 130cm.

	FDD (cm)					
	80	90	100	110	120	130
Attenuator thickness (mm)	121.8	120.5	120.1	121.2	119.5	118.9

Table 6.2: the attenuator thickness estimated using the average effective linear attenuation coefficient, μ_{eff}, values from 50 Monte Carlo simulations at each focus to detector distance (FDD), at 75kV_p

As shown in table 6.2, there is little difference in the estimated attenuator thickness as a result of the variation in μ_{eff} from a varying FDD (a 2.9mm (2.4%) deviation between extremes of FDD). As would be expected, this was also the case for 70, 80, 85 and 90kV_p.

This experiment shows that the use of a single value of μ_{eff} for all FDDs only contributes a low uncertainty to the estimate of thickness made by the computational model. Nevertheless, in order to reduce the uncertainty in the estimate of μ_{eff} by the computational model as much as possible, and for completeness, a correction for FDD was added to the estimate of μ_{eff} in the final computational model.

6.2.5.3 Calculation of initial air kerma, k_0

As shown in §3.3.1, k_0 can be estimated using either the radiation output (using equation 3.2, §3.3.1.1) or the examination KAP (using equation 3.5, §3.3.1.3). Whereas equation 3.2 accounts for the possibility of an examination not undertaken at 100cm FDD with the correction factor k_{FDD}, equation 3.5 is only correct at 100cm FDD because the values of k_{field} calculated using equation 3.4 are dependent on the FDD. Values of k_{field} were calculated from measurements made on the Fuji FDR Go digital mobile x-ray unit at FDDs of 80, 90, 110, 120 and 130cm using the methods described in §3.3.1.3. The results are shown in figure 6-4.

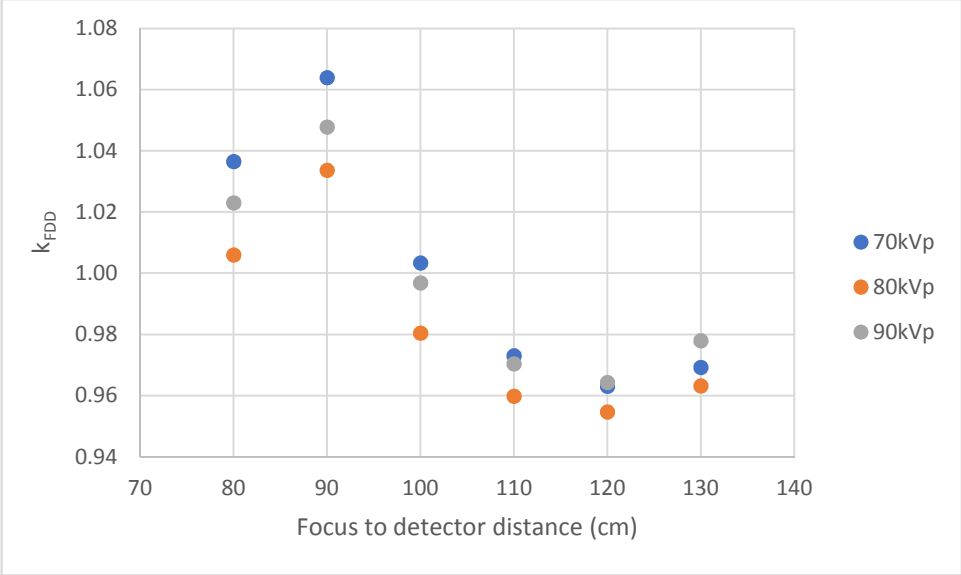

Figure 6-4: the variation in correction factor k_{FDD} with focus to detector distance (FDD) at 70, 80 and 90kV_p

Figure 6-4 shows that the k_{FDD} correction factor is empirically observed to vary with FDD. No explanation for the variation in k_{FDD} with FDD is offered, as there was no particular relationship expected and nor was one seen. The values of k_{FDD} shown in figure 6-4 can be used to generate a value for any FDD between 80 and 130cm by interpolation. With a maximum difference between k_{FDD} values of 0.1 for a single kV_p, it is clearly important that this correction be used when estimating the value of k_0 in the computational model.

6.2.6 Clinical validation study design

The design for the clinical validation study was as follows;

- 20 adult patients referred for AP abdominal x-ray examinations would be recruited. Rohrig et al [137] discuss how to calculate the necessary sample size for a clinical validation study. The calculation first requires knowledge of the analytical test to be used on the results. An unpaired t-test with two different standard deviations

requires an estimate of the results μ_1 and μ_2, the standard deviations σ_1 and σ_2 and the selection of the study power, z, (the confidence that a result will be detected) and the level of significance. The sample size can then be calculated using;

$$n \approx \left[\frac{2(Z_{power}+Z_{1-\alpha})}{\frac{2(\mu_1-\mu_2)}{\delta}}\right]^2 \qquad \text{[equation 6.1]}$$

Typical values for study power and significance are 80% and 2.5% respectively [137]. The difficulty of applying a calculation of this nature to this clinical validation study is an inability to estimate the means or standard deviations. If the means and standard deviations from the single composition attenuator work undertaken on the Fuji FDR Go digital mobile x-ray unit are applied, as derived from the results in table 4.7 in §4.4.4.4, the calculated sample size is 3 participants. This is because the standard deviation from those results is less than the mean difference between μ_1 and μ_2. It is not anticipated that the agreement will be as good for patients as it was for the single composition attenuator. If the mean difference between the estimates is 10mm and the standard deviation is 15mm, the number of participants would be 18. This gives some confidence in the selection of 20 patients for the study, which was also considered a good balance between enough patients to assess the accuracy of the computational model and an achievable number of patients within the timescales of this work

- All patients would give informed consent before participating; this would follow a conversation with the principal investigator who would go through the content of the patient information sheet (PIS)
- The inclusion criteria were any patient referred for an AP abdomen x-ray who was aged 18 or over
- The exclusion criteria were any patient in acute abdominal pain, any patient unable to give informed consent and any patient who had had an examination using

contrast media within the previous 24 hours as the μ_{eff} values used by the computational model would not account for this

- The principal investigator would not approach the patient directly. A radiographer would ask each patient if they would like to participate in the clinical validation study; if invited to do so, the principal investigator would then explain the clinical validation study to the patient and take their consent. The patient would be given a PIS as part of this process
- Patients participating in the clinical validation study would have their examination on the Fuji FDR Go digital mobile x-ray unit, instead of the fixed radiographic system that would be used if they were not participating in the clinical validation study
- The radiographer undertaking the examination would position the patient, select the exposure factors and undertake the examination without any influence from the principal investigator
- The measurement of AP abdominal thickness would be made immediately prior to x-ray exposure by the principal investigator with the patient in the examination position using a bespoke measuring device
- The principal investigator would record all of the exposure factors for each examination, along with the patient's gender. This would be recorded anonymously under an incrementally increasing participant identification number
- A copy of the patient's image would be made and reprocessed to apply minimal processing (using the 'sensitivity' processing option on the Fuji FDR Go digital mobile x-ray unit). This is the image that would be used by the computational model

6.2.7 Ethical approval application

An IRAS application was completed and submitted to the West of Scotland Research Ethics Committee 3 with all supplementary documents. The supplementary documents included;

- The study protocol – the protocol includes the study objectives, the study design, the study population, the inclusion and exclusion criteria for participants, the process for participant enrolment, a study safety assessment, a description of data collection and management, a description of the data analysis and statistics, a description of the arrangements for study management and oversight, a description of the arrangements for good clinical practice, the identification of the study team and their roles and responsibilities and the arrangements for reporting and publication of the study results
- The PIS – information for potential participants about the study and what they should expect if they participate. All participants should be offered a PIS as part of the informed consent process. It was made clear in the IRAS application that the patient would receive the PIS at the time of the consent process. Generally, participants in a clinical validation study would have the PIS well before the consent process to allow them to fully review it. This was not possible in this clinical validation study, since patients were only identified at the time of their AP abdomen x-ray examination. It was argued in the IRAS application and the study protocol that the clinical validation study and PIS were sufficiently straightforward that the patients would not require any significant time to consider them. The PIS is included in appendix 4
- The informed consent form – a form for the study participants to record their consent to participate in the study

- The reply slip – a form for the study participants to sign to record they are happy to speak to the principal investigator about the study
- The patient study form – the form on which the information relating to each examination would be recorded. This includes patient gender, examination kV_p, mAs, KAP and FDD and whether the x-ray couch mattress was used

6.2.8 Clinical validation study methodology

Ninewells Hospital undertakes many AP abdomen x-ray examinations every day. Referrals for these examinations come from various departments within Ninewells Hospital for inpatients and from many National Health Service (NHS) clinics and GP surgeries in the greater Tayside area for outpatients. The examinations themselves are undertaken in whichever radiology department at Ninewells Hospital is most convenient for the patient. This complicates arrangements where the examinations for the clinical validation study need to be undertaken on a single mobile digital radiographic unit. To simplify logistics, the clinical validation study was undertaken after 5pm in the accident and emergency (A&E) department at Ninewells Hospital. This is the only x-ray department open out of normal working hours and the Fuji FDR Go digital mobile x-ray unit is available there all night. All radiographers were informed of the clinical validation study and had been asked to discuss all referrals for AP abdomen x-ray examinations with the principal investigator for an assessment of the patient's suitability to participate in the study prior to their being called for their x-ray examination. If the patient met the inclusion criteria, the radiographer asked them if they would be willing to speak to the principal investigator about participation. If they were, the patient completed the reply slip, which allowed the principal investigator to approach the patient. The principal investigator explained the clinical validation study to the patient, ran through the details of the PIS and took the patient's informed consent.

The radiographer set up the patient for the examination. The measurement of abdominal thickness was made immediately prior to the x-ray exposure with the patient in the examination position using a bespoke measuring device, as shown in figure 6-5.

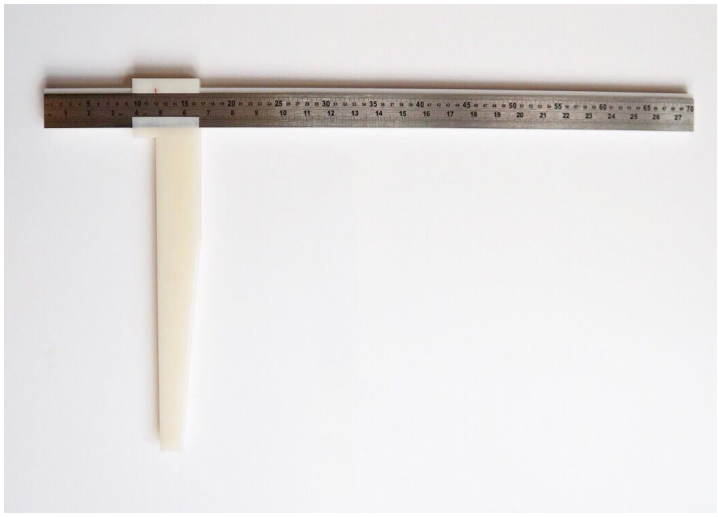

Figure 6-5: the bespoke measuring device used to make measurements of the patient's anterior-posterior (AP) abdominal thickness

The bespoke measuring device used to make the measurement of each patient's AP abdominal thickness was constructed by the mechanical workshop of the Medical Physics Department at Ninewells Hospital. Using the World Health Organisation's (WHO) definition [138], the bespoke measuring device does not constitute a medical device, therefore there was no need for CE marking or to follow Medicines and Healthcare products Regulatory Agency (MHRA) guidance.

The principal investigator recorded all of the exposure factors for each examination, including examination kV_p, mAs, KAP, FDD and whether or not the x-ray couch mattress was used. The patient's gender was also recorded, as it was demonstrated in §5.5.1.3.1 that gender specific values of μ_{eff} should be applied for abdomen examinations.

The examination applied post-processing that was appropriate for the abdomen to produce a diagnostically acceptable image. All of the DDI and STP calibrations undertaken in §4.4

used the 'sensitivity' processing algorithm, which applies as little processing to the image as possible. At the completion of each examination, a duplicate of the AP abdomen image was created and then re-processed using the 'sensitivity' processing algorithm. The reprocessed image was undiagnostic but meant that the DDI and STP calibrations undertaken in §4.4 could be applied, making it possible to estimate k_d.

6.3 Undertaking the clinical validation study

6.3.1 Ethical approval

The study was granted ethical approval following a proportionate review by the West of Scotland Research Ethics Committee 3 on 21st December 2017. Research and development management approval was also granted by the University of Dundee and NHS Tayside on 21st December 2017. The study was registered on the public registry of clinical trials www.clinicaltrials.gov; the NCT number was 03341546.

6.3.2 Conducting the clinical validation study

20 patients were recruited to the clinical validation study. The first was recruited on 13th March 2018, the last on 7th May 2018. Patients were recruited sequentially over this time period, all of the patients who met the inclusion criteria agreed to take part. There were 10 male and 10 female patients recruited (this was by coincidence, not design). The kV_p for the examinations ranged from 70 – 90. 11 of the examinations used the mattress between the patient and the detector.

6.3.3 Clinical validation study results

A summary of the measured patient AP abdominal thicknesses is shown in the boxplot in figure 6-6.

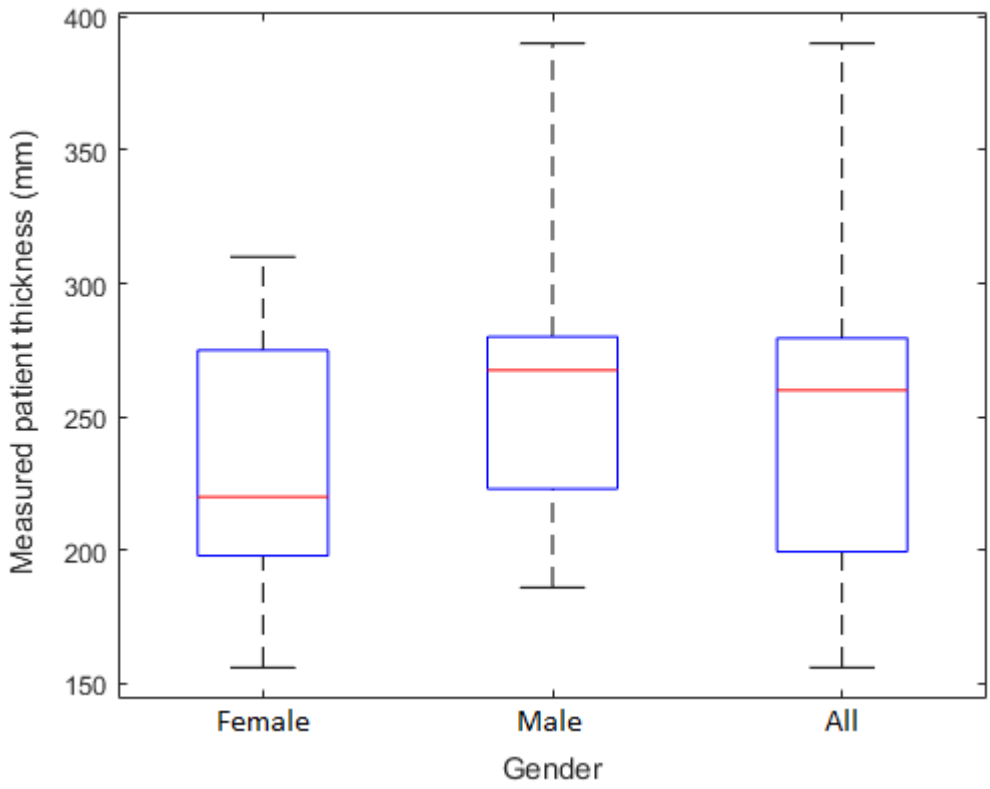

Figure 6-6: minimum, first quartile, median, third quartile and maximum values of measured patient anterior-posterior (AP) abdominal thickness for examinations of female, male and all patients enrolled in the clinical validation study

The measured patient thickness ranged from 156 to 390mm. There was a much greater variation in diameter for male patients, with one patient in particular (measuring 390mm) who was far larger than all other participants. The next largest patient was 310mm. The range of patient diameters for the 50 abdomen patients used to create the Monte Carlo models in §5.5.1.2 was 176mm to 366mm. This means the largest and smallest patients included in the clinical validation study were both outside the diameter range used to derive the values of μ_{eff} for abdomen examinations. As the μ_{eff} values used for these

patients were extrapolated rather than interpolated, this could have had an effect on the accuracy of the estimate of patient thickness at the extremes of the participant diameter range.

The measured patient AP abdominal thickness and that estimated by the computational model for each patient is shown in table 6.3.

Patient ID	Gender	Patient thickness (mm)			% difference
		Measured	Estimated	Difference	
1	M	260	240	-20	-7.7
2	F	285	259	-26	-9.0
3	F	198	192	-6	-2.9
4	F	310	290	-20	-6.4
5	M	390	304	-86	-22.0
6	M	260	242	-18	-6.7
7	F	275	251	-24	-8.8
8	F	215	228	13	6.1
9	M	280	262	-18	-6.5
10	M	186	177	-9	-4.6
11	F	175	167	-8	-4.5
12	M	223	228	5	2.1
13	F	225	243	18	7.9
14	M	279	287	8	2.8
15	M	195	184	-11	-5.8
16	F	264	249	-15	-5.6
17	F	156	152	-4	-2.8
18	F	201	207	6	3.2
19	M	294	295	1	0.2
20	M	275	272	-3	-0.9

Table 6.3: the patient anterior-posterior (AP) abdominal thickness measured at the time of the examination and as estimated by the computational model for each participant in the clinical validation study

For 9 patients, the absolute deviation between the estimated and measured patient AP abdominal thickness is within ±10mm. For 17 patients it is within ±20mm and for 19 patients it is within ±26mm. For one patient, the estimated thickness was 86mm lower than the measured thickness. This was the largest patient in the cohort, measuring 390mm.

The percentage deviation from the estimated and measured thickness for each patient is shown in figure 6-7.

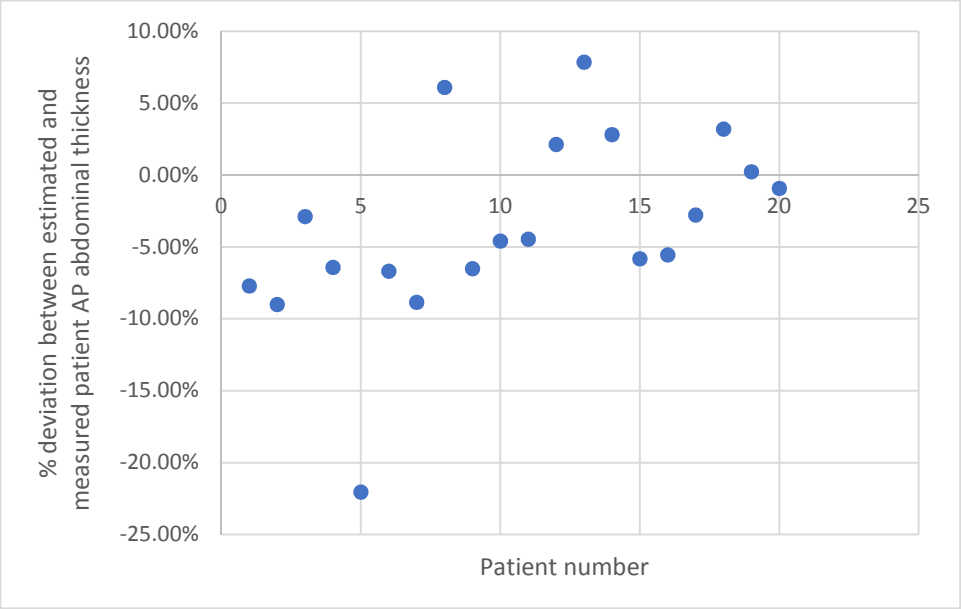

Figure 6-7: the percentage deviation between the estimated and measured patient AP abdominal thickness for sequential patients recruited to the clinical validation study

The estimated patient AP abdominal thickness agrees with the measured patient AP abdominal thickness to within ±5% for 9 patients and to within ±9% for 19 patients. The estimated thickness is 22% lower than the measured thickness for the largest patient.

A Bland-Altman plot [139] analyses the agreement between two means of measuring the same variable. A Bland-Altman plot for the measured and estimated patient thicknesses is shown in figure 6-8.

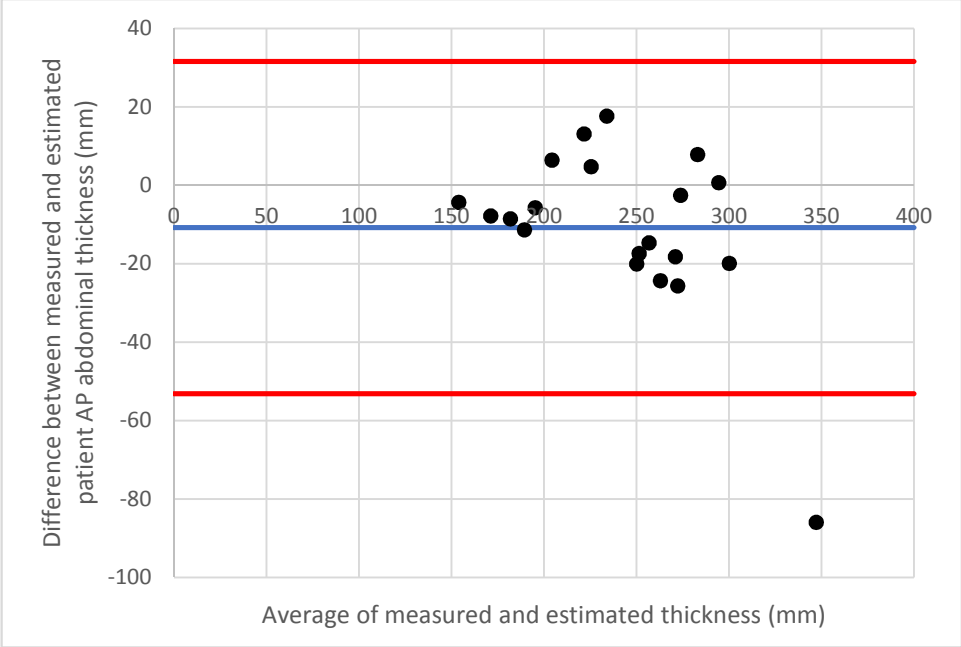

Figure 6-8: a Bland-Altman plot for the measured and estimated patient anterior-posterior (AP) abdominal thicknesses for the participants in the clinical validation study. The red lines show the upper and lower 95% confidence intervals, the blue line shows the average difference between measured and estimated thickness

The Bland-Altman plot shows that the bias (the discrepancy between the results) is low. The 95% confidence intervals were calculated using (1.96 x Standard Deviation). The 95% confidence interval limits are narrow enough as to suggest the methods are similar. There is no trend between the difference between the methods and the average of the measured and estimated patient thickness and the variation is consistent throughout.

6.3.4 Discussion

The deviation between the estimated and measured patient AP abdominal thickness is within ±9% for all except one patient. This patient was the largest to participate in the clinical validation study by some distance. The patient was also larger than any of the 50

patients that were used to create Monte Carlo models for AP abdomen examinations in §5.5.1.2.

The significant deviation between the estimated and measured patient AP abdominal thickness is a result of an inaccurate value of μ_{eff} used by the computational model for this patient. The patient thickness estimated by the computational model underestimated the measured thickness, which means the value of μ_{eff} used by the computational model was too high.

The μ_{eff} value for this patient has been extrapolated from the range of values derived from the Monte Carlo simulations in §5.5.1.3.1 rather than interpolated. This may well account for a significant amount of the deviation since the model does not include patients of that diameter within the scope of its design.

There are other possible explanations; it was demonstrated in §5.5.1.4 that increased amounts of adipose tissue led to lower values of μ_{eff}. With this patient being larger than any other, it is likely they had a higher percentage of body fat. This would mean the true value of μ_{eff} would be lower than the value used by the computational model, as is obvious for this patient. Given the modest difference to μ_{eff} from an increased body fat percentage as shown in §5.5.1.4, the patient's increased body fat does not fully explain the discrepancy between estimated and measured patient AP abdominal thickness. The patient may have other anatomical variations that mean the method used by the computational model to determine a value of μ_{eff} is flawed. This would be the case if the patient were osteoporotic for example. In this case, the spongiosa used in the Monte Carlo model would not be an appropriate surrogate for patients who had bones of lower density than a healthy population.

The deviation between estimated and measured patient AP abdominal thickness may be related to the patient's large size, or this could be a coincidence. There is not enough

information to make a definitive conclusion, however it is prudent to regard the computational model as only being effective within a range of patient thicknesses. This is not likely to impact upon its intended use for a paediatric population.

6.4 Conclusions

This chapter presented the preparations for, and results of, a clinical validation study of the computational model for a cohort of adult patients undergoing AP abdomen examinations. A Monte Carlo model of the Fuji FDR Go digital mobile x-ray unit was created, optimised and validated using the methods described throughout chapter 2. The simulated results were within the uncertainty of measurement for all of the validation exposures undertaken.

Initial testing of the Fuji FDR Go digital mobile x-ray unit in clinical use revealed that it would be necessary for the computational model to account for a range of examination FDDs, kV_p values and the frequent, but not universal, use of a mattress placed between the digital detector and the patient. The Monte Carlo model was used to derive μ_{eff} values at varying FDD, kV_p and with and without the mattress. Correction factors for the calculation of k_0 from the examination KAP were calculated at different examination FDDs.

With all of the necessary data for the computational model in place, ethics approval was obtained from the West of Scotland Research Ethics Committee 3 and 20 patients recruited to a clinical validation study. A measurement was made of the patient's AP abdominal thickness in the examination position and the results compared to the estimate made by the computational model using the x-ray image and relevant factors from the LUTs guided by the parameters of the examination. The agreement between measured and estimated patient thickness was generally excellent at ±9% for 19 of the 20 patients. The deviation

for the remaining patient was significant at 22% which demonstrates there are limitations to the use of the computational model. These probably suggest it cannot be used accurately outside of a range of patient thicknesses, however there is not enough data to definitively conclude this.

Chapter 7 – summary and further work

Overview

This chapter summarises all of the work reported throughout this thesis and draws some overall conclusions. The work necessary to develop the computational model for use with a paediatric patient cohort is discussed.

7.1 Overall summary

The current methods for dose audit of paediatric radiographic examinations require a measurement of patient size - be it a direct measurement of thickness, equivalent cylindrical diameter (ECD) calculated from measured patient height and weight or simply measured patient weight itself – so that examinations can be appropriately compared. Data pertaining to patient size is generally not measured at the time of the examination throughout the UK, meaning there has been no update to the National Diagnostic Reference Levels (NDRLs) for paediatric radiographic examinations since 2000. There have been significant improvements made to the image receptors used for x-ray examinations since 2000; the lack of up to date data with which to compare inhibits local optimisation efforts for paediatric radiographic examinations.

This thesis presents a method for automating the estimation of patient thickness for radiographic examinations using only the radiographic image, the exposure factors with which the examination was undertaken and a priori knowledge relating to the x-ray unit and digital detector on which the examination was undertaken. This computational method is based on the Beer-Lambert law and relies on being able to accurately estimate the air kerma at the image receptor in the absence of an attenuator, k_0, the kerma at the image receptor, k_d, and the effective linear attenuation coefficient, μ_{eff}. Whereas estimates of k_0 and k_d rely on look up tables (LUT) populated with the results of extensive measurement and calibration, values of μ_{eff} are derived from Monte Carlo simulations using BEAMnrc.

The computational model was developed for an adult cohort, since far more data was available for adults and there is a far greater throughput of adult patients undergoing x-ray examinations locally for a clinical validation of the computational model. Its intended

application remains for paediatric patients. The work required to develop the computational model for a paediatric patient cohort is discussed in §7.3.

To ensure accurate results from Monte Carlo simulations, a Monte Carlo model of a specific Philips Optimus 50 radiographic x-ray unit in use at Ninewells Hospital was created, optimised and validated. The validation was comprehensive; the validation method investigated the accuracy of the simulated x-ray field size at a 100cm focus to detector distance (FDD) by comparing against the nominal value and compared the energy fluence spectrum at a 75cm FDD with that produced by the Institute of Physics and Engineering in Medicine's (IPEM) report 78 spectrum generator. Quantitative validation examined how the output varied across the full extent of the x- and y-axes in 1cm increments, calculated the 1^{st} and 2^{nd} half value layers (HVLs) for x-ray field sizes measuring 10x10cm and 40x40cm and derived values of μ_{eff} for varying thicknesses of both water and solid water high equivalency (HE) attenuators, comparing each with the equivalent result from measurements made directly on the x-ray unit.

The computational model was first created for the specific case of deriving the thickness of a single composition attenuator – solid water HE. This presented the simplest scenario to which the computational model could be applied as it involves only a very narrow range of μ_{eff} values and allows the methods for estimating k_0 and k_d to be tested such that the estimates could be compared against measured values. Values of k_0 were estimated in two ways; the first used measurements of the x-ray unit's output that had been made previously and made corrections for the effect of kV_p, mAs, FDD, focal spot selection and field size. The second used the measured kerma area product (KAP) and made corrections for the effect of field size and kV_p. In both cases, correction factors were measured for each variable across a clinically relevant range.

Values of k_d were estimated using both the examination detector dose indicator (DDI) and a measurement of average pixel value (PV) made at the centre of the radiographic image. These values were used with a single calibration relating DDI or PV to kerma at the equivalent kV_p. These calibrations had been measured for both DDI and the signal transfer property (STP) across the relevant kV_p range. Values of kerma for any DDI or PV can be interpolated between calibrations at kV_p values that are as close as possible to that used for the examination if there was no calibration undertaken at that specific kV_p. This is possible as it was demonstrated that the quality of the x-ray beam as it exits the attenuator for a broad field, inclusive scatter geometry is observed not to vary much for an attenuator in excess of that equivalent to 100mm of solid water HE for a single kV_p.

Values of μ_{eff} were estimated from the relationship between the estimated $\frac{k_d}{k_0}$ and values calculated from kerma measurements made at the exit surface of varying depths of water and thicknesses of solid water HE.

The computational model was used to estimate the thickness of a single composition attenuator on a Philips Optimus 50 radiographic x-ray unit with Fuji computed radiography (CR) system, a Fuji direct digital radiography (DDR) mobile unit and an Xograph-Canon DDR system. The agreement between the attenuator thickness estimated by the computational model and the known thickness of the attenuator was excellent for all x-ray units. The largest deviation between the two across all three x-ray units was 7%. The largest deviation in the estimates of k_0, k_d and μ_{eff} across all three x-ray units were 6.3%, 7.3% and 3.5% respectively.

Having demonstrated that the computational model works accurately for a single composition attenuator on a range of x-ray units, the model was then modified to account for attenuators composed of multiple materials. Patient data from 50 computed tomography (CT) examinations that had been undertaken locally for abdomen, chest and

pelvis examinations was used to create patient models for Monte Carlo simulation. These were added to the existing Monte Carlo model and were used to provide a range of clinically relevant μ_{eff} values, derived as they were from real patients. A second set of simulations was run for each patient, in which the patient was simulated lying on top of an x-ray couch mattress. For chest and pelvis examinations, a single value of μ_{eff} can be used by the computational model as there is no reliable relationship between μ_{eff} and $\frac{k_d}{k_0}$ with which to select a value of μ_{eff} for any given examination. For abdomen examinations, a more accurate estimate of μ_{eff} can be selected using the relationships between patient thickness, μ_{eff} and $\frac{k_d}{k_0}$. An analysis of the effect of varying the percentage body fat on μ_{eff} revealed that the differences were not significant. All simulations assumed a 20% contribution of adipose tissue to all of the soft tissues measured on each patient's CT examination. The computational model was used to estimate the anterior-posterior (AP) thickness of each of the patients included in the cohort of 150 used to create the patient models for Monte Carlo simulation. For abdomen examinations, all 50 estimates were within ±6% of the measured thickness, for chest examinations, 47 estimates were within ±10% of the measured thickness and for pelvis examinations, 41 estimates were within ±10% of the measured thickness.

Having demonstrated the greatest accuracy for patient thickness estimation, abdomen examinations were selected as the focus for a clinical validation study of the computational model. Ethics approval was granted for a clinical validation study that would apply the computational model to 20 patients undergoing AP abdomen x-ray examinations as part of their routine care. The estimates of patient thickness made by the computational model were then compared with measurements made directly on the patient at the time of the examination. The results were excellent; for 19 of the 20 patients, the AP abdominal thickness estimated by the computational model agreed with that measured to within ±9%.

7.2 Overall conclusions

The following conclusions can be drawn from this work;

- It is possible to create a Monte Carlo model using BEAMnrc of a specific radiographic x-ray unit in a broad beam geometry that produces results for x-ray field size that are close to the nominal value and an energy fluence spectrum that is close to that produced by the IPEM report 78 spectrum generator. Further, the model produces results for the variation in output across the full extent of the x- and y-axes, values for 1^{st} and 2^{nd} HVL and values of μ_{eff} that agree with measurements made on the x-ray unit to within the uncertainty of measurement
- The BEAMnrc Monte Carlo model can be used to accurately derive the values of μ_{eff} required throughout this work
- The computational model calculates k_0 to within an average of 0.96% of the measured value using the output method and to within an average of 3.18% of the measured value using the KAP method
- The computational model calculates k_d to within an average of 2.88% of the measured value using the exposure DDI and to within an average of 3.37% of the measured value using the PV method
- The computational model calculates μ_{eff} to within an average of 2.25% of the measured value for a single composition attenuator
- The computational model calculates the thickness of a single composition attenuator to within 7% for a range of exposures across three x-ray different units
- Monte Carlo simulations demonstrated that the value of μ_{eff} does not vary significantly with an increased adipose tissue contribution to soft tissue composition. It is reasonable to use a fixed value of 20% contribution of adipose tissue to all soft tissues for all simulations

- Following a clinical validation study, it is concluded that the computational model is generally accurate when used to estimate the AP abdominal thickness of an adult patient. The agreement between measured and estimated patient thickness was ±9% for 19 of the 20 patients. The deviation for the remaining patient was significant at 22% which demonstrates there are limitations to the use of the computational model
- It is likely the computational model cannot be used accurately outside of a range of patient thicknesses, however there is not enough data to definitively conclude this. This does not have a significant bearing on the computational model's intended use as a tool to assist with paediatric patient dose audit for radiographic examinations

7.3 Further work; adapting the model for a paediatric cohort

The computational model was created using adult data and the accuracy of the computational model was assessed using an adult cohort. As the intended application for the computational model is to facilitate patient dose audit of radiographic examinations of paediatric patients, the computational model needs to be adapted for a paediatric cohort. This adapted computational model should then be tested on a paediatric cohort.

7.3.1 Adapting the computational model

The computational model relies on the accurate estimation of k_0, k_d and μ_{eff}. The method of estimating a value of k_0 is independent of the attenuator, therefore will work as accurately for a paediatric cohort. Where paediatric patients are generally smaller than adults, it is expected that collimation will be used. This is adequately accounted for by the correction factor k_{field} already applied in equations 3.2 and 3.5 (§3.3.1.1 and §3.3.1.3).

It was demonstrated throughout §3.3.2.5 - 3.3.2.7 that a single calibration of detector dose indicator (DDI) or signal transfer property (STP) is all that is required to accurately estimate k_d, provided the calibration was undertaken in a broad beam geometry with an attenuator equivalent to a thickness greater than 10cm of solid water high equivalency (HE). Those calibrations were undertaken using the maximum field size. This is appropriate for a computational model for an adult patient cohort as there is very seldom any need for collimation for examinations of the trunk (i.e. chest, abdomen and pelvis). Indeed it is often necessary to undertake two examinations to cover the entire abdomen. For a paediatric cohort however, it is expected that collimation would be applied for many patients. In anticipation of this, it would be necessary to evaluate the effect of a varying field size on the DDI and STP calibrations and to investigate the effect of attenuators of different sizes (i.e. 15x15 and 10x10cm square attenuators).

New values of μ_{eff} will be required for paediatric patients. The method with which μ_{eff} was estimated for adult patients throughout chapter 5 – by making measurements of adult patients having undergone computed tomography (CT) examinations and using these to create Monte Carlo simulations – is sound. It will be necessary to repeat this process using CT images of paediatric patients for each clinical site. As well as assessing gender specific values of μ_{eff}, age specific values should be investigated as well. Whilst age is not a good indicator of patient diameter, it is a good indicator of patient development [124]. It is likely that bone density and soft and adipose tissue composition will show a variation with patient age that would mean different values of μ_{eff} should be used for selected patient age ranges.

7.3.2 Clinical validation study for the adapted computational model

With the investigatory work as identified in §7.3.1 having been undertaken, and with the computational model having been adapted for a paediatric patient cohort, it will be necessary to validate the computational model's performance for a paediatric cohort. This will require further clinical validation studies, each concentrating on a dedicated clinical site. Abdomen, chest and pelvis examinations are the three clinical examinations for which the computational model is expected to work and for which there is a need for patient dose audit.

Once a location has been identified for these clinical validation studies, there is a lot of work to be undertaken in preparation. The x-ray unit will need to have a corresponding Monte Carlo model. This can be created quickly using the model presented in this work as a starting point before adjusting for any unique differences in the design of the x-ray units. The validation method presented in this work should be applied. Measurements of x-ray tube output and KAP and image receptor calibrations will be required to facilitate the estimates of k_0 and k_d. For k_d, those additional considerations outlined in §7.3.1 should be considered. Measurements to allow the estimate of all of the correction factors used for the estimate of k_0 will have to be made. A range of paediatric examinations will need to be simulated using the Monte Carlo model to derive values of μ_{eff}. These should consider gender and age specific values, as discussed in §7.3.1. This will require access to CT examinations for a large number of paediatric patients to fully account for the differences in patient diameter across the paediatric age range for both genders. These should be available at a dedicated paediatric imaging department or children's hospital.

7.3.3 Implementation of the computational model

The computational model could be implemented by a medical physics department for any imaging facility if they had the necessary skills and resources. This would lead to a significant duplication of effort however, as it could be conceived that Monte Carlo simulations and image receptor calibrations would be repeated for the same make and model of x-ray equipment across many sites. It would be expected that the results for all of these would be very close (theoretically the same, certainly within experimental uncertainty). Further, the selection of appropriate values of μ_{eff} would require each site to have access to a large number of paediatric CT examinations on which to base Monte Carlo simulations, which may not be the case. Estimating the thickness on a patient by patient basis would also require the re-processing of clinical images to make the required measurement of PV using the processing for which the image receptor calibrations were made. This would be an inefficient and resource intensive method for patient dose audit.

The optimal solution is to have the computational model built into the x-ray units themselves. For a DDR system, the x-ray unit will have access to all of the exposure and image information required to estimate each of the variables used by the computational model. The manufacturers would only have to develop one Monte Carlo model per imaging system and make one set of image receptor calibrations per kV_p. One single set of μ_{eff} values or relationships could be made available for any manufacturer wishing to incorporate this computational model into their equipment. The process of making a copy of each image using minimal processing and of making a measurement of the average PV at the centre of the image could also be automated within the software for paediatric patients, allowing the x-ray system itself to produce an estimate of patient thickness for entry into the patient record by the operator. Patient dose audit could then proceed in much the way it does now; either through the use of a dose management system (DMS),

the use of manually completed forms (to which a field for estimated patient thickness can be added) or following an audit of data downloaded from the radiology information system (RIS) which could include a field for estimated patient thickness (there are already multiple fields for recording patient dose). This would allow users the benefit of the computational model with the minimum of global effort in producing it.

7.3.4 Using the computational model for paediatric patient dose audit

As discussed in §1.5 there is a problem with paediatric patient dose audit in the UK (and beyond) in that insufficient data containing some measurement of patient size (e.g. a direct measurement of patient diameter or patient weight) is submitted to national patient dose audits to allow for any NDRLs to be proposed.

The best and most accurate solution is for measurements of patient diameter in the examination orientation, or of patient weight, to be made for every paediatric patient undergoing a radiographic x-ray examination. This is in keeping with all current national and international recommendations [40, 42-44]. Further education for operators on the importance of these measurements of patient size is required.

Were it to work for a paediatric patient cohort, the computational model would produce an estimate of patient diameter that is comparable to a direct measurement. This has the advantage that any data acquired by direct measurement and using the computational model can be used in the same pool to analyse with a view to recommending NDRLs. This is not the case where patient weight has been measured. The disadvantage of the computational model is the extensive and complex work required for its implementation. This will prevent widespread adoption unless the manufacturers of x-ray equipment can incorporate it into their equipment.

There have been no other documented attempts to automate the estimation of patient diameter for radiographic imaging. The 'MyXrayDose' DMS does offer a water equivalent thickness for the patient following each radiographic examination. Whilst there is no white paper or publication available for this feature, it is known to use information from the Digital Imaging and Communications in Medicine (DICOM) header, specifically that related to the signal at the detector (via the detector dose indicator (DDI)) and the intensity of the beam that exited the x-ray tube (via the kerma area product (KAP) or exposure factors). The estimate of water equivalent thickness is further refined using the results of GEANT4 Monte Carlo simulations. The water equivalent thickness could be used as a representative measure of patient size. The advantage of this metric is that it is much easier to implement than the computational model described throughout this work. One disadvantage is that the water equivalent thickness is not the same as patient thickness, therefore patient dose audit data including a direct measurement of patient thickness or an estimate of patient thickness as made using the computational model described in this work cannot be used alongside data that includes an estimate of water equivalent thickness for the purposes of paediatric patient dose audit. For water equivalent thickness to become the patient size metric of choice would require a universal adoption which is not likely at present since it is only offered by a single DMS – one of at least 10 available on the market [46, 140-148].

Appendix 1: References

1. ICRP, 2007. *The 2007 Recommendations of the International Commission on Radiological Protection*. ICRP Publication 103. Ann. ICRP 37 (2-4).
2. Sumner, D., Wheldon, T. and Watson, W. (1991) *Radiation risks*, 3rd edition. Glasgow, UK: Tarragon Press.
3. IAEA. (2014) *Diagnostic Radiology Physics*. Vienna: International Atomic Energy Agency.
4. NRC. (2006) *Health risks from exposure to low levels of ionising radiation: BEIR VII phase 2*. Washington: The National Academies Press.
5. Wagner, L.K., Eifel, P.J. and Geise, R.A. *Potential biological effects following high X-ray dose interventional procedures.* J Vasc Interv Radiol, 1994. **5**(1): p. 71-84.
6. Smith, F.A. (2000) *A primer in applied radiation physics*. Singapore: World Scientific Publishing Co.
7. UNSCEAR. Sources, Effects and Risks of Ionizing Radiation. UNSCEAR 1988 Report. *United Nations Scientific Committee on the Effects of Atomic Radiation, 1988 Report to the General Assembly, with annexes*. United Nations sales publication E.88.IX.7. United Nations, New York, 1988.
8. UNSCEAR. Sources and Effects of Ionizing Radiation. UNSCEAR 1993 Report. *United Nations Scientific Committee on the Effects of Atomic Radiation, 1993 Report to the General Assembly, with scientific annexes*. United Nations sales publication E.94.IX.2. United Nations, New York, 1993.
9. UNSCEAR. Sources and Effects of Ionizing Radiation. UNSCEAR 1996 Report. *United Nations Scientific Committee on the Effects of Atomic Radiation, 1996*

Report to the General Assembly, with scientific annex. United Nations sales publication E.96.IX.3. United Nations, New York, 1996.

10. Committee on the Biological Effects of Ionizing Radiation. (cited 2019 16/01/2019). *BEIR homepage*. https://www.euronuclear.org/info/encyclopedia/beir.htm.

11. 11. United Nations Scientific Committee on the Effects of Atomic Radiation. (cited 2019 16/01/2019). UNSCEAR homepage. http://www.unscear.org/.

12. International Commission on Radiological Protection. (cited 2019 16/01/2019). *ICRP homepage*. http://www.icrp.org/index.asp.

13. ICRP, 1966. *Recommendations of the International Commission on Radiological Protection*. ICRP Publication 9. Pergamon Press, Oxford.

14. Kathren, R.L. (1985) *Radiation Protection*. Medical Physics Handbooks 16. Bristol, UK: Adam Hilger Ltd.

15. Doss, M., Little, M.P. and Orton, C.G. *Point/Counterpoint: low-dose radiation is beneficial, not harmful.* Med Phys, 2014. **41**(7): p. 070601.

16. Shore, R.E., Beck, H.L., Boice, J.D., Caffrey, E.A., Davis, S., Grogan, H.A., Mettler, F.A., Preston, R.J., Till, J.E., Wakeford, R., Walsh, L. and Dauer, L.T. *Implications of recent epidemiological studies for the linear nonthreshold model and radiation protection*. J Radiol Prot. 2018 38(3): 1217-1233.

17. National Council on Radiation Protection and Measurements. (cited 2019 16/01/2019). *NCRP homepage*. https://ncrponline.org/.

18. Council Directive 2013/59 Euratom of 5 December 2013, laying down basic safety standards for protection against the dangers arising from exposure to ionising radiation. Official Journal of the European Union L13.

19. *IR(ME)R Ionising Radiation (Medical Exposure) Regulations 2017* (SI 2017 No 1322) London, HMSO.

20. Committee on Medical Aspects of Radiation in the Environment. (cited 2019 16/01/2019). *COMARE homepage*. https://www.gov.uk/government/groups/committee-on-medical-aspects-of-radiation-in-the-environment-comare.

21. COMARE, 2014. *Sixteenth Report: Patient radiation dose issues resulting from the use of CT in the UK*. COMARE report 16. Chilton: Public Health England.

22. ICRP, 2004. *Managing Patient Dose in Digital Radiology*. ICRP Publication 93. Ann. ICRP 34 (1).

23. Royal College of Radiologists. (cited 2019 16/01/2019). *RCR homepage*. https://www.rcr.ac.uk/.

24. Public Health England. (cited 2019 16/01/2019). *PHE homepage*. https://www.gov.uk/government/organisations/public-health-england.

25. NRPB, 1990. Patient dose reduction in diagnostic radiology. Chilton: National Radiological Protection Board.

26. ICRP, 1991. *1990 Recommendations of the International Commission on Radiological Protection*. ICRP Publication 60. Ann. ICRP 21 (1-3).

27. Institute of Physics and Engineering in Medicine. (cited 2019 16/01/2019). *IPEM homepage*. https://www.ipem.ac.uk/.

28. IPSM, 1992. *National Protocol for Patient Dose Measurements in Diagnostic Radiology*. Chilton: National Radiological Protection Board.

29. ICRP, 1996. *Radiological Protection and Safety in Medicine*. ICRP Publication 73. Ann. ICRP 26 (2).

30. Department of Health and Social Care. (cited 2019 16/01/2019). *DoHSC homepage*. https://www.gov.uk/government/organisations/department-of-health-and-social-care.

31. IPEM, 2004. *Guidance on the Establishment and Use of Diagnostic Reference Levels for Medical X-Ray Examinations.* IPEM report 88. York: Institute of Physics and Engineering in Medicine.

32. Hart, D., Hillier, M.C., Wall, B. F., Shrimpton, P.C. and Bungay, D. (1996) *Doses to patients from medical x-ray examinations in the UK – 1995 review.* NRPB-R289. Chilton, National Radiological Protection Board.

33. Hart, D., Hillier, M.C. and Wall, B. F. (2002) *Doses to patients from medical x-ray examinations in the UK – 2000 review.* Chilton, National Radiological Protection Board.

34. Hart, D., Hillier, M.C. and Wall, B. F. (2007) *Doses to patients from radiographic and fluoroscopic x-ray imaging procedures in the UK – 2005 review.* Chilton, Health Protection Agency.

35. Hart, D., Hillier, M.C. and Shrimpton, P.C. (2012) *Doses to patients from radiographic and fluoroscopic x-ray imaging procedures in the UK – 2010 review.* Chilton, Health Protection Agency.

36. Department of Health and Social Care. (cited 2019 16/01/2019). *Current UK National DRLs*. https://www.gov.uk/government/publications/diagnostic-radiology-national-diagnostic-reference-levels-ndrls/national-diagnostic-reference-levels-ndrls.

37. IR(ME)R Ionising Radiation (Medical Exposure) Regulations 2000 (SI 2000 No 1059) London, HMSO.

38. The Ionising Radiation (Protection of Persons Undergoing Medical Examination or Treatment) Regulations 1988 (SI 1988 No 778) London, HMSO.

39. European Commission (1996) *European guidelines on quality criteria for diagnostic radiographic images in paediatrics*. Luxembourg, European Commission.

40. Hart, D., Wall, B. and Shrimpton, P.C. (2000) *Reference doses and patient size in paediatric radiology.* NRPB-R318. Chilton, National Radiological Protection Board.

41. International Atomic Energy Agency. (cited 2019 16/01/2019). IAEA homepage. https://www.iaea.org/.

42. International Atomic Energy Agency (2013) *Report 24 – dosimetry in diagnostic radiology for paediatric patients*. Vienna, International Atomic Energy Agency.

43. ICRP, 2013. *Radiological protection in paediatric diagnostic and interventional radiology*. ICRP Publication 121. Ann. ICRP 42(2).

44. ICRP, 2017. *Diagnostic reference levels in medical imaging*. ICRP Publication 135. Ann. ICRP 46(1).

45. Martin, L., Ruddlesden, R., Makepeace, C., Robinson, L., Mistry, T. and Starritt, H. *Paediatric x-ray radiation dose reduction and image quality analysis.* J Radiol Prot, 2013. **33**(3): p. 621-33.

46. Myxraydose. (cited 2019 24/04/2019). *Myxraydose dose management system*. https://myxraydose.com/.

47. Agostinelli, S. et al. *Geant 4 - a simulation toolkit.* Nuclear Instruments and Methods in Physics Research; Section A: Accelerators, Spectrometers, Detectors and Associated Equipment, 2003. **506**(3).

48. Lunt, B. (2017) *Benchmarking Image Quality as well as dose - adding a critical piece of the jigsaw*. Dose management in contemporary radiological practice, Birmingham, Institute of Physics and Engineering in Medicine.

49. Kawrakow, I. (1999) *The Monte Carlo simulation of radiation transport.* AAPM annual conference, Nashville; TN, The American Association of Physicists in Medicine.

50. Sheikh-Bagheri, D., Kawrakow, I., Walters, B. and Rogers, D.W.O. (2006) *Monte Carlo simulations: Efficiency improvement techniques and statistical considerations*. Proceedings of the 2006 AAPM summer school, Madison; WI, Med. Phys. Publ.

51. Berger, M.J. (1963) *Monte Carlo calculation of the penetration and diffusion of fast charged particles*. Washington D.C, National Bureau of Standards.

52. MCNPX-5 Monte Carlo Team. (2003) *MCNP – a general Monte Carlo N-Particle transport code, version 5, Vol. I: Overview and theory*. Oak Ridge, TN, Los Alamos National Laboratory.

53. Salvat, F., Fernandez-Varea, J. M., Baro, J. and Sempau, J. *PENELOPE: an algorithm for Monte Carlo simulation of the penetration and energy loss of electrons and positrons in matter.* Nucl. Instrum. Meth., 1995. **B100**: p. 31-46.

54. Ferrari, A., Fasso, A., Ranft, J. and Sala, P.R. (2005) *FLUKA: a multi-particle transport code (program version 2005).* CERN-2005-10, **INFN/TC-05/11**(SLAC-R-773).

55. Kawrakow, I., Mainegra-Hing, E., Rogers, D.W.O., Tessier, F. and Walters, B.R.B. (2017) *The EGSnrc Code System: Monte Carlo simulation of electron and photon transport*. Technical Report PIRS-701. Ottawa, National Research Council: Canada.

56. Ay, M.R., Shahriari, M., Sarkar, S., Adib, M. and Zaidi, H. *Monte Carlo simulation of x-ray spectra in diagnostic radiology and mammography using MCNP4C.* Phys Med Biol, 2004. **49**(21): p. 4897-917.

57. Guthoff, M., Brovchenko, O., de Boer, W., Dierlamm, A., Muller, T., Ritter, A., Schmanau, M. and Simonis, H-J. *Geant4 simulation of a filtered X-ray source for radiation damage studies.* Nuclear Instruments and Methods in Physics Research; Section A: Accelerators, Spectrometers, Detectors and Associated Equipment, 2012. **675**: p. 118-122.

58. Badano, A. and Sempau, J. *MANTIS: combined x-ray, electron and optical Monte Carlo simulations of indirect radiation imaging systems.* Phys Med Biol, 2006. **51**(6): p. 1545-61.

59. Skordis, E., Vlachoudis, V. and Welsch, C.P. (2017) *A Monte Carlo approach to imaging and dose simulations in realistic phantoms using compact x-ray source*. IPAC2017, Copenhagen, International Particle Accelerator Conference.

60. Bhat, M., Pattison, J., Bibbo, G. and Caon, M. *Off-axis x-ray spectra: a comparison of Monte Carlo simulated and computed x-ray spectra with measured spectra.* Med Phys, 1999. **26**(2): p. 303-9.

61. Rogers, D.W., Faddegon, B.A., Ding, G.X., Ma, C.M., We, J. and Mackie, T.R. *BEAM: a Monte Carlo code to simulate radiotherapy treatment units.* Med Phys, 1995. **22**(5): p. 503-24.

62. Mackie, T., Reckwerdt, P.J., Wells, C.M., Yang, J.N., Deasy, J.O., Podgorsak, M., Holmes, M.A., Rogers, D.W.O., Ding, G.X., Faddegon, B.A., Ma, C-M.C., Bielajew, A.F. and Cygler, J.E. *The OMEGA project: comparison among EGS4 electron beam simulations, 3D Fermi-Eyges Calculations and dose measurements*. 2010: ResearchGate.

63. Ali, E.S. and Rogers, D.W.O. *Benchmarking EGSnrc in the kilovoltage energy range against experimental measurements of charged particle backscatter coefficients.* Phys Med Biol, 2008. **53**(6): p. 1527-43.

64. Rogers, D.W.O., Ma, C-M., Ding, G.X. and Walters, B. (2013) *BEAM User's Manual. NRC Report PIRS-0509(a)* RevL. Ottawa, National Research Council: Canada.

65. Kawrakow, I., Mainegra-Hing, E., Rogers, D.W.O., Tessier, F. and Walters, B.R.B (2013) *The EGSnrc Code System: Monte Carlo simulation of electron and photon transport. NRCC Report PIRS-701*. Ottawa, National Research Council: Canada.

66. Roeck, W.W. *X-ray source assembly acceptance testing.* Medical Physics Monograph No. 20, 1994. Specifications, acceptance testing and quality control of diagnostic x-ray imaging equipment: p. 26.

67. Kuhn, H., Gajewski, H. *The extra-focal radiation from rotating anode x-ray tubes and its effect on the quality of the radiograph.* Electrom Edica, 1971. **4**: p. 125 - 130.

68. Rao, G. *Influence of off-focal radiation on radiographic resolution and patient exposure.* Applied Radiology, 1974: p. 45-49.

69. Jackson, W. *Measurement of kilovoltage by the penetrameter - theoretical aspects.* Phys Med Biol, 1975. **20**(2): p. 268-81.

70. Weaver, K.E., Robert, M.S. and Wagner, F. *Performance considerations of x-ray tube focal spot*, in *SPIE - Medical X-ray Photo-Optical Systems Evaluation 56*. 1975. p. 150-158.

71. Birch, R. *The spectrum and intensity of extra-focal (off-focus) radiation.* Br J Radiol, 1976. **49**(587): p. 951-5.

72. Roeck, W.W., Martin, J.T. and Beach, R. *Analysis of contributing factors to the occurrence of off-focus radiation (OFR).* Med Phys, 1992. **19**(5): p. 1201-4.

73. Cranley, K., Gilmore, B.J., Fogarty, G.W. and Desponds, L. (1997) *Catalogue of diagnostic x-ray spectra and other data; CD edition, electronic version prepared*

by D Sutton. Technical report 78. York, The Institute of Physics and Engineering in Medicine.

74. Shen, S.Z., Bloomquist, A.K., Mawdsley, G.E., Yaffe, M.J. and Elbakri, I. *Effect of scatter and an antiscatter grid on the performance of a slot-scanning digital mammography system.* Med Phys, 2006. **33**(4): p. 1108-15.
75. Ali, E.S. and Rogers, D.W.O. *Quantifying the effect of off-focal radiation on the output of kilovoltage x-ray systems.* Med Phys, 2008. **35**(9): p. 4149-60.
76. Sobol, W.T. *High frequency x-ray generator basics.* Med Phys, 2002. **29**(2): p. 132-44.
77. Meredith, W.J. and Massey, J.B. (1977) *Fundamental physics of radiology, 3rd edition*. Bristol: John Wright and Sons Ltd.
78. Ma, C-M.C., Rogers, D.W.O. (2017) *BEAMDP as a general-purpose utility*. Ottawa, National Research Council: Canada.
79. Ma, C-M.C., Rogers, D.W.O. (2013) *BEAMDP User's Manual. NRC report PIRS-0509(c) Rev A*. Ottawa, National Research Council: Canada.
80. Philips Healthcare. (2009) *RO 1750 ROT 360 service information; x-ray tube assembly*. Best, Philips Healthcare.
81. Ed Fagan Inc. [cited 2018 13/09/2018]. *Refractory Metals and Alloys*. http://www.edfagan.co.uk/refractory-molybdenum-tungsten-alloy-tantalum-niobium-rhenium-europe.php.
82. Hill, D.R. (1975) *Principles of Diagnostic X-Ray Apparatus*. Philips Technical Library, London and Basingstoke: The Macmillan Press Ltd.
83. Meijers, S., Caicedo-Martinez, C. [cited 2019 17/01/2019]. *Impurities in Aluminium*. http://core.materials.ac.uk/search/detail.php?id=2861.
84. Sutton, D.G. and Reilly, A.J. (2015) *IPEM report 78 spectrum processor*. The Institute of Physics and Engineering in Medicine.

85. Gammex. (2010) *Tissue Mimicking Materials (TMM) Nominal Characteristics*. Melbourne, FL, SunNuclear.

86. AAPM (2015) *Monte Carlo Reference Data Sets for Imaging Research; the report of AAPM task group 195*. College Park, MD, American Association of Physicists in Medicine.

87. International Electrotechnical commission (2012) *Medical Electrical Equipment – Dosimeters with Ionization Chambers and/or Semiconductor Detectors as used in X-ray Diagnostic Imaging. International Electrotechnical Committee.*

88. Martin, C.J. *An evaluation of semiconductor and ionization chamber detectors for diagnostic x-ray dosimetry measurements.* Phys Med Biol, 2007. **52**(15): p. 4465-80.

89. Raysafe. [cited 10/10/2019] *Raysafe Xi product specification*. http://mediabank.raysafe.com/downloadAsset.jsp?catalog=RaySafe+Media+Bank&id=1604&.

90. International Atomic Energy Agency (2007) *Dosimetry in diagnostic radiology: an international code of practice*, *Technical Report 457*. Vienna: International Atomic Energy Agency.

91. Worrall, M. and Sutton, D.G. *Developing a method and deriving an uncertainty budget for the internal calibration of dosemeters for radiographic equipment.* J Radiol Prot, 2015. **35**(1): p. 209-22.

92. Birch, R. and Marshall, M. *Computation of bremsstrahlung X-ray spectra and comparison with spectra measured with a Ge(Li) detector.* Phys Med Biol, 1979. **24**(3): p. 505-17.

93. 93. Birch, R., Marshall, M. and Ardran, G.M. (1979) *Catalogue of spectral data for diagnostic X-rays*. London: Hospital Physicist's Association.

94. Ali, E.S.M. (2007) *Making the EGSnrc/BEAMnrc system more efficient, accurate and realistic in simulating kilovoltage x-ray systems.* Carleton University, Department of Physics.

95. Salehi, Z., Ya Ali, N.K. and Yusoff, A.L. *X-ray spectra and quality parameters from Monte Carlo simulation and analytical filters.* Appl Radiat Isot, 2012. **70**(11): p. 2586-9.

96. Berger, M.J., Inokuti, M., Anderson, H.H., Bichsel, H., Dennis, J.A., Powers, D., Seltzer, S.M. and Turner, J.E. (1984) *Stopping powers for electrons and positrons*. Bethesda, MD, International Commission on Radiation Units and Measurements.

97. National Institute of Standards and Technology. [cited 2018 15/11/2018] *Database of mass attenuation coefficients.* https://www.nist.gov/pml/x-ray-mass-attenuation-coefficients.

98. Gammex. [cited 2017 21/06/2017] *Solid Water HE & TMM product data sheet: 2015*. https://www.sunnuclear.com/documents/datasheets/SolidWaterHE-TMM_D070115.pdf.

99. Raysafe. [cited 2019 18/01/2019] *Raysafe Xi User Manual*. http://www.raysafe.com/Support/Product%20Support/RaySafe%20Xi.

100. Medicines and Healthcare products Regulatory Agency (2006) *Radiation Dose Issues with Digital Radiography Systems, MHRA Notice*. London, Medicines and Healthcare products Regulatory Agency.

101. International Electrotechnical commission (2008) *Medical electrical equipment - Exposure index of digital X-ray imaging systems - Part I: Definitions and requirements for general radiography*, in *IEC 62494-1*. Geneva, International Electrotechnical commission.

102. Tucker, D.M. and Rezentes, P.S. *The relationship between pixel value and beam quality in photostimulable phosphor imaging.* Med Phys, 1997. **24**(6): p. 887-93.

103. The Institute of Physics and Engineering in Medicine (2012) *Measurement of the performance characteristics of diagnostic X-ray systems. Part VII digital imaging systems*. IPEM report 32. York, The Institute of Physics and Engineering in Medicine.

104. Asai, Y., Uemura, M., Matsumoto, M. and Kanamori, H. *Dependence of radiographic sensitivity of CR imaging plate on X-ray tube voltage.* Radiol Phys Technol, 2008. **1**(1): p. 100-5.

105. Joint Committee for Guides in Metrology (2008) *Evaluation of measurement data - Guide to the expression of uncertainty in measurement*. Bureau International des Poids et Mesures.

106. The Institute of Physics and Engineering in Medicine (2005) *Recommended standards for the routine performance testing of diagnostic X-ray imaging systems*. IPEM report 91. York, The Institute of Physics and Engineering in Medicine.

107. Fujifilm medical systems USA Inc. (2014) *CR users guide*. Lexington, MA, Fujifilm medical systems USA Inc.

108. Rasband, W.S. (1997-2017) *ImageJ*. Bethesda, MA, U.S. National Institutes of Health.

109. The Institute of Physical Sciences in Medicine (1991) *Data for estimating X-ray tube total filtration.* York, The Institute of Physical Sciences in Medicine.

110. The MathWorks Inc (2018) *MATLAB 8.0 and Statistics Toolbox 8.1*. Natick, MA, The MathWorks Inc.

111. The National Institute for Health and Care Excellence (2014) *Head injury: assessment and early management*, in *Clinical guidelines*. London, The National Institute for Health and Care Excellence.

112. Shi, C. and Xu, X.G. *Development of a 30-week-pregnant female tomographic model from computed tomography (CT) images for Monte Carlo organ dose calculations.* Med Phys, 2004. **31**(9): p. 2491-7.

113. Xu, X.G., Chao, T.C. and Bozkurt, A. *VIP-Man: an image-based whole-body adult male model constructed from color photographs of the Visible Human Project for multi-particle Monte Carlo calculations.* Health Phys, 2000. **78**(5): p. 476-86.

114. Zubal, I.G., Harrell, C.R., Smith, E.O., Rattner, Z., Gindi, G. and Hoffer, P.B. *Computerized three-dimensional segmented human anatomy.* Med Phys, 1994. **21**(2): p. 299-302.

115. Kramer, R., Khoury, H.J., Vieira, J.W. and Lima, V.J. *MAX06 and FAX06: update of two adult human phantoms for radiation protection dosimetry.* Phys Med Biol, 2006. **51**(14): p. 3331-46.

116. Lee, C., Williams, J.L., Lee, C. and Bolch, W.E. *The UF series of tomographic computational phantoms of pediatric patients.* Med Phys, 2005. **32**(12): p. 3537-48.

117. Petoussi-Henss, N., Zanki, M., Fill, U. and Regulla, D. *The GSF family of voxel phantoms.* Phys Med Biol, 2002. **47**(1): p. 89-106.

118. Bruder, H., Flohr, T., Fuchs, T., von der Haar, T., Karolczak, M., Kachelriess, M., Lauritsch, G., Schaller, S., Seibert, U., Sourbelle, K., Stierstorfer, K., Watzke, O. and Stenner, P. [cited 2019 18/01/2019] *The FORBILD thorax phantom*. http://www.imp.uni-erlangen.de/phantoms/.

119. Zhu, J., Zhao, S., Ye, Y. and Wang, G. *Computed tomography simulation with superquadrics.* Med Phys, 2005. **32**(10): p. 3136-43.

120. Han, E.Y., Bolch, W.E. and Eckerman, K.F. *Revisions to the ORNL series of adult and pediatric computational phantoms for use with the MIRD schema.* Health Phys, 2006. **90**(4): p. 337-56.

121. Peter, J., Jaszczak, R. and Coleman, R. *Composite quadric-based object model for SPECT Monte-Carlo simulation.* J. Nucl. Med, 1998. **39**.

122. Pretorius, P.H., King, M.A., Tsui, B.M., LaCroix, K.J. and Xia, W. *A mathematical model of motion of the heart for use in generating source and attenuation maps for simulating emission imaging.* Med Phys, 1999. **26**(11): p. 2323-32.

123. Segars, W.P. and Tsui, B.M. *MCAT to XCAT: The Evolution of 4-D Computerized Phantoms for Imaging Research: Computer models that take account of body movements promise to provide evaluation and improvement of medical imaging devices and technology.* Proc IEEE Inst Electr Electron Eng, 2009. **97**(12): p. 1954-1968.

124. Martini, F.H. (2004) *Fundamentals of Anatomy and Physiology*. 6th ed. USA: Pearson Education International.

125. International Commission on Radiation Units and Measurements (1989) *Tissue substitutes in radiation dosimetry and measurement*. Bethesda, MD, International Commission on Radiation Units and Measurements.

126. Clark, K., Vendt, B., Smith, K., Freymann, J., Kirby, J., Koppel, P., Moore, S., Phillips, S., Maffitt, D., Pringle, M., Tarbox, L. and Prior, F. *The Cancer Imaging Archive (TCIA): maintaining and operating a public information repository.* J Digit Imaging, 2013. **26**(6): p. 1045-57.

127. Roche, C., Bonaccio, E. and Filippini, J. [cited 2019 18/01/2019] *Radiology data from The Cancer Genome Atlas Sarcoma collection. The Cancer Imaging Archive 2016*. http://doi.org/10.7937/K9/TCIA.2016.CX6YLSUX.

128. Gallagher, D., Heymsfield, S.B., Heo, M., Jebb, S.A., Murgatroyd, P.R. and Sakamoto, Y. *Healthy percentage body fat ranges: an approach for developing guidelines based on body mass index.* Am J Clin Nutr, 2000. **72**(3): p. 694-701.

129. National Health Service. [cited 2019 18/01/2019] *What is the body mass index (BMI)?* https://www.nhs.uk/common-health-questions/lifestyle/what-is-the-body-mass-index-bmi/

130. AAPM (2011) *Size-specific Dose Estimates (SSDE) in Pediatric and Adult Body CT Examinations; the report of AAPM task group 204.* College Park, MD, American Association of Physicists in Medicine.

131. Zhao, Binsheng, Schwartz, Lawrence, H. and Kris, M.G. [cited 2019 18/01/2019] *Data from RIDER_Lung CT. The Cancer Imaging Archive 2015*. http://doi.org/10.7937/K9/TCIA.2015.U1X8A5NR.

132. The Medicines for Human Use (Clinical Trials) Regulations 2004 (SI 2004 No 1031) London, HMSO.

133. NHS Health Research Authority [cited 2019 26/01/19] *Roles and responsibilities*. https://www.hra.nhs.uk/planning-and-improving-research/research-planning/roles-and-responsibilities/.

134. Fujifilm medical systems USA Inc. [cited 2019 26/01/19] *Virtual grid*. https://www.fujifilmusa.com/products/medical/digital-x-ray/image-processing/virtual-grid/.

135. Fujifilm medical systems USA Inc. [cited 2019 26/01/19] *Fujifilm - FDR Go technical manual.* https://www.medwrench.com/equipment/9720/fujifilm-fdr-go.

136. American Chemistry Council. [cited 2019 18/01/2019] *How polyurethane is made*. https://polyurethane.americanchemistry.com/How-Polyurethane-is-Made/.

137. Rohrig, B., du Prel, J.B., Wachtlin, D., Kwiecien, R. and Blettner, M. *Sample size calculation in clinical trials: part 13 of a series on evaluation of scientific publications.* Dtsch Arztebl Irnt, 2010. **107**(31-32): p. 552-6.

138. World Health Organisation. [cited 2019 18/01/2019] *Medical device - full definition*. https://www.who.int/medical_devices/full_deffinition/en/.

139. Bland, J.M. and Altman, D.G. *Statistical methods for assessing agreement between two methods of clinical measurement.* Lancet, 1986. **1**(8476): p. 307-10.

140. GE Healthcare. [cited 10/10/2019] *GE Dosewatch*. https://www.gehealthcare.com/products/dose-management/dosewatch-explore.

141. Bayer. [cited 10/10/2019] *Radimetrics.* http://radiology.bayer.co.uk/products/radiation-dose-monitoring/radimetrics/.

142. Qaelum. [cited 10/10/2019] *DOSE.* https://qaelum.com/.

143. Infinitt. [cited 10/10/2019] *doseM.* https://www.infinitt.com/en.

144. PACSHealth. [cited 10/10/2019] *DoseMonitor.* http://www.pacshealth.com/products/dosemonitor/.

145. Sectra. [cited 10/10/2019] *DoseTrack*. https://medical.sectra.com/product/sectra-dosetrack/.

146. Philips Healthcare. [cited 10/10/2019] *Dosewise.* https://www.philips.co.uk/healthcare/clinical-solutions/dosewise.

147. OpenREM. [cited 10/10/2019] *OpenREM*. https://openrem.org/.

148. Siemens. [cited 10/10/2019] *teamplay.* https://www.siemens-healthineers.com/infrastructure-it/digital-ecosystem/teamplay.

Appendix 2: papers and presentations related to this work

Peer reviewed papers

Published

3. Worrall, M. and Sutton, D.G. *Developing a method and deriving an uncertainty budget for the internal calibration of dosemeters for radiographic equipment.* J Radiol Prot, 2015. **35**(1): p. 209-22.
4. Worrall, M., Vinnicombe, S. and Sutton, D.G. *Determining paediatric patient thickness from a single digital radiograph – a proof of principle.* Br J Radiol 2018; **91**: 20180139.
5. Worrall, M. and Sutton, D.G. *Validation of a BEAMnrc Monte Carlo simulation of a broad beam diagnostic x-ray unit.* Rad. Prot. Dosim, 2019, pp 1-12, ncz032, https://doi.org/10.1093/rpd/ncz032.

Under review

1. Worrall, M., Vinnicombe, S. and Sutton, D.G. *Determining patient thickness from a single digital radiograph with a computational model: clinical results from a proof of concept study. Submitted to Clinical Radiology May 2019.*

Conference paper

1. Worrall, M., Vinnicombe, S. and Sutton, D.G. *Estimating patient thickness from a single radiograph – a proof of principle.* International Conference on Radiation Protection in Medicine: Achieving Change in Practice, December 2017, Vienna, Austria. International Atomic Energy Agency.

Presentations

1. *Development of a method for automating paediatric patient diameter estimation for digital radiography*, IPEM Optimisation in Paediatric Imaging meeting, London, 27th April 2016
2. *Estimating patient thickness from a single radiograph – proof of principle*, IPEM MPEC annual meeting, London, 13-14th September 2017.

Posters

1. *Estimating patient thickness from a single radiograph; proof of principle*, IAEA International Conference on Radiation Protection in Medicine: Achieving Change in Practice, Vienna, Austria, December 2017.

Appendix 3: Prizes and awards related to this work

1. 2nd place; best oral presentation for a non-laboratory project. University of Dundee Medical School postgraduate student symposium, Dundee, 12th June 2015.
2. The British Institute of Radiology (BIR) and General Electric (GE) Healthcare – Radiation Safety Award 2017. https://www.bir.org.uk/media-centre/press-releases/2017/october/bir-ge-radiation-safety-award-2017/.
3. The University of Dundee postgraduate research travel award, June 2017.

Appendix 4: The patient information sheet for the clinical trial

Patient Information Sheet

Study title: **Validation of a computational model to estimate patient anterior-posterior dimension from an abdominal radiograph**

Chief Investigator: Dr Sarah Vinnicombe
Principal Investigator: Mark Worrall

Please read this information carefully

We are asking you to consider taking part in a research study that forms part of my PhD project within the School of Medicine at the University of Dundee. My supervisors are Dr Sarah Vinnicombe and Dr David Sutton.

Before you decide whether to participate, we need to be sure that you understand why we are doing the study and what it would involve if you agreed to take part. We are therefore providing you with this information. Please take time to read it carefully, ask any questions, and, if you want, discuss it with others. We will do our best to explain and provide any further information you may ask for now or later.

What is the purpose of this study?

A computational model has been created to estimate the abdominal depth of a patient from a single x-ray image. The model has been tested using phantoms; this study aims to test the accuracy of the model with patients and in a clinical setting.

If the model is found to be accurate following this study, it can be applied to paediatric x-ray examinations. Knowing the paediatric patient abdominal depth will improve imaging technique and should result in lower radiation doses to children.

The computational model is non-commercial. If it is accurate, it will be published so as to allow other hospitals to use it.

Who has reviewed the study?

The study has been reviewed and approved by the East of Scotland Research Ethics Service who are responsible for reviewing research which is conducted on humans and who have raised no objections.

Why have I been invited to take part?

You are eligible for this study as you are having an abdomen x-ray examination. At this stage, the computational model is only being tested on abdomen exams. If you do decide to take part but later decide to withdraw, all data held about you will be deleted from the study database. It is our intention to recruit 20 patients onto the study.

Do I have to take part?

It is up to you to decide. Participation in this study is entirely voluntary and you are free to refuse to take part or to withdraw from the study at any time without having to give a reason and without this affecting your future medical care or your relationship with medical or nursing staff looking after you.

How long will I be in the study?

Your participation in the study will only involve the measurement of your abdominal depth during your clinical abdomen x-ray examination. There is no follow up, you will not have to attend any further appointments for the benefit of the study and you will not be contacted by any of the study team.

University of Dundee NHS Tayside

If I take part what will it involve?

The Principal Investigator for the study will speak with you about the study to make sure you understand why it is being undertaken and what it will involve for you. This is your opportunity to ask any questions you might have about the study. If you change your mind about participation at this stage, the principal investigator will leave and your x-ray examination will proceed without any measurement being made. If you are happy to take part, the Principal Investigator will ask you to sign a consent form confirming this. Before signing the consent form, you will see the ruler that will be used for the measurement.

If you change your mind after the examination, your data will not be used and will be deleted from the study records.

You will have your x-ray as normal, but a measurement of your abdominal depth will be made when you are on the x-ray couch just before the x-ray is performed. This measurement will involve placing a ruler on top of your body for a few seconds with only minimal physical contact from the operator.

We will also record the reason given by your doctor for the x-ray examination to see if this affects the accuracy of the estimate.

Once your x-ray is complete, your participation in the study ends. There are no follow up measurements. Your x-ray will be reported as normal.

Do I have to take part?

It is up to you to decide. Participation in this study is entirely voluntary and you are free to refuse to take part or to withdraw from the study at any time without having to give a reason and without this affecting your future medical care or your relationship with medical or nursing staff looking after you.

Will I receive anything for taking part?

No, there is no payment for participation.

Will my personal information be kept confidential?

Identifiable information about you and your collected study data will be stored locally on a password-protected database in NHS Tayside and designated members of the research team will have access to this information.

Your data will be archived securely for five years after the end of study, after which it will be destroyed. Identifiable information about you will not be published or otherwise shared. Your anonymous study data may be shared with other researchers in the UK.

Are there any disadvantages to taking part?

By taking part in this study you will have the same abdomen x-ray examination that you would have if you didn't take part. All x-ray examinations use ionising radiation, however your exposure to ionising radiation will be the same whether you take part in the study or not.

What are the benefits of taking part?

There are no benefits to you. If the computational model is demonstrated to be accurate however, its application to paediatric x-ray examinations could see radiation dose reduced to children across the UK from x-ray examinations as a result of better optimised exposures.

Who is sponsoring this research?

The study is sponsored by the University of Dundee and NHS Tayside. The study was organised by Dr Sarah Vinnicombe and Dr David Sutton.

What if something goes wrong?

If you have any concerns about your participation in the study you have the right to raise your concern with a researcher involved in conducting the study or a doctor involved in your care.

If you have a complaint about your participation in the study, you should first talk to a researcher involved in the study. However, you have the right to raise a formal complaint. You can make a complaint to a senior member of the research team or to the NHS Complaints Officer for NHS Tayside;

Complaints and Feedback Team
NHS Tayside
Ninewells Hospital
Dundee DD1 9SY
Freephone: 0800 027 5507
Email: feedback.tayside@nhs.net

In the event that you think you have suffered harm as a result of your participation in the study there are no automatic financial compensation arrangements. However, you may have the right to make a claim for compensation. Where you wish to make a claim, you should consider seeking independent legal advice but you may have to pay for your legal costs.

The University of Dundee and Tayside Health Board are Co-Sponsoring the study. The University of Dundee maintains a policy of public liability insurance which provides legal liability cover in respect of damages, costs and expenses arising out of claims.

Tayside Health Board is a member of the NHS Scotland Clinical Negligence and Other Risks Insurance Scheme (CNORIS) which provides legal liability cover of NHS Tayside in relation to the study.

As the study involves University of Dundee staff undertaking clinical research on NHS Tayside patients, such staff hold honorary contracts with Tayside Health Board which means they will have cover under Tayside's membership of the CNORIS scheme.

You should be aware that if you apply for health, life, travel or income protection insurance you may be asked questions about your health, including medical history, pre-existing medical conditions, if you have had any genetic test or your participation in this study. It is not anticipated that your involvement in the study will adversely affect your ability to purchase insurance but some insurers may use this information to limit the offer of cover, apply exclusions or increase any premium. If you have a diagnosed medical condition, even where the condition is diagnosed as part of a research study, the insurer may take this in to consideration when deciding whether to offer insurance to you.

Further information and contact details

If you have any questions about the study, please contact:

Principal Investigator; Mark Worrall, Clinical Scientist, Ninewells Hospital on 01382 632 177

Email: markworrall@nhs.net

Chief Investigator; Dr Sarah Vinnicombe, Ninewells Hospital on 01382 383 286

Clinical Supervisor; Dr David Sutton, Ninewells Hospital on 01382 632 700

You can contact us Monday – Friday between 09:00-17:00.

Thanks for taking time to read this information and for considering participating in this study.

If you would like to participate in the study, or if you need more information before deciding, please complete the attached reply slip and the principal investigator will speak with you before your x-ray.